Etude expérimentale et simulation numérique des propriétés mécaniques à gradient d'aciers 316L générées par SMAT

Yangcan Wu

Thèse
de doctorat
de l'UTT

Yangcan WU

Experimental Study and Numerical Simulation of the Gradient Properties of 316L Steels Generated by SMAT

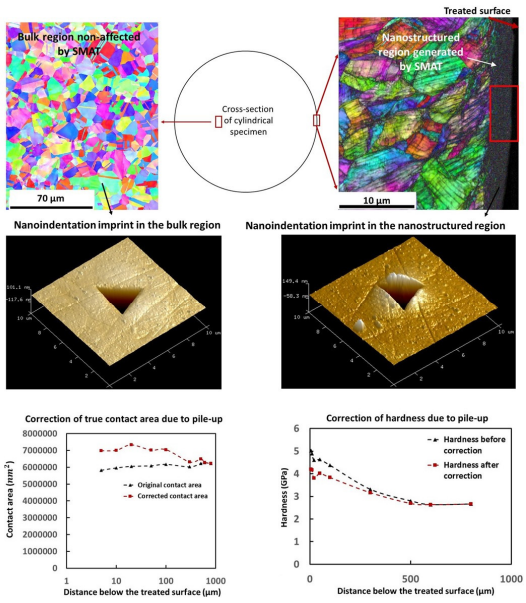

Champ disciplinaire :
Sciences pour l'Ingénieur

2019TROY0011

Année 2019

utt
UNIVERSITÉ DE TECHNOLOGIE
TROYES

THESE

pour l'obtention du grade de

DOCTEUR
de l'UNIVERSITE DE TECHNOLOGIE DE TROYES

EN SCIENCES POUR L'INGENIEUR

Spécialité : MATERIAUX, MECANIQUE, OPTIQUE, NANOTECHNOLOGIE

présentée et soutenue par

Yangcan WU

le 30 avril 2019

Experimental Study and Numerical Simulation of the Gradient Properties of 316L Steels Generated by SMAT

JURY

M. S. BENAYOUN	PROFESSEUR DES UNIVERSITES	Président
Mme S. BOUVIER	PROFESSEURE DES UNIVERSITES	Rapporteure
M. G. MAUVOISIN	PROFESSEUR DES UNIVERSITES	Rapporteur
Mme S. CASTAGNE	PROFESSOR	Examinatrice
M. B. MERLE	DOCTEUR INGENIEUR	Examinateur
Mme A. MERTENS	CHARGEE DE COURS	Examinatrice
Mme D. RETRAINT	PROFESSEURE DES UNIVERSITES	Directrice de thèse
M. Z. SUN	ENSEIGNANT CHERCHEUR UTT	Directeur de thèse

To my family, my teachers and my friends.

ACKNOWLEDGEMENTS

Foremost, I would like to express my deepest gratitude to my supervisors, Dr. SUN Zhidan and Pr. RETRAINT Delphine, for their superior guidance, considerable support and encouragement throughout my PhD study at UTT. Their kindness, patience and encouragement have helped me overcome those difficult periods during my PhD career. Even when the thesis wasn't going well, all I hear are words of encouragement and all I see are two big warm smiles.

I would also like to extend my sincere thanks to Dr. GUELORGET Bruno, for his countless help all these years. It is true that some heroes don't wear cape. All you need to do is writing an e-mail or making a phone call, and that he will just fly right to the scene and get everything covered up. Bruno is also a walking French dictionary. I learn a lot from him. But sometimes I got confused when seeing some of his phrases, for instance 'A pluche'. At first glance, I thought that might be a new word and I looked it up in a dictionary and there is not such a word.

Moreover, I would like to express my special thanks to all my friends in UTT for their company and friendships all these years. I will try to make a list, but if I forget someone, please don't be mad. You know you are in my heart. They are:

ZHU Shijie, TANG Feng, ZHOU Jianqiang, ZHANG Kai, DAI Fang, HUANG Yi, MA Xiao, LI He, MA Jinrui, MA Jianbo, ZHOU Lan, GE Dandan, HAN Yurui, JIA Ci, ZHANG Feifei, WANG Shijian, CHEN Hongshi, XU Xiaolun, MENG Yuan, WANG Binbin, ZHU Yunlong, ZHOU Junze, WANG Xixi, WANG Zhimao, LI Yizhuo, CHEN Zhenglin, HU Ronghua, YANG Tian, SERVEAUX Jérémy, PERROT Nathan, TOMASELLI Victor, RENAUD Thibaud, FILEUX Antoine, VALLON Thomas, MARTIN Félix, BICHET Jean.

My sincere thanks should also go to the rest of the thesis committee members: Mme BOUVIER Salima, Mr. MAUVOISIN Gérard, Mr. BENAYOUN Stéphane, Mme

CASTAGNE Sylvie, Mme MERTENS Anne and Mr. MERLE Benoît for their patience to examine my work and giving insightful comments.

I am also grateful to the colleagues in UTT, who gave me much help in technical support, experimental experiences, and valuable advices. They are Mr. WEIL François, Pr. GONG Xiaolu and other colleagues of LASMIS.

Last but not least, I would like to show my most sincere thanks to my family, especially my mother who always treats me as a nine-year-old child even though I am thirty already. We had a few disputes over this but she keeps doing that. In her own words: “even when you are 40 or more, you are still a little boy to me”. Well, a mother’s love is a mother’s love. One can’t possibly argue with that.

Yangcan WU

January 2019, at Troyes

Abstract

This work focuses on experimental characterization of the gradient microstructure of 316L steels treated by SMAT, which could be roughly divided into the nanostructured layer, transition layer and bulk region. Grain refinement, compressive residual stress and strain hardening are three major SMAT-induced parameters as a result of severe plastic deformation. Consequently, the enhanced properties of the gradient microstructure are due to the combined effects of these SMAT-induced changes. However, emphasis was mainly placed on the global properties of the gradient microstructure and little effort was devoted to the individual characterization of each layers. The aim of this work is to investigate individually the mechanical properties of each layers by means of various characterization techniques.

Characteristics of the gradient microstructure of a 316L steel treated by SMAT are characterized by SEM, EBSD, XRD, AFM. In regard with the mechanical properties, nanoindentation and micro-pillar compression are applied for the individual investigation of each layers of the gradient microstructure. It should be clarified that these three parameters all vary as function of the distance below the treated surface, leading to different mechanical properties of each layer. In this work, nanoindentation and micro-pillar compression allow to perform tests at different layers of the gradient microstructure and the corresponding mechanical properties could be subsequently derived.

Another part of this work involves using Finite element method for the simulation of nanocrystalline material despite of its limitations. A crystal plasticity model was used and efforts were made to take into account the length scale effects by modifying several parameters, such as volume fraction of grain boundaries, critical resolved shear stress. The Voronoi diagram and Level-Set function were applied for the generation of a two-dimensional FEM models.

Keywords: Shot peening, Austenitic stainless steel, Nanoindentation, EBSD.

Résumé

Ce travail porte sur la caractérisation expérimentale de la microstructure de gradient de l'aciers 316L traité par SMAT, qui pourrait être divisée approximativement en zone nanostructurée, zone de transition et zone du matériau à cœur non-affectée. Le raffinement du grain, les contraintes résiduelles compressive et écrouissage sont trois paramètres majeurs induits par SMAT en raison d'une déformation plastique sévère. Par conséquent, les propriétés améliorées de la microstructure de gradient sont dues aux effets combinés de ces changements induits par SMAT. Cependant, l'accent a surtout été mis sur les propriétés globales de la microstructure de gradient et peu d'efforts ont été consacrés à la caractérisation individuelle de chaque couche. L'objectif de ce travail est d'étudier individuellement les propriétés mécaniques de chaque couche au moyen de différentes techniques de caractérisation.

Les caractéristiques de la microstructure de gradient d'un acier 316L traité par SMAT sont caractérisées par SEM, EBSD, XRD, AFM. En ce qui concerne les propriétés mécaniques, la nanoindentation et la compression de micro-piliers sont appliquées pour l'étude individuelle de chaque couche de la microstructure de gradient. Il convient de préciser que ces trois paramètres varient tous en fonction de la distance sous la surface traitée, ce qui conduit à des propriétés mécaniques différentes pour chaque couche. Dans ce travail, la nanoindentation et la compression micro-pilier permettent d'effectuer des essais sur différentes couches de la microstructure de gradient et les propriétés mécaniques correspondantes peuvent ensuite être dérivées.

Une autre partie de ce travail consiste à utiliser la méthode des éléments finis pour la simulation des matériaux nanocristallins malgré ses limites. Un modèle de plasticité cristalline a été utilisé et des efforts ont été faits pour prendre en compte les effets de l'échelle en modifiant plusieurs paramètres, tels que la fraction volumique de joints des grains, la contrainte de cisaillement critique résolue. Le diagramme de Voronoi et la fonction Level-Set ont été utilisés pour générer des modèles FEM bidimensionnels.

Mots clés : Grenaillage de précontrainte, Acier inoxydable austénitique, Nanoindentation, Analyse EBSD.

CONTENTS

List of Tables

List of Figures

General introduction

Since the remarkable article written by H. Gleiter in 1989 [1], efforts have been devoted to a new direction in materials science. In this article, Gleiter highlights the remarkable possibilities of nanocrystalline (NC) materials. These NC materials are polycrystals, typically characterized by a grain size of less than 100 nm. As a result of these extremely small dimensions, the NC materials have a large volume fraction of grain boundary that can significantly alter a variety of their physical, mechanical or chemical properties compared to their conventional counterparts with micrometer scale grains. In fact, most of the properties of NC materials are often recognized to be superior, compared to their conventional counterparts. For example, NC materials exhibit higher hardness and mechanical resistance [2][3].

NC materials can be synthesized either by consolidating small clusters or breaking down the polycrystalline bulk material into crystalline units with dimensions of nanometers [3]. These approaches have been classified into bottom-up and top-down. In the bottom-up approach we have to arrange the nanostructure atom-by-atom, layer-by layer. In the top-down approach we start with the bulk material and break down the microstructure into a nanostructure. The principal synthesis methods are: Inert gas condensation [1], Mechanical alloying [4], Electrodeposition [5], Crystallization from amorphous material [6], Severe plastic deformation [7] etc. In terms of the great diversity of nanocrystallization methods, there are differences in microstructure and mechanical behaviour of NC materials synthesized by different methods, which could be referred to grain size, porosity rate and different contamination rate depending on the technique used. We should also note that most of these processes only allow the synthesis of small volume samples.

Surface Mechanical Attrition Treatment (SMAT) is one of the most promising mechanical surface treatment techniques to generate NC materials. It is based on the repetitive multi-directional impacts between the surface of a part and spherical shot boosted by an ultrasonic generator [8][9]. The near surface region is mechanically affected by SMAT. It can lead to a progressive grain size refinement due to severe plastic deformation,

whereas the bulk of the part is not mechanically deformed, so that its characteristics remain unchanged as well as its mechanical properties. A gradient microstructure is thus formed from the treated surface to the interior region of the material [10]–[13]. The particularity of SMAT with respect to conventional shot peening lies in the fact that it can transform the top surface layer of materials from coarse grains to nano-sized grains [8][9]. This nanostructured layer, even if it is thin in general [12], could have significant effect on the performance of materials, since engineering components are mostly loaded on their surface, for example in the case of friction, torsion or contact loadings .

To understand the mechanical behaviour of SMATed materials, it is important to characterize the mechanical properties of different regions, for example the nanostructured layer and the mechanically deformed region. Characterization of the local mechanical behaviour of the nanostructured layer is difficult, given its very small thickness (from several microns to tens of microns, depending on the treatment intensity). In the literature, nanoindentation technique was widely used to study the local mechanical behaviour of materials [14],[15] such as thin films [16]–[18], multi-phased materials [19]–[21] etc. Although nanoindentation seems to be one of the best methods to study local mechanical behaviour at small length scale, there are some limitations for this technique. For instance, the indenter heads are often three-sided Berkovich tips or spherical tips and the load is applied on the surface of the sample. As a result, these indenter tips can cause non-uniform stress field in the near contact region, and only typical load-penetration curves can be obtained. This prevents from straightforward access to the mechanical properties of material, for example in the form of stress-strain curve which is of primary interest for engineers.

Micro-pillar compression was originally used to investigate the mechanical properties and understand the deformation mechanisms of single crystals [22][23]. Thanks to its simplicity and capacity of direct access to uniaxial mechanical behaviour of materials at micrometer scale, it is becoming a popular method to quantitatively characterize the local mechanical properties of materials. Using this technique, stress-strain curve can be easily calculated from the load-displacement curves obtained after compression tests, and obtaining other information such as yield stress is more straightforward than for example the nanoindentation technique. However, the micro-pillar compression technique has not yet been widely used to study materials processed by mechanical surface treatments such as SMAT.

In this work, the local mechanical behaviour of gradient microstructure of 316L stainless steel generated by SMAT was investigated using the micro-pillar compression technique and nanoindentation.

In the first chapter, several methods available for the generation of nanocrystallized materials are introduced, followed by a detailed description of SMAT technique (treatment devices, improved properties of SMAT and grain refinement mechanism etc.). A brief introduction about the generation mechanism of nanostructure for some materials is also presented. At last, as the mechanical properties of NC materials are of major interest, the novel properties of NC materials along with their deformation mechanisms are discussed in details.

The second chapter is dedicated to demonstrate all the characterization methods used in this thesis work. Detailed descriptions of all the characterization methods are given. The techniques used for microstructure characterization (SEM, EBSD, AFM) are introduced. As for the characterization of the mechanical properties after SMAT treatment, instrumental nanoindentation and micro-pillar compression are used.

For the third chapter, the microstructure characterizations results by SEM and EBSD are presented. First, the initial microstructure of the 316L stainless steel is examined by SEM, followed by detailed investigations of the microstructure by EBSD after SMAT. A detailed comparison between the initial microstructure and the final one is discussed in the end.

The fourth chapter begins with a discussion about three major changes induced by SMAT that will affect the nanoindentation measurements. Then, the results obtained are listed (load-displacement curves, Young's modulus, hardness indentation size effect and pile-up behavior) followed by detailed interpretations. Besides monotonic loading tests, the results of cyclic loading tests are presented and discussed as well.

The fifth chapter is dedicated to micro-pillar compression tests. First, several factors affecting the compression tests are discussed, followed by the experimental results and interpretations. Besides monotonic tests, cyclic loading tests were simultaneously performed on micro-pillars.

The sixth chapter is dedicated to simulations using finite element method. A crystal plasticity model was used to simulate the mechanical properties of SMATed material. Corresponding results are interpreted subsequently.

Chapter 1: Literature review

In this chapter, several methods available for the generation of nanocrystallized materials are first introduced, followed by a detailed description of the technique SMAT (treatment devices, improved properties of SMAT and grain refinement mechanism etc.). A brief introduction about the generation mechanism of nanostructure for some materials is also presented. At last, as the mechanical properties of NC materials are of major interest, the novel properties of NC materials along with their deformation mechanisms are discussed in details.

1.1 Principal synthesis methods for nanocrystalline materials

Nanocrystalline materials can be synthesized either by consolidating small clusters or breaking down the polycrystalline bulk material into crystalline units with micscopic dimensions. These approaches have been classified into bottom-up and top-down. In the bottom-up approach we have to arrange the nanostructure atom-by-atom, layer-by layer. In the top-down approach we start with the bulk material and break down the microstructure into a nanostructure. The principal synthesis methods are:

-Inert gas condensation

-Mechanical alloying

-Electrodeposition

-Crystallization from amorphous material

-Severe plastic deformation

-Plasma synthesis

Here we will briefly describe the five most commonly used techniques.

1.1.1 Inert gas condensation

The inert gas condensation (IGC) technique, conceived by Gleiter [1], consists of evaporating a metal inside a chamber that is evacuated to a very high vacuum and then backfilled with a low-pressure inert gas like helium (Fig. 1.1(a)) [24]. These evaporated atoms possess a certain amount of kinetic energy and condense in the form of small particles as a result of collisions with the gas atoms. The heating of the inert gas by the evaporation source and the cooling of the liquid nitrogen-filled collection device generates convection currents that will transport the condensed fine powders to the collector device.

The deposit is later scraped off for compaction in order to form a fully-dense structure. The compaction is realised by two processes: (a) low pressure compacted pellet; (b) high pressure vacuum compaction. It should be emphasized that a ultrahigh vacuum conditions is required during the scraping and compaction so as to avoid contamination of the sample and minimize the amout of trapped gases. The characteristic of IGC technique consists in the fact that this method synthesizes equiaxed (3D) crystallites. The crystal size of the powder is typically a few nanometers and the size distribution is narrow. The crystal size is determined by the inert gas pressure, the evaporation rate, and the gas composition. For example, decreasing the gas pressure in the chamber or the evaporation rate or using light inert gases are both favorable for the formation of extremely fine particles.

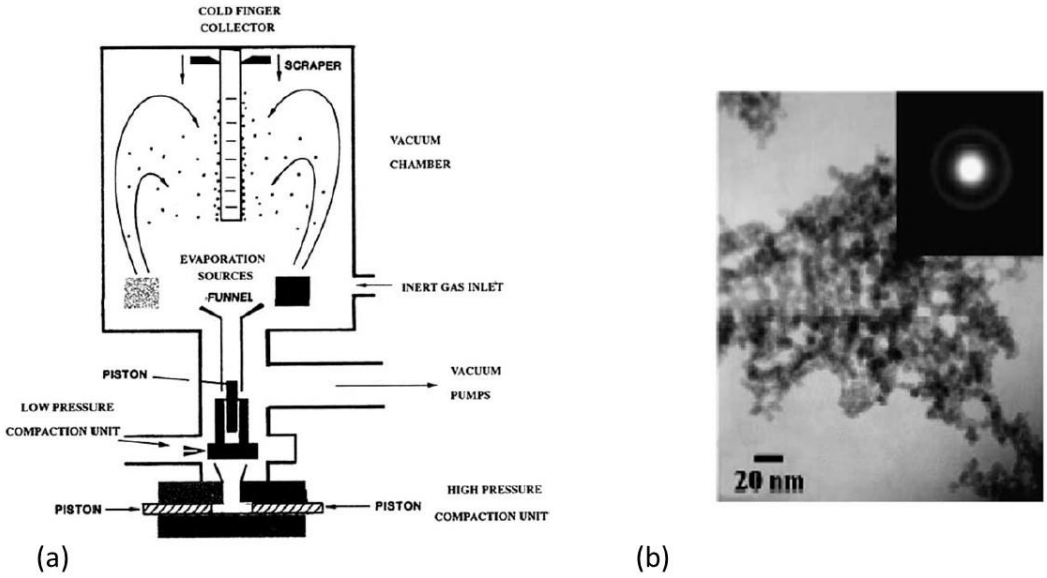

Fig. 1.1 (a) Schematic drawing of the inert gas condensation technique for production of nanoscal powder [24], (b) bright field TEM micrograph of TiO2 nanoparticles prepared by inert gas condensation [25].

IGC technique was the major synthesis method for the early studies of NC materials. However, one disadvantage is the possibility of contamination of powders and porosity by reason of deficient consolidation. In addition, imperfect bonding between particles can be another problem since most of the early work used cold consolidation. Imperfections will in turn lead to reduced elastic modulus, decrease of yield stress [2] etc. Fig. 1.1(b) shows the bright field TEM micrograph of TiO_2 nanoparticles prepared by this technique [25].

1.1.2 Mechanical alloying

Mechanical alloying [4] produces nanostructured materials by the structural fragmentation of coarse-grained structure as a result of severe plastic deformation.

The principle of mechanical alloying lies in repeated deformation of powder particles in a dry high-energy ball mill until the desired composition is realised. During this process, a protective atmosphere is set under which the powders undergo heavy grinding. Fig. 1.2(a) shows the set-up for ball milling process [26]. It has been demonstrated that nanometer-sized structures can be achieved in almost any material if the milling time is sufficiently long. As a matter of fact, the grain size decreases with milling time but the achievable grain size has a minimum limit below which an increase in milling time will cause an opposite effect for the grain size. Fig. 1.2(b) [26] shows a dark-field TEM micrograph of an Al-Mg alloy processed by ball milling at 77 K and annealing at 150°C. The grain size distribution ranging from 20 to 200 nm is clearly observed.

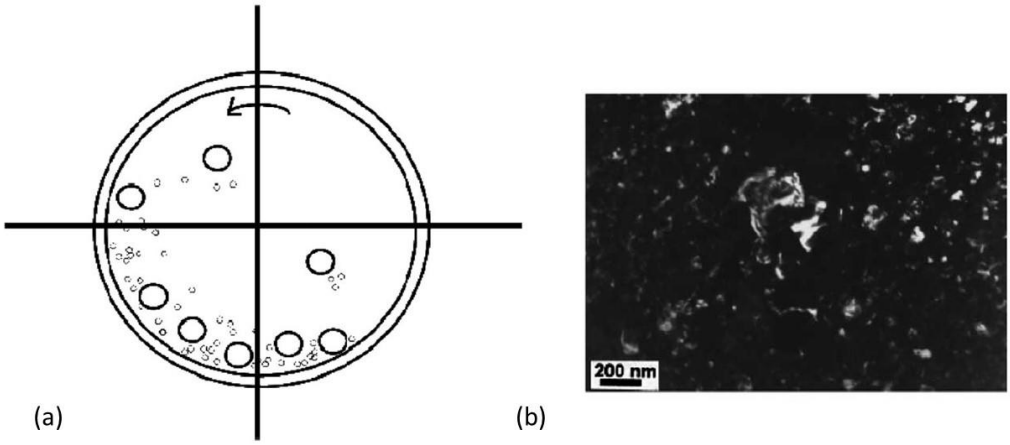

Fig. 1.2 (a) Mechanical milling as a means of synthesis of nanostructured material. (b) Dark field image of nanocrystalline Al-Mg alloy synthesized by cryogenic ball milling [26].

1.1.3 Electrodeposition

The principle of electrodeposition [5] is inducing chemical reactions in an aqueous electrolyte solution with the help of applied voltage. It's the process of using electrical current to coat an electrically conductive object with a relatively thin layer of metal. Fig. 1.3(a) illustrates schematically the pulse electrodeposition sequence. As the current spikes, the metal cations are deposited in crystalline and amorphous patches. Fig. 1.3(b) shows the TEM micrograph of pulse electrodeposited Ni sample [3].

Compared to other synthesis methods, the electrodeposition technique has several appealing advantages that make it outstanding: (1) capability of synthesizing various kinds of materials – pure metals, alloys and composite systems, (2) low cost, (3) high production

rates, (4) few size and shape limitations, and (5) high probability of transferring this technology to existing electroplating and electroforming industries [3].

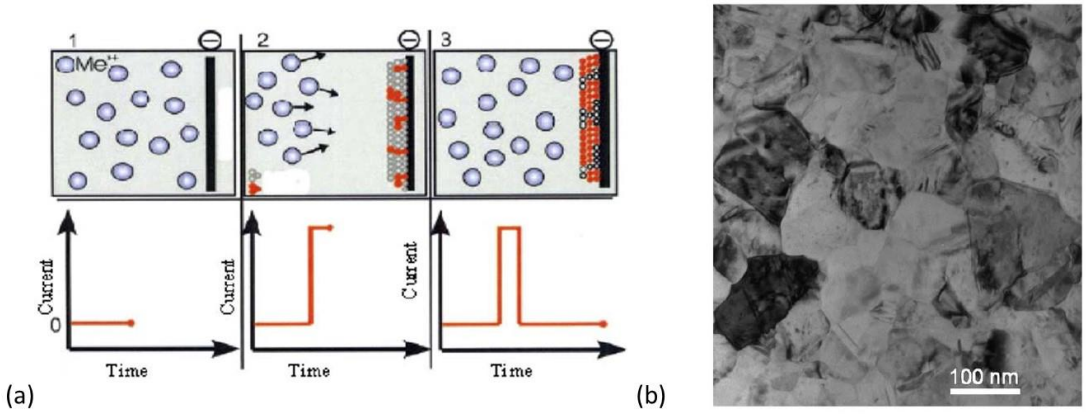

Fig. 1.3 (a) Pulse electrodeposition set-up for synthesizing nanocrystalline materials, (b) Pulse electrodeposited Ni.

1.1.4 Crystallization from amorphous solids

The basic principle for the crystallization method from the amorphous state [27] is to control the crystallization kinetics by optimizing the heat treatment conditions, which allows the transition from amorphous phase to polycrystalline phase with the formation of ultrafine crystallites. Successful synthesis of nanocrystalline Fe-, Ni-, and Co-based alloys has been achieved by crystallization of amorphous solids [6], [27]–[29]. One appealing advantage of crystallization of amorphous solids is that porosity-free structures can be produced. The driving force for the transition from amorphous phase to crystalline phase is the difference in the Gibbs free energy between the two phases as crystalline solids are more stable. As a result, amorphous solids can be easily converted when subjected to heat treatment [30], irradiation [31], or even mechanical attrition. TEM images and the selected area diffraction patterns of Ni-25at%W alloys annealed at 723 K and 873 K for 24 h in vacuum show that extremely small sized grains can be crystallized from amorphous materials as shown in Fig. 1.4 [32].

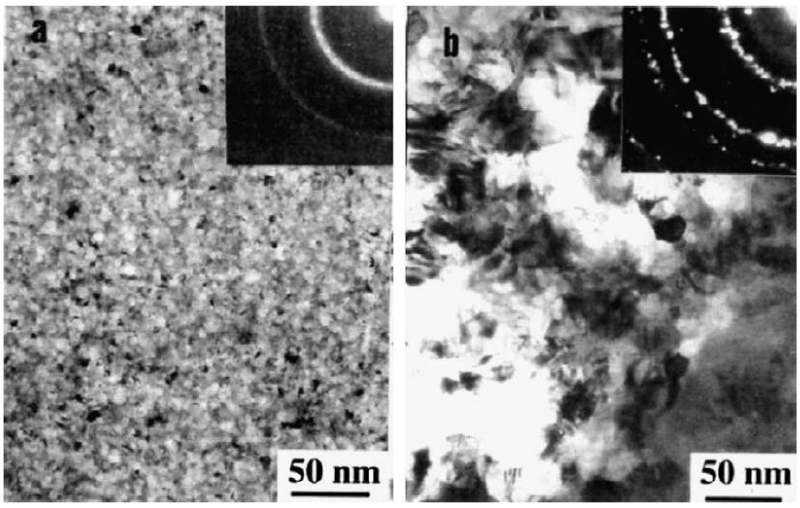

Fig. 1.4 TEM images and selected area diffraction patterns in the Ni–25.0at%W alloy annealed from amorphous state at (a) 723 K and (b) 873 K for 24 h in vacuum [32].

1.1.5 Severe plastic deformation

Severe plastic deformation (SPD) is a top-down approach which allows grain refinement by the fragmentation of coarse-grained structure [7]. It is one of the most widely used processes for producing bulk ultra-fine grained materials. In particular, SPD methods could overcome a number of difficulties connected with residual porosity in compacted samples, impurities from ball milling, processing of large scale billets and practical application of the given materials. There are several available SPD methods, and the most commonly used ones are high pressure torsion (HPT) [33] and equal channel angular pressing (ECAP) [34]. A schematic illustration of these two methods is shown in Fig. 1.5 [7].

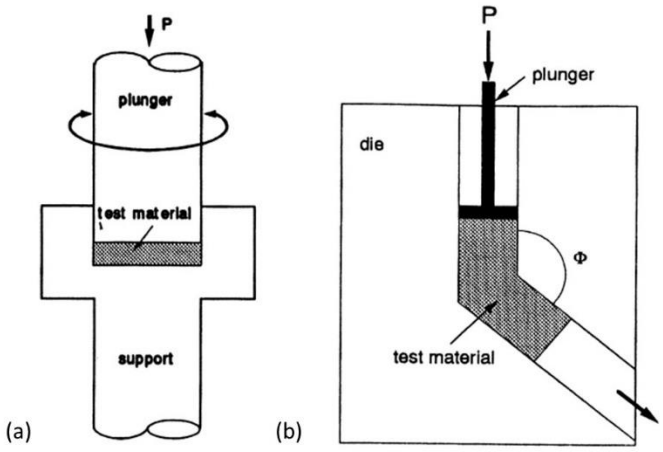

Fig. 1.5 Devices of SPD methods: (a) torsion under high pressure, (b) equal channel angular pressing [7].

Fig. 1.5(a) shows the principle of HPT. A disk-formed sample with a diameter of 10-20 mm and a thickness of about 1 mm is held under high pressure and then subjected to straining in torsion under an applied pressure of several GPa. The lower anvil turns and friction forces result in shear straining of the sample. Fig. 1.5(b) demonstrates the device of ECAP. During ECAP a billet is multiply pressed through a special die using an equal channel angular facility in which the angle of interSection of two channels is usually 90°. SPD methods exhibit great applicability to various metals and are promising as for producing NC materials in bulk form. However, current difficulties of synthesizing larger dimension and sufficient homogenous nanostructure are still to be overcome.

1.2 Surface mechanical attrition treatment (SMAT) as a nanostructure synthesis method

1.2.1 Description of SMAT

As a kind of ultrasonic peening technologies, Surface Mechanical Attrition Treatment (SMAT) is one of the most promising mechanical surface treatment techniques. It is based on the repetitive multi-directional impacts between the surface of a part and spherical shot boosted by an ultrasonic generator [8][9]. It allows introducing severe plastic deformation at the surface of the treated sample and as a result, a surface nanocrystalline layer is formed subsequently while the microstructure of the bulk material is unchanged. SMAT can be classified as one of the SPD synthesis methods for nanocrystalline materials as mentioned earlier.

Fig. 1.6 schematically illustrates the experimental setup of SMAT. Spherical shots with smooth surfaces are placed in a closed chamber and are boosted by the vibration generator. During the treatment process, the surface of the sample is subjected to repetitive impacts by a large number of shots with high velocity over a short period of time. It should be pointed out here that the directions of the flying shots onto the sample surface are quite random. These repetitive multidirectional impacts are able to induce plastic deformation with a high strain-rate in the top surface of the sample. As a consequence, a nanostructured layer is formed at the surface of the sample [9]. Nevertheless, the microstructure of the bulk material remain unchanged. Hence, a gradient of microstructure from the top surface to the bulk material of the sample is formed.

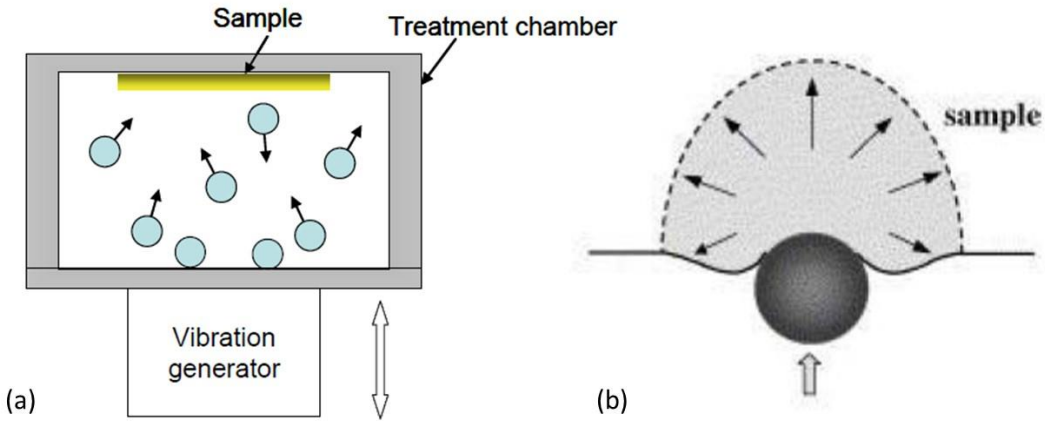

Fig. 1.6 Principle of SMAT: (a) experimental setup, (b) the localized plastic deformation in the surface layer induced by the impact of the ball [9].

1.2.2 Improved properties after the treatment

The mechanical and chemical properties of the treated sample after SMAT can be significantly improved as a result of the grain refinement. For example, the hardness of the nanostructured layer generated by SMAT can be 2 to 3 times higher than that of the unaffected bulk material [35]–[37]. A harder surface can consequently improve the friction and wear properties [38]–[40]. Another important enhanced property is the yield strength, as higher yield strength is a fundamental fact about nanocrystalline materials [2][3]. The mechanism of enhanced yield strength will be addressed in details in Section 1.4.2. The fatigue property can also be enhanced. SMAT treatment is able to induce high compression residual stress and grain refinement at the top surface of the treated sample, which are capable to resist crack initiation and propagation [10], [12]. As a nanostructured layer is formed at the top surface after SMAT, the volume fraction of grain boundaries of this layer has also been significantly increased. These grain boundaries serve as favourable diffusion channels, hence the atomic diffusivity in the nanostructured surface layer is largely enhanced compared with their conventional coarse-grained counterparts [41], [42]. This improved diffusivity might be applied for some traditional surface chemical treatment, such as the nitriding process of steel [41], [42].

1.3 The surface nanocrystallization mechanism of different materials

As mentioned above, SMAT is able to generate a nanostructured layer at the top surface of the treated sample while the bulk material of the sample is not affected. Thus, a microstructure gradient is formed. Consequently, the grain size at the top surface can be

down to tens of nanometers and for the bulk material the grain size usually ranges from a few to tens of micrometers. The reason behind this phenomenon is that the strain and strain-rate induced during the treatment vary as a function of the depth to the treated surface. The strain and strain-rate are highest at the top surface and decrease as a function of the depth from the treated surface, as schematically shown in Fig. 1.7 [9].

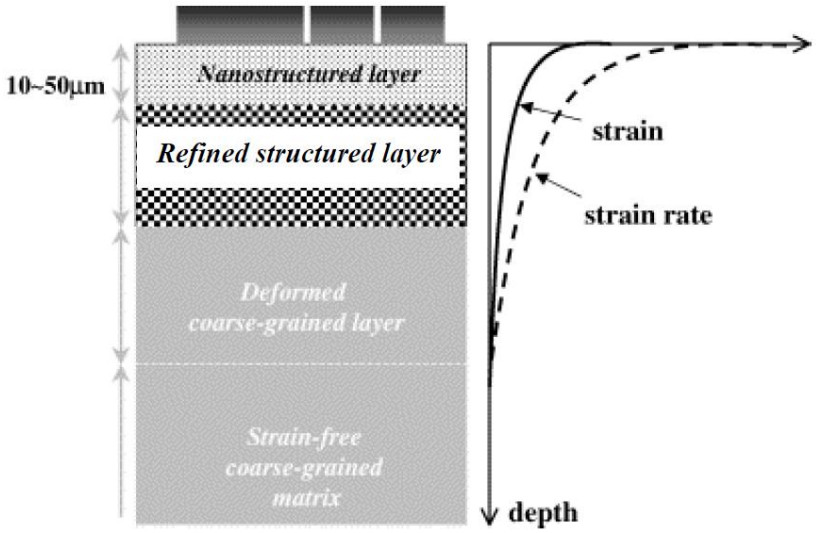

Fig. 1.7 Microstructure characteristics and distributions of strain and strain-rate along depth in the surface layer subjected to SMAT [9].

The formation mechanisms of nanostructured materials have been systematically investigated in numerous reports [43]–[49]. As is known, the lattice structure and stacking fault energy (SFE) have a crucial influence on the plastic deformation behaviour and dislocation activities in metals, and the formation mechanism of the nanostructured layer is different accordingly for materials with different structures and stacking fault energy. In general, three formation mechanisms can be identified as a function of stacking fault energy of the treated sample. For materials with high SFE, such as Fe (about 200 mJ/m^2), the grain refinement and microstructure development during SMAT can be summarized as follows [8], as shown in Fig. 1.8.

-1) Development of dense dislocation walls (DDWs) and dislocations tangle (DTs) in original grains and in the refined cells;
-2) Transformation of DDWs and DTs into sub-boundaries with small misorientations separating individual cells or sub-grains;
-3) Evolution of sub-boundaries into highly misoriented grain boundaries;
-4) Formation of nanostructures in the top layer.

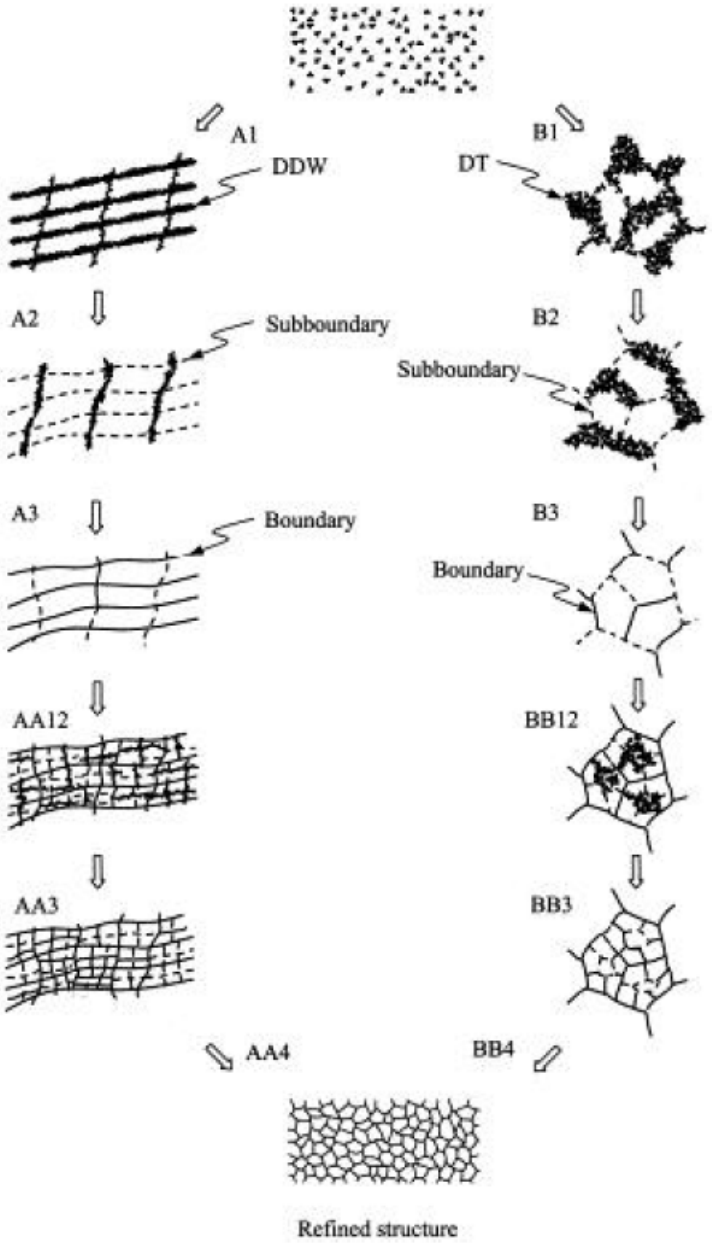

Fig. 1.8 Grain refinement of Fe [8].

For materials with low SFE, such as AISI 304 stainless steel (about 17 mJ/m^2), the grain refinement mechanisms during SMAT are summarized as follows [44], as shown in Fig. 1.9.

-1) Formation of planar dislocation arrays and mechanical twins;
-2) Grain subdivision by twins and martensitic transformation;
-3) Formation of randomly oriented nanocrystallites.

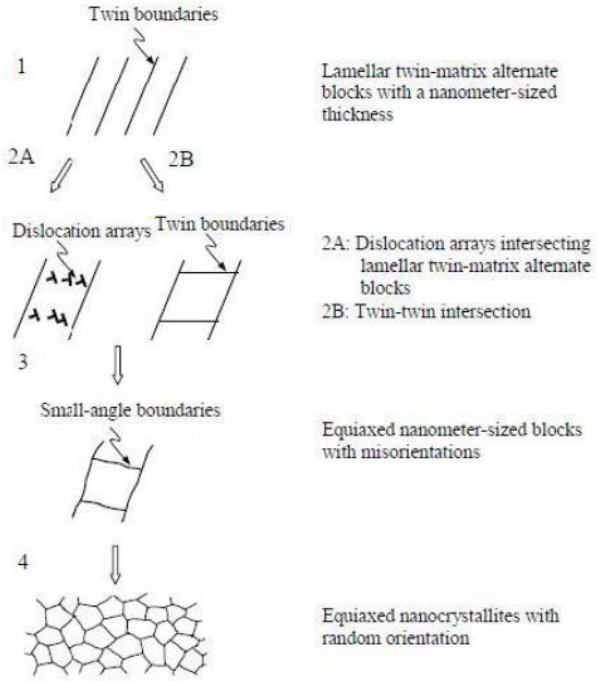

Fig. 1.9 Grain refinement mechanism during SMAT for AISI 304 stainless steel [44].

For materials with medium SFE, such as Cu (about 78 mJ/m^2), the grain refinement mechanisms during SMAT are summarized as follows [47].

For the top surface layer (thickness < 25μm):

-1) Formation of high-density, nanometer-thick twins dividing the original coarse grains into T–M lamellae;

-2) Development of dislocation walls that further subdivide the T–M lamellae into equiaxed nanosized blocks;

-3) Evolution of these preferentially oriented blocks into randomly oriented nanosized grains;

-4) Formation of nanostructures in the top layer.

For the subsurface layer (thickness > 25μm):

-1) Formation of dislocation cells (DCs) in original grains;

-2) Transformation of DC walls into sub-boundaries with small misorientations separating the initial grains into individual sub-grains;

-3) Evolution of sub-boundaries into highly misoriented grain boundaries.

1.4 Properties and deformation mechanisms of nanocrystalline materials

As mentioned above, properties of a material could be significantly improved by reducing the grain size down to nanometer scale while the chemical composition of the material is unchanged. Novel properties thanks to nano-grain have drew attentions of many researchers. In this project, mechanical properties of NC layer generated by SMAT are our main concern. Therefore, the mechanical responses of NC metals, such as Hall-Petch effect, yield strength, hardness, ductility and deformation mechanism will be discussed in detail in this Section.

1.4.1 Hall-Petch law

The Hall-Petch law which reveals the relationship between grain size and yield strength was initially discovered by Hall [50] and Petch [51] independently in the 1950s. Interestingly, they found the same conclusion when studying different mechanical behaviors. Hall studied the relationship between the yield stress of a single crystal and the maximum length of the slip band while Petch investigated the relationship between the cleavage strength and the mean intercept length. It turned out that these two factors were both related to the grain size. The Hall-Petch law suggests that yield stress increases with the inverse of the square root of the grain size:

$$\sigma_y = \sigma_0 + kd^{-1/2} \qquad (1\text{-}1)$$

where σ_y is the yield strength for materials with grain size d, σ_0 is the friction stress and k is a constant. The mechanism of Hall-Petch law is believed to be that the increasing fraction of grain boundaries with decreasing grain size which serve as obstacles for dislocation movements. Hence, dislocation piles up at the grain boundaries in which case higher stress is necessary as plastic deformation proceeds.

However, as grain size decreases down to the nanometer regime, the volume fraction of grain boundaries increases considerably and deformation mechanism seems to change. In recent years, many researchers have reported a deviation from the Hall-Petch law or even the inverse Hall-Petch relation [52]–[56] when the grain size is below a critical value (seen in Fig. 1.10) [3]. It should be noted that the dependence of yield stress on grain size in metals is well established in the conventional polycrystalline range (micrometer and larger sized grains). As for smaller grain size, there could be significant decrease in the slope for

Hall-Petch law or even inverse Hall-Petch relation. Meyers et al. [3] summarized the Hall-Petch trends for a range of grain sizes from the microscopic to the nanoscopic regime from different sources for four different metals: Cu, Fe, Ni and Ti, which is shown in Fig. 1.11 [3].

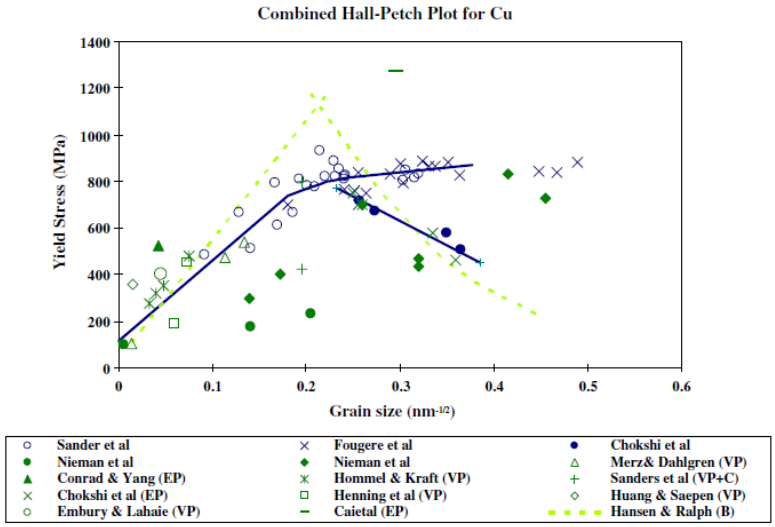

Fig. 1.10 Compiled yield stress versus grain size plot for Cu from various sources ranging from coarse to nanograin size. The plots show different trend as the grain size falls below a critical size [3].

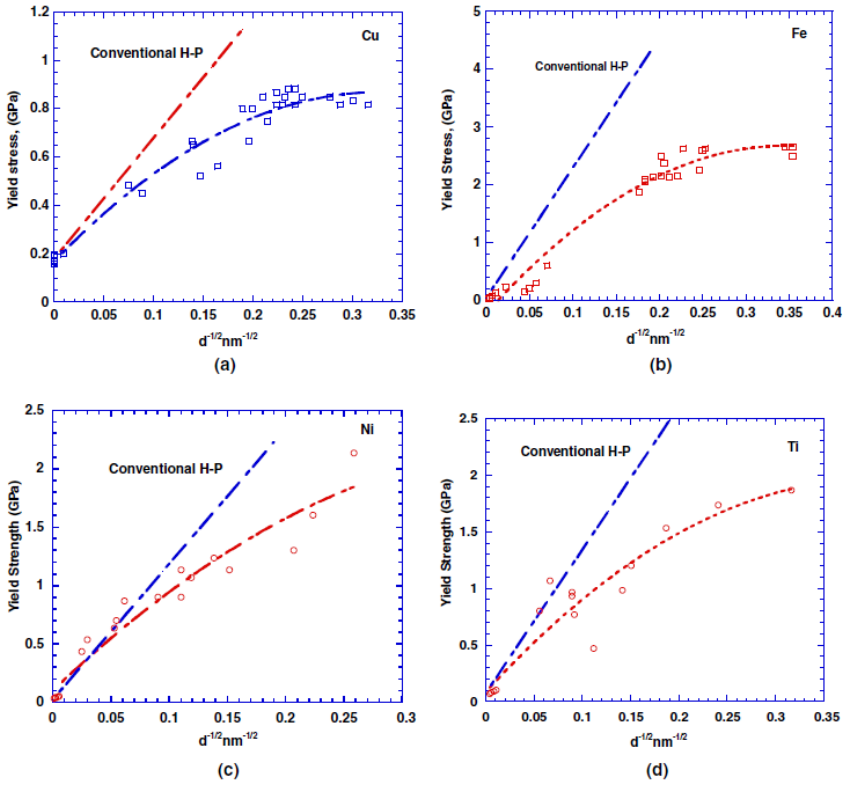

Fig. 1.11 Plots showing the trend of yield stress with grain size for different metals as compared to the conventional Hall–Petch response: (a) copper, (b) iron, (c) nickel and (d) titanium [3].

Chokshi et al. [55] were the first to report the negative Hall–Petch effect by performing measurements on NC Cu and Pd samples made by inert gas condensation. They attributed this negative trend to diffusional creep in NC samples at room temperature which was analogous to grain-boundary sliding in conventionally-grained samples at high temperature. Nevertheless, weertman [57] suggested that the change of Hall-Petch law could be due to the imperfections (flaw, porosity etc.) and contamination caused by certain synthesis methods like IGC. One commonly accepted opinion is that when grain size is down to a critical value (10 nm, for example), deformation mechanisms such as grain boundary sliding [58]–[60], grain rotation [61], [62], nano-twins [63], [64] and grain boundary diffusion [55], [65], [66] begin to intervene in the deformation process or even dominate the plastic deformation. It is argued that when grain size is down to 10 nm, the size of grain approaches the size of dislocations therefore, there are few dislocations inside a nano-grain hence dislocation-mediated mechanism is not considered as a dominant mechanism and grain boundary-mediated deformation is thought to be the major mechanism. However, Koch [67] argued that whether the so-called Hall-Petch effect is fact or artifact remains debatable. He summarized the data of divers reports and proposed that many factors could contribute to the measurement of the strength of materials like distribution of grain size, porosity and grain morphology, etc. Therefore, only a few measurements about the inverse Hall-Petch phenomenon are thought to be reliable and the critical value below which the inverse Hall-Petch law appears is about 10 nm [59], [68].

1.4.2 Yield stress and hardness

A fundamental fact about NC materials revealed by various experimental studies is that NC materials possess ultra-high strength which is often several times that of the coarse-grained counterparts [2], [69]. This is true for both yield strength and hardness, which also obeys the Hall-Petch relation by replacing the yield stress (σ) in Eq. 1-1 by hardness (H) [70]. This Hall-Petch strengthening due to grain size refinement can be explained by two major factors: dislocation movement across grain boundaries and the number of dislocations within a grain. It is based on the observation that grain boundaries impede dislocation movement [60], [71], [72] and that the number of dislocations within a grain have an effect on how easily dislocations can traverse grain boundaries and travel from grain to grain. Firstly, when the grain size is reduced, the volume fraction of grain

boundaries increases and the grain boundaries act as obstacles impeding further dislocation propagation. This is due to the fact that the structure of grain boundaries is much more disordered than the structure inside the grain, which prevents the dislocations from moving in a continuous plane. Thus, impeding dislocation movement will increase the yield stress of the material. Secondly, decreasing the grain size will decrease the amount of dislocations within a grain [73], [74]. Under an applied stress, existing dislocations and dislocations generated by Frank-Read (Fig. 1.12) sources will move through a crystalline lattice until encountering a grain boundary. As more dislocations propagate to this boundary, dislocation pile-up (Fig. 1.12) occurs as a cluster of dislocations. Dislocations generate repulsive stress fields, which acts as a driving force to reduce the energetic barrier for diffusion across the boundary [73], [74]. Decreasing grain size decreases the amount of possible pile-up at the boundary, which increases the amount of applied stress necessary to move a dislocation cross a grain boundary. The higher the applied stress needed to move the dislocation, the higher the yield strength.

Obviously, there is a limit to this mode of strengthening, as infinitely strong materials do not exist. Grain sizes can range from about 100 µm to 1 µm. Lower than this, the size of dislocations begins to approach the size of the grains. At a grain size of about 10 nm [59], [68], [73], [74], only one or two dislocations can fit inside a grain. This scheme prohibits dislocation pile-up and instead results in grain boundary diffusion/sliding. The lattice resolves the applied stress by grain boundary sliding resulting in a decrease in the material's yield strength [55]–[57], [59], [67], [68], [72]–[74].

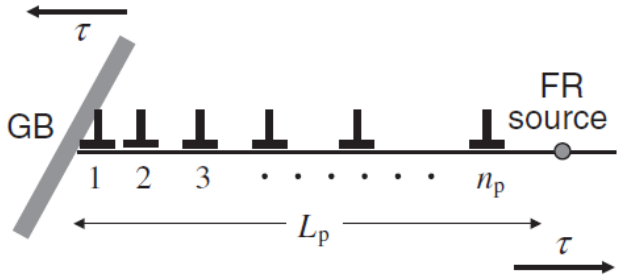

Fig. 1.12 Dislocation pile-up at a grain boundary

In addition, attention needs to be paid to the imperfections of NC materials when we evaluate their yield stress. The porosity and incomplete bonding among the grains was a major concern for the early bottom-up synthesis methods as imperfections like porosity could degrade the properties of NC materials. Fig. 1.13 shows the Young's modulus [2] and yield stress [3] as a function of porosity for nanocrystalline Pd and Cu. The decrease in

Young's modulus and strength is obvious. The existing pores provide initiation sites for fractures.

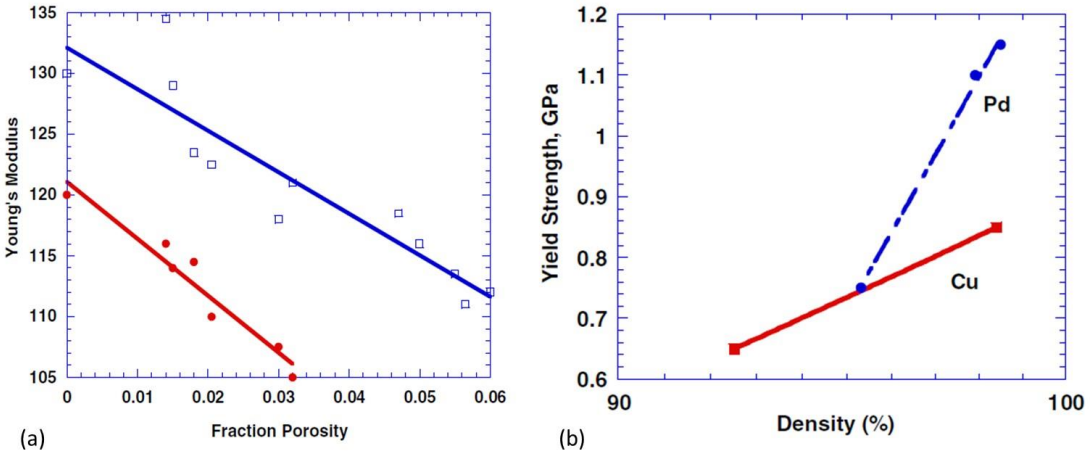

Fig. 1.13 (a) Young's modulus as a function of porosity for nanocrystalline Pd and Cu [2], (b) Compressive yield strength of Cu and Pd as a function of consolidation density [3].

1.4.3 Ductility and strain hardening

Although the mechanical strength of NC material is significantly improved, the ductility of the material is often decreased [9], [45], [75]. According to Zhang [76] and Zhu [77], the reduction of ductility with respect to grain size is reduced to the nanometer regime (Fig. 1.14). There is an obvious drop in ductility as grain size changes from 238 nm to 23 nm. However, in the conventional grain size regime, usually a reduction in grain size leads to an increase in ductility, which is not the case for most NC metals with grain size <25 nm. Many studies show that most NC metals have a small ductility while their coarse-grained counterparts have an elongation to rupture of 40-60% [78]. It is believed that change in plastic deformation mechanism could be the reason. As a matter of fact, different plastic deformation mechanisms as a function of grain size have been suggested [79]–[81]. (a) in the smallest grain size regime (d < 10 nm), there is little intra-granular dislocation activity occurring and grain-boundary shear/sliding/rotation are thought to be dominant in the plastic deformation mechanism. (b) In the regime of grain size d > 1 μm, unit dislocations and work hardening govern the plasticity. (c) In the regime of grain size 10 nm < d < 1 μm, the deformation mechanism is not yet very clear. However, according to Conrad [79]–[81], grain boundary shear promoted by dislocation pile-ups was the dominant mechanism and the main effect of grain size was on the number of dislocations and on the number of grain boundary atom sites. Nevertheless, more investigations need to be made in order to better understand the deformation mechanism in this regime.

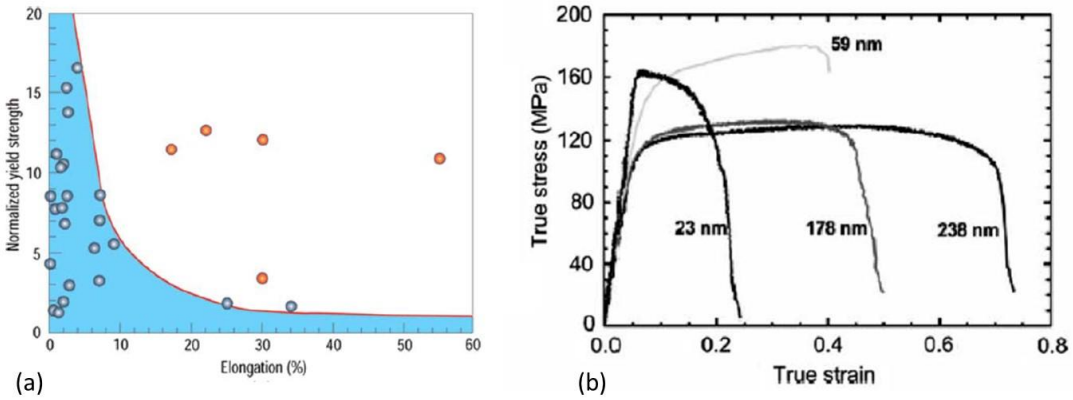

Fig. 1.14 (a) Decreased ductility in the nanocrystalline regime as indicated by experimental points in left-hand side of diagram [77], (b) reduction of ductility as grain size is reduced for ball milled Zn tested at a constant strain rate [76].

While the deformation mechanism for grain size ranging from 10 nm to 1 μm is not fully understood, several methods are available to improve the ductility of NC metals, such as annealing [82], developing bimodal model [83] and inducing twinning [84]. Annealing is able to relieve the stress between the grain boundaries, thus, regains the ductility while sacrificing a certain amount of strength. Materials with bimodal structure may have a large gain in work hardening and are able to achieve a uniform strain with only a small loss of strength. Twinning with nano-scale spacing provides room for dislocation storage and strengthens the materials. The intention here is to synthesize NC materials with reasonable ductility to promote their applications without losing too much strength.

While talking about the low ductility of NC materials, one should always address the strain hardening of NC materials as well because these two properties are closely linked. NC and UFG materials can generally not maintain uniform tensile elongation. Several reports virtually show no strain hardening after an initial stage of rapid strain hardening over a small plastic strain regime (about 1–3%), which is different from the response of coarse-grained polycrystalline metals [7], [78], [85]. Fig. 1.15 shows the stress–strain curves in compression and tension for UFG copper [3] produced by ECAP (8passes). The work hardening (in compression) is virtually absent, which leads to necking at the yield stress in tension, and the net consequence is a low tensile ductility. Moreover, the stress–strain response of NC Cu shows a rapidly reached peak and subsequent softening due largely to necking while the absence of strain hardening in compression causes localized deformation, which has been reported by several authors [86], [87].

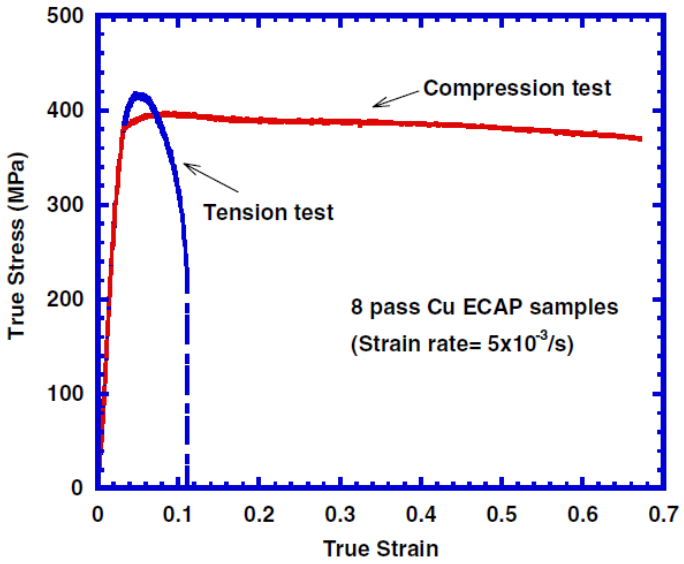

Fig. 1.15 Compression and tension stress–strain curves for copper elaborated with ECAP [3].

1.4.4 Strain-rate sensitivity

A great deal of studies have been conducted to evaluate the strain-rate sensitivity of metals as a function of changing grain size. For NC metals with grain size in the nanocrystalline regime, some results show a decrease in strain-rate sensitivity compared to the coarse-grained counterpart for body center cubic (bcc) NC metals [88] while opposite effect for fcc NC metals was observed [89]. It seems that the decrease/increase of strain-rate sensitivity as a function of changing grain size is related to the crystalline structure of the metals.

The engineering parameter measuring strain-rate sensitivity, m, is commonly defined as:

$$m = \left.\frac{\partial log\sigma}{\partial log\dot{\varepsilon}}\right|_{\varepsilon,T} \tag{1-2}$$

where σ is the flow stress and $\dot{\varepsilon}$ the corresponding strain-rate. The strain-rate sensitivity, m , is one of the crucial engineering parameters which is closely related to the deformation in metals. For example, materials with a high value of m, such as Cu, are able to resist localized deformation and therefore it is usually expected to be ductile. For fcc metals, a decrease in grain size often results in an increase in strain rate sensitivity.

Fig. 1.16 summarizes the variation of m as a function of grain size d and twin lamellar spacing λ for Cu samples from some of the recent important publications [90]–[95]. The different measured values show a clearly tendency that m is significantly increased as the

grain size is decreased, especially for grain size below 100 nm. For instance, the value of m for the grain size of 10 nm was 0.06 while for conventional coarse-grained Cu, this value goes down to about 0.002 which is much smaller. Higher values of m have also been reported for nanocrystalline Ni [96], nanocrystalline Au [97], and electrodeposited Cu [98]. The reason for such an extraordinary high values of m is still not fully understood. However, Lu et al. [95] argued that the higher strain-rate sensitivity is indicative of a smaller activation volume. This is thought to be connected to a change in the nanostructure/deformation mechanism.

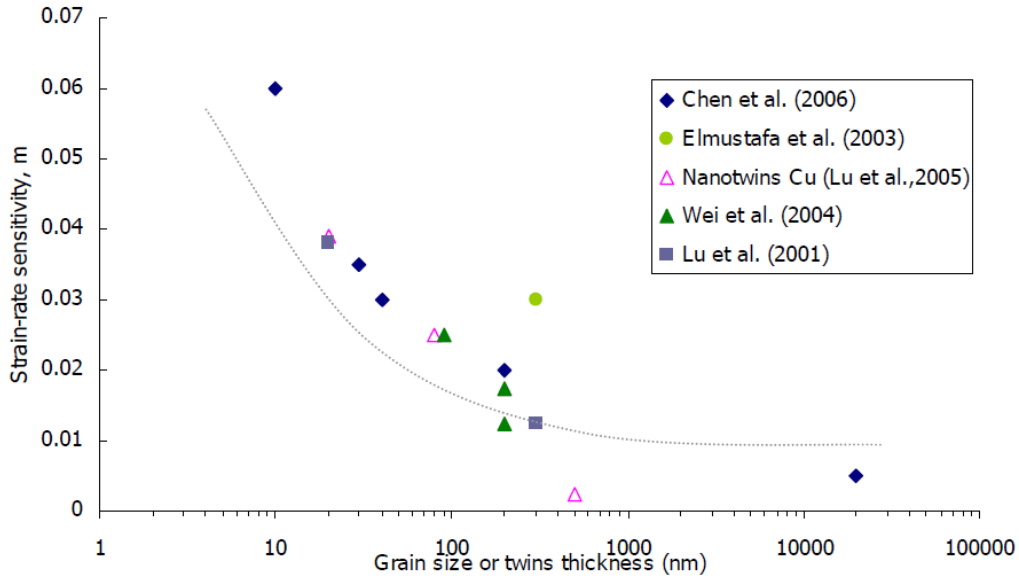

Fig. 1.16 The variation of m as a function of grain size d and twin lamellar spacing λ for Cu samples from some important publications [3].

1.4.5 Structure of nanocrystalline materials

The properties of materials are directly determined by their microstructure. Apparently, there exists significant difference regarding the microstructure of NC metals given their novel properties compared to their coarse-grained counterparts. In this Section, we will discuss some of the characteristics of the microstructures of NC metals, followed by the presentation of several models proposed by some researchers.

NC materials are characterized by a large volume fraction of grain boundaries, which may significantly alter their physical, mechanical, and chemical properties in comparison with conventional coarse-grained polycrystalline materials. Fig. 1.17(a) shows a schematic depiction of the structure of a nanocrystalline material [99]. The grain-boundary atoms and crystallite atoms are represented by white and black dots respectively. With the decrease of

grain size, the volume fraction of the grain boundary atoms increases. In Fig. 1.17(b), the evolution of the volume fraction of inter-crystal regions and that of triple-junctions is plotted as a function of grain size [100]. Assuming that the grains have the shape of spheres or cubes, the volume fraction of interfaces in the nanocrystalline material may be estimated as 3D/d (where D is the average interface thickness and d is the average grain diameter). Thus, the volume fraction of interfaces can be as much as 50% for 5 nm grains, 30% for 10 nm grains, and about 3% for 100 nm grains [3].

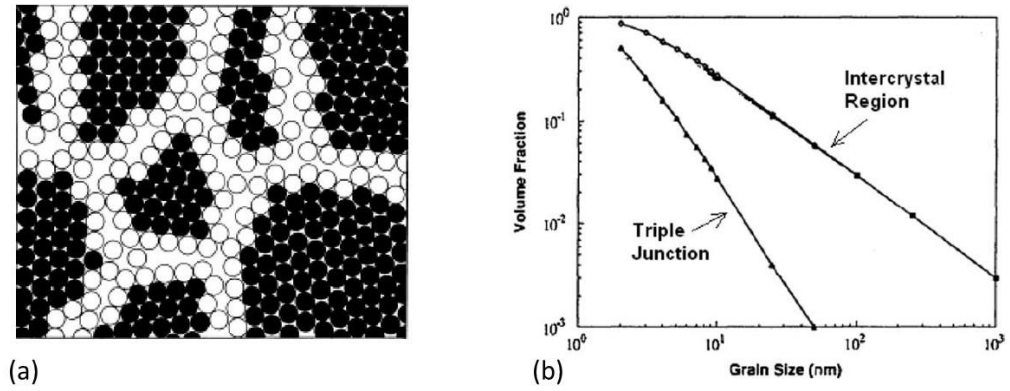

Fig. 1.17 (a) Two-dimensional model of a nanostructured material [99], (b) the effect of grain size on calculated volume fractions of inter-crystal regions and triple junctions [100].

In recent years, a great deal of efforts have been devoted to the studies of grain boundaries of NC materials with the help of various observation tools. Based on divers obtained experimental results, several models have been proposed by different researchers individually. It should be noted that some of these models are contrary to each other and some remain debatable. There is still not a unified model so far. In the following Section, we will briefly go through some of these models to give an overall idea of the advances and knowledge with respect to the structure of grain boundary of NC materials.

1.4.5.1 Gas-like model

Gleiter [101] and co-workers were ones of the first researchers who have proposed a model to describe the microstructure of grain boundaries of NC materials. In order to evaluate the microstructure of grain boundaries, the interference function of nanometer-sized crystalline iron (6-nm crystal size) was measured by x-ray diffraction. It was found that the structure of grain boundaries of NC materials exhibited neither long-range order (like crystals) nor short-range order (like glasses). It is rather a gas-like structure which is highly disordered. However, this model has always been debatable. Shortly after the

proposition of this model, more and more experimental results have led to different conclusions. Therefore, the gas-like model has been abandoned gradually. Even though this model failed to describe the grain boundary of NC materials, Gleiter and co-workers have been real pioneers in the field of NC materials and their research work has promoted the advances of study in this field.

1.4.5.2 Well-ordered model

In this model, it is argued that grain boundaries in NC metals are ordered. This opinion is widely accepted by many researchers. For example, Thomas and Siegel [102] used high resolution electron microscopy to study nanocrystalline Pd and found no evidence that the extended, disordered boundary regions differ from the boundaries in coarse-grained materials. In other words, the grain boundary of NC metals is just the same as that of conventional metals in nature. Eastman [103] investigated the grain boundaries of several NC materials by x-ray and Extended X-Ray Absorption Fine Structure (EXAFS) and they concluded, based on the experimental results, that atomic arrangements in the interfaces of NC metals are well-ordered. Wunderlich [104] has also observed ordered structure in the interfaces of NC Pd using high resolution electron microscopy. In addition, twinning, stacking fault and dislocations were detected as well. These crystallographic defects are thought to exist only in well-ordered crystallites. Thus, they concluded that the structure of the interfaces of NC metals is extendedly-ordered, if not perfectly-ordered like a crystallite. Lupo [105] examined the interface structures of nano-phase Si sample by molecular statics and molecular dynamics simulation and found out that the interface structures are dependent on the distance between atoms in the interfaces, R_a. When $R_a < d/2$ (where d is the grain size), the interfaces structures are well-ordered. Otherwise the grain boundaries tend to have an amorphous structure.

1.4.5.3 Mixed model

The basic idea of this model is that the structure of grain boundaries cannot simply be defined as ordered or disordered. Firstly, grain boundaries of NC metals make up a large percentage of the overall volume compared to their coarse-grained counterparts. The atoms located in the interfaces are numerous. Secondly, the arrangements of these atoms in the interfaces are strongly affected by many factors such as crystallographic orientation of the adjacent crystallites, crystallographic defects, impurities etc. [101][106]. The mixed-model believe that the interface structure is a mixture of all. In one NC sample, one can observe

ordered and disordered structure of interfaces, and/or even structures in between [103], [107]. The overall distribution of these different structures are considered to be heavily dependent on synthesis method, temperature and pressure, etc. The advantage of this model is that it can perfectly explain why both ordered and disordered interface structures were observed in divers NC samples [106].

1.4.6 Deformation mechanisms of nanocrystalline materials

Since the emergence of synthesized NC materials in the 1980s, NC materials have become one of the most popular research topics in the field of materials science. In the one hand, the unique structure of NC materials (large fraction of grain boundaries, etc.) has provided a good opportunity to study the relationship between structure and mechanical properties; in the other hand, their superior mechanical and physical properties are potentially valuable for numerous industrial applications. Compared to their coarse-grained counterparts, NC materials have an enormous potential in mechanical engineering field thanks to their improved properties, such as higher mechanical strength and hardness [2], [37]. As is known, the mechanical properties (strength, hardness, etc.) of materials are closely linked to their deformation mechanism. The improved mechanical properties of NC materials imply that there might be a new deformation mechanism different from that of conventional materials in the microcrystalline regime. As is discussed previously, the relationship between mechanical strength and grain size of materials follow the Hall-Petch law in the conventional microcrystalline regime. The reason for this phenomenon is that grain boundaries serve as obstacles which cause dislocation pile-up at the grain boundaries [60], [71], [72]. However, the deformation mechanism for NC materials are believed to be different. As grain size decreases, the fraction of grain boundaries increases. Moreover, it is believed that there are much fewer dislocations within a nano-grain compared to a micro-grain. Thus, there is an agreement that grain boundaries play an important role in the deformation mechanism of NC materials [60], [68]. It seems to have a transition from dislocation-mediated deformation to grain boundary-mediated deformation. Some researchers argue that dislocation activities are still dominant for grain size larger than 30 nm [108]. For smaller grain size, numerous deformation mechanisms theories such as grain-boundary sliding [59], [60], [68], grain-boundary rotation [60]–[62], grain-boundary diffusion [65], [66] and partial dislocations [64], [109]–[111] etc. were proposed to explain

the plastic deformation of NC materials. Unfortunately, it is impossible to reach an agreement for the moment due to divers experimental and numerical results.

So far, it is commonly believed that there are not dislocation activities inside a nano-grain for grain size below 10 nm. In this case, the only possible mechanism is grain boundary-mediated deformation. Many researchers believe that this transition from dislocation-mediated mechanism to grain boundary-mediated mechanism is responsible for the softening of NC materials when grain size is decreased down to 10-15 nm (inverse Hall-Petch law) [55], [56], [59]. Nevertheless, some experimental results revealed that dislocations can still be observed inside a nano-grain with a grain size of 10 nm [110]. As a whole, the current deformation mechanism theories proposed by a great deal of researchers cannot well explain the experimental results and the deformation mechanism of NC materials is not fully understood.

Understanding the plastic deformation of NC materials is crucial both for advances in basic research and potential industrial applications. For plastic deformation of metals in the microcrystalline regime, there is already a unified theory to explain their deformation mechanism (dislocation-mediated mechanism) [72]. However, the deformation mechanism for metals in the nanocrystalline regime is still not clear. Discoveries, such as inverse Hall-Petch law [55], nano-twins [64] and grain boundary rotation [61], are not enough to explain the deformation mechanism. As mentioned earlier, grain boundary-mediated mechanism is thought to be dominant due to large fraction of grain boundary when grain size is decreased down to nanocrystalline regime. The structure of grain boundary of NC metals was initially thought to be highly disordered and similar to an amorphous structure [101], but it was later [103], [104] found out that there exists dislocations in the grain boundaries and its structure is quite similar to that of conventional materials in the microcrystalline regime. One difference is that the volume fraction of grain boundary for NC metals is relatively higher, especially below a critical grain size value. For example, the volume fraction of grain boundaries of a NC sample with a grain size of 10 nm can be up to 30% [3]. Hence, the influence of grain boundary activities is relatively more significant when the NC metals are subjected to plastic deformation.

The deformation mechanisms proposed so far include grain boundary sliding [60], [68], [109], grain boundary rotation [61], [62], grain boundary diffusion [65], [66], partial dislocations [64], [109]–[111], etc. Schiotz [59], [68] studied the microstructure of nanocrystalline Cu before and after plastic deformation and found out that most of the sliding took place at the grain boundaries. Therefore, they concluded that grain boundary

sliding was the main mechanism of NC metals and was responsible for inverse Hall-Petch phenomenon when grain size is down to a critical value (10-15 nm). Swygenhoven [112] found out that deformation started at triple points, with grain boundary sliding followed by the creation of intragrain partial dislocations. Murayama et al. [62] first observed disclinations in a mechanically milled Fe sample and suggested that the generation of partial disclination defects provided an alternative mechanism to grain-boundary sliding. Shan [65] observed microstructure of nanocrystalline Ni thin film before and after plastic deformation under TEM and they claimed that grain boundary diffusion was the main mechanism for NC metals. Chen [64] observed nano-twins in nanocrystalline Al sample and they inferred that the deformation mechanism for NC materials below a critical grain size (10- 20 nm) is dominant by partial dislocations. Interestingly, Li [58] proposed that the deformation mechanisms for NC metals are strain-dependent. The deformation behavior as a function of applied strain was studied in a nanostructured Ni-Fe alloy using the in situ synchrotron diffraction technique. It was found that the plastic deformation process consists of two stages, undergoing a transition with applied strain. At low strains, the deformation is mainly accommodated at grain boundaries, while at large strains, the dislocation motion becomes probable and eventually dominates. Other experimental results demonstrated that grain boundary sliding coupled with grain boundary rotation is the most important deformation mechanism for NC metals [113]. Weissmuller [113] tried to summarize all these different deformation mechanisms of NC metals and he suggested that it is not enough to only consider the deformation mechanism as a function of grain size. Instead, strain rate and grain size should be taken into account at the same time. Fig. 1.18 summarized the deformation mechanisms as a function of both strain rate and grain size [113].

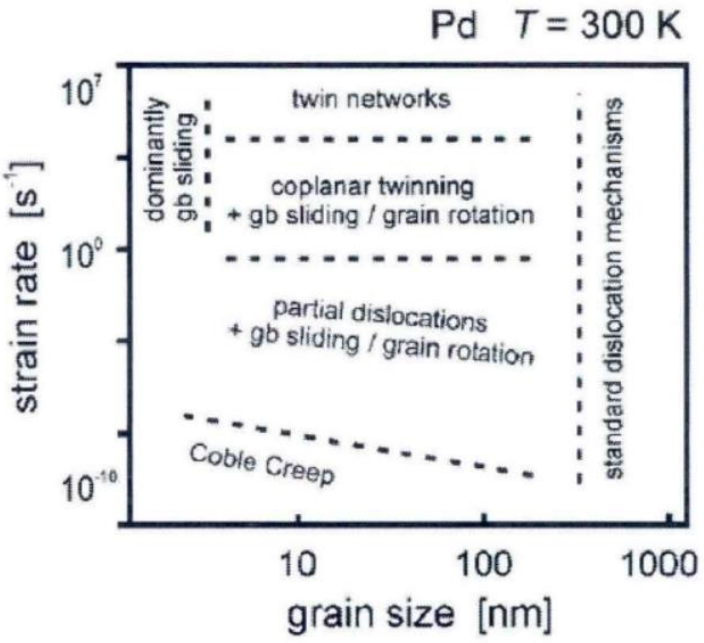

Fig. 1.18 Deformation mechanism of nanocrystalline Pd as a function of grain size and strain rate [113].

Judging from all these chaos of different theories based on a variety of results, there is still a long way to go in order to establish a unified theory for the deformation mechanism of NC metals. This is an even tougher mission when Shan [110] observed the presence of dislocation inside the grain for a nanocrystalline Ni sample with a grain size of 10 nm and Chen [114] discovered dislocation activities inside the grain of a nanocrystalline Ni sample with ultrafine grain size of 3 nm. While on the contrary, it is traditionally believed that there are not dislocation activities inside a nano-grain for grain size below 10 nm. Apparently, dislocation activities inside NC metals cannot be neglected when we try to evaluate the corresponding deformation mechanism.

In the following Section, we will focus on a few key deformation mechanisms proposed so far (grain boundary sliding, grain boundary rotation, dislocation activities), with detailed discussion about their definitions and divers models proposed to describe these mechanisms.

1.4.6.1 Grain boundary sliding

Grain boundary sliding has been considered to be at the root of superplasticity [115]. With decreasing grain size of the material (or increasing ratio of grain boundary thickness w to grain size d), for metallic systems a transition from dislocation dominated plastic deformation to grain boundary sliding occurs at a critical grain size when the stress required for dislocation motion/formation becomes larger than the stress required for grain boundary sliding [3]. Fig. 1.19 shows a schematic description of one layer of grains which slides with

respect to the other, resulting in a shear strain in the process. Plastic deformation is formed by means of the sliding of the top layer grains moving to the right with respect to the bottom layer grains. This is achieved by grain boundary sliding and is considered to be the reason for superplasticity. As a result of these processes, the internal stresses which built up are reduced and plastic deformation can proceed.

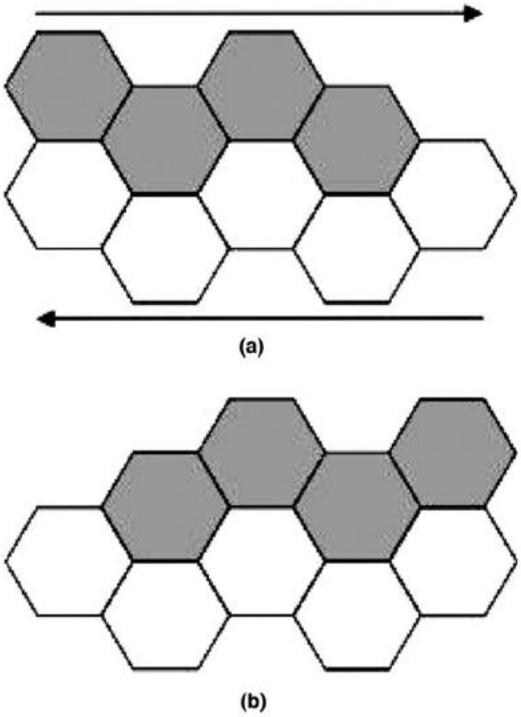

Fig. 1.19 Grain boundary sliding model: (a) initial position of grains and (b) position after top layer has slid to right [3].

Hahn et al. [116] proposed two hardness relationships:

$$H_v = H_0 + \frac{K}{\sqrt{d}} \tag{1-3}$$

$$H_v = H_{v0} - \frac{m_1}{d}(d - m_2)^{1/2} \tag{1-4}$$

where m_1, m_2, and k are material parameters and d is the grain size. Eq (1-3) is for the dislocation dominated regime and Eq (1-4) is for the grain boundary sliding regime. Here, he argued that for metallic systems the deviation from the Hall-Petch relation, which eventually leads to the inverse Hall-Petch behavior, can be attributed to the competition

between grain boundary sliding controlled process and dislocation dominated deformation. Evidently, when grain boundary sliding is dominant, grain refinement will weaken the material (inverse Hall-Petch), while grain refinement will strengthen the material when crystallographic deformation is dominant (conventional Hall-Petch).

Conrad and Narayan [117], employing the concept of thermally-activated shear, proposed that the macroscopic shear rate produced by the independent, atomic shear events at grain boundaries is given by

$$\dot{\gamma} = N_v A b \nu \, exp\left[\frac{-\Delta G(\tau_e)}{kT}\right] \tag{1-5}$$

where N_v is the number of places per unit volume where thermally-activated shear can occur, A is the area swept out per successful thermal fluctuation, b the atomic diameter, ν the frequency of vibration and ΔG the Gibbs free activation energy. Note that ΔG is a decreasing function of the effective shear stress $\tau_e=\tau-\tau_0$, where τ is the applied stress and τ_0 the back stress or threshold stress. Reasonable expansions for the parameters on the right side of Eq. (1-5) are: $N_v = \delta / db^3$, where $\delta \approx 3b$ is the grain boundary width, $A = b^2$, $\nu = \nu_D$ ($\approx 10^{13} s^{-1}$) the Debye frequency and $\Delta G = \Delta F - V\tau_e$, where ΔF is the Holmholtz free energy and $v = b^3$ refers to the activation volume. Inserting the above values into Eq. (1-5) and considering both forward and backward jumps, it gives the following relation:

$$\dot{\gamma} = \frac{6\delta\nu_D}{d} \sinh\left(\frac{V\tau_e}{kT}\right) exp\left(\frac{-\Delta F}{kT}\right) \tag{1-6}$$

where sin hx ≈ x for $x \leq 0.5$ and sin hx ≈ ½ exp x for $x \geq 2$. This equation thus gives that τ_e is proportional to d for small values of $V\tau_e/KT$ and varies as ln d with large values.

Conrad [79] analyzed data about the effect of grain size d in the range of mm to nm on the flow stress of Cu. He proposed that, in the nanocrystalline regime ($d \leq 10$ nm), grain boundary shear is considered to dominate in the process of deformation. The corresponding equation is given as:

$$\tau - \tau_0 = \left(\frac{kT}{V} ln\left(\frac{\delta\nu_D}{\dot{\gamma}}\right) + \frac{\Delta F^*}{V}\right) + \frac{kT}{V} lnd \tag{1-7}$$

where ΔF* is the Helmholtz free energy, V is the activation volume, τ_0 is threshold stress for shearing, δ is the grain-boundary width, and ν_D is the frequency of vibration (about 10^{13} s^{-1}).

1.4.6.2 Grain boundary rotation/ grain coalescence

Grain boundary rotation was observed and used to explain the coalescence of sub-grains during recrystallization. In 1962, Hu [118] discovered the coalescence of sub-grains during recrystallization and the disappearance of the grain boundaries between the sub-grains. Later, the possibility of rotation of a sub-grain with respect to its neighbors as a natural process during recrystallization was studied by Li [119] in 1962. He concluded that this process was both thermodynamically and kinetically possible. Fig. 1.20 [119] demonstrates coalescence of two subgrains by rotation. The two sub-grains are initially separated by a grain boundary and one sub-grain is undergoing a rotation until it reaches the same orientation of the neighboring sub-grain. Grain boundary migration process begins and eventual coalescence of two sub-grains is achieved by the disappearance of the grain boundary. It is believed that coalescence of two sub-grains by rotation allows the system to reach a more stable state by decreasing the internal energy. Harris [120] used transmission electron microscopy to observe the microstructural development of thin films of gold during annealing at different temperatures and found out that individual grains were constantly rotating and that this contributed to the rearrangement of grain boundaries by allowing their individual energies to vary. They calculated the changes of grain boundary energy which was thought to be the driving force of grain rotation and discovered that small grains were more easily subject to rotation than bigger grains.

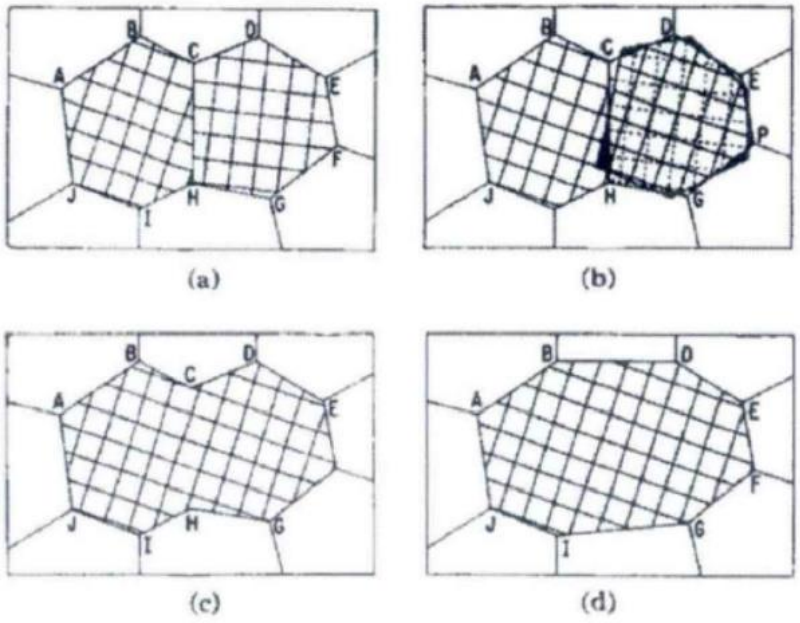

Fig. 1.20 Schematic description of grain boundary rotation and grain coalescence: (a) the original subgrain structure before coalescence; (b) one subgrain is undergoing a rotation; (c) the subgrain structure just after coalescence; (d) the final subgrain structure after some subboundary migration [119].

Margulies [120] investigated grain rotation during tensile deformation of coarse-grained pure aluminum based on diffraction with focused hard x-rays. The results suggested that when the polycrystals were subjected to an applied stress, grain rotation occurred in order to counterbalance the applied stress. Murayama [62] discovered that grain rotation also existed for NC materials. High-resolution transmission electron microscopy was used to observe mechanically milled NC Fe, and it showed that the formation and migration of partial disclination dipoles during severe plastic deformation allow crystallites to fragment and rotate at the nanometer level. Ovid'ko [121] argued that motion of disclination dipoles (as indicated in triangles in Fig. 1.21) could cause crystal lattice rotation and that grain boundary sliding and grain rotation were the main deformation mechanisms for NC materials. It should be noticed here that a disclination is a line defect characterized by a rotation of the crystalline lattice around its line [121].

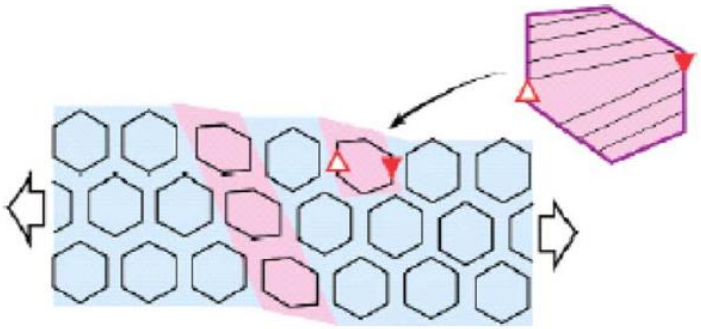

Fig. 1.21 Rotation deformation of nanocrystalline material under loading (grain undergoing rotation is shown with two opposite arrows and is represented in magnified fashion in upper right corner) [121].

Since Read and Shockley [122] came up with a dislocation model of grain boundary to describe grain rotation, dislocation activities in the grain boundary have been considered to be responsible for grain boundary sliding and grain rotation. The basic idea of Read is that under an applied stress the grain boundary activities increase with the decrease of grain size. In other words, smaller grains are more prone to undergo rotation under a fixed stress compared to bigger grains. Cahn [123] proposed the concepts of sliding and coupling for planar interfaces with an applied stress which are illustrated in Fig. 1.22. Fig. 1.22 (a) is an original bicrystal, showing grain boundary and the trace of a plane in each crystal. The position of atoms along this trace is followed in the other parts of this figure. Fig. 1.22 (b) demonstrates sliding without interface motion (greased boundary) while Fig. 1.22 (c) shows the coupling of relative tangential translation of crystals without sliding and Fig. 1.22 (d) is the coupling of relative tangential translation of crystals with sliding.

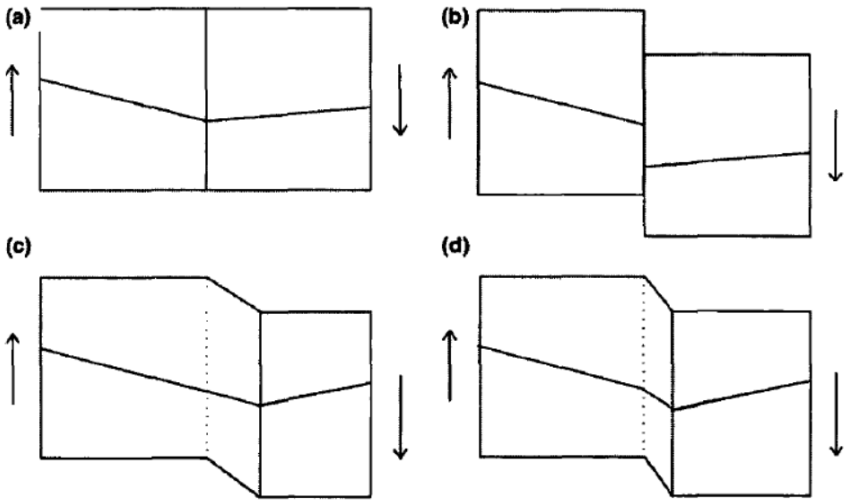

Fig. 1.22 Tangential motion of crystals along planar grain boundary: (a) original bicrystal, (b) sliding without interface motion, (c) coupling of relative tangential translation of crystals without sliding and (d) coupling of relative tangential translation of crystals with sliding [123].

Chan [123] studied grain boundary in gold by crystallite rotation via transmission microscopy and the results suggested that the rotations occurred conservatively by the motion of screw grain boundary dislocations. Upmanyu [124] performed a series of molecular dynamics simulations, and the results showed that grain boundary migration and grain rotation occurred simultaneously. Gorkaya also [125] observed simultaneous shear coupling and grain rotation experimentally during grain boundary migration in high-purity Al bicrystals subjected to an external mechanical stress at elevated temperatures. He argued that the grain boundary dislocations were responsible for the shear coupling and grain rotation with the following explanation. Grain boundary dislocation can be viewed to be mixed edge–screw dislocation (seen in Fig. 1.23 (e)). The Burgers vector of such dislocations has three constituents: an edge component, which is directed normal to the boundary plane, and two screw components that are oriented perpendicular to the first one as well as to each other and lie within the boundary plane (seen in Fig. 1.23 (b), (c) and (d)). A shear stress applied to the boundary plane causes a force on each dislocation. Due to its edge component, such a mixed dislocation will be displaced in the direction normal to the boundary plane and will produce a shear. The concurrent displacement of the two screw components in the same direction must cause two additional perpendicular shears/rotation (seen in Fig. 1.23 (b), (c) and (d)). Wang [61] observed grain rotation in tensile-loaded Pt thin films under a high-resolution transmission electron microscope. They proposed that the

mechanism underlying the grain rotation was dislocation climb at the grain boundary, rather than grain boundary sliding or diffusional creep.

As a whole, grain rotation has attracted tremendous interests with regard to the explanation for the deformation mechanism for NC materials. During grain rotation, several processes can interfere such as grain boundary migration, lattice diffusion, grain boundary dislocation activities and disclinations etc. Great progress has been made with regard to the understanding of deformation mechanisms based on grain boundary rotation.

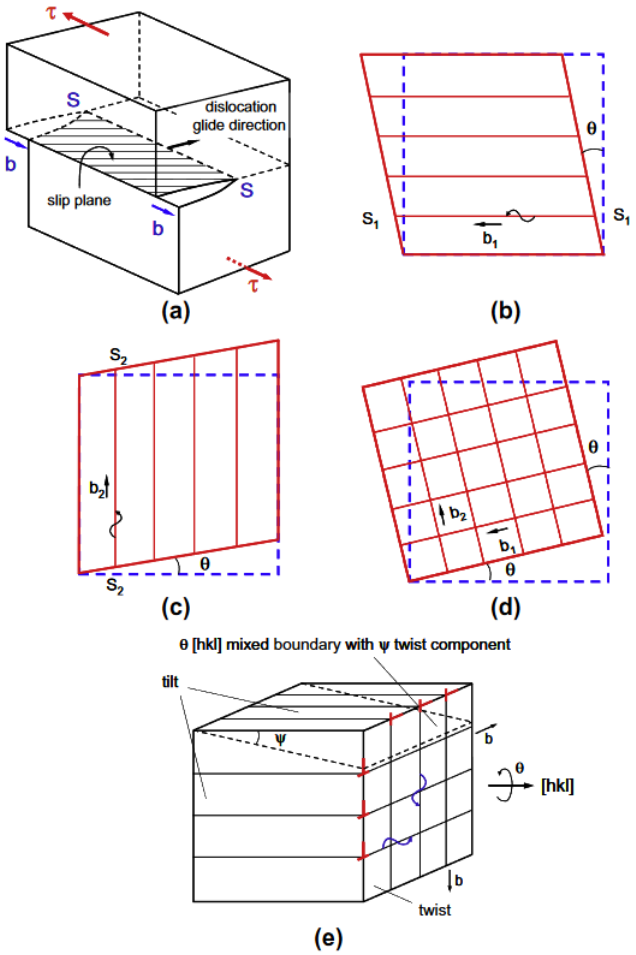

Fig. 1.23 (a) glide of screw dislocation under an applied shear stress, (b–d) dislocation structure of a low-angle twist grain boundary. One set of parallel screw dislocations causes a shear, but two perpendicular sets produce a rotation of adjacent crystals around the axis normal to the boundary plane, (e) dislocation structure of the grain boundary of a low-angle misoriented volume element [125].

1.4.6.3 Dislocation activities inside nanocrystalline materials

In conventional microcrystalline regime, plastic deformation proceeds as a result of dislocation movement and dislocation multiplication [71], [72]. In fact, the size of a Frank-Read source must be smaller than that of a grain. At the same time, the stress required to generate dislocation multiplication is inversely-proportional to the size of a Frank-Read source. Accordingly, this dislocation-mediated mechanism is considered to be to the main mechanism for grain size larger than 1 μm below which other mechanisms begin to interfere [126]. It is reasonable to assume that due to the restrictions of the grain size, NC metals cannot accommodate this kind of dislocation source.

Despite the fact that dislocation-mediated mechanism is no longer the dominant deformation mechanism in the nanocrystalline regime, there are still dislocation activities inside NC metals. Dislocation activities are reported to exist both in the grain boundaries and inside the nano-grains [64], [109]–[111], [114], [122].

Molecular dynamics simulations carried out primarily by Van Swygenhoven and coworkers [60], [109], [112] with TEM observations showed that grain boundary in NC metals can be both source and sink for dislocations. Fig. 1.24 shows this mechanism in a schematic fashion [3]. Dislocations, which were generated at one grain boundary, run unimpeded until they encounter the opposite grain boundary (on right-hand side).

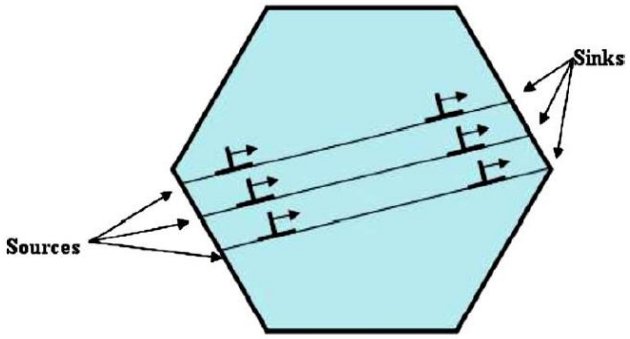

Fig. 1.24 Grain boundary source-sink model [3].

One argument about this mechanism is that when grain size is down to nanometer regime, the mean free path of dislocation is limited, and therefore dislocation interactions, cross slip and other mechanisms of dislocation multiplication are largely prevented. Yamakov [126] studied the nucleation of extended dislocations from the grain boundaries in nanocrystalline aluminum (grain size up to 70 nm) by molecular-dynamics simulation. The results revealed that the mechanical behavior of the material depended on the

dislocation splitting distance, r_{split}, with respect to grain diameter d. For $r_{split} > d$, the first partials nucleated from the boundaries glide across the grains and become incorporated into the boundaries on the opposite side, leaving behind a grain transected by a stacking fault. For $r_{split} < d$, two Shockley partials connected by a stacking fault are emitted consecutively from the boundary, leading to a deformation microstructure similar to that of coarse-grained aluminum. Kumar [108] investigated the mechanisms of deformation and damage evolution in electrodeposited, fully dense, NC Ni with an average grain size of 30 nm and their observations clearly revealed that dislocation-mediated plasticity played a dominant role in the deformation of NC Ni with grain size above 30 nm. Swygenhoven [60] performed MD simulations to investigated atomic mechanism for dislocation emission from nanosized grain boundaries and his results suggested that grain boundaries could emit a partial dislocation during deformation by local atomic shuffling and stress-assisted free volume migration. Chen [64] reported TEM observations of deformation twinning in plastically deformed NC Al with grain size in the range of 10 to 35 nm which was not observed in coarse-grain pure Al. They proposed a dislocation-based model and suggested that partial dislocations were responsible for the formation of twinning. Their results underscored a transition from deformation mechanism controlled by normal slip to that controlled by partial dislocation activities when grain size decreases to tens of nanometers.

Dislocations activities have also been observed inside a nano-grain. Shan [110] observed the presence of dislocation inside the grain on a NC Ni sample with a grain size of 10 nm and Chen [114] discovered dislocation activities inside the grain of a nanocrystalline Ni sample with ultrafine grain size of 3 nm. It is argued that dislocation activities occurred inside a nano-grain most possibly when the nano-grain is directly subject to an external applied stress [126].

From all the above discussion, we can conclude that dislocation activities remain significant for grain size above 30 nm for NC metals [108]. For smaller grain size, dislocation activities both in the grain boundaries and in the grain interior play a less important role during plastic deformation. Instead, deformation mechanisms such as grain boundary sliding, grain rotation etc., begin to interfere. Nevertheless, the dislocation activities in NC metals cannot be neglected because those activities make up an important part of the plastic deformation process and provide essential insights for understanding the deformation mechanism of NC metals.

1.5 Conclusion

In this chapter, several methods available for the generation of nanocrystalline materials are first introduced. The advantages and disadvantages of these techniques are also addressed. For example, samples synthesized by inert gas condensation are often reported to have incomplete bonding and porosity problems. Contamination is also of great concern for this synthesis method. On the other hand, synthesis methods by severe plastic deformation are able to generate samples free of porosity and contamination, which makes it stand out among other synthesis methods. Surface Mechanical Attrition Treatment (SMAT) can be classified as one of these SPD synthesis method. A detailed description of the technique SMAT is presented in this chapter. Several mechanical and chemical properties can be improved after SMAT, such as hardness, friction and wear properties, yield strength, fatigue and diffusion properties. Subsequently, the formation mechanisms of the nanostructured layer are described for materials with different stacking fault energy. In the last Section of this chapter, the novel properties of NC materials (yield strength, ductility, strain-rate sensitivity and structure of NC materials) are discussed in detail. A brief introduction about the current understanding of the deformation mechanisms of nanocrystalline metals is presented. The deformation mechanisms proposed so far include grain boundary sliding, grain boundary rotation, grain boundary diffusion, partial dislocations etc. At the end of this chapter, we focus on a few models of three main deformation mechanisms (grain boundary sliding, grain boundary rotation and dislocation activities). This chapter is dedicated for the literature review and will be applied subsequently for the interpretation of the experimental results in the following chapters.

Chapter 2: Materials Characterization Techniques

This chapter lists a variety of characterization techniques that have been used to characterize the properties of the SMAT treated sample, such as scanning electron microscopy (SEM), transmission electron microscopy (TEM), X-ray diffraction (XRD), electron backscattered diffraction (EBSD), focused ion beam (FIB), nanoindentation, micro-pillar compression and atomic force microscopy (AFM). The microstructure of the sample was investigated by means of SEM, TEM, XRD and EBSD. The mechanical properties of the SMATed samples were mainly examined by nanoindentation and micro-pillar compression. AFM measurements were perform to investigate the pile-up behaviour of SMATed material. The details of the characterization techniques are described as follows.

2.1 Scanning Electron Microscopy (SEM)

A scanning electron microscope (SEM) [127] is a type of electron microscope that produces images of a sample by scanning the surface with a focused beam of electrons. The signals used by a SEM to produce an image result from interactions of the electron beam with atoms at various depths within the sample. These signals include secondary electrons (SE), backscattered electrons (BSE) and characteristics X-rays and so on. In Fig. 2.1 [128], we can see the various signals that are possible as a result of the interaction between electron beam and the sample. All these different types of signals carry different useful information about the sample and it's up to the observer to decide which signal to capture. Each of these signals should be captured by a corresponding detector. Normally, all SEMs are equipped with secondary electron detectors, but it's rare for a single machine to have detectors for all other possible signals.

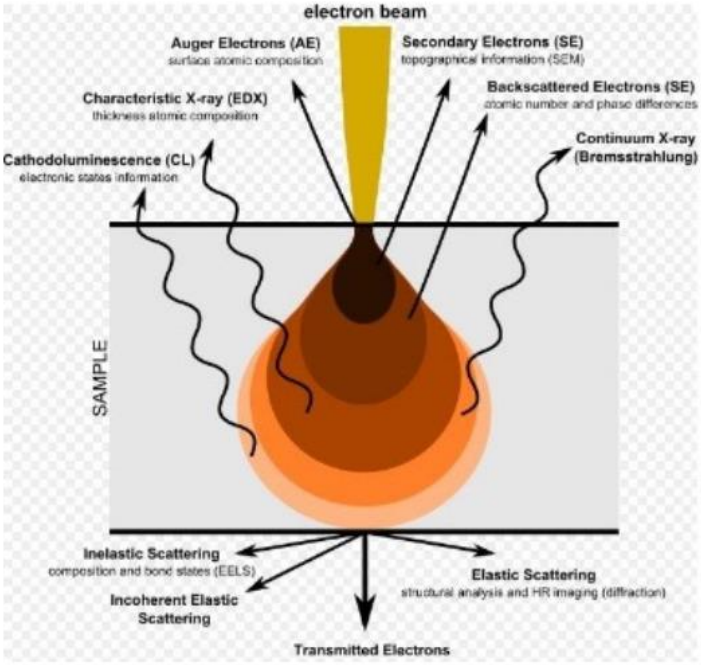

Fig. 2.1 Various signals produced by the interactions between electron beam and the sample [128].

SE are the electrons emitted from the sample surface as a result of the irradiation of the scanning electron beam. As a result, SE is capable of producing very high-resolution images of the sample surface. As indicated, BSE are electrons that are scattered back by the atoms of the sample by elastic scattering. They come from deeper zones within the sample and consequently, its resolution is lower than SE images. According to the fact that it's easier for heavy atoms to scatter electrons than light ones, the signals provided by BSE give out information of elements in the material. The irradiation of the electron beam also results in the emission of X-rays. The analysis of the dispersed energy of the characteristic X-rays can be used to identify the chemical composition of the sample.

Inside a vacuum chamber, several detectors capture the interaction signals produced by the impact of the beam on the surface of the sample. By scanning the surface of the sample, signals captured by those detectors are able to be processed so as to form desired images about the sample. It should be stressed that the observed sample must be conductive to ensure the required electronic interactions for the detectors. In the case of non-metallic samples, the sample must be treated to ensure conductivity. In this project, SEM was performed using FEG Hitachi SU 8030, as shown in Fig. 2.2.

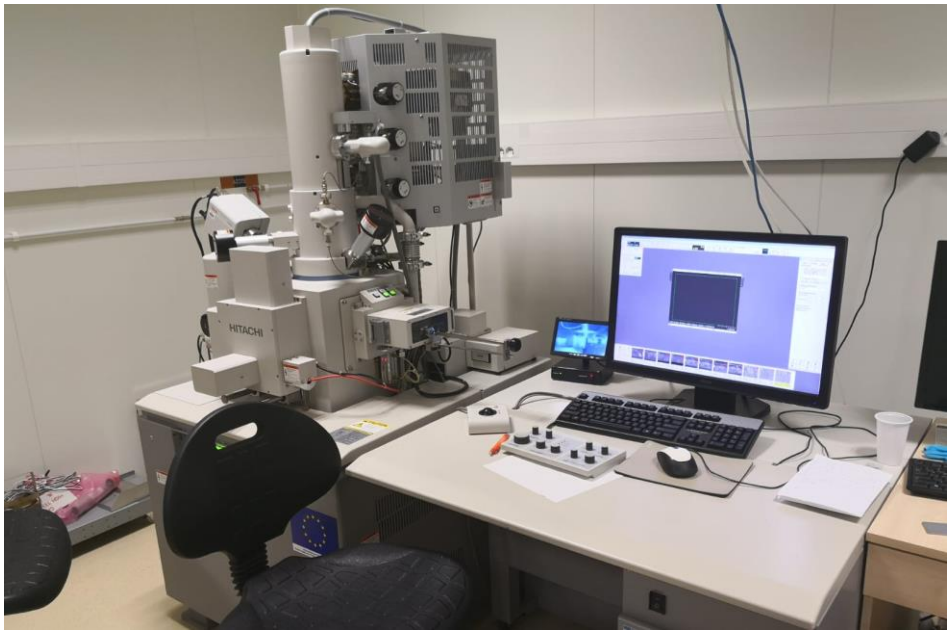

Fig. 2.2 Scanning electron microscopy used in our project (FEG Hitachi SU 8030).

2.2 Transmission Electron Microscopy (TEM)

TEM [129] is a microscopy technique which allows a beam of electrons to transmit through a sample to form an image. The transmitted electrons (Seen in Fig. 2.1) are detected which will give information on the sample's inner structure. The principle of high resolution of TEM lies in the small wavelength of electron beam as the resolution of microscopy is determined by the wavelength of the source. Hence, TEM possess much higher resolution than optical microscopy. Consequently, TEM is able to reveal delicate details about the structure of the sample up to atomic scale, for example, a single column of atoms. TEM is a rather important and common technique in material science, especially in nanotechnology.

The sample for TEM observation is usually prepared in the form of ultrathin Section or a suspension on a grid to allow the transmission of electrons through the sample, which are later captured and processed to form an image. Electrons are emitted from the source and travel through the vacuum column of the microscope. Theses electrons are subsequently focused by the electromagnetic lens into a beam before passing through the sample. As a result, the electron beam interacts with the sample and the unscattered electrons later form the image on the fluorescent screen with its different parts displayed in varied darkness according to the density of the materials. The information about morphology and structure of the sample can be extracted from the bright field, dark field and diffraction pattern.

2.3 X-ray Diffraction (XRD)

XRD [130] is commonly utilized as a characterization method in material science. It is capable of revealing the crystalline structure and material composition and can be used for a vast variety of materials.

A beam of electrons is generated from the hot tungsten filament and these electrons are accelerated towards the anode with a high potential difference between the cathode and anode (target). Anode is mainly Cu, Mo, Al and Mg. After striking the anode the electrons generate X-rays. While monochromatic source is preferred, the X-rays beam actually consists of several characteristic X-rays lines.

When an X-ray beam hits an atom of the sample, the electrons around the atom start to oscillate with the same frequency as the incoming beam. As the pattern of atoms in a crystal is regularly arranged, the constructive interference could happen in several possible directions. Indeed, the incident rays will interact with the sample and produce constructive interference when Bragg's Law is satisfied, which is expressed in equation 2.1.

$$n\lambda = 2d \sin\theta \qquad (2\text{-}1)$$

where n is an integer, λ is the wavelength of the incident X-rays and d is the interplanar spacing. Subsequently the x-ray beams leave the sample at various directions rendering the information of orientation and interplanar spacings of the planes in the crystal (shown in Fig. 2.3) [131]. The Bragg's Law demonstrates the relationship between the wavelength of electromagnetic radiation, the diffraction angle and the lattice spacing in a crystalline sample. The spacing can be extracted by conversion of the diffraction peaks, which allows the identification of the mineral since each mineral has a set of unique spacing. To achieve the identification of the mineral, the obtained results should be compared with standard reference patterns.

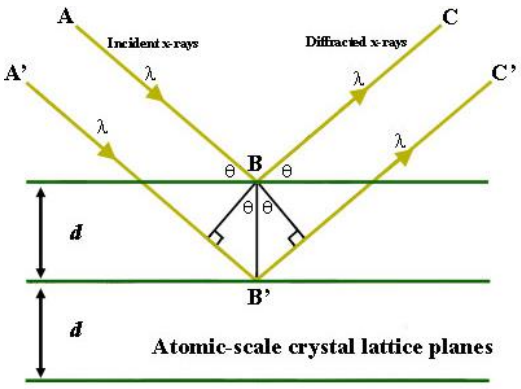

Fig. 2.3 Illustration of Bragg's Law [131].

Results obtained by XRD can be presented in different forms, such as pole figures and powder diffraction diffractogram etc. Pole figures illustrate the texture information while powder diffraction diffractogram reveals crystalline structure and grain size. As the grain size decreases, the peaks of the powder diffraction diffractogram are broadened. The crystallite size can be calculated according to the Scherrer formula [132]:

$$d = \frac{K\lambda}{w_{hkl}\cos\theta_{hkl}} \qquad (2\text{-}2)$$

where d is averaged grain size; K a constant that varies (0.89<K<1); λ the wavelength of the incident X-rays; w_{hkl} the width of the peak of a special phase (hkl); and θ the angle of the center of the peak. XRD is a non-destructive technique to identify crystalline phase and orientation. It can also be used to determine structural properties, such as strain, grain size, phase composition, thermal expansion and order-disorder transformation and so on.

In this project, X-ray diffraction analysis was carried out on a Rigaku D/max X-ray diffractometer (12 kW) with Cu Kα radiation. The equipment is shown in Fig. 2.4.

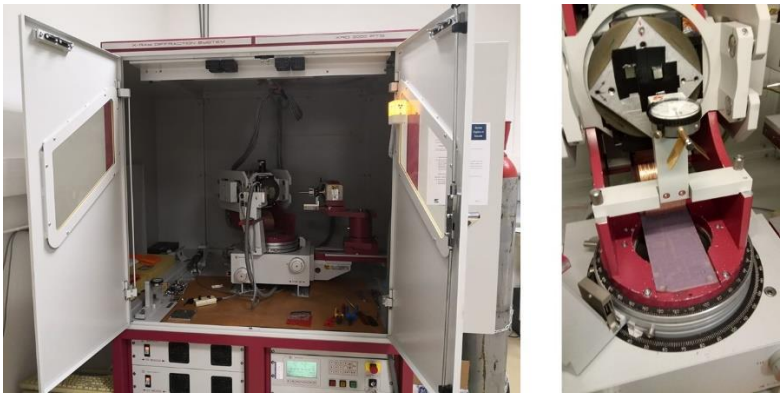

Fig. 2.4 XRD equipment used in this project.

2.4 Electron backscattered diffraction (EBSD)

Electron backscatter diffraction (EBSD) [133] is characterisation technique to investigate the crystallographic microstructure of crystalline materials. It is capable of revealing the structure, crystalline orientation and phase of materials. As mentioned in Section 2.1, backscattered electrons are one of the signals produced when an electron beam hits the sample. Therefore, the working environment of EBSD requires a specific detector for backscattered electrons in a SEM. EBSD has a significant advantage in studying microstructures, revealing texture, defects, grain morphology and deformation.

EBSD observation is performed inside a SEM equipped with an EBSD detector. Usually, a commercially available EBSD system consists of at least a phosphor screen, compact lens and low light CCD camera, as illustrated in Fig. 2.6. At least two CCD cameras are necessary in an EBSD system, one for fast measurements with relatively lower resolution, the other for slow measurements with higher resolution. The sensitivity of EBSD detector is of major concern since it is directly linked to the resolution of the obtained diffraction pattern. A higher sensitivity enables to revealing more detailed information within the diffraction pattern.

With regard to the sample preparation, the sample needs to be flat to be attached on the sample stage. In addition, the surface of the sample should be polished to a mirror-like state to ensure good quality imaging. Imperfections of the sample surface, such as contamination, mechanical scratch due to insufficient polishing and oxidation of the surface, lead to poor quality imaging. The well-prepared sample is placed in the SEM vacuum chamber at a highly tilted angle (~70°) relative to the diffraction camera (seen in Fig. 2.6), with the intention to improve the contrast in the final diffraction pattern. The phosphor screen is placed inside the specimen chamber of the SEM, coupled to a compact lens which focuses the image from the phosphor screen onto the CCD camera. When the tilted crystalline sample is struck by the electron beam and henceforth the diffracted electrons form a pattern on the screen. This pattern provides the crystal structure and orientation of the observed region of the sample. A map of the crystal orientation of the sample can be formed afterwards containing information of grain morphology, orientations, grain size and grain boundaries.

In this project, EBSD was performed using a scanning electron microscope FEG-SEM SUPRA 55 VP operating at 20 kV equipped with the OIM™ software system.

2.5 Focused ion beam (FIB)

Focused ion beam (FIB) [134] is a technique widely used in a variety of areas, such as semiconductor industry, material science and nanotechnology. The advantage of FIB lies in the capability to perform delicate site-specific analysis, deposition and ablation of materials in the micrometer scale. Similar to a SEM in which an electron beam is used, a focused beam of ions is used in a FIB setup in the chamber and the generated secondary electrons are collected to form images of the sample. Moreover, FIB can also be incorporated in a system with both electron and ion beam columns which enables the sample to be investigated by either of the beams. In regard to the ion source, liquid gallium ion source is extensively used in most FIB instruments. Indeed, a gallium metal is placed in contact with a tungsten needle. When the gallium is heated, the huge electric field at the tip will lead to ionization and emission of the gallium atoms. Thereafter, those ions are accelerated to an energy of 1-50 keV and focused by electrostatic lenses. Although FIB system is capable of high resolution imaging, SEM is still preferred for the reason of higher resolution imaging and preventing the damage to the sample surface. Consequently, a system combining SEM and FIB enables the advantages of both techniques to be applied, as illustrated in Fig. 2.5.

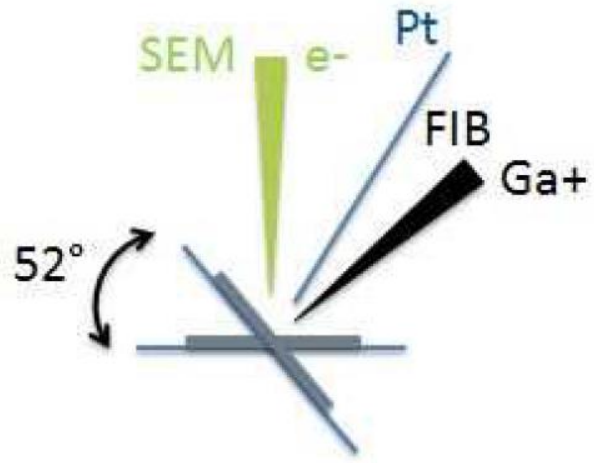

Fig. 2.5 Illustration of the principal of focused ion beam.

One of the distinct characteristics of FIB is that the ion beam is destructive to the sample and is capable of modifying the structure by means of milling small holes in the sample at well localized sites. Atom on the surface of the sample will be sputtered when struck by the ion beam. In the other hand, the gallium atoms will also be implanted into the

top few nanometers of the surface which can be considered as contamination. The implantation of gallium ions on the top surface of the sample can also lead to modification of local structure, for instance, rendering the local structure amorphous [135], [136]. Owing to its destructive capability, FIB is applied as micro- and nano-machining tool. FIB micro machining has become a common practice which allows the preparation of sample at micrometer scale, for example, the fabrication of micro-pillar of a few micrometers. FIB can also be applied to prepare samples for TEM.

In this project, the FIB is performed with a gallium Liquid Metal Ion Source for the fabrication of micro-pillars on a SMATed 316L sample. The equipment is shown in Fig. 2.6.

Fig. 2.6 Focused Ion Beam equipment used in this project.

2.6 Nanoindentation

Hardness can be seen as the capability of a solid material to resist to a permanent shape change when pressing a penetrator onto its surface. As macroscopic hardness is linked to the intermolecular bonds of a specific material, some materials exhibit higher hardness than others. Several methods have been proposed for the measurement of hardness like Brinell, Rockwell, Vickers and Knoop. The basic principle of these measurements is to evaluate the material's resistance to penetration of a hard indenter with a given geometry, which is usually diamond tungsten carbide. Nevertheless, different geometries of indenters are utilised for the aforementioned methods and the mechanical behaviour of solid material under load is quite complex. Even if the hardness measured via those methods is

represented in different units, for example, HV for Vickers hardness and HB for Brinell hardness [137]. It is always expressed as the ratio between the applied force (F) and the area of the indentation impression (A), as indicated in equation (2-3).In this way, hardness as the dimension of a pressure.

$$H = P_m = \frac{F}{A} \tag{2-3}$$

As implied by equation (2-3), two experimental parameters are essential for the calculation of indentation hardness, the applied force of the indenter and the projected area of indentation impression. For traditional microindentation, a prescribed load is applied to an indenter in contact with the specimen and the load is then removed. The area of the residual impression is measured afterwards. The applied force is often in the range of 1 to 1000 N in order to form an observable impression under optical microscope. This implies that microindentation is not capable of measuring hardness at smaller scale. Nanoindentation [14], on the other hand, is able to perform delicate hardness measurement at smaller scale. The applied force can be as low as tens of mN. In nanoindentation, the indenter is usually a Berkovich tip (three-sided based pyramid), the contact area is the projected one and the hardness is expressed in GPa. The area of contact at full load is determined by the depth of the impression and the know angle or radius of the indenter. The hardness is found by dividing the load by the area of contact. Moreover, shape of the unloading curve provides measurement of the elastic modulus. The principle of nanoindentation will be addressed in more details in the following Section.

In this work, indentations tests were carried out with a Nanoindenter XP (Nanoinstruments, Knoxville, TN), as shown in Fig. 2.7.

Fig. 2.7 Nano indenter®XP instrumented indentation system.

2.6.1 Measurement of hardness

Nanoindentation is able to perform delicate hardness measurement of a specific force or displacement which could be controlled and measured simultaneously and continuously over a complete loading cycle. As mentioned previously, nanoindentation gains popularity owing to the fact that it can record small load and displacement with high accuracy and precision. Many material properties, such as Young's modulus, hardness [14], yield strength [138], [139], work-hardening exponent [139]–[142], fracture toughness [143], small-scale mechanical behavior (for instance, indentation size effect, pressure-induced phase transformation) [144],[145], and so on, can be investigated using this test. Fig. 2.8 illustrates the schematic of an indentation system [14]. Since its commercialization in the middle of 1980s, instrumented indentation has become a powerful tool for measuring small-scale mechanical properties of materials.

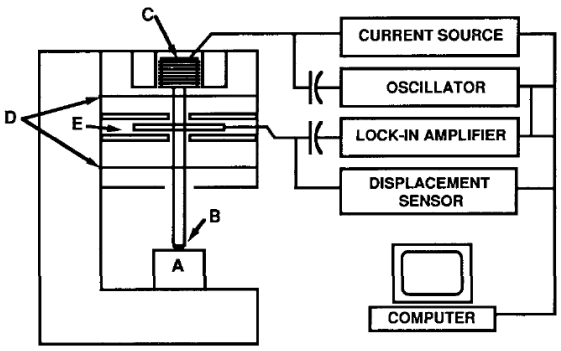

Fig. 2.8 Schematic of nanoindentation device with (A) sample; (B) indenter;
(C) load application coil; (D) indentation column guide springs;
(E) capacitive displacement sensor [14].

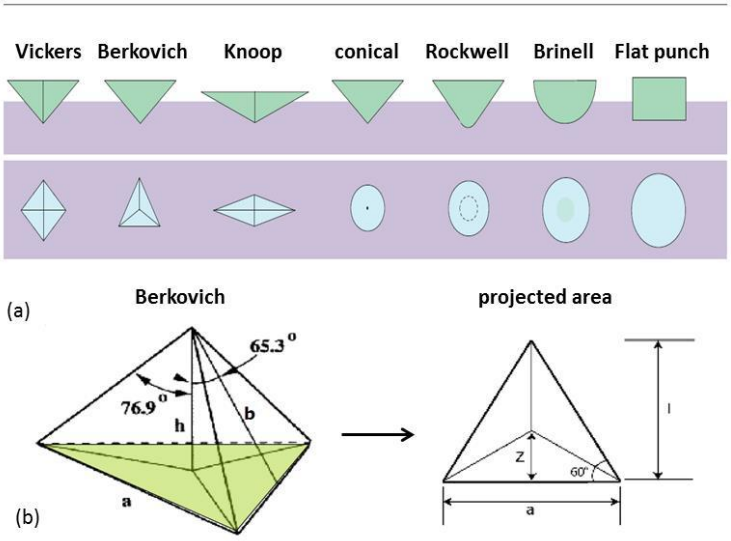

Fig. 2.9 (a) Various indenter tips with different geometries [146], (b) Berkovich indenter tip.

Various indenter tips are available for indentation hardness measurement, as illustrated in Fig. 2.9 [146]. Specific attention is paid to Berkovich indenter because most of the tests in this project were carried out using a diamond Berkovich tip [147]. As illustrated in Fig. 2.9 (b), it is a three-sided pyramid which is geometrically self-similar, with a face angle of 65.3°, measured from the axis to one of the pyramid sided face. As it is three sided, it is easier to grind these tips to a sharp point than a four-sided pyramid (Vickers tip) and so is more readily employed for nanoindentation tests. For this reason, Berkovich tip is widely used in tremendous scientific reports [148]–[153]. In addition, its self-similar geometry results in a regular stress/strain field as the indenter penetrates the sample. Consequently, the projected area can be calculated easily owing to the symmetrical shape of a Berkovich tip. Equation (2-4) demonstrates the projected area as a function of the contact depth (h_c) into the sample [14].

$$A_{proj} = 3\sqrt{3}h_c^2 tan^2 65.3° = 24.56h_c^2 \qquad (2\text{-}4)$$

Indenters used in practical nanoindentation testing are not ideally sharp. Therefore, tip geometry calibration or area function calibration is needed. A series of indentations is made on fused quartz at depths of interest [14]. A plot of A_{proj} versus h_c can be curve fit according to the following equation

$$A_{proj} = 24.56h_c^2 + C_1h_c^1 + C_2h_c^{1/2} + C_3h_c^{1/4} + \cdots + C_8h_c^{1/128} \qquad (2\text{-}5)$$

where C_1 through C_8 are constants. The first term describes a perfect Berkovich indenter, the others describe deviations from the Berkovich geometry due to blunting of the tip.

It should be stressed out here that the total displacement into the sample (h) is not the contact depth. According to Oliver [14], their relationship is illustrated in equation (2-6). Fig. 2.10 (a) [14] shows a cross Section of an indentation and identifies the parameters used in the analysis. At any time during loading, the total displacement (h_{max}) can be decomposed as the sum of contact depth (h_c) and the displacement of the surface (h_s) at the perimeter of the contact. Here, it can be clearly observed that h_c is the actual displacement of indenter into the sample and that h_s should be subtracted regarding the calculation of projected area.

$$h_{max} = h_c + h_s \tag{2-6}$$

At peak load, the load and displacement are P_{max} and h_{max}, respectively, and the radius of the contact circle is a. Upon unloading, the elastic displacements are recovered, and when the indenter is fully withdrawn, the final depth of the residual hardness impression is h_f (seen in Fig. 2.10 (a)).

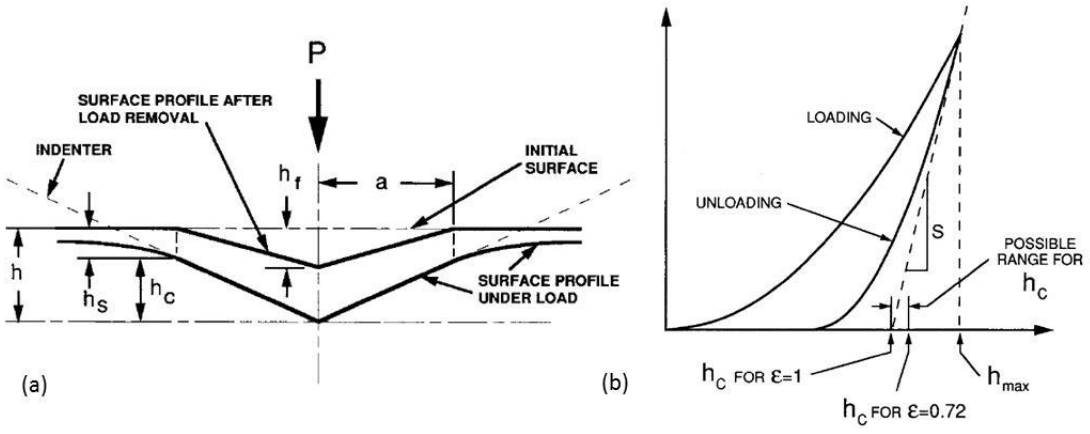

Fig. 2.10 (a) A schematic representation of a Section through an indentation showing various quantities used in the analysis, (b) A schematic representation of load versus indenter displacement showing quantities used in the analysis as well as a graphical interpretation of the contact depth [14].

The hardness is determined by the projected area of the indenter at peak load, which is subsequently linked to the contact depth, h_c. Oliver et al. [14] assumed that the indenter

geometry could be described by an area function F (h) which related the cross-Sectional area of the indenter to the distance from its tip, h. Since the indenter is made of diamond which is not expected to deform significantly, the projected contact area at peak load can then be computed from the relation:

$$A_{proj} = F(h_c) \tag{2-7}$$

Where $h_c = h_{max} - h_s$, as mentioned in equation (2-6). Here, h_{max} can be measured experimentally while it's difficult to calculate directly h_s. According to Sneddon (Sneddon 1965), h_s can be estimated by

$$h_s = \epsilon \frac{P_{max}}{S} \tag{2-8}$$

where P_{max} is the maximum load, S = d P/ dh is the experimentally measured stiffness of the upper portion of the unloading data, and ϵ is a coefficient relative to the geometry of the indenter. For cylindrical, spherical and conical indenters, the values for this coefficient are ϵ=1, ϵ=0.75 and ϵ=0.727, respectively [14]. Thus, the contact depth h_c can be calculated with the estimation of h_s. Woirgard et al. demonstrated that ϵ varies between 0.727 and 1 for a pyramidal indenter [154], as indicated in Fig. 2.10 (b). From all the above discussion, the calculation method of hardness proposed by Oliver and Pharr could be summarized by the following charts (Fig. 2.11). From the experimentally measured indentation curves, three parameters could be extracted: the maximum load, P_{max}, the maximum displacement h_{max} and the stiffness S. Subsequently, the contact depth h_c, which is exploited to resolve the projected area A_{proj}, could be calculated with the coefficient ϵ. Finally, the hardness is found by dividing the load by the projected area.

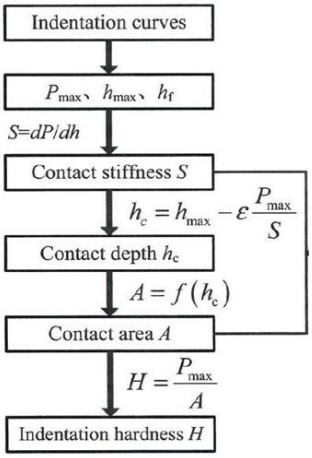

Fig. 2.11 Summary of the calculation of hardness with the contact depth h_c , proposed by Oliver and Pharr.

2.6.2 Measurement of stiffness and Young's modulus

Young's Modulus is a mechanical property that measures the stiffness of a solid material. It defines the relationship between stress and strain (proportional deformation) in a material in the linear elasticity regime of a uniaxial deformation. One of the advantages of instrumented indentation is that it allows rapid, accurate and low-cost measurement of Young's modulus of a material compared to other methods such as tension/compression test, bending test and natural frequency vibration test.

Fig. 2.12 illustrates a typical load-displacement curve during a complete loading-unloading cycle. Sneddon derived general relationships among the load, displacement, and contact area for any punch that can be described as a solid of revolution of a smooth function [155]. His results showed that the load-displacement relationship for many simple punch geometries could conveniently be written by a power law

$$P = \alpha h^m \tag{2-9}$$

where P is the load, h is the displacement and α and m are constants. Values of the exponent m for some common punch geometries are: m = 1 for flat cylinders, m = 2 for cones, m = 1.5 for spheres in the limit of small displacements, and m = 1.5 for paraboloids of revolution [14]. In order to calculate the Young's modulus, a new parameter E_r, reduced modulus, is introduced to account for the effects of non-rigid indenters on the load-displacement behaviour, as expressed by

$$\frac{1}{E_r} = \frac{(1-\nu^2)}{E} + \frac{(1-\nu_i^2)}{E_i} \tag{2-10}$$

where E and ν are Young's modulus and Poisson's ratio for the specimen and E_i and ν_i are the same parameters for the indenter. With the help of E_r, the stiffness S of the material can be calculated by

$$S = \frac{dP}{dh} = \frac{2}{\sqrt{\pi}} E_r \sqrt{A} \tag{2-11}$$

where A is the projected area of the elastic contact. It should be pointed out here that S is the experimentally measured stiffness of the upper portion of the unloading data, as indicated in Fig. 2.12. By measuring the initial unloading stiffness and assuming that the contact area is equal to the optically measured area of the hardness impression, the modulus can thus be derived. Good agreement was noted between generally accepted values of modulus and values computed from equation (2-11) by King [156]. Thus, instrumented indentation provides an alternative method to measure rapidly and accurately Young's modulus with a relative low cost.

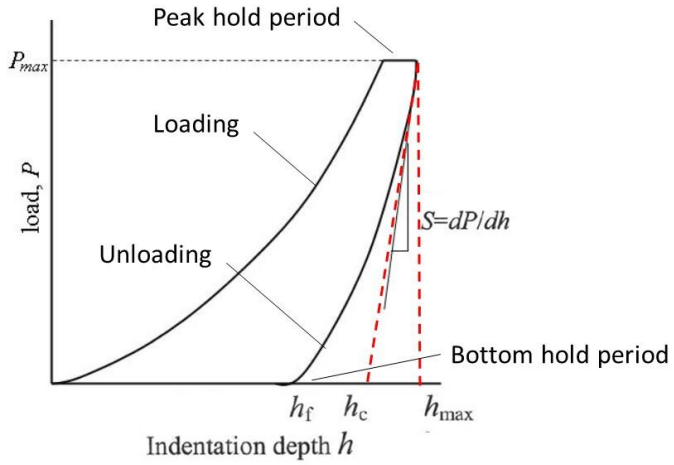

Fig. 2.12 Typical load-displacement curve of an indentation test.

If we take a close look at Fig. 2.12, we can find that there is a peak hold period besides loading and unloading curves during a classical indentation test. One important practical question that arises in the analysis procedure is how the initial unloading stiffness, S, should be measured from the unloading data. One simple way to accomplish the measurement is to fit a straight line to a fraction of the upper portion of the unloading curve and use its slope as a measure of the stiffness, as illustrated in the above figure. But according to Oliver [14], different values of stiffness measured for tungsten were found from the first and last unloading (seen in Fig. 2.13). In other words, it may not be accurate

to measure stiffness using directly the unloading data. The reason for this is that there is a significant amount of creep during the first unloading, resulting in the slope of the upper portion of the unloading curve to be abnormally high. These effects can be minimized by the inclusion of peak load hold periods in the loading sequence to diminish time dependent plastic effects. Thus, more precise measurement of stiffness can be made using the data after the peak hold period. In addition to the peak hold period, there is also a bottom hold period at 90% of the unloading, as indicated in the figure. This bottom hold period is meant to incorporate the corrections due to thermal drift, which will be addressed in the following Section.

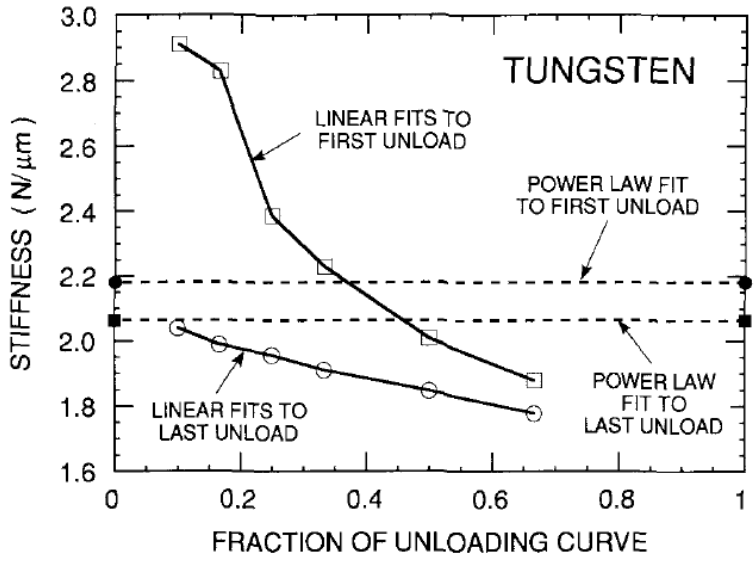

Fig. 2.13 Different values of stiffness measured for tungsten using the first and last unloading [14].

2.6.3 Continuous Stiffness Measurement method (CSM)

In the previous Section, the Oliver-Pharr method to calculate the hardness and Young's modulus with instrumented indentation was introduced. Parameters like the maximum load P_{max}, the maximum displacement h_{max}, stiffness at unloading S, projected area A_{proj} are derived from only one point (P_{max}, h_{max}) of the load-displacement curve. In order to obtain the evolution of hardness (H)/Young's modulus (E) as a function of indentation depth, we need to perform several individual tests with different indentation depth, which is very time-consuming. For the convenience of rapid measurement, the continuous stiffness measurement (CSM) method is established for obtaining elastic modulus and hardness data continuously during a nanoindentation process. This method is

accomplished by applying a small oscillation load signal, $P = P_0 \exp(i\omega t)$, to the force signal at a relatively high frequency, as shown in Fig. 2.14 (a) [14]. To avoid influence on the deformation process due to the addition of the force oscillation, the amplitude of the imposed force should be kept sufficiently small. To be able to measure the stiffness S continuously, we need to understand first the response of the entire system, a dynamic model which is shown in Fig. 2.14 (b).

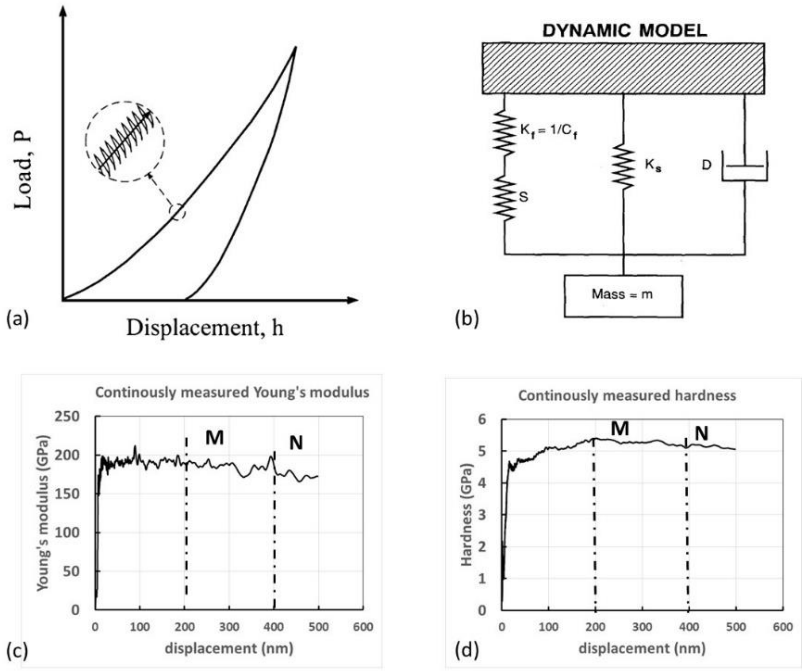

Fig. 2.14 (a) Schematic of the CSM loading cycle, (b) Schematic of the dynamic indentation model [14], (c) and (d) Example of continuously measured Young's modulus and hardness as a function of indentation depth from a single test.

An analysis of this model reveals that the stiffness of the contact, S, can be calculated from the amplitude of the displacement signal from

$$\left|\frac{P_{os}}{h(\omega)}\right| = \sqrt{\left\{\left(S^{-1} + C_f\right)^{-1} + K_s - m\omega^2\right\}^2 + \omega^2 D^2} \qquad (2\text{-}12)$$

or from the phase difference between the force and displacement signals from

$$\tan(\phi) = \frac{\omega D}{\left(S^{-1} + C_f\right)^{-1} + K_s - m\omega^2} \qquad (2\text{-}13)$$

Where

C_f = the compliance of the load frame ;

K_s = the stiffness of the column support springs ;

D = the damping coefficient ;

P_{os} = the magnitude of the force oscillation ;

h (ω) = the magnitude of the resulting displacement oscillation ;

ω = frequency of the oscillation ;

ϕ = the phase angle between the force and displacement signals ;

m = mass of indenter.

With the obtained instantaneous stiffness S, we can calculate the contact depth and contact area using the original Oliver-Pharr method described previously. Thus, hardness and elastic modulus data can be continously obtained along the entire applied loading process, which is a major improvement compared to the conventional Oilver-Pharr method. Fig. 2.14 (c) and Fig. 2.14 (d) give an example of continously measured Young's modulus and hardness as a function of indentation depth from a single test. An average value of Young's modulus and hardness will also be calculated to represente the overall properties of this single test using the continously measured data with a user-defined interval from data point M to N, indicated in Fig. 2.14 (c) and Fig. 2.14 (d).

As a matter of fact, the application of CSM method has been found in many areas to accurately obtain material properties in small scale. For instance, the CSM technique can be used to study the mechanical properties of graded materials and multilayered structures by monitoring the change in contact stiffness, elastic modulus, and hardness as a function of indentation contact depth [157]. In addition, one of the promising applications of the CSM technique is indentation creep testing. Compared to conventional tensile creep tests, the CSM indentation creep experiment gives a direct measure of mean stress and contact stiffness, and being insensitive to drift, allows the accurate observation of creep in small indents to be carried out over a long time period [158]. And as the CSM technique provides force cycles of a sinusoidal shape at high frequencies that can be used to perform nanoscale fatigue tests [159].

2.6.4 Factors affecting nanoindentation

In conventional indentation test, the projected area between the indenter and the sample at maximum load, the contact depth and stiffness at unloading are usually employed to calculate hardness and Young's modulus. In practice, various factors could interfere during the acquisition of these parameters, causing deviation from reliable and accurate measurements. Some of these factors arise from environmental changes during the test and

non-ideal shape of the indenter, others are materials related issues that could affect the validity of the results, like indentation size effect and pile-up/sink-in phenomenon. The sensitivity of nanoindentation test to these factors is a subject of continuing research. In this Section, we will briefly review some of the most encountered factors and methods to accounting for them.

2.6.4.1 Thermal drift

There are two types of drift behaviour that could take place during a nanoindentation test which will affect the recording of the depth data. The first is creep within the specimen material as a result of plastic flow when the load is held constant, on the other hand, the displacement continue to proceed. This problem was briefly addressed in the previous Section in which a solution was proposed by the addition of a peak hold period. The second type of drift comes from a change in dimensions of the instrument due to thermal expansion or contraction of the apparatus. This is termed thermal drift which will impose an error to the real depth data. To account for this phenomenon, the rate of change of depth with time needs to be measured for a constant value of load during an indentation test, for example, by adding a bottom hold period at 90% unloading in the final step of an indentation test. With this measured rate of change of depth, then the thermal drift rate can be computed and we can correct the depth data throughout the test accordingly. Fig. 2.15 gives an example of load-displacement curves before and after the correction of thermal drift [160].

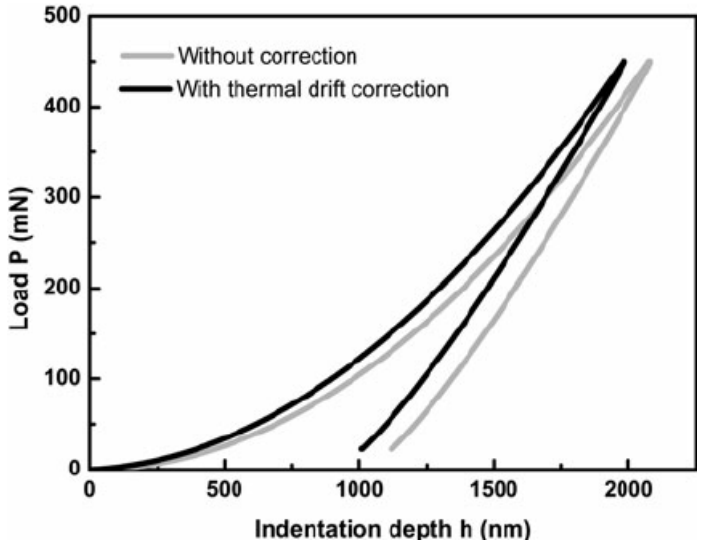

Fig. 2.15 Load-displacement curves before and after the correction of thermal drift [160].

2.6.4.2 Pile-up and Sink-in

In Section 2.6.1 and 2.6.2, we have discussed in details the conventional Oliver-Pharr method to calculate the hardness and Young's modulus in which the key parameters are the contact depth, stiffness and projected area between the indenter and the material. During an indentation test, pile-up and sink-in phenomena may occur which will in turn affect the measurement of the projected area and lead to deviation of accurate measurement accordingly.

The analysis of Oliver-Pharr method is based on an elastic solution and works well for hard materials when sink-in pre-dominates (i.e., the indented material around the indenter is moved below the original surface plane, as indicated by Fig. 2.16). But in the case of soft materials where pile-up phenomenon takes place [152], [153], the contact area will be underestimated using the Oliver-Pharr method. Moreover, the higher the load-displacment applied to a soft material during indentation, the severe the pile-up phenomenon is. As a result, the hardness calculated with an underestimated contact area will be higher than the true value. Although some correction procedures have been proposed, the real contact area measurement requires imaging of indentation impressions.

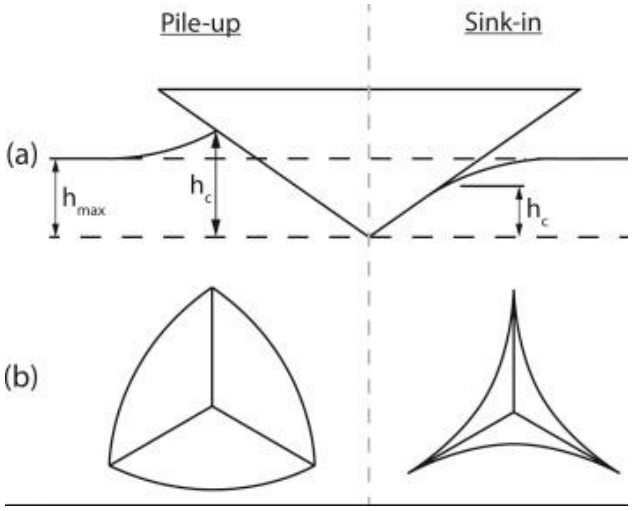

Fig. 2.16 (a) Pile-up and Sink-in phenomena during nanoindentation, (b) corresponding overestimated and underestimated contact areas [161].

2.6.4.3 Determination of initial contact point

In the beginning of an indentation test, the indenter needs to be brought into contact with the surface of the sample. Ideally, the penetration depth is measured from the level of the sample's free surface as a function of the controlled load. However, in the real case, the

indenter must first make contact with the sample surface before the depth measurement can be taken [162]. Therefore, it is necessary to make actual contact with the sample surface to enable the recording of depth. With this intention, an initial contact point, is given to bring in contact the indenter and the sample in the very beginning of the test. This value is often set as small as possible to minimize the corresponding errors. But no matter how small the initial indentation depth is, there is always a corresponding error regarding the indentation depth data, as shown in Fig. 2.17. P_i and h_i are the initial contact load and initial penetration depth which should be corrected afterwards. According to the Hertz equations [163], which predict that the relationship between load and penetration for an elastic response is of the form

$$h \propto P^n \tag{2-14}$$

where n is constant depending on the geometry of the indenter. During the initial loading, the instrument measures P and h_t where the initial indentation depth should be taken into account. Thus, we have

$$h_t + h_i \propto P^n \tag{2-15}$$

$$h_t \propto k(P^n - P_i^n) \tag{2-16}$$

where k is a constant depending on the shape of the indenter and P_i is the initial contact load. More details can be found elsewhere for the correction of initial indentation depth [162].

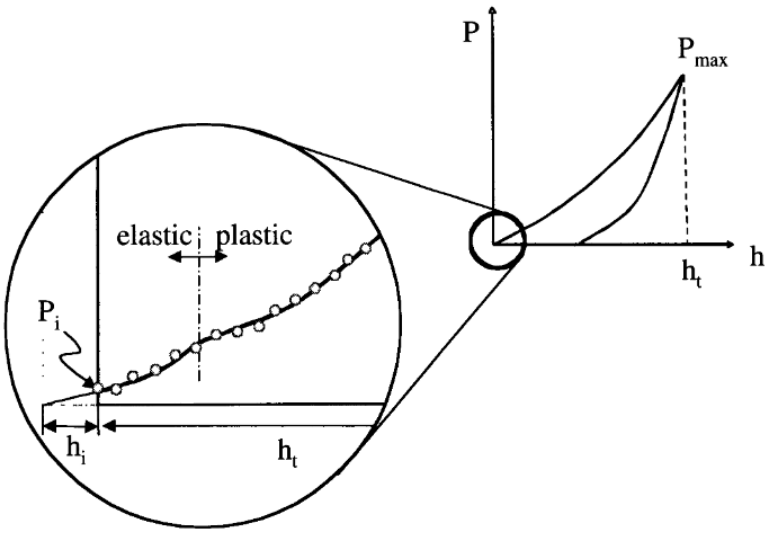

Fig. 2.17 Schematic of the effect of initial penetration depth on load-depth data for a depth-sensing indentation test [162].

2.6.4.4 Indentation size effect

Indentation size effect is often observed during nanoindentation in some materials. It is exhibited by a variation of hardness and/or modulus with indentation depth. Fig. 2.18 (a) illustrates an example of continuously measured hardness as a function of indentation depth. It is observed that the measured hardness is higher for small depth while for a homogeneous, isotropic material, it is expected to measure one value of hardness/modulus regardless of the indentation depth. A few factors are considered be the cause for this phenomenon, such as the thin oxide layer formed in the near surface of the sample with different mechanical properties other than the bulk material, residual stress, strain hardening arising from sample preparation and polishing process and friction between the indenter and the sample [162]. But the above mentioned factor can all be minimized. Nevertheless, even if these effects are minimized, an indentation size effect is still observed [144].

For materials with indentation size effect, the indentation hardness is observed to increase with decreasing indentation depth as a result of the nucleation of dislocations within the plastic zone [144]. Two types of dislocations are created, the statistically stored dislocation (SSD) and geometrically necessary dislocation (GND). Fig. 2.18 (b) shows an example of the distribution of GND as the indenter penetrates the sample[164]. The presence of dislocations will increase the effective yield strength and in turn results in an increase in hardness. Nix and Gao [144] proposed the calculation of the density of GND within the plastic deformed zone bounded by the circle of contact for a conical indenter

$$\rho_g = \frac{3}{2bh} tan^2\theta \qquad (2\text{-}17)$$

where b is the Burger vector and θ is the angle of the cone made with the specimen free surface and h is the indentation depth. The presence of GND can be linked to the existence of strain gradients generated in the vicinity of the indentation. The increase in hardness due to GND is more pronounced when the indentation depth is small. This is because that in the case of small indentation depth, the strain gradient is relatively larger, as indicated by equation (2-17). With the increase of indentation depth, the influence of GND becomes smaller and smaller. Normally, we expect little indentation size effect for hard materials. For soft material, and especially crystalline materials, we do expect a significant indentation size effect [162].

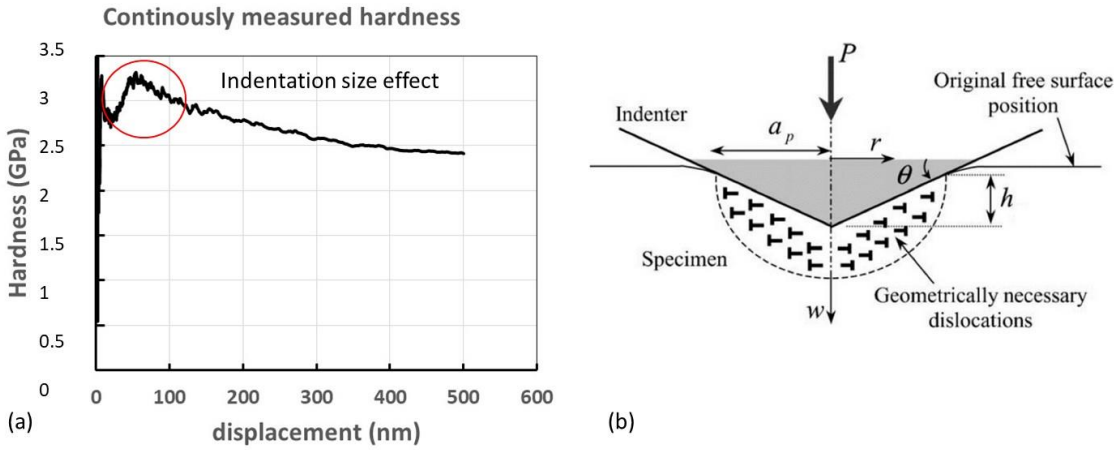

Fig. 2.18 (a) Variation of hardness as a function of indentation depth, (b) Geometrically necessary dislocations in the plastic zone created by a conical indenter [164].

2.6.4.5 Influence of residual stress

Residual stresses are often generated by inhomogeneous heat treatment or local plastic deformation involving bulk solids [165],[166], thin films [167], [168], and coatings [169],[170] used in various industrial components. The existing residual stress field in these components has a significant effect on their performance such as mechanical properties [171], fatigue strength [172] wear and fracture properties [173] etc. The existence of residual stress may be beneficial or detrimental, depending upon its value and the potential application. In the case of nanoindentation measurements, residual stress has been reported to have effects on the measurements of hardness and Young's modulus [174], load-displacement curves [149], [175], pile-up [151], [175], [176] and true contact area [177], [178]. Fig. 2.19 [149] gives an example of the influence of residual stress on the loading and unloading curves. In the case of compressive residual stress, a higher indentation load is needed for a fixed indentation depth and the unloading curve shifts to the left while opposite effects have been found for tensile residual stress. However, the influence of residual stress on nanoindentation measurements can be extremely complicated and controversial. For example, both hardness and elastic modulus were found to increase with compressive stress and decrease with tensile stress [174] when the nanoindentation data were analyzed by standard methods. However, the elastic modulus which is an intrinsic property of the material should not be affected by stresses. It is argued that compressive residual stress tends to increase the amount of pile-up and affect the true contact area, which leads to inaccurate measurements. Once the proper contact area is used, the hardness and elastic modulus are significantly independent of stress [149], [174]. It could be even

more complicated when other factors (for example, low strain hardening) affecting nanoindentation co-exist with residual stress. For instance, in addition to residual stress, pile-up deformation behaviour is related with the ratio h_f/h_{max} and work hardening behaviour [179]. The pile-up amount is large when h_f/h_{max} is close to 1 and the degree of work hardening is small. When h_f/h_{max} is less than 0.7, very little pile-up occurs no matter what the work hardening behaviour of materials. Hence, it is a real challenge to accurately determine the influence of residual stress individually.

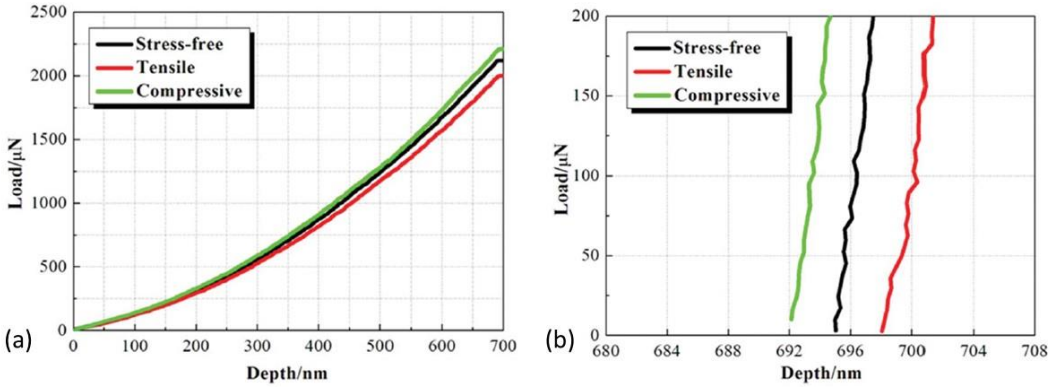

Fig. 2.19 Influence of residual stress on (a) the loading curve, (b) the unloading curve [149].

2.6.5 Cyclic loading method for nanoindentation

Nanoindentation is a technology that is extensively applied to probe material properties at the nanoscale. Commercially available nanoindentation instruments are usually equipped with two operation modes, namely, the quasi-static loading mode [180], in which load is quasi-statically applied, and the continuous stiffness measurement (CSM) mode or dynamic mode, in which an oscillatory load signal is superimposed on a background, slowly varying load schedule of the indenter tip [14]. In the Section 2.6.3 the CSM method has been discussed in details as well as its application in tremendous areas for obtaining accurately mechanical properties at nanoscale. In this Section, we will briefly introduce two quasi-static cyclic loading methods available for nanoindentation tests, which are presented in Fig. 2.20. The main required input parameters for the first cyclic loading method with constant P_{max} are the pre-defined value of P_{max}, number of cycles, the percentage to unload, peak hold time and bottom hold time. A complete single cycle

includes loading and unloading. It should be specified here that for the unloading parts during the cyclic test, the contact between the indenter and the sample surface should always be maintained. The parameter, percentage to unload (which is often set to be 90%), is used for this purpose, which signifies that the indenter unloads 90% of the peak load instead of complete unloading, as indicated by red circle in Fig. 2xa. It is also possible to include a peak hold period and bottom hold period (which is addressed in Section 2.6.2) to account for time dependent plastic effects and thermal drift. As for the second cyclic loading method with linearly-increasing P_{max}, one more parameter is needed compared to the first one. A maximum penetration depth, h, should be pre-defined. This maximum penetration depth, h, will be divided by the number of cycles, n, which consequently forms several evenly-distributed intervals. And the test ceases when the indentation depth reaches the value of the maximum penetration depth. These two cyclic loading methods provide the possibility to study the cyclic deformation/fatigue behaviour of a variety of materials at micro-scale [21], [181]–[184]. However, special attention needs to be paid to the thermal drift during the cyclic test as a typical cyclic test might last for hours, causing the thermal drift to be extremely high and affecting the validity of the results. It should be specified that the strain rate of the indentation test is constant (0.05 s^{-1}). In order to achieve a constant strain rate in the case of Berkovich indenter, $\frac{dP/dt}{P}$ is kept constant where P is the load and t is the time.

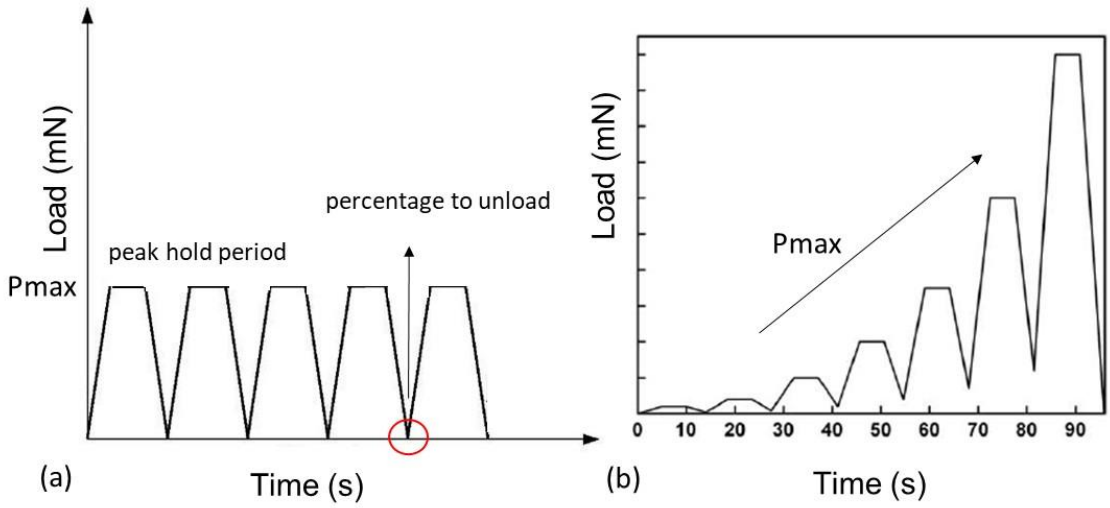

Fig. 2.20 (a) Cyclic loading method with constant P_{max} and (b) Cyclic loading method with linearly-increasing P_{max}.

2.6.6 Plastic work and elastic work during a nanoindentation test

Generally speaking, a nanoindentation test can be decomposed into an elastic-plastic loading followed by an elastic unloading in which the load P and the indentation depth h can be expressed by a power law, as mentioned in equation (2-9) in the previous Section. There exists a novel way to interpret this process of an indentation test in the view of energies involved. A schematic of the energies involved during this process is given in Fig. 2.21 [185]. The work done by the applied load can be represented by the plastic and elastic strains within the specimen. Thus, the total work done can be divided into plastic work and elastic work as indicated by two enclosed areas in Fig. 2.21. It should be mentioned that the contribution to the elastic recoverable energy to the total energy depends only weakly on the geometry of the indenter and is characteristic of the hardness of the material [186]. Therefore, it is possible to determine the hardness of the material by investigating the recoverable energy during an indentation test by [149],[180], [139]:

$$H_{W_t} = \frac{kP_{max}^3}{9W_t^2} \tag{2-18}$$

$$H_{W_p} = \frac{kP_{max}^3}{9W_p^2} \tag{2-19}$$

The plastic work and elastic work done during the indentation test can be exploited to identify the mechanical properties of the material or to explain phenomena taken place during the test. For example, an increased ratio between the plastic work and the total work may imply a crack initiation/damage initiation for brittle materials [20]. In addition, the initial unloading stiffness may be expressed in terms of the elastic work and the hardness may be evaluated from the total work done using the energy-based analysis method [149]. Therefore, this energy-based analysis method provides an alternative way to interpret the indentation data.

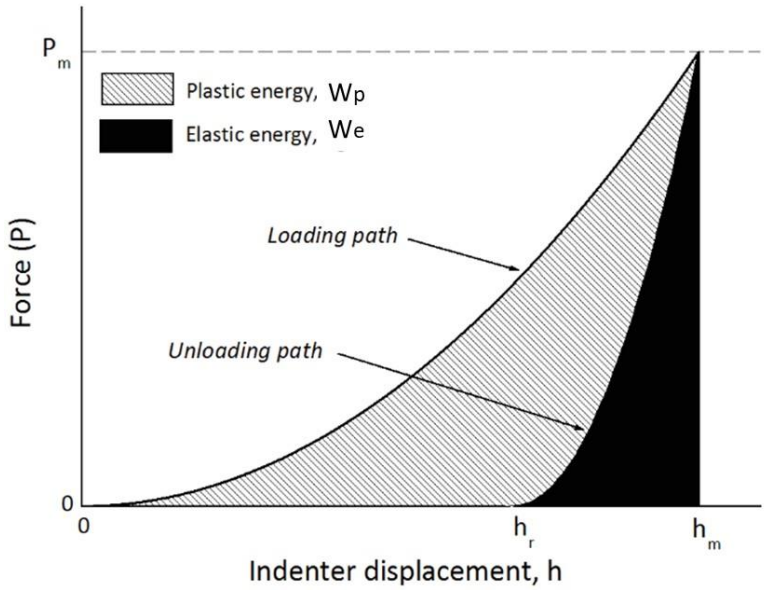

Fig. 2.21 Schematic of a typical load-unload curve for a nanoindentation test showing elastic and plastic deformation energies [185].

2.7 Micro-pillar compression tests

Micro-pillar compression was originally used to investigate the mechanical properties and understand the deformation mechanisms of single crystals [22]. Thanks to its simplicity and capacity of direct access to uniaxial mechanical behavior of materials at micrometer scale, it is becoming a popular method to quantitatively characterize the local mechanical properties of materials. The micro-pillars, whose size ranges often from a few micrometers to tens of micrometers, are fabricated either on a bulk sample with the same material or a substrate of a different material. The principle is to apply a compressive load via a flat punch, which is placed in contact with the upper surface of the micro-pillar. An illustration is given in Fig. 2.22. During the compression, the data of load as a function of displacement will be recorded, which will be used to calculate the stress-strain curve subsequently. One major advantage of micro-pillar compression is that it provides a straightforward characterization method for mechanical properties at micro-scale. Properties like yield strength and strain hardening can be easily obtained from the calculated stress-strain curve.

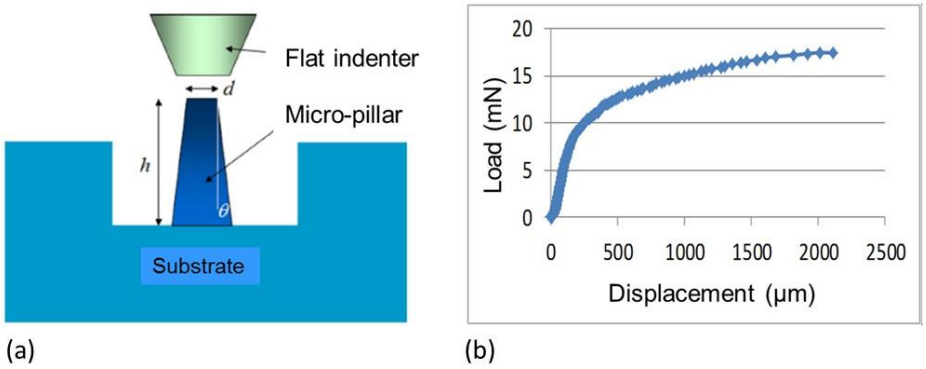

Fig. 2.22 (a) Schematic of the micro-pillar compression test, (b) Load-displacement curve obtained subsequently.

2.7.1 Fabrication of micro-pillars

Focused ion beam (FIB), which is addressed in Section 2.5, is widely used for the fabrication of micro-pillars. A system combining SEM and FIB is used during this process to enable the in-situ observations of manipulation and the angle between the electron incident beam and focused ion beam is about 55°, as shown in Fig. 2.23 (a) [187]. In this project, the micro-pillars were milled using a FIB operating with a gallium Liquid Metal Ion Source. The milling process includes three steps. First, a rough cut around the micro-pillar was made with a high current of 21nA. Then, the micro-pillar was shaped using an intermediate probe current of 0.8nA. Finally, the surface of the micro-pillar was polished with the same current in order to obtain a smooth lateral surface. The micro-pillars have a truncated cone shape. The upper and the lower diameters are respectively 2.5 and 3.5μm, and the height is 10μm. Their taper angle (the angle between the axis and the conical circumferential surface) is about 2°. It should be specified here that the taper angle needs to be inferior to 3°, which is crucial to obtain a reliable stress-strain curve according to previous work presented in the literature [187].

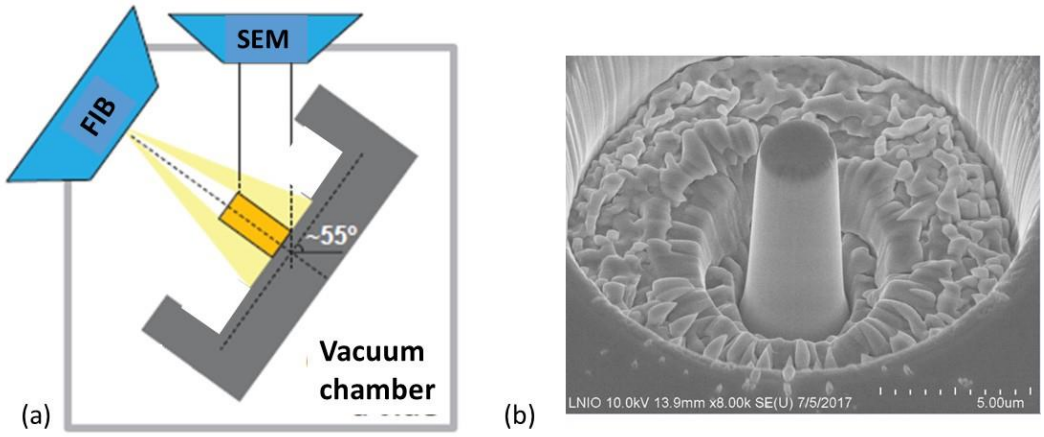

Fig. 2.23 (a) Schematic of a system combined with both FIB and SEM [187], (b) An example of the fabricated micro-pillar in this project.

2.7.2 Influence of FIB

As discussed in Section 2.5, FIB is destructive to the sample which enables the milling of micro-pillars. On the other hand, the gallium atoms will also be implanted into the top few nanometers of the surface which can be considered as contamination or damage [188]. In addition, a perfect cylinder-form pillar cannot be achieved by FIB. This is why the pillars fabricated by FIB have a truncated cone shape [189]. A large taper angle strongly affects the validity of the obtained stress-strain curve [187]. One simple solution to minimize the taper angle is to delicately shape and polish the micro-pillar with a small current, as aforementioned [189], [190]. Some researchers propose to completely shape the lateral surface of the pillar in order to obtain a perfect cylinder-form [190]. But this is very time-consuming and exposure to FIB over a long period of time will surely lead to other concerns like damage and contamination of the sample. Another concern arising from FIB is interaction of gallium ions with the target material. The fabrication of pillar causes long-time exposure to the focused ion beam. Consequently, the implantation of gallium ions on the top surface of the sample can lead to modification of local structure, for instance, rendering the local structure amorphous [135], [136]. The affected zone is estimated to be in the range of about tens of nanometers [188]. When the size of micro-pillar approaches that of the affected zone, the influence of FIB cannot be neglected.

2.8 Atomic force microscope

Atomic force microscopy (AFM) [191] or scanning force microscopy (SFM) is a very high resolution type of scanning probe microscopy, with demonstrated resolution on the

order of fractions of a nanometer. The information is obtained by scanning the surface with a mechanical probe. One major ability of AFM is surface topography imaging, the reaction of the probe to the forces that the sample imposes on it can be used to form an image of the three-dimensional shape (topography) of a sample surface at a high resolution.

Fig. 2.24 (b) shows a schematic illustration of the principles of AFM. The small spring-like cantilever (1) is carried by the support (2). Optionally, a piezoelectric element (typically made of a ceramic material) (3) oscillates the cantilever (1). The sharp tip (4) is fixed to the free end of the cantilever (1). The detector (5) records the deflection and motion of the cantilever (1). The sample (6) is mounted on the sample stage (8). An xyz drive (7) permits to displace the sample (6) and the sample stage (8) in x, y, and z directions with respect to the tip apex (4). The detector (5) of AFM measures the deflection (displacement with respect to the equilibrium position) of the cantilever and converts it into an electrical signal. The probe is placed on the end of a cantilever (which one can think of as a spring). The amount of force between the probe and sample is dependant on the spring constant (stiffness) of the cantilever and the distance between the probe and the sample surface. This force can be described using Hooke's Law. The probes are typically made from Si_3N_4 or Si. In this project, an Atomic Force Microscope (Bruker ICON) was used with a silicon probe, as illustrated in Fig. 2.24 (a).

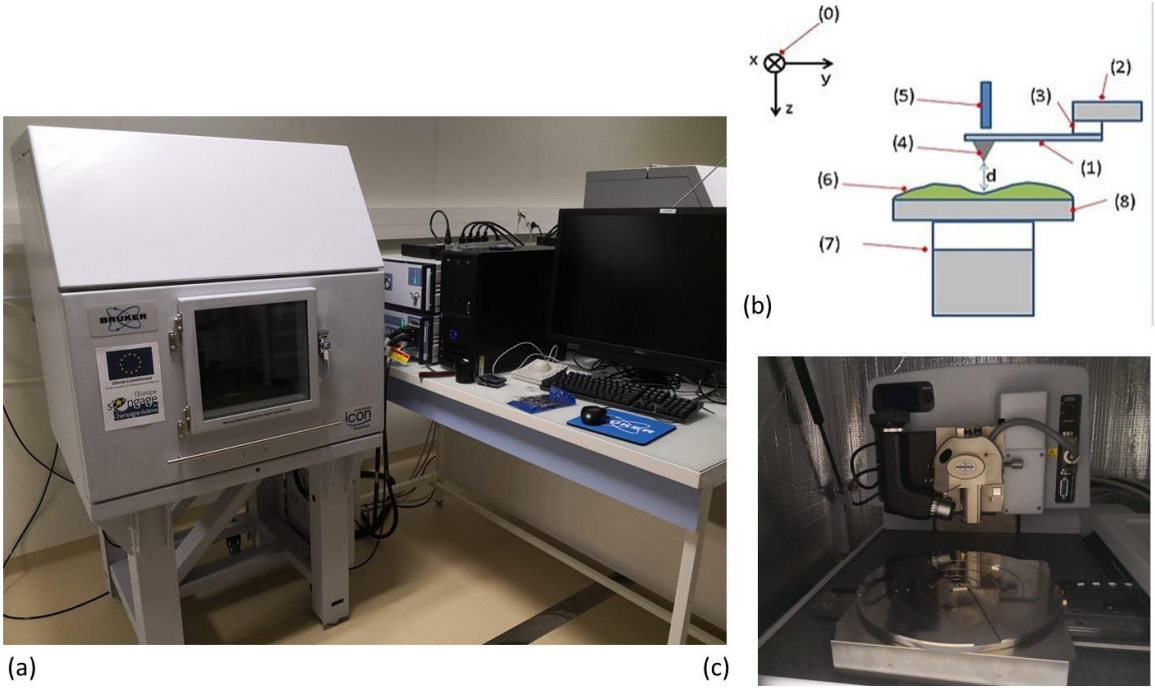

Fig. 2.24 (a) AFM equipment used in this project, (b) Typical configuration of an AFM: (1) Cantilever, (2) Support for cantilever, (3) Piezoelectric element, (4) Tip, (5) Detector of deflection and motion of the cantilever, (6) Sample, (7) xyz drive, (8) Stage and (c) Inside of the AFM equipment.

2.9 Conclusion

The gradient microstructure generated by SMAT has beneficial effects in terms of improving the mechanical properties of the treated component. The thickness of the gradient microstructure is in the micro-scale, especially the nanostructured layer in the near surface which ranges from several micrometers to tens of micrometers depending on the treatment intensity. For this reason, characterization techniques at micro- or nano-scale provide direct accesses for the investigations of the local microstructure characteristics and mechanical properties. This chapter lists a variety of characterization techniques that have been used for the individual characterization of different layers in the gradient microstructure and each is capable of revealing important information about the properties of the tested regions. For instance, the microstructure (grain size distribution and phase transformation etc.) of the sample was investigated by means of SEM, TEM, XRD and EBSD. The mechanical properties of the SMATed samples were mainly examined by nanoindentation and micro-pillar compression. AFM measurements were perform to investigate the pile-up behaviour of SMATed material. The details of the characterization techniques have been described.

Chapter 3: Microstructure of material treated by SMAT

In chapter 2, several characterization methods (SEM, TEM, XRD, EBSD) were presented for studying the microstructure of materials treated by SMAT. These characterization methods have their own advantages and disadvantages and are capable of revealing different information about the microstructure of the treated sample. In this chapter, an overall introduction of the materials studied in this project will be first given, including its chemical and physical properties as well as crystal structure. In the following Section, we will mainly focus on the characteristics of microstructures revealed by the aforementioned techniques before and after SMAT and a comparison will also be made subsequently.

3.1 General introduction about iron and steels

Iron is the base metal of steel whose crystal structure is either body centered cubic (BCC) or face centered cubic (FCC), depending on the temperature. At room temperature, pure iron has a BCC structure which is called alpha iron or α-iron. Only a small concentration of carbon can be dissolved into alpha iron (no more than 0.005% at 0 °C) and the inclusion of carbon in alpha iron is called ferrite. At 910 °C pure iron transforms into a FCC structure, called gamma iron or γ-iron. The inclusion of carbon in gamma iron is called austenite. The more open FCC structure of austenite can dissolve considerably more carbon, as much as 2.1% [192]. Pure iron has a crystal structure with little resistance. As a result, pure iron is often ductile and easily deformed. Modifications of the properties of iron can be realized by adding other elements within the crystal structure. These elements act as hardening agents that impede the dislocation movements.

Steel is an alloy of iron and carbon and other elements. Due to its low cost and excellent mechanical/chemical properties, steel has been widely used in buildings, infrastructure, tools, ships, automobiles, machines, etc. To satisfy diverse needs of various applications, other elements are intentionally added to fabricate steel alloys with desired properties, such as manganese, nickel, chromium, molybdenum, boron, titanium, vanadium, tungsten, cobalt, and niobium. For instance, the addition of nickel and manganese can

improve the tensile strength of steels and the stability of the austenite structure of iron-carbon mixture, while the addition of chromium can increase the hardness, the melting temperature and the resistance to corrosion [192].

When a large amount of chromium is added to steel, known as stainless steel, so that a hard oxide forms on the metal surface to inhibit corrosion. According to their crystal structure, stainless steel alloys can be defined as austenitic stainless steel, ferritic stainless steel and martensitic stainless steel. Young's modulus for these steel alloys is about 200 GPa regardless of their chemical composition. But other properties are more dependent on chemical composition and other applied treatments like heat treatment.

In this project, an austenitic stainless steel AISI 316 is chosen as a target material for the treatment of SMAT and the subsequent studies. Its chemical composition is listed in Table 1. As mentioned above, divers elements added to the steel can modifier specific properties. The combination of numerous elements contributes to an excellent performance of 316L stainless steel, consequently, it is commonly used in chemical and petrochemical industry, in food processing and pharmaceutical equipment, in potable water and wastewater treatment, in marine applications and architectural applications near the seashore or in urban areas [192]. Table 2 gives typical mechanical properties of the studied 316L stainless steel [193].

Table 1 – Chemical composition (wt.%) of the studied 316L stainless steel.

Fe	C	Mn	Si	P	S	Cr	Ni	Mo	Cu	N	Ti	V
Balance	0.013	1.7	0.26	0.017	0.003	17.37	14.52	2.80	0.08	0.088	<0.005	0.07

Table 2 – Typical mechanical properties of the studied 316L stainless steel.

Grade	Tensile strength (MPa)	Yield strength Of 0.2% deformation (MPa)	Elongation (% in 50mm)	Hardness Hv	Elongation at rupture
316L	490	170	40%	195	<60%

As presented in Chapter 2, to observe the microstructure, after a series of polishing steps, the cross-section of the specimens was chemically attacked and then observed using digital optical microscopy. The microstructure is presented in Fig. 3.1. It shows that the as-received material has an initial grain size of about 10-20 μm.

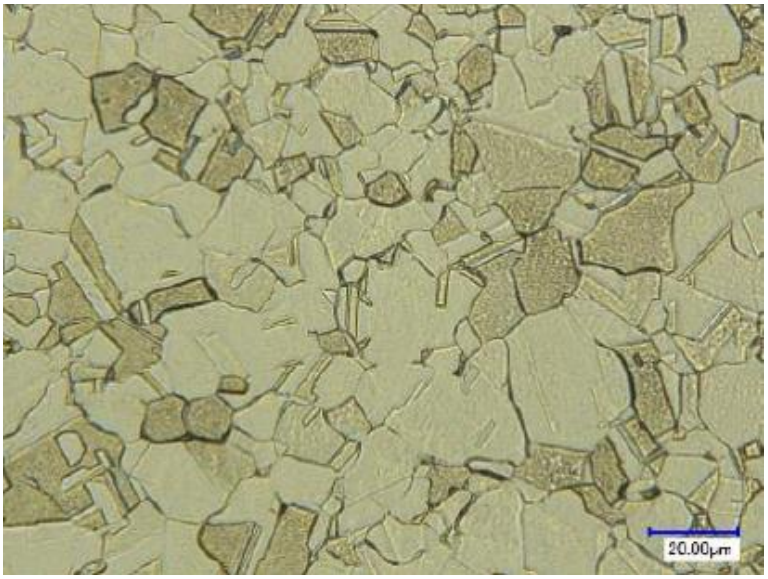

Fig. 3.1 Initial microstructure of a 316L stainless steel.

Regardless of the great resistance to corrosion as a result of the addition of several elements, certain types of corrosion could still take place for stainless steel, for instance, intergranular corrosion. Intergranular corrosion occurs due to chromium depletion at the grain boundaries caused by chromium carbide ($M_{23}C_6$) precipitation [194]–[198]. Consequently, the amount of chromium is gradually reduced at grain boundaries which is detrimental for the protection against corrosion. In addition, when austenitic stainless steels are exposed to heat treatment in the range of 500°C to 900°C, the precipitation of various phases, beside $M_{23}C_6$, might occur, such as M_6C and the sigma, chi and Laves intermetallic phases [199]–[201]. Among these intermetallic phases that might precipitate in stainless steels, the sigma phase is richer in chromium and molybdenum than the austenite phase. Therefore, its precipitation at the grain boundaries causes the impoverishment of these elements in the adjacent matrix. One solution to decrease the susceptibility of intergranular corrosion in stainless steel is reducing their carbon content to less than 0.03 wt.%, for example, for AISI 304L and 316L. However, a low content of carbon decreases further the low yield strength of the austenite in these steels [198]. For this concern, nitrogen could be added to compensate the loss of yield strength due to low content of carbon, as is the case of AISI 316L. Indeed, the inclusion of nitrogen in the structure of austenite phase can improve the strength and the stability of austenite as well as the pitting resistance [202], [203].

3.2 Experimental procedure

3.2.1 SMAT treatment

The material investigated in this work is an austenitic stainless steel AISI 316l as mentioned previously. Typical 316L stainless steel sheet and dumbbell shape specimens for fatigue test were chosen for the treatment of SMAT, as illustrated in Fig. 3.2. The steel sheet has a rectangular shape with a length of 240 mm and a width of 120mm. The thickness of the sheet is 1 mm. For the dumbbell shape specimen, the gauge length is 12 mm with a diameter of 6 mm. The dimensions of these different specimens are illustrated in Fig. 3.2. SMAT was performed separately on both the samples to generate a gradient microstructure. SMAT is based on the vibration of spherical shot (3 mm diameter) boosted by a high frequency (20 kHz) ultrasonic generator. In this work, the specimens were subjected to a treatment of 15 min with a generator power of 27%, followed by a treatment of 5 min with a generator power of 50%. The SMAT conditions are listed in Table 3.

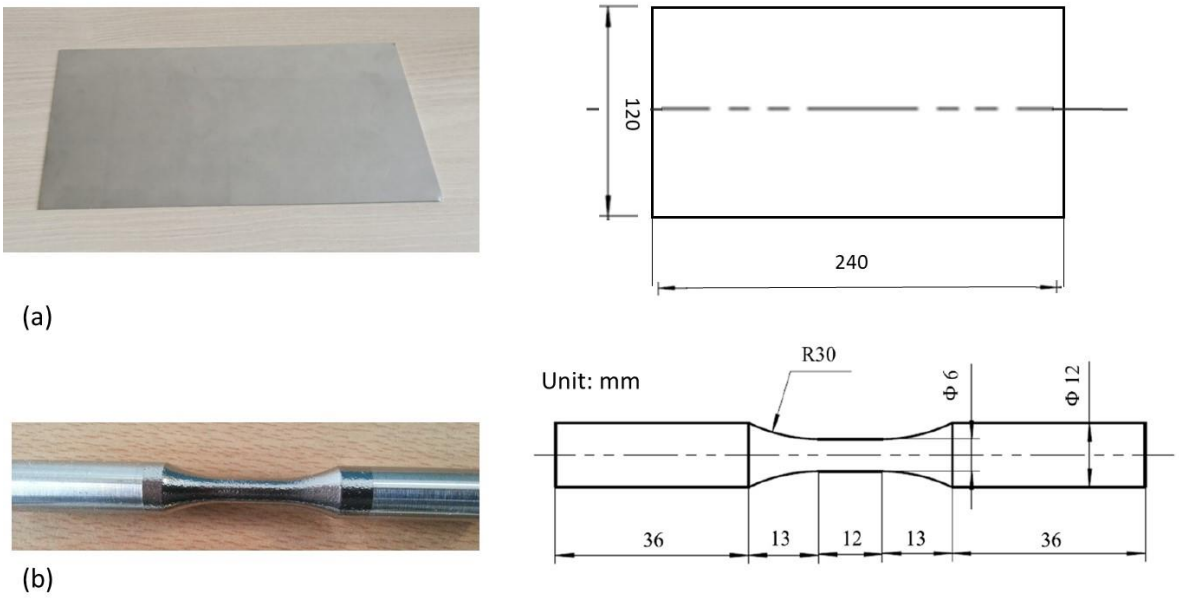

Fig. 3.2 (a) 316L stainless steel sheet and its dimensions (b) 316L dumbbell shape sample for fatigue test and its dimensions.

Table 3 SMAT conditions for 316L stainless steel.

Sample	316L austenitic stainless steel	
Generator power	27%	50%
Duration	15 minutes	5 minutes

Shot	Material: 100 Cr 6, diameter: 3mm
Distance	12 mm

3.2.2 Sample preparation

Specimens were cut both from the central part of the dumbbell shape sample and the treated region of the sheet sample. The specimens were then molded with conductive carbon resin, as shown in Fig. 3.3. Two parallelepiped steel bars (non-SMATed) were placed in contact with the specimen cut from the dumbbell sample to protect the nanocrystalline layer generated in the near surface. For the same purpose, two bars cut from the SMATed regions of the sheet sample were placed in contact each other, as illustrated in Fig. 3.3. The use of conductive carbon resin is essential for the SEM/EBSD observations. The molded samples were then mechanically ground and polished to a mirror-like finish and then polished with an OPS solution.

EBSD/SEM/Nanoindentation are delicate experiments at small scale for the characterization of microstructural and mechanical properties of materials. Fine sample preparation is crucial for obtaining reliable and accurate results. Thus, the preparation of samples for the above mentioned experiments can be a real challenge, especially the samples for EBSD observations. For conventional experiment sample at macroscopic scale, the roughness and the topography of the sample are usually of major concerns, which is also the case for experiments at microscopic scale. However, more factors should be taken into account for sample preparation at small scale. For example, care should be taken to avoid unwanted strain hardening due to machining/mechanical polishing which will lead to an increase in hardness measured during nanoindentation. This phenomenon will be discussed in Chapter 4. In addition, we have encountered some difficulties regarding the preparation of EBSD sample in this project. In a first attempt, bad conditions of the sample surface have led to poor quality diffraction patterns and little information could be extracted from the obtained results. It turned out that various factors could affect the image quality of EBSD, such as presence of dislocations, grain boundaries, plastic strain/lattice deformation, amorphous regions in the sample, porosity, surface topography and EBSD camera noise [204]. Most of these factors degrade the EBSD pattern due to the presence of local lattice curvature/deformation. The degradation of EBSD pattern is demonstrated by Indexing

Success Rate (ISR). Fig. 3.4 gives an example of ZrO_2 samples with different ISR [204]. Ideally speaking, a 100% indexing success rate is often the goal for sample preparation but this can be a real challenge in some cases. To sum up, the EBSD patterns are formed from a depth of 10-50 nm of the sample surface, and any residual surface deformation introduced during the preparation must be minimized in this region to maximize the pattern quality.

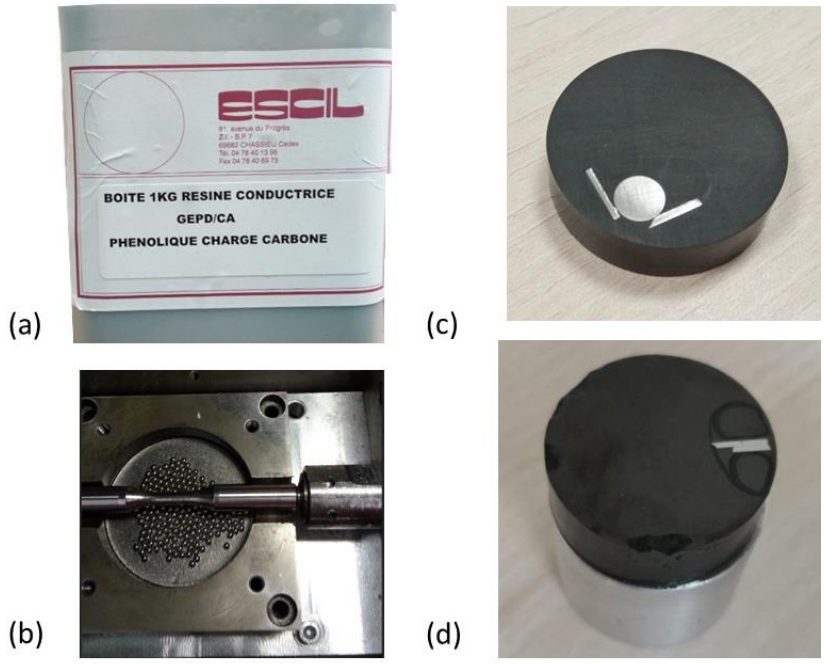

Fig. 3.3 (a) Conductive carbon resin used for the molding of the sample, (b) Example of treated sample after SMAT and (c) Piece cut from the dumbbell sample and molded in resin and (d) Pieces cut from the sheet sample.

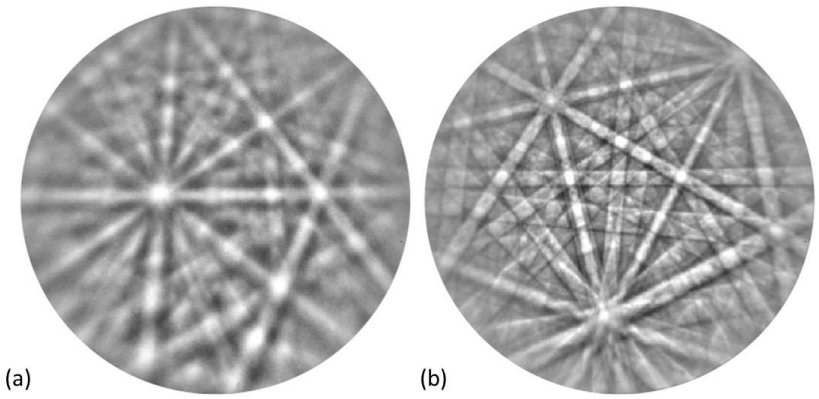

Fig. 3.4 EBSD diffraction patterns of ZrO_2 samples with (a) low ISR and (b) high ISR [204].

After our first failure of EBSD observation due to very bad pattern quality, we have consulted some colleagues who have performed successfully EBSD observations regarding the sample preparation and changed our polishing process accordingly. The detailed polishing process is listed in Table 4. During the polishing procedure, the surface state of the sample is constantly monitored under optical microscope. It should be mentioned here that even with new polishing strategy, a low indexing success rate and poor quality imaging still occurred during our second observation. The problem might be that the specimen was polished one day prior to the EBSD observation and during this period, an oxide layer might form at the sample surface which leads to poor quality imaging. Subsequently, our solution is to slightly polish the sample with OPS solution a few minutes right before the observation. Therefore, a good indexing success rate was achieved in this way. More detailed investigations need to be carried out to study the relation between oxide layers of metallic samples and poor EBSD imaging quality.

Table 4 Polishing procedure for a 316L specimen treated by SMAT.

	Step 1	Step 2	Step 3	Step 4	Step 5	Step 6	Step 7
Abrasive	320 Grit	600 Grit	800 Grit	1200 Grit	6 µm	3 µm	0.05 µm
Type	Silicon Carbide	Silicon Carbide	Silicon Carbide	Silicon Carbide	diamond	diamond	Colloidal Suspension+ 1% H_2O_2
Cooling	Water	Water	Water	Water	Lube	Lube	Water
Speed	200 rpm	200 rpm	200 rpm	200 rpm	150 rpm	150 rpm	150 rpm
Force	10-20 N	10-20 N	10-20 N	10-20 N	0-20 N	0-20 N	0-20 N
Time	10-20 min	10-20 min	10-20 min	10-20 min	10-40 min	10-40 min	Several hours

3.3 Mechanism of grain refinement of 316L stainless steel subjected to SMAT

The mechanisms of grain refinement due to SMAT for the 316L stainless steel have been studied using Transmission Electron Microscopy (TEM) by Roland et al. [37]. Fig. 3.5 (a) [37] shows a micrograph of the top surface layer of a stainless steel subjected to SMAT. It can be observed that nanograins are characteristic of highly random

crystallographic orientations. By investigating several electron micrographs, a mean grain size can be estimated which is about 20 nm for this SMATed material. Another information that can be extracted is that the SMATed sample consists of both austenite (FCC) and martensite phase (BCC). It can be inferred that strain-induced phase transformation took place and certain amount of austenite has been transformed into martensite. Fig. 3.5 (b) [37] is a micrograph of a specific nanograin at higher magnification. The grain boundary is well defined. A high density of stacking faults induced by deformation is observed within the grain.

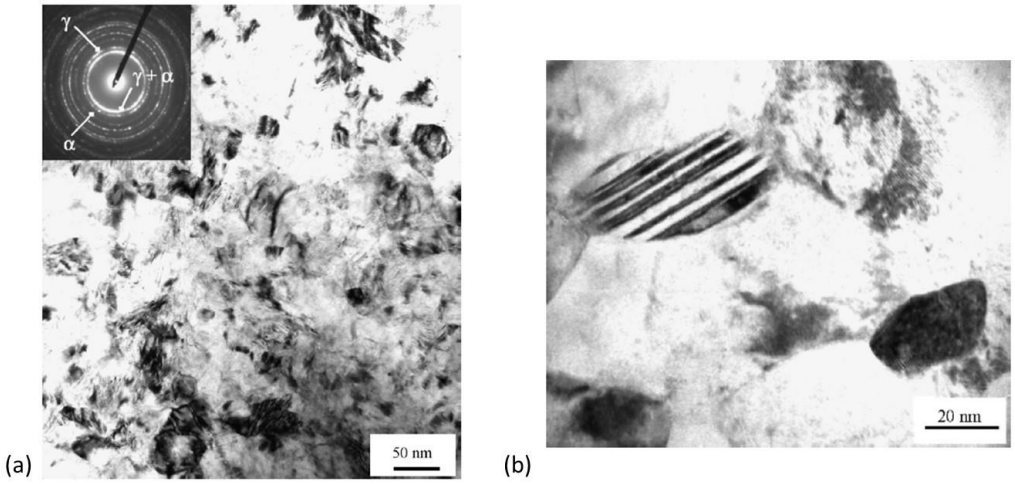

Fig. 3.5 TEM observations of 316L stainless steel treated by SMAT (a) Typical plane view of the top treated surface, (b) bright field image of ultrafine grain with twins [37].

In order to clarify the mechanism of the formation of nanograins in the top surface layer, the microstructures of the top surface layer at different stages of straining need to be investigated. Indeed, SMAT induced straining varies as a function of the depth beneath the treated surface. Thus, a gradient microstructure is formed from the top surface to the non-affected core material. The microstructure observation at various depths beneath the treated surface can, therefore, provide information on grain refinement mechanisms. Fig. 3.6 (a) [37] is a micrograph taken at about a depth of 200 µm beneath the treated surface and the strain level at this depth is relatively low. The micrograph reveals the presences of unidirectional parallel mechanical twins which lead to the formation of a twin-matrix lamellar structure. A high density of dislocation can also be highlighted. Some dislocations are arranged into planar arrays which are particularly characteristic of material with low stacking fault energy [205]. Fig. 3.6 (b) [37] is a micrograph taken at 50 µm beneath the treated surface where the strain level is relatively high. As demonstrated in the micrograph,

twin-twin interactions occur with the increase of strain, which are able to subdivide the original austenitic grains into smaller blocks and, ultimately, lead to the formation of nanocrystallites (range from 50 to 400 nm) involving mechanisms such as boundary sliding and rotation of crystalline domains [62], [65], [206]. Consequently, SMAT generates a grain size gradient and structural defects through the mechanically affected region below the surface of the material.

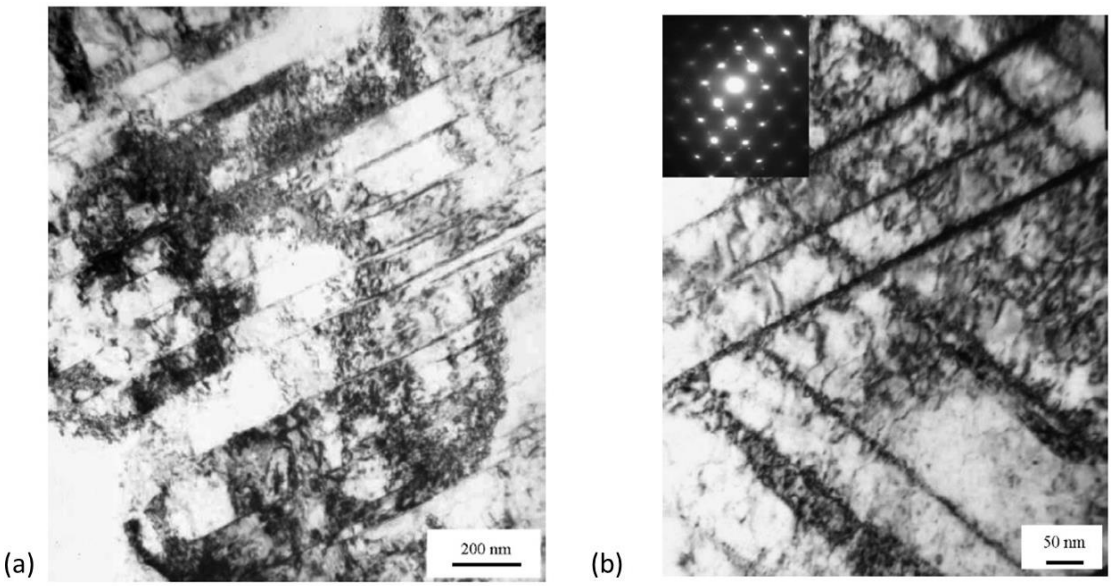

Fig. 3.6 TEM observations of 316L stainless steel treated by SMAT (a) Microstructure of the subsurface layer at a depth of about 200 µm from the treated surface, (b) Twin-twin interactions taken place at 50 µm beneath the treated surface [37].

3.4 XRD analysis of 316L stainless steel treated by SMAT

XRD analysis of 316L stainless steel treated by SMAT has revealed several microstructural characteristics. Fig. 3.7 shows X-ray diffraction profiles of the as-received sample and the as-SMATed sample (the two first profiles) with an inset showing the volume fraction of martensite [37], [193]. It can be observed that the initial sample has a purely austenitic structure while the as-SMATed sample consists of both austenite phase and martensite phase (about 15% of volume fraction) as a result of the strain-induced martensitic transformation [207]–[209]. SMAT is capable of generating strain along the depth beneath the treated sample and the distribution of martensite phase varies as a function of the strain level at different depths. Therefore, the volume fraction of martensite

phase is highest in the top surface layer where the strain level is the most elevated and according to Roland, the martensite phase is present to a depth of about 150 μm [37], [193]. It should be noted here that only about 15% volume of martensite phase has been formed due to the fact that 316L stainless steel has a more stable austenitic structure. The addition of molybdenum is detrimental for martensite formation. An opposite example can be found on the SMATed sample of 304L stainless steel with a less stable austenitic structure, where nearly 100% volume of martensite phase is generated at the top surface [210].

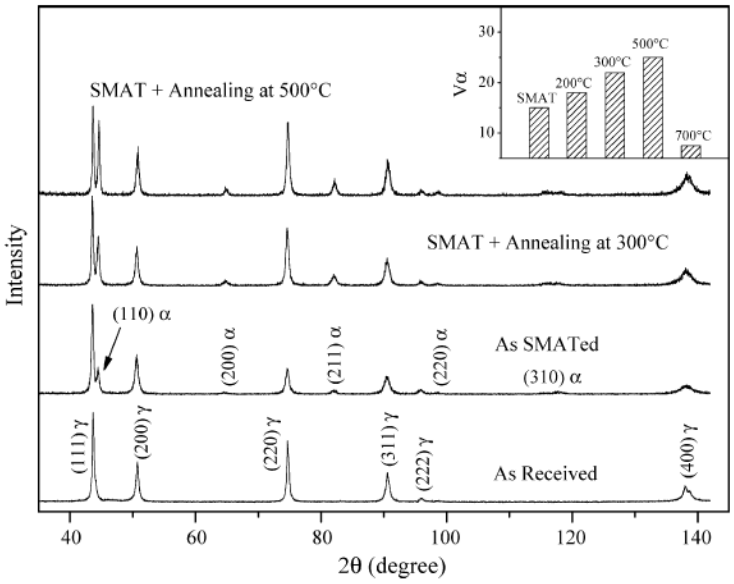

Fig. 3.7 XRD profiles of the as-received stainless steel and of the samples subjected to SMAT. Inset is the volume fraction of martensite (γ, austenite, α, martensite) [37].

Contrary to the results of Roland, the phase transformation of martensite in SMATed 316L stainless steel has been respectively studied by Zhou and Waltz [211], [212] with XRD using a Cr-Kα radiation. The results show that no martensitic transformation occurred during SMAT. They considered that this difference was due to the difference of the chemical composition between the studied materials. However, more detailed investigations need to be carried out to reveal whether strain-induced martensitic transformation occurred during SMAT for 316L stainless steel with a stable austenitic structure.

Efforts have been made to investigate the grain size distribution of SMATed 316L stainless steel along the depth beneath the treated surface. The grain size was calculated from line broadening of Bragg diffraction peaks using the Scherrer and Wilson method [132], as discussed previously in Section 2.3. From the top surface layer, evident

broadening of Bragg diffraction peaks was seen due to a grain refinement and/or an increase of lattice strain at atomic level. According to Roland, the average grain size at the top surface is about 12 nm for the austenitic phase and 8 nm for the martensite phase. These results will later be compared with the EBSD observations in the following Section. Indeed, whether the grain size calculated by the peak broadening is reliable remains debatable because a variety of factors can contribute to the width of a diffraction peak besides grain size, such as instrumental effect, microstrain (non-uniform lattice distortions/ faulting/dislocations etc.), twinning, microstress, grain boundaries/sub-boundaries, coherency strain, chemical heterogeneities and temperature, etc. Some of other imperfections may also result in peak shift, peak asymmetry, anisotropic peak broadening, or affect peak shape [213]. If all the effects of peak broadening due to factors except grain size are eliminated, it is reasonable to assume that the grain size calculated by XRD is overestimated. The Scherrer formula would be applied only when all other contributions (except grain size) to the peak width were zero [213].

3.5 EBSD analysis of 316L stainless steel treated by SMAT

Electron BackScatter Diffraction (EBSD) was used to characterize gradient microstructure generated by SMAT. The microstructure was examined to determine the mean grain sizes, the grain size distributions and the grain misorientation, etc. The experimental data were obtained using a scanning electron microscope FEG-SEM SUPRA 55 VP operating at 20 kV equipped with the OIM™ software system.

One way to represent EBSD results is to show individual orientation measurements as points in the pole figure [214]. The individual point orientation measurements from the whole sample plotted together on the pole figure reveal the texture of the sample. The orientation distribution close to a particular texture component will appear as a cluster of points on the pole figure. Another way to represent the EBSD results is to plot the measured points in the form of inverse pole figure [215], in which the information about grain size and grain size distribution can be clearly extracted.

In a first attempt, a SMATed 316L rectangular sheet sample described in Section 3.2 was prepared for EBSD observations. Fig. 3.8 (b) is an inverse pole figure of a selected zone (250 x 100 µm) with a scanning step of 1 µm while Fig. 3.8 (a) is an inverse pole figure orientation map of a selected zone (12 x 2 µm) in the near surface of the SMATed sample. A small scanning step of 0.05 µm was applied. These inverse pole figures are raw images where the white areas probably correspond to heavily strained regions, giving rise

to blurred or overlapped Kikuchi patterns that could not be indexed [11]. As explained in Section 3.3, the mechanism of the grain refinement of 316L stainless steel lies in the strain induced by SMAT where high density of mechanical twins and dislocation arrays are present in low-strained areas and twin-twin interactions are responsible for subdividing the original coarse grains into randomly oriented nano-grains in high-strained areas [37]. Hence, SMAT produces gradients in grain size and structural defects through the depth below the surface. These structural defects, in turn, lead to bad indexing success rate for EBSD observations.

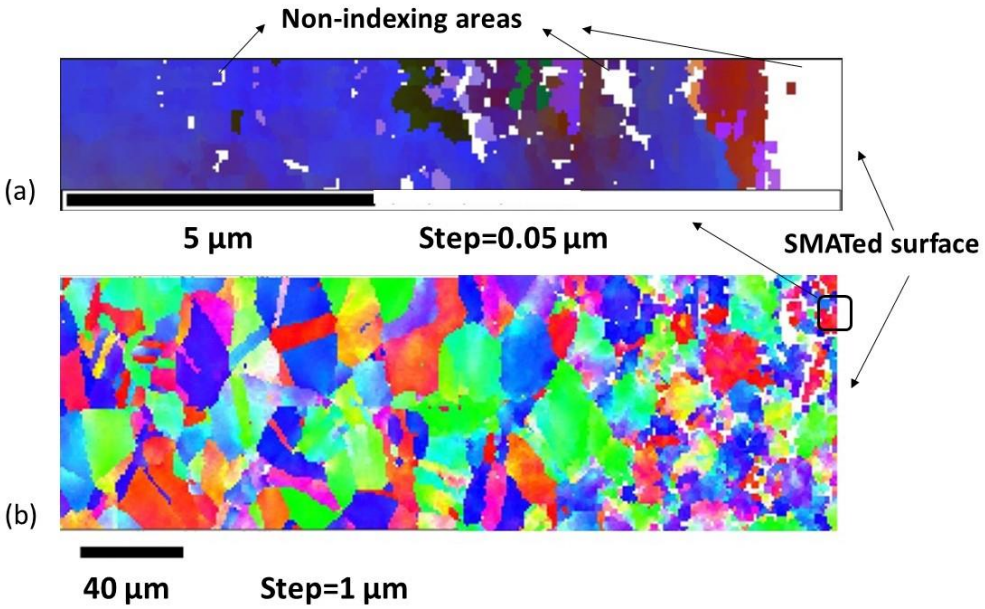

Fig. 3.8 EBSD observations. (a) Inverse pole figure in the near surface of the SMATed sample (12x2µm), (b) Inverse pole figure orientation map of the SMATed sample (250x100µm).

Indeed, the presence of dislocations, grain boundaries, plastic strain/lattice deformation will affect the image quality of EBSD diffraction pattern [204]. As shown in Fig. 3.8 (b), the indexing rate is relatively low in the near surface where the structure is heavily deformed and gradually increases as a function of the depth below the treated surface. As the distance from the surface increases, the indexing rate increases and the EBSD technique starts recording fine domains that clearly originate from grain and subgrain divisions. Most of these domains are highly misoriented [11]. For the core material where the structure is not affected by SMAT, a satisfying indexing rate is achieved.

Fig. 3.8 (a) shows an inverse pole figure orientation map of the nanocrystalline layer, as indicated by the outlined rectangular zone. Large fraction of non-indexing areas can be

noted, especially in the first 1µm area below the treated surface where only one point was indexed. This bad indexing rate resulted from the characteristics of the structure of nanocrystalline materials. As discussed in Section 1.4.5, nanocrystalline materials are structurally characterized by a large volume fraction of grain boundaries, which may significantly alter their physical, mechanical, and chemical properties in comparison with conventional coarse-grained polycrystalline materials [7], [99]. A large fraction of grain boundary areas will generate multiple crystallographic orientations, causing overlapping of EBSD patterns [204], [215], as illustrated in Fig. 3.9. Moreover, grain boundaries in nanocrystalline materials are reported to contain twinning, stacking fault, dislocations and porosity or even small portion of amorphous areas as discussed in Section 1.4.5 [102]–[105]. These structural defects will lead to lattice deformation/distortion of the original periodic crystalline structure, resulting in the degradation of the quality of EBSD pattern and non-indexing areas. It should be emphasized here that the EBSD camera noise and the resolution of the EBSD equipment are also of great importance because they are not sample-related factors that will cause degradation and non-indexing of the EBSD pattern [204]. Thus, a sufficiently small scanning step is recommended for nanocrystalline materials.

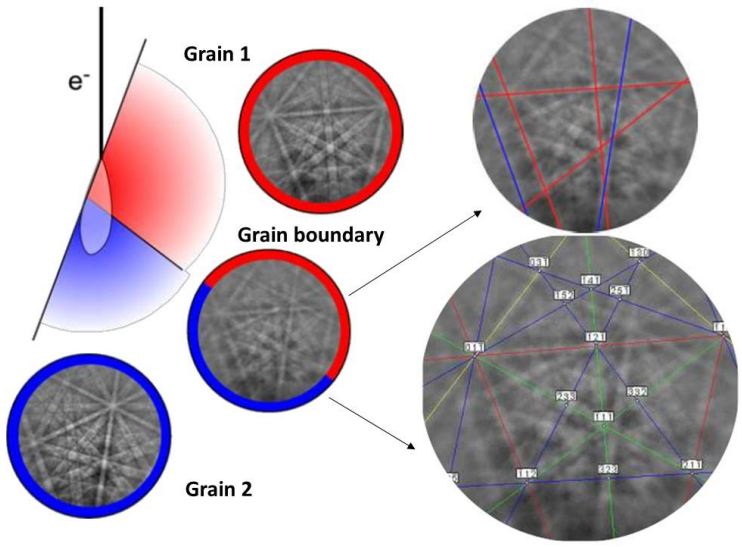

Fig. 3.9 Overlapping of EBSD patterns at grain boundary [204].

In a second attempt, a SMATed 316L dumbbell shape sample described in Section 3.2 was prepared for EBSD observations. Fig. 3.10 (a) shows the inverse pole figures orientation may of the global gradient microstructure generated by SMAT on the transverse cross-section of the dumbbell specimen while Fig. 3.10 (b), (c), (d) and (e) are inverse pole figures of different regions below the treated surface revealing unique characteristics of the

observed areas. In order to obtain high quality diffraction patterns, the used scan step size is 25 nm for the nanocrystalline region and 0.1 µm for the coarse-grained region. In addition, the diffraction patterns were post-corrected using the OIM™ software system to further improve the image quality. From Fig. 3.10 (a), it can be observed that the random impacts of flying shots with high velocity on the treated sample generate a gradient microstructure. This microstructure can be roughly divided into three regions, namely the non-affected region, transition region and the nanocrystalline surface region.

Fig. 3.10 (b) illustrates the non-affected region where the initial microstructure is maintained with an average grain size ranging from 10 to 20 µm. In this region, neither deformed grains nor plastic slip traces can be detected. In addition, a large fraction of twins can be observed in this region. The transition region is located between the non-affected region and the nanocrystalline region. Therefore, the microstructure in this transition region is a mixture of coarse-grained structure and ultrafine-grained structure. Fig. 3.10 (c) reveals the characteristic of the beginning of the transition region located at about 200 µm beneath the treated surface. Although no change in grain size in this area can be detected, several different colors can be observed in a single grain. This indicates that the grains are slightly affected by SMAT but the influence of SMAT is not strong enough to divide the grains. On the other hand, plastic slips can be clearly observed in a grain, as shown in the upper right corner of Fig. 3.10 (c). These plastic slips occurring in different slip systems are caused by multi-directional impacts of the shot during SMAT. Thus, we can conclude that the original grains in this region are subdivided by plastic slips and no new grains are formed. This observation is consistent with the literature [12], [37]. As the depth decreases, a clear tendency of grain refinement can be observed which is due to more severe plastic deformation induced by SMAT. As a result of increased volume fraction of grain boundaries due to grain refinement and structural defects generated by SMAT, a degradation of the EBSD pattern can be noted in the edge area of the transition region near the top surface. Fig. 3.10 (d) shows the end of the transition region located at about 15 µm below the treated surface where new smaller grains are formed due to higher intensity of SMAT. The grain size in this area can be as small as a few micrometers. Finally, the nanocrystalline region is located in the top 10 µm layer below the treated surface. As indicated by the global inverse pole figure, the indexing rate in this region is nearly zero and a smaller scan step size is necessary to obtain higher quality diffraction pattern. Fig. 3.10 (e) is an inverse pole figure orientation map of the nanocrystalline region obtained with a scan step size of 25 nm. The grain size ranges from 50 nm to 300 nm and the nano-

grains are equiaxed. The thickness of the nanocrystalline layer is about 5 µm. The grain size measured with EBSD is larger than that measure by Roland [37] using XRD which most likely implies that measuring grain size by XRD is not accurate if other factors affecting the broadening of the peak are not excluded. However, as mentioned above, the scan step size is of 25 nm, and in this case, the smaller grains even they exist in the nanocrystalline region cannot be observed through this technique.

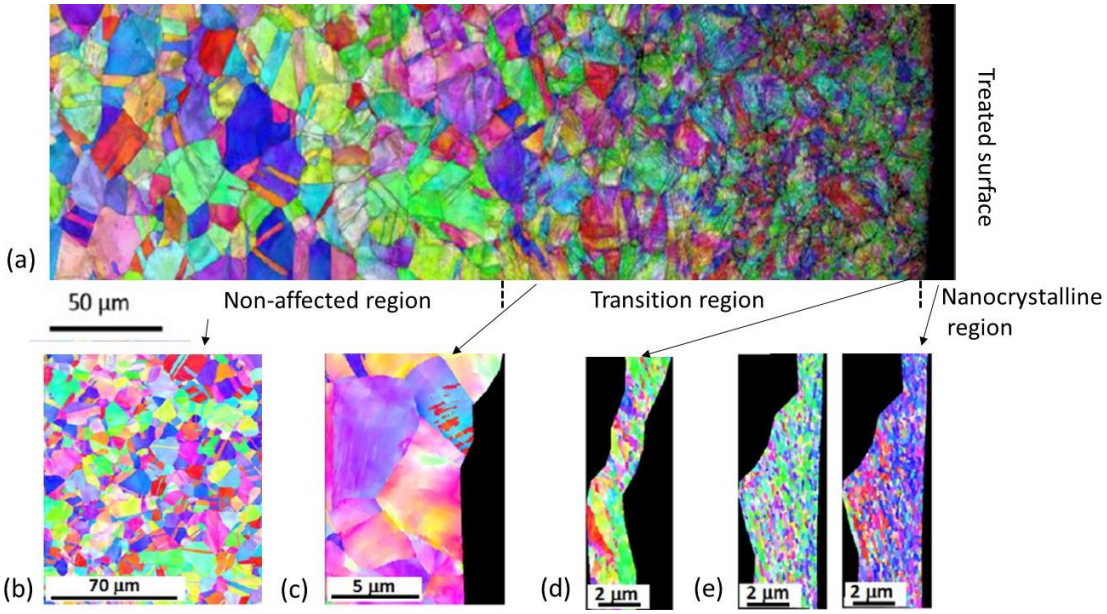

Fig. 3.10 EBSD observations of a 316L stainless steel sample prepared with a dumbbell shape specimen. (a) Inverse pole figure of the gradient microstructure generated by SMAT, (b) Non-affected region, (c) Beginning of the transition region, (d) End of the transition region and (d) nanocrystalline surface region.

The individual point orientation measurements from the whole sample plotted together on the pole figure reveal the texture of the sample as aforementioned. Fig. 3.11 (a) and Fig. 3.11 (b) are pole figures of the non-affected region and nanocrystalline region respectively. It can be observed from Fig. 3.11 (a) that the orientation distribution is rather random and no texture is present in the non-affected region. While in the nanocrystalline region, the ultra-fine grain are oriented with a large fraction of <111> axes parallel to the sample radius (SR) and a major <110> axis parallel to the sample revolution axis (SRA). The formation of this texture is due to the SMAT as no further mechanical load has been applied [12].

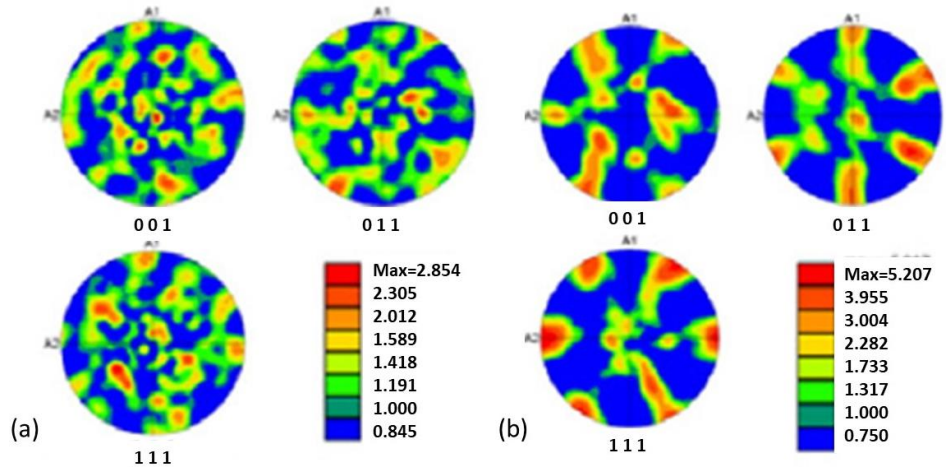

Fig. 3.11 (a) Pole figure of the non-affected region, (b) Pole figure of the nanocrystalline region.

The grain size distribution at different areas with and without twin taken into account are also investigated. The results are plotted in Fig. 3.12 (a) where curves of area fraction versus grain size are quantitatively presented. Almost no twins can be distinguished in the nanocrystalline region as the curves including and excluding twins for this area are nearly the same. This conclusion can be confirmed by the previously shown inverse pole figure of the nanocrystalline region. As a matter of fact, twin-twin interactions are responsible for the division of coarse grains and consequently, those twins disappear due to the grain refinement effect of SMAT. For the transition region, the curves including and excluding twins are slightly different. A small amount of twins are still present as the SMAT treatment intensity is relatively lower in this area compared to the nanocrystalline region. As for the non-affected region, a large fraction of twins can be detected as the curves including and excluding twins are clearly different. This can also be confirmed by the previously shown inverse pole figure of this area.

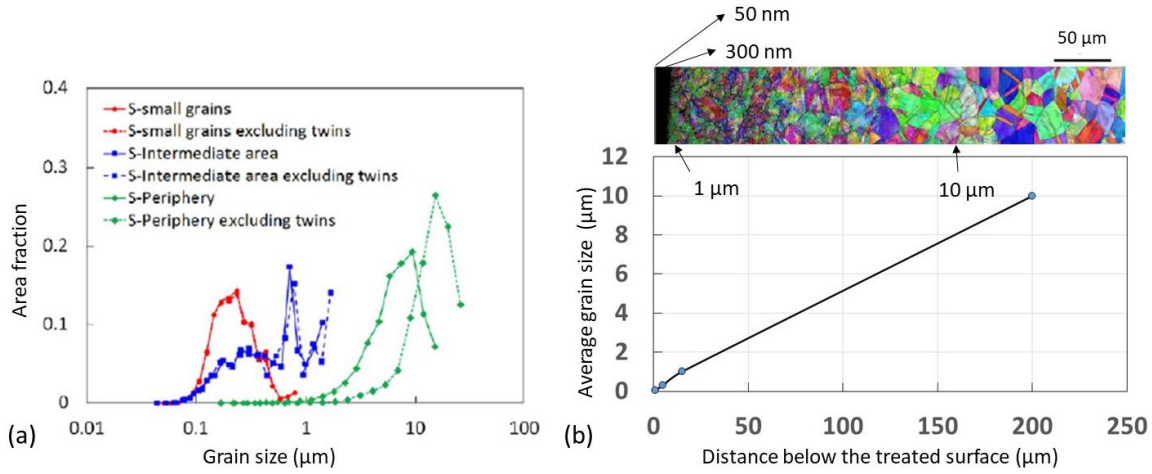

Fig. 3.12 (a) Distribution of grain size evaluated in different areas with and without twins taken into account and (b) Estimated grain size distribution as a function of distance below the treated surface.

Based on the above mentioned results, the average grain size as a function of the distance below the treated surface is estimated and the results are plotted in Fig. 3.12 (b). Four representative points are chosen, as indicated by black arrows: average grain sizes of 10 µm, 1 µm, 300 nm, 50 nm with the corresponding distances below the treated surface 200 µm, 15 µm, 5 µm and 1 µm, respectively. This profile of average grain size as function of distance below the treated surface will be exploited for the interpretation of the nanoindentation results as grain size is a crucial factor that affects the measurements of nanoindentation. This will be addressed in Chapter 4.

EBSD technique is capable of measuring the Grain Orientation Spread (GOS) which characterizes the intragranular misorientation. Fig. 3.13 (a) shows the average Grain Orientation Spread through the SMATed sample radius. The GOS value is about 1.3° for the non-affected region which is characteristic of a recrystallized material. As this area is not affected by SMAT, the initial microstructure is maintained. As a result of the strain induced by SMAT, the values of GOS increase for the transition region (about 5.8° and 5.3° at the beginning and the end of the transition region, respectively) where plastic slips can be observed and grain refinement occurs. As for the nanocrystalline region, the GOS value is about 1.8° which indicates that the ultrafine grains are less misoriented because they are actually well formed by severe plastic deformation due to SMAT [12].

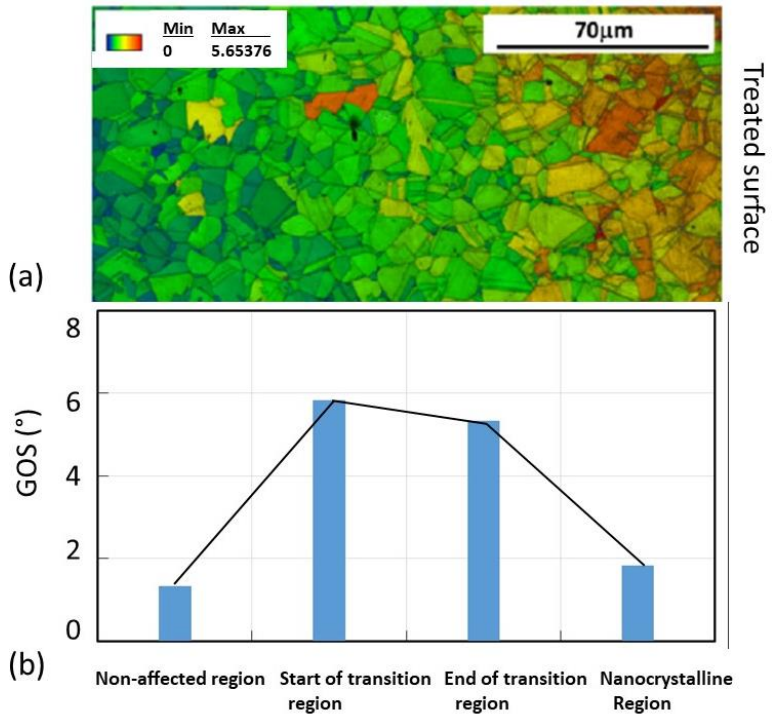

Fig. 3.13 (a) GOS map of the SMATed sample and (b) GOS distribution calculated in different areas: Non-affected region, beginning of the transition region, end of the transition region and nanocrystalline region.

3.6 Thermal stability of the microstructure generated by SMAT

In-situ Electron BackScatter Diffraction (EBSD) was used to study the thermal stability of a 316L stainless steel nanocrystallized by SMAT. In this work, the chemical composition and SMAT conditions are listed in Table 5 and Table 6.

Table 5 – Chemical composition (wt.%) of the studied 316L stainless steel.

Fe	C	Mn	Si	P	S	Cr	Ni	Mo	Cu	N	Ti	V
48.4	0.013	1.7	0.26	0.17	0.003	17.37	14.52	2.80	0.08	0.088	<0.005	0.07

Table 6 SMAT conditions of the 316L stainless steel.

Sample	316L austenitic stainless steel	
Mass of shots	20g	
Amplitude/Duration	±12.5 µm (15 min)	±25µm (5 min)
Shot	Material: 100 Cr 6, diameter: 3mm	
Distance	20 mm (max)	

For the SMAT process, spherical steel shots of 3 mm diameter were boosted by vibration of ultrasonic generator at a high frequency (20 kHz). The specimen was subjected to a treatment of 15 minutes with an amplitude of ±12.5 µm (15 min), followed by a treatment of 5 minutes with an amplitude of ±25 µm.

In-situ EBSD technique was used to characterize the eventual evolution of grain state with the temperature increased up to 720 °C. The observation was performed using a scanning electron microscope FEG-SEM SUPRA 55 VP equipped with a platinum based heating system. For the specimen preparation, the specimen was successively SMAT processed, cut along cross-section, molded, mechanically ground, polished to a mirror-like finish and then polished with an OPS solution.

During the in-situ EBSD observation, the temperature was controlled in order to follow a programmed increase path. The recorded temperature increase path is shown in Fig. 3.14. Globally, the temperature was increased with a rate of about 40°C per minute. For several temperature levels, the temperature was kept almost constant so as to perform EBSD measurements at different temperatures up to 720 °C.

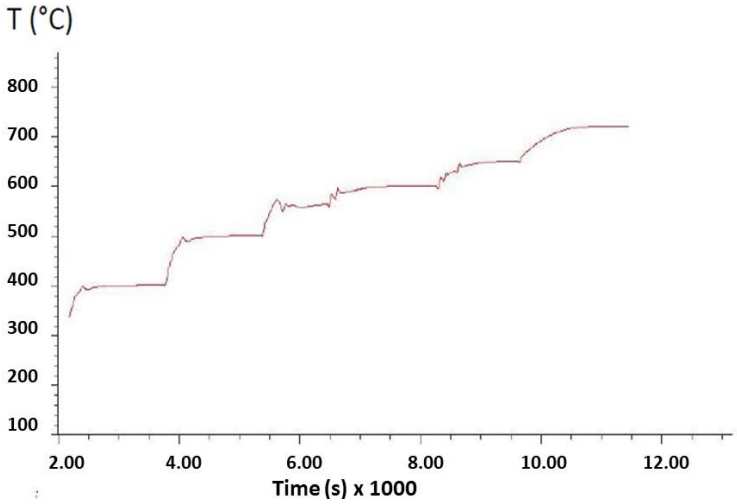

Fig. 3.14 Recorded temperature increase path for the in-situ EBSD investigation.

EBSD observations on cross-Sectional surface reveal a microstructure gradient in the SMAT affected region, as shown in Fig. 3.15 (a). It can be seen that the severe plastic deformation induced by the impingement of flying shots produced a refinement of coarse grains down to nanometer scale in the top surface region (Fig. 3.15 (b)). The thickness of the nanostructured layer is about 5 µm, followed by a mixed grain size region, where both ultra-fine grains and relatively large grains are present. In this region, the impact intensity was actually lower than in the top surface region so that only a part of original grains could be transformed to new ultra-fine grains while the size of other grains was not changed by the treatment. Underneath this mixture region is the work hardened region where the initial grain boundaries have not been much modified by SMAT and they still can be clearly distinguished. However, the color (which gives information about grain orientation) in each grain is no longer uniform due to the effect of SMAT. As a matter of fact, the grains in this work hardened region were subdivided by plastic slips. These plastic slips occurring in different slip systems are caused by the multi-directional impacts of the shots during SMAT, as indicated in [9].

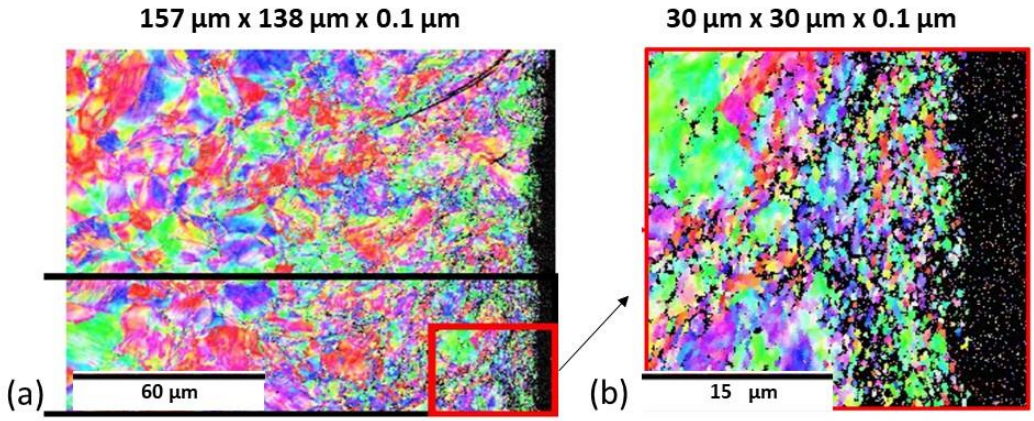

Fig. 3.15 (a) Initial state of material processed by SMAT showing a microstructure gradient from the top surface to the specimen center, (b) a zoom view showing the presence of nanostructured region on the top surface.

Fig. 3.16 illustrates the obtained cartographies as function of temperature increase from 400 °C to 720 °C. It can be seen that with the increase of temperature, some areas progressively became dark, which means that these areas were no longer well indexed due to the degradation of indexation quality which occurred during the observation. It can be seen that this phenomenon is more significant in the areas with small grains, especially in the nanostructured layer immediately beneath the treated surface. At 720 °C, the indexation was totally lost. According to the analysis based on Fig. 3.17, this loss of EBSD indexation quality is due to the oxidation effect which seems more easily occur on small grains as larger fraction volume of grain boundaries might provide access for oxidation. Fig. 3.17 presents SEM observation of characteristic areas of different oxidation levels. It can be seen that in the area far from the treated surface, the material was subjected to thermal etching and the oxidation level is low according to the analysis using EDS (Energy Dispersive X-ray Spectrometry), and therefore the indexation quality remains good (Fig. 3.17 (b)). However, in the transition area where the material was strongly plastically deformed due to SMAT, there is the presence of oxidation on the surface of the observed cross-Section, and the indexation quality is degraded by the oxidation, as revealed by Fig. 3.17 (c). In the nanostructured layer where the grains are small, the oxidation effect is so significant that the indexation quality becomes too poor to correctly observe the microstructure (Fig. 3.17 (d)). In the last two regions which are close to the treated surface, the oxidation level is much higher than in the center of the specimen, as indicated by the EDS analysis (Fig. 3.17 (d)). The phenomenon of oxidation is linked to the relatively poor oxidation resistance of fine grained materials. As a matter of fact, in the region where the grain size is small, the fraction of grains boundaries is higher. It is well known that at grain boundaries, the atomic

arrangement is less regular than in the interior of grain. Thus grain boundaries can provide short circuit diffusion path for oxygen to more easily penetrate in the material. In the case of an austenitic stainless steel, another mechanism can be involved in the oxidation process. When austenitic stainless steels are heated to the temperature range of 425 to 815 ° C, chromium carbides can be precipitated at the grain boundaries. These carbides have a high chromium content compared to the matrix. As a result, the narrow areas immediately adjacent to the grain boundaries are highly depleted in chromium and oxidation may easily occur in these areas [196], [197], [201], [202], [216], [217].

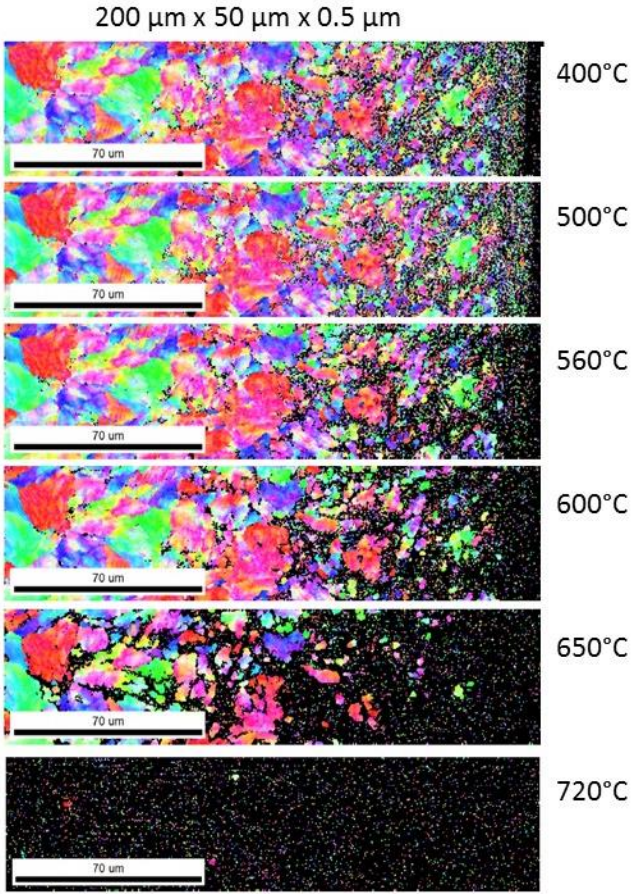

Fig. 3.16 EBSD cartographies showing microstructure state as function of temperature increase from 400 °C to 720 °C. Appearance of dark areas indicates that the indexation quality is significantly degraded especially when the temperature is beyond 600°C.

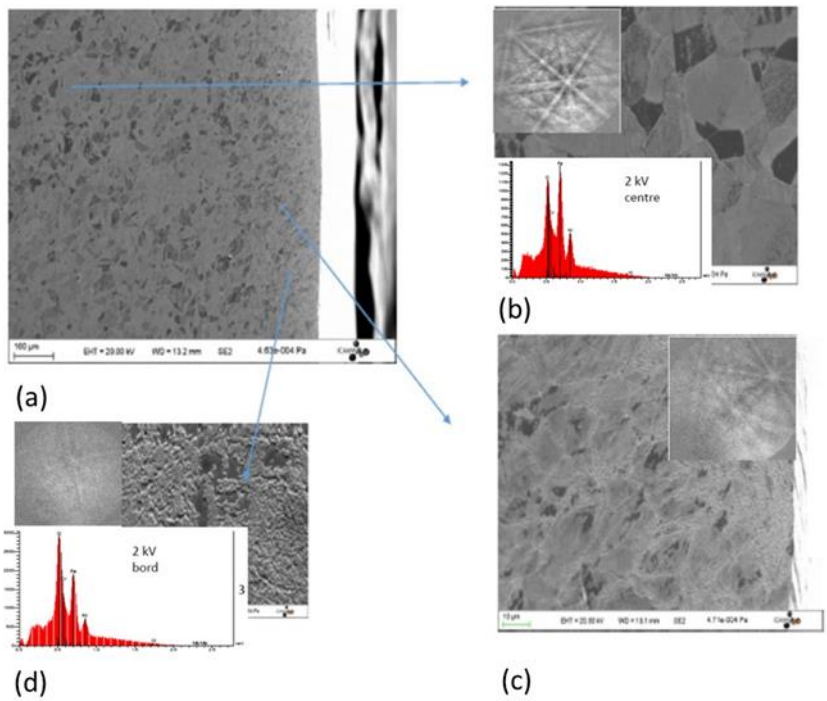

Fig. 3.17 Highlighting of surface characteristic showing oxidation coverage level particularly high in the area close to the top surface. Kukuchi diffraction patterns corresponding to each area are also shown.

In order to investigate whether the microstructure was changed following the exposure to temperature at 720 °C, an ionic polishing was carried out. This technique allows to remove a superficial oxidized layer on the surface of the EBSD specimen. After the ionic polishing, the indexation quality became much better according to the Kikuchi diffraction pattern shown in Fig. 3.18, and most of the area could be correctly indexed. The microstructure shown in Fig. 3.18 looks very similar to the initial microstructure obtained after SMAT, which means that the grain morphology is not obviously changed due to the exposure to temperature. First qualitative analysis of GOS (Grain Orientation Spread) seems indicate that there is a slight growth of grain size when the temperature is beyond 600 °C. This investigation is consistent with the results presented in the literature concerning the thermal stability of nanostructured layer generated by SMAT. For example, in the work performed for 316L steels, grain size seems begin to change at about 600 °C [37] or beyond 0.5 T_m (T_m is the melting temperature) [218]. However, in future work, a methodology of in-situ EBSD analysis should be developed in order to quantitatively characterize the microstructure change due to temperature exposure.

The investigation presented above illustrated that in-situ EBSD technique is a feasible and promising tool to study the thermal stability of materials nanocrystallized by SMAT. Compared to ex-situ observation techniques, the in-situ EBSD allows to observe the real

time evolution of the microstructure, which can provide valuable information concerning grain evolution mechanisms. However, as shown in this paper, a major technical difficulty lies in the oxidation phenomenon which is significantly accelerated when the temperature is high.

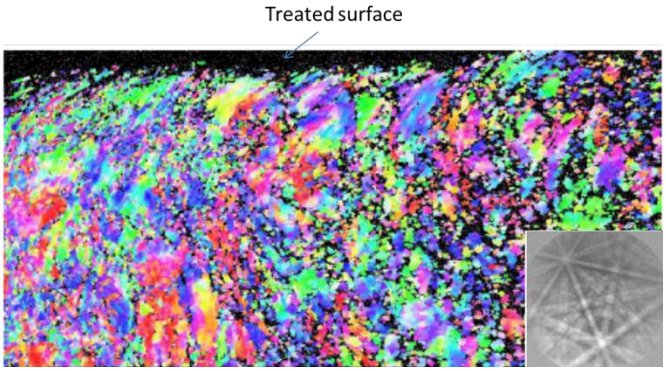

Fig. 3.18 EBSD observation performed after the ionic polishing to remove the oxidized surface. Compared to the initial microstructure state obtained after SMAT, it seems that the microstructure characteristic is not much changed by the temperature exposure at 720 °C.

3.7 Conclusion

In this chapter, a brief introduction about iron and its alloys was first given and 316L austenitic stainless steel was chosen as the target material for SMAT treatment and subsequent studies. The SMAT conditions for the 316L stainless steel and sample preparation procedure for EBSM/Nanoindentation/SEM were listed as well. Special attention needs to be paid to the sample preparation for EBSD observation as delicate smooth state of the sample surface is required to ensure a good pattern quality. Otherwise, bad condition of the sample surface will lead to degradation of the imaging quality and non-indexing areas.

The mechanisms of grain refinement due to SMAT for the 316L stainless steel have been studied using TEM by Roland. It was shown that at low strain level, the microstructure is characterized by high density of mechanical twins and dislocation arrays. With the increase of strain during SMAT, twin-twin interactions occur, which are able to subdivide the original austenitic grains into smaller blocks and, ultimately, lead to the formation of nanocrystallites involving mechanisms such as boundary sliding and rotation of crystalline domains.

XRD analysis conducted by Roland showed that about 15% volume of martensite has been formed due to strain-induced transformation while opposite results have been found by Zhou and Waltz where no transformation of martensite was observed. This difference is

considered to be due to the difference in chemical composition. In addition, the grain size measured by XRD might not be accurate because other factors affecting the broadening of the peak were not excluded.

In a first attempt of EBSD observation, the indexing rate was relatively low, especially for the nanocrystalline regions. The reason for this phenomenon is that SMAT induced plastic deformation on the treated sample results in high density of mechanical twins and dislocation arrays are present. These structural defects affect the EBSD image quality. The indexing rate is lowest in the nanocrystalline layer as a large fraction volume of grain boundaries degrades the diffraction pattern. Moreover, grain boundaries in nanocrystalline materials are reported to contain twinning, stacking fault, dislocations and porosity or even small portion of amorphous areas as discussed in Section 1.4.5. These structural defects will lead to lattice deformation/distortion of the original periodic crystalline structure, resulting in the degradation of the quality of EBSD pattern and non-indexing areas.

In a second attempt, good quality of EBSD images was obtained, and they showed the gradient structure generated by SMAT. The grain size for the nanocrystalline region ranges from 50 nm to 300 nm. GOS (Grain Orientation Spread) was measured along the gradient microstructure and GOS is highest in the transition region (about 5.8°) and relatively low for the non-affected region and nanocrystalline region (about 1.3° and 1.8°, respectively). Based on the results of inverse pole figure and grain distribution measured, a profile of average grain size along the cross-section of the treated sample was estimated.

In-situ EBSD was used to study the thermal stability of a SMATed 316L stainless steel. The result showed that the microstructure generated by SMAT was stable up to 600°C which is consistent with the literature. In addition, the nanocrystalline region is more prone to oxidation due to large fraction volume of grain boundaries which provide short circuit diffusion path for oxygen to more easily penetrate in the material.

Chapter 4: Nanoindentation

This chapter begins with a brief introduction about three major changes induced by SMAT that will affect the nanoindentation measurements. The obtained results (load-displacement curves, Young's modulus, hardness indentation size effect and pile-up behavior) are interpreted subsequently in terms of these SMAT induced changes along the cross-section of the SMATed sample. Besides monotonic loading tests, the results of cyclic loading tests are presented and discussed as well.

4.1 Factors affecting nanoindentation in the case of SMATed material

As discussed in Section 2.6.4 about conventional nanoindentation test, the projected area between the indenter and the sample at maximum load, the contact depth and stiffness at unloading are usually employed to calculate hardness and Young's modulus. In practice, various factors could interfere during the acquisition of these parameters, leading to changes of the measured results. In this Section, we will mainly focus on the factors affecting nanoindentation measurements in the case of SMATed material which arise from changes of the local microstructure and mechanical properties. As aforementioned, SMAT is capable of introduce severe plastic deformation along the cross-section of the sample. Thus, a gradient microstructure is formed which can be roughly divided into three regions, namely nanocrystalline region, transition region and non-affected region. In the non-affected region, the initial microstructure (grain size, grain orientation etc.) of the material is maintained. Nevertheless, nano-grains are formed in the top surface of the sample, called nanocrystalline region, due to the grain refinement effect of SMAT. The transition region is located between the nanocrystalline region and the non-affected region with grain size

ranging from a few micrometers to tens of micrometers as a function of the depth below the treated surface. Besides grain refinement effect, compressive residual stress and strain hardening are also present as a result of SMAT treatment. In the following Section, the grain refinement effect, residual stress and strain hardening induced by SMAT will be briefly discussed.

4.1.1 Grain refinement effect

Grain refinement can be realised by many mechanical treatment technologies via severe plastic deformation, such as SMAT [8], shot peening [219], deep rolling [220], grinding [221]. Indeed, synthesis of nanocrystalline material by severe plastic deformation has gained a great interest in recent years. To create nanostructures in bulk metallic materials, several requirements need to be met: (1) prevailing high angle grain boundaries, thus a qualitative change in material properties can occure; (2) the processed material should have stable properties; (3) no mechanical damage and cracks should be generated during large plastic deformation [7]. Compared to some bottom-up synthesis methods like inert gas condensation, producing nanostructure by severe plastic deformation has several appealing advantages, for instance, synthesis of nanostructure in a short period of time with a relatively low cost and a nanostructure with little porosity.

Mechanical properties are often determined by the corresponding microstructure of the material. Thus, materials with a nanocrystalline structure usually exhibit superior physical and chemical properties compared to their coarse-grained counterpart. For instance, higher yield strength [2], [222], friction and wear [39] and low strain hardening [3], [7]. In the case of nanoindentation, grain refinement has significant effects on the measurements of hardness (Hall-Petch law) [70], indentation size effect [144], cyclic loading behavior [21], [181], [184], [223]–[225] and so on, which will be discussed in details in the following Section. In Chapter 3, the microstructure of SMATed 316L stainless steel has been investigated by various techniques (SEM, TEM, XRD and EBSD), and the grain size distribution along the cross-section of the treated sample has been obtained (Fig. 3.12). Accordingly, grain refinement seems to occur up to a depth of 100µm, farther than which the SMAT intensity is not strong enough to divide the coarse grains and only plastic slips were generated. Four representative points are chosen: average grain sizes of 10µm, 1µm, 300nm, 50nm with the corresponding distances below the treated surface 200µm, 15µm,

5μm and 1μm, respectively. These results will be subsequently applied for the interpretation of nanoindentation results.

4.1.2 Residual stress

Besides grain refinement effect, SMAT is capable of introducing residual stress along the cross-section of the treated sample, as illustrated in Fig. 4.1. The presence of residual stress is beneficial for the yield strength and fatigue properties due to the fact that compressive residual stress can increase the surface resistance to crack initiation and reduce the crack propagation rate through modifying the stress field [226]–[228].

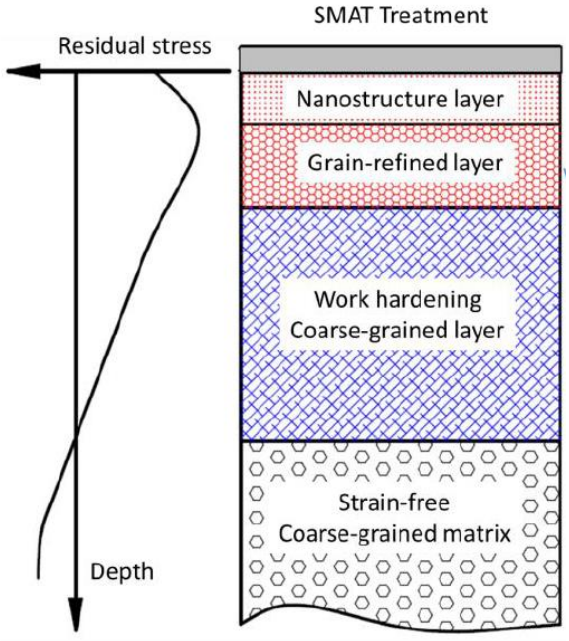

Fig. 4.1 Illustration of residual stress along the cross-section of the treated sample [212].

From length scale perspective, residual stress are often classified as Type I, II and III based on the length over which the stresses equilibrate [226], [227]. Type I stresses self-equilibrate over macroscopic dimension of the component. It ignores the polycrystalline or multiphase nature of the material. Type II residual stresses self-equilibrate over the dimension of several grains as a result of strain incompatibility between grains, which is created by the orientation dependent elastic and plastic anisotropy. Type III stresses exist over atomic dimensions and balance within a grain. Generally speaking, the Type I residual stresses, also named as macroscopic residual stresses, are widely used to increase the mechanical properties of materials in engineering fields. The Type II and III residual

stresses, as inter- and intra- granular residual stresses, are mainly studied to analyze materials from a physical viewpoint, such as slip bands and defects at the grain level [229].

In Section 2.6.4.5, the influence of residual stress on nanoindentation measurements has been briefly discussed. In summary, residual stress has been reported to have effects on the measurements of hardness and Young's modulus [174], load-displacement curves [149], [175], [176], pile-up [150], [151], [175], [230] and true contact area [175], [178]. Thus, the state (tensile or compressive) of residual stress can be determined by comparing the load-depth curve, pile-up height (seen in Fig. 4.2) [178], and true contact area of stressed material with those of stress-free reference material. Numerous studies have shown that the true contact area has an almost linear relationship with the residual stress and increases with increasing compressive stress, while it decreases with increasing tensile stress [151], [175], [176], [231]. The determination of true contact area for pile-up material has been a hot and difficult research topic in recent years. Atomic force microscope is usually used to determine the true contact area. It is argued that once the true contact area is accounted, the hardness and Young's modulus are significantly independent of stress [149], [175].

Among the three parameters, it is easiest to obtain load-depth curve from nanoindentation data. However, only residual stress state can be qualitatively determined by simple comparison of load-depth curves for stressed and stress-free materials. To determine quantitatively the magnitude of residual stress in the materials, specific relationship between residual stress and nanoindentation parameters should be extracted from analysing load-depth curves. At present, there is no one set method that can be applied to the calculation of residual stress for all materials. Indeed, several models usually used to quantitatively determine residual stress from analysing load-depth curves are proposed including Suresh model, Lee models, Xu model, and Swadener models [149].

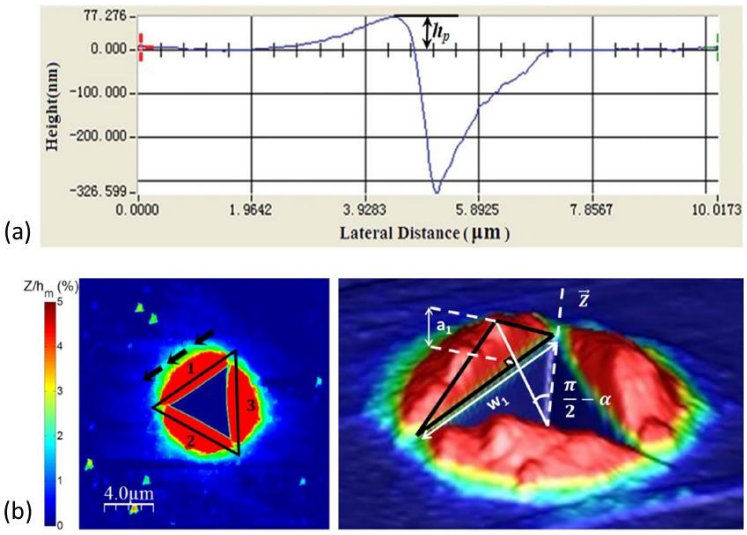

Fig. 4.2 (a) Pile-up height h_p [149], (b) Example of actual contact area in the case of pile-up [178].

In this project, a SMATed dumbbell shape specimen (discussed in Section 3.2) was used for the measurement of residual stress using XRD. In-depth variation of residual stress were evaluated using classical $\sin^2\psi$ method [232]. In the case of a cylindrical sample, a set of axial and circumferential stresses (σ_z^m, σ_θ^m) can be obtained by removing the outer surface layer step by step (Fig. 4.3) in which case electrolytic polishing was used. It should be emphasized here that when a periphery volume of material is removed by electrolytic polishing, the cylindrical sample will have a new self-equilibrium state, leading to a change of residual stress field. Therefore, the measured stresses using XRD are the ones after re-equilibrium, which are different from the true residual stress present in the as-treated sample. Based on the self-equilibrium and stress coupling relationship in a cylindrical coordinate system, the residual stress present in the treated sample (σ_r^{rs}, σ_θ^{rs}, σ_z^{rs}) can be corrected from the measured stresses (σ_z^m, σ_θ^m) using the following equations [232].

$$\sigma_r^{rs}(r^m) = -\int_{r^m}^{R} \sigma_\theta^m \frac{d_r}{r} \tag{4-1}$$

$$\sigma_\theta^{rs}(r^m) = \sigma_\theta^m(r^m) + \sigma_r^{rs}(r^m) \tag{4-2}$$

$$\sigma_z^{rs}(r^m) = \sigma_z^m(r^m) - 2\int_{r^m}^{R} \sigma_z^m \frac{d_r}{r} \tag{4-3}$$

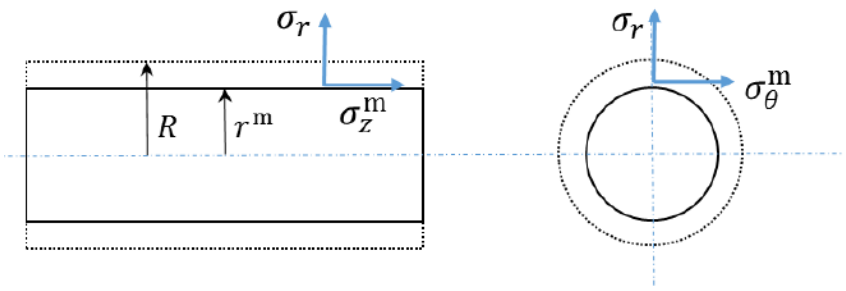

Fig. 4.3 Description of XRD measurements with an iterative material removal method on a cylindrical sample [212].

The three corrected true residual stresses (radial, circumferential, axial) are presented in Fig. 4.4. It is observed that the presence of compressive residual stress can reach up to a depth of about 550 µm. Moreover, the axial residual stress is higher than the circumferential residual stress in the near surface region and as the depth increases, the axial residual stress changes from compressive stress to tensile stress at a depth of about 570 µm beneath the treated surface as a result of the self-equilibrium characteristic of residual stress. This profile of residual stress as function of the depth beneath the treated surface will be used for the following interpretation of nanoindentation measurements.

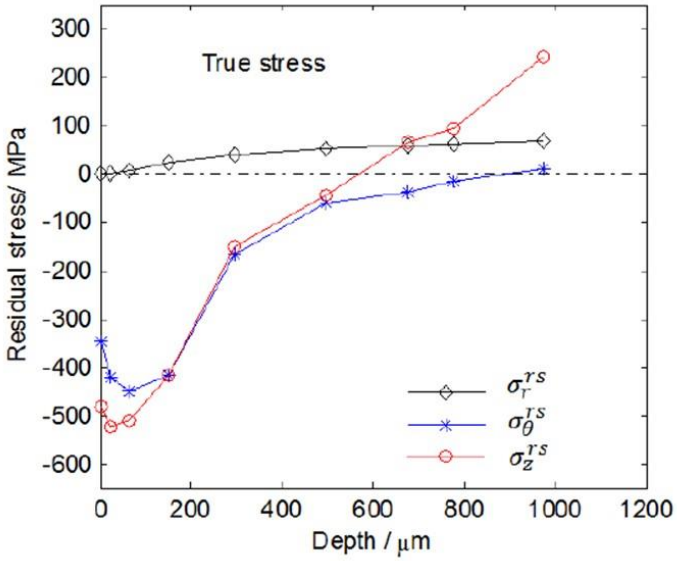

Fig. 4.4 In-depth variation of the true residual stress [212].

4.1.3 Work hardening

In addition to grain refinement effect and the generation of compressive residual stress along the cross-section of the SMATed sample, stain hardening is introduced at the same

time. Work hardening, also named strain hardening, is a macroscopic description of most metals which become strengthened as the plastic deformation proceeds. Plastic deformation can be described through dislocation generation and movement within the crystalline structure. Therefore, the hardening of material occurred as dislocations encounter and interact with each other or crystalline defects [233]. Strain hardening behavior is often characterized by strain hardening exponent, n, where $\sigma=K\varepsilon^n$ (σ represents the applied stress on the material, ε is the strain and K is the strength coefficient) [234].

The work hardening process can be divided into four stages according to the dislocation storage and recovery mechanism [235]. In the early stage of plastic deformation, namely Stage I, only easy glide takes place during single slip in single crystal. The corresponding work hardening rate is low due to storage of dislocation dipoles and multipoles on the primary slip system. As for Stage II, the strain level becomes higher and the work hardening rate is higher as a result of storage of dislocation tangles on multiple slip systems. The Stage III corresponds to a monotonic decrease of the work hardening rate with an increase of the flow stress and a saturated stress is reached by the end of this stage where recovery balances dislocation storage. As the plastic deformation continue to proceed, Stage IV intervenes with a further decrease of hardening rate without marked changes in the character of obstacles to dislocation movement.

Work hardening can be induced either intentionally or unintentionally. An example of unintentional work hardening arises from machining where the surface of component is inadvertently hardened. This type of work hardening will be discussed with a non-SMATed 316L sample in the following Section. Another type of work hardening occurs in metalworking processes where plastic deformation is induced intentionally to strengthen the mechanical parts at the expense of ductility. Either way, work hardening present in a mechanical part may have a significant effect on its subsequent mechanical properties. Fig. 4.5 gives two examples of work hardening behaviors. Cold working of the metal increases the tensile yield strength, as illustrated in Fig. 4.5 (a). On the other hand, while more tensile cold working increases the tensile yield strength, the local initial compressive yield strength after tensile cold working is actually reduced, which is termed Bauschinger effect, as shown in Fig. 4.5 (b). The Bauschinger effect [236] is normally associated with conditions where the yield strength of a metal decreases when the direction of strain is changed. It is a general phenomenon found in most polycrystalline metals. The above examples imply that the mechanical properties of a component can be path dependent with regard to the loading history. In summary, strain hardening results from interaction and multiplication of

dislocations during plastic deformation. With increasing dislocation density the mean free path decreases, which results in the requirement of larger stress for dislocation movement.

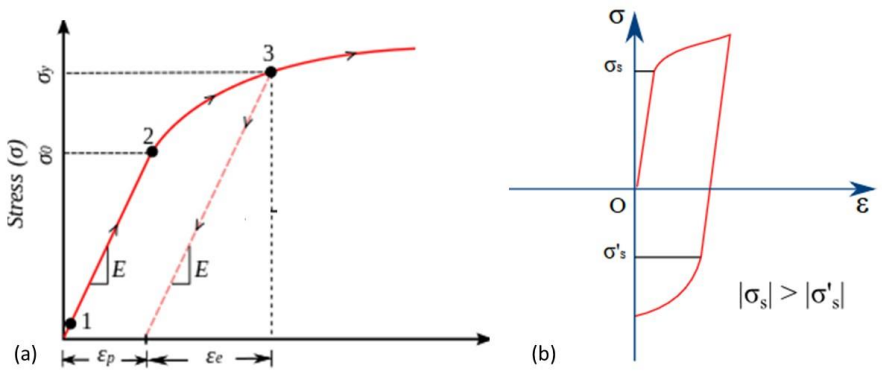

Fig. 4.5 (a) Example of typical work hardening plastic behavior of materials in uniaxial compression [237], (b) Bauschinger effect [238].

SMAT has been proven to be an effective technique for the enhancement of various mechanical properties. But most of the studies focused on the grain refinement effect and residual stress induced by SMAT and little attention was paid to the work hardening that was introduced simultaneously. Indeed, it is rather difficult to characterize and evaluate work hardening, for which reason its influence tend to be neglected. Nevertheless, the above discussion has shown that work hardening can also affect the local microstructure [239],[240], such as dislocation density, grain misorientation, plastic slips [241] and twins [228], [242], [243] and mechanical properties (increase/decrease of yield strength) [37], [193], [212]. In fact, decrease of crystalline size and increase of microstrain during work hardening can induce a large diffraction peak broadening, as discussed previously [244]. Some authors have qualitatively correlated the work hardening to plastic strain using the value of diffraction peak broadening through, for example the equivalent true plastic strain [244]–[246]. In this project, Full Width at Half-Maximum (FWHM) of XRD patterns was used to correlate qualitatively work hardening to the induced plastic deformation of a SMATed sample cut from dumbbell shape specimen (discussed in Section 3.2.2). A non-SMATed reference sample was also measured. The results are plotted in Fig. 4.6 (a) [212].

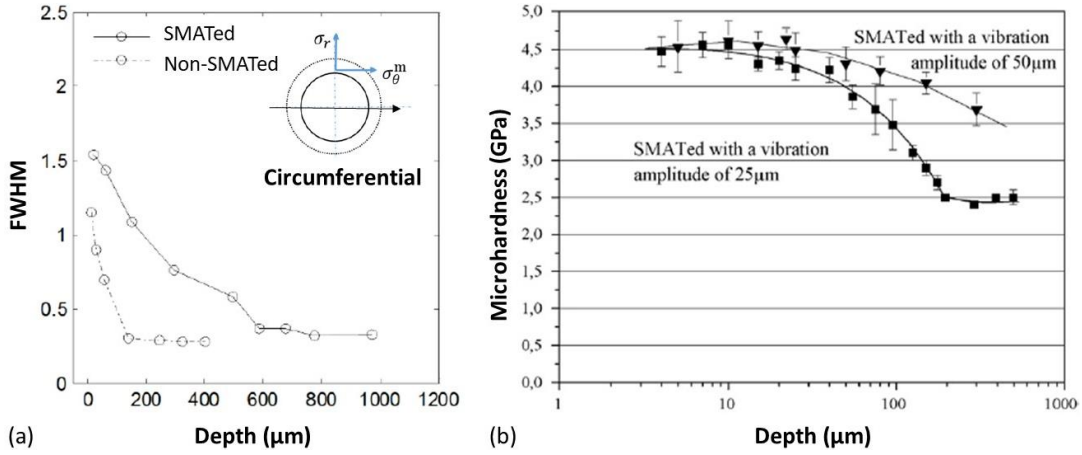

Fig. 4.6 (a) In-depth variation of FWHM value measured on SMATed and non-SMATed samples [212], (b) Microhardness measured from 316L stainless steel for two different SMAT conditions [37].

A sharp decrease of FWHM value can be observed from the top surface to farther regions below the treated surface in circumferential direction. This tendency is very similar to the microhardness results measured by Roland, as illustrated in Fig. 4.6 (b) [37]. The FWHM curve indicates that the plastically affected region of a SMATed sample can reach to a depth of about 600µm. Interestingly, the measurements of residual stress discussed in Section 4.1.2 has led to similar conclusion where compressive residual stress is present at a depth up to about 600µm. It should be noted that even for non-SMATed sample, FWHM value is also higher in the near surface which implies the presence of plastic deformation/work hardening. This is attributed to work hardening arising from machining where the surface of component is inadvertently hardened as aforementioned. The work hardened layer is about 170µm according to the measured FWHM value.

In summary, grain refinement effect, compressive residual stress and strain hardening occur simultaneously as a result of SMAT treatment during severe plastic deformation. These three factors co-exist along the cross-section of the treated sample and will affect significantly the measurement of nanoindentation. Indeed, it will be rather challenging to investigate individually the influence of a single factor. Based on the results obtained previously on grain refinement effect, compressive residual stress and strain hardening of SMATed samples, the influence of SMAT on nanoindentation measurements will be discussed in details in the following Sections.

4.2 Analysis of the load-displacement curves

In this project, the gradient microstructure generated by SMAT is of our concern, especially the nanocrystalline layer in the top surface of the treated sample. The variation of hardness/Young's modulus with depth beneath the treated surface was measured on a cross-Sectional sample (dumbbell shape specimen in Section 3.2.2) using a Nano Indenter XPTM fitted with a Berkovich indenter. The maximum displacement into the sample was 500 nm with a strain rate of 0.05 and the distance between any two neighbouring indentations was 15μm. This distance is chosen to avoid possible influence of stress field caused by the neighbouring indentation. In fact, the stress field generated by a Berkovich indenter is illustrated in Fig. 4.7. [247]. It is suggested that the distance between two neighbouring indentation should be larger than 3d where d is the size of indentation impression [247].

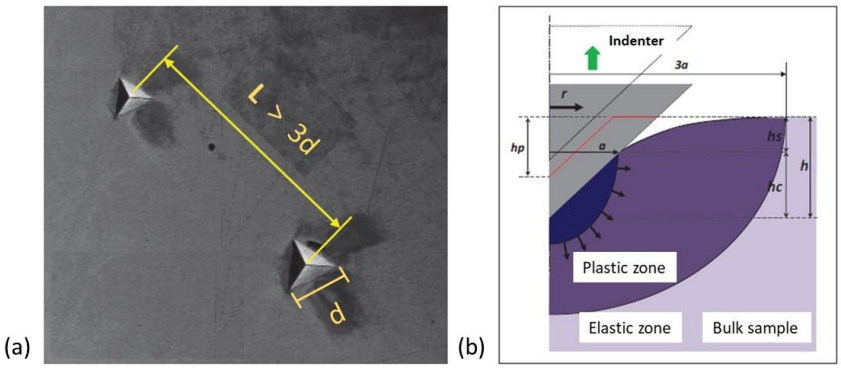

Fig. 4.7 (a) Distance between two neighbouring indentations, (b) Stress field caused by a Berkovich indenter [247].

A number of distances below the treated surface were chosen for indentations which are 5, 10, 20, 30, 50, 70, 100, 150, 200, 250, 300, 350, 400, 450, 500, 550, 600, 700, 800, 900, 1000μm respectively. Fig. 4.8 shows SEM observations of the residual indentation impression. For each distance, five indentations were carried out, as indicated in Fig. 4.8 (a). It should be mentioned here that the thickness of nanocrystalline region generated by SMAT is about 5μm. Thus, indentations in this region were located at a depth of 5μm beneath the treated sample, as illustrated in Fig. 4.8 (b) where the size of impression ranges from 3.5μm to 3.7μm. Observations of the residual impressions reveal that pile-up occurred for all indentations located up to a depth of 500μm, farther than which no pile-up was observed.

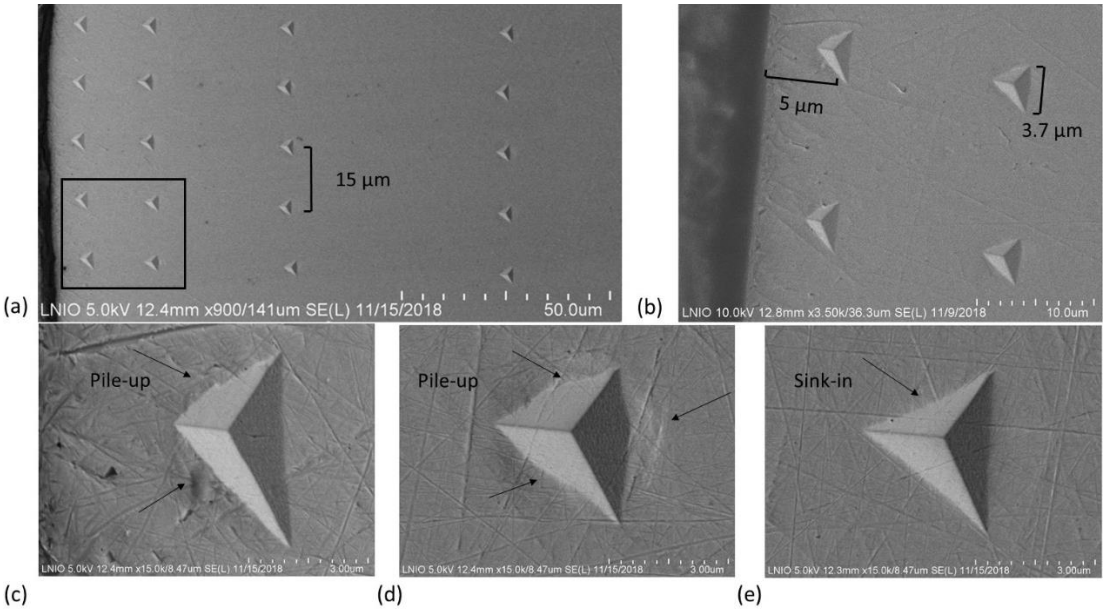

Fig. 4.8 (a) Illustration of nanoindentation carried out on the SMATed sample, (b) Enlargement of the outlined zone, (c), (d) and (e) Indentation impressions at 5µm, 50µm and 600µm beneath the treated surface, respectively. Black arrows indicate pile-up/sink-in which occurred during nanoindentation.

Pile-up behaviour of various materials has been a popular research topic and it can be correlated to material's the strain hardening exponent, residual stress, ratio of E/Y (Young's modulus/yield stress) etc. [148], [150], [151], [175]–[177], [179], [230], [231]. For 316L stainless steel with a high strain hardening exponent and a high ratio of E/Y, sink-in phenomenon is expected. According to our experimental results, sink-in occurred for nanoindentations performed in the regions non-affected by SMAT (at least 500 µm below the treated surface) where the initial microstructure and mechanical properties were unchanged. Fig. 4.8 (e) gives an example of indentation located at 600µm below the treated surface where sink-in occurred. On the other hand, the reason for pile-up observed in the SMAT-affected regions can be attributed to the change of the local microstructure and mechanical properties which are mainly grain refinement, residual stress and strain hardening, as discussed in Section 4.1. The pile-up behaviour of SMATed material depends on several factors which will be addressed in details in Section 4.4 in which more delicate measurements of pile-up were conducted with atomic force microscope.

Following the indentations conducted along the cross-section of the SMATed sample, the load-displacement curves were subsequently obtained. The corresponding results were plotted in Fig. 4.9. For a sharp indenter, the curve generally follows the relation $P=Ch^2$ [148], where P is the load and h is the displacement into the sample and C is the loading curvature which is a measure of the "resistance" of the material to indentation [148], [176].

The shape of the load-displacement curve, namely the loading curvature, C, gives important information about the indented material. It is reported that mechanical properties of the indented material and residual stress have influence on the loading curvature [149], [150], [176]. For example, Zhu [176] performed indentations on single crystal copper with different stress states (stress-free, compressive residual stress and tensile residual stress) and found out that for an indentation depth of 700nm and a magnitude of -137.4MPa residual stress, the loading curvature, C, increased by about 4%, as compared to stress-free sample. Another important mechanical property that influences the loading curvature is the strain hardening exponent, n, according to the studies of Mady [150] who performed a series of simulations on thin ceramic films with varying residual stress and strain hardening exponent. His studies showed that the strain hardening exponent has a major influence on the loading curvature while the residual stress has a relatively small influence which is consistent with the results of Zhu. According to the simulation results of Mady, a decrease of about 26% of loading curvature was found when strain hardening exponent varied from 0.5 to 0.1 for the stress-free simulations.

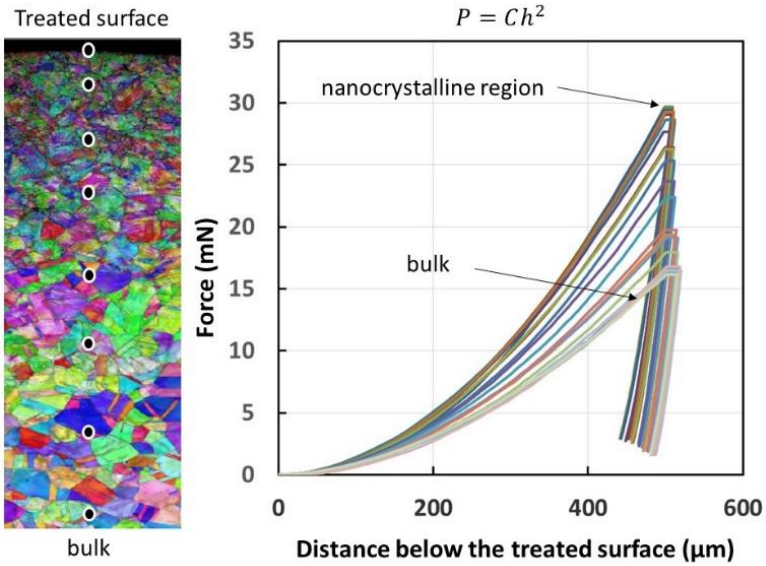

Fig. 4.9 Force-displacement curves of indentations at different distances below the treated surface.

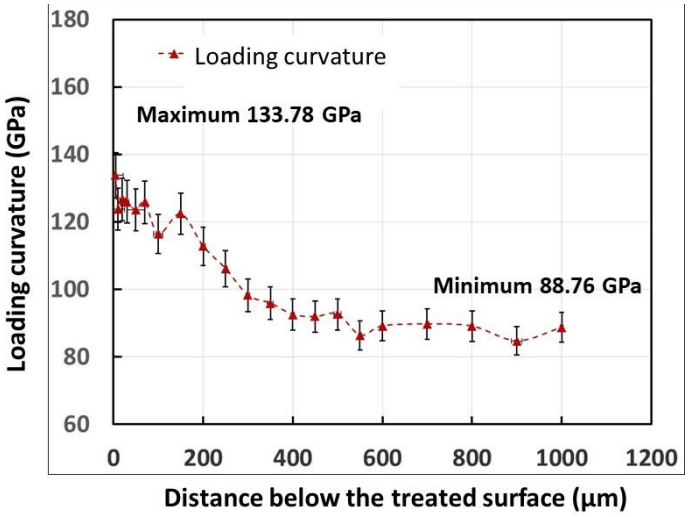

Fig. 4.10 Variation of loading curvatures for indentations curves along the cross-section of SMATed sample.

The loading curvatures of the load-displacement curves of our sample are plotted in Fig. 4.10. It can be observed that the loading curvature is highest in the nanocrystalline region with a maximum value of about 133.78 GPa and stabilizes at a depth of about 550 µm below the treated surface. A variation of about 50% of the loading curvature value can be detected between the nanocrystalline region and the bulk interior of the non-affected region. It should be mentioned that 316L stainless steel has a high initial strain hardening exponent. When subjected to severe plastic deformation, the strain hardening exponent for the SMAT-affected region could change. When the SMAT treatment intensity is low and no grain refinement occurs, the material is only cold hardened and the work hardening exponent is not changed. In regard to high intensity of SMAT treatment, grain refinement occurred and the strain hardening exponent decreased accordingly [7], [234]. Petit et al. [234] established a multilayer model for the macroscopic mechanical behaviour of a SMATed 316L plate. The cross-section of the SMATed sample was divided into core material layer, transition layer and nanocrystalline layer. His results showed that the strain hardening exponents for the nanocrystalline layer and core material layer are 0.0712 and 0.733 respectively. The strain hardening exponent decreased by 10 times due to SMAT treatment for the nanocrystalline region. Combining the results of Petit and Mady, a lower loading curvature is expected for the nanocrystalline region as a result of a low strain hardening exponent. But opposite results have been found in our case. The reason for this is because that in the studies of Mady, the grain size of the simulated material is a constant parameter and that strain hardening exponent was varied individually. In the case of

SMATed material, not only the strain hardening exponent changes, but also the grain size decreases as a result of grain refinement effect. Smaller grain size results in higher yield stress according to the famous Hall-Petch law which is the explanation of higher loading curvature observed in our experiments.

Corresponding maximum loads and ratios of h_f/h_{max} for indentations along the cross-section of our SMATed sample are also demonstrated in Fig. 4.11. The maximum load in the nanocrystalline region is about 30 mN which is about twice higher compared to the bulk which is not affected by SMAT. The maximum indentation load is stabilized at a depth of about 550 µm below the treated surface. This indicates that the depth affected by SMAT is at least 550 µm. Three factors induced by SMAT (grain refinement, compressive residual stress and strain hardening, respectively) contribute to higher indentation load. In this work, efforts have been made to attempt to distinguish individually the influence of each of these three factors.

Firstly, it should be clarified that when SMAT intensity is high, three major changes, such as grain refinement, superficial compressive residual stress and strain hardening, are significantly induced, as compared to the non-affected region. While SMAT intensity is low and no grain refinement takes place, the material is merely slightly work hardened with limited amount of compressive residual stress. Therefore, it would be a real challenge to understand individually their roles with regard to their contributions to higher local strength in the strongly affected regions [12], [228]. In the literature, systematic studies were conducted to investigate the influence of residual stress on nanoindentation load [149], [175], [230]. For example, Zhu et al. [176] performed nanoindentation (penetration depth of 700 nm) on single crystal copper with different residual stress states. The magnitude of the residual stress ranged from -137.4 MPa to 68.4 MPa. Their results showed that the influence of residual stress on indentation load is in the range of a few µN, which was negligible compared to the magnitude of the maximum load (several mN). Bolshakov et al. [175] used finite element method to study the behaviour of 8009 aluminium alloy during indentation to investigate how the indentation process was influenced by residual stress. The residual stress ranged from -300 MPa to +350 MPa for a series of simulations. The results showed that the maximum indentation load increased by about 1 mN for simulation with residual stress of -300 MPa. Similar results were found by Mady [150] for ceramic films simulated using finite element method. For a compressive residual stress of -5 GPa, the maximum load increased by only 2 mN as compared to stress-free state. In fact, when the imposed load exceeds the yield strength of the material (as it is the case during

nanoindentation), residual stress has small effects because the elastic misfit strains are small and soon washed out by plasticity [227].

In our case, the study material is a 316L stainless steel, and it has a higher Young's modulus and hardness compared to copper and aluminum. According to our previous work, the compressive residual stress generated by SMAT is about -450 MPa in the strongly affected region [228]. Based on the above discussion, compressive residual stresses are not assumed to be a major factor which contributes to higher local strength. In the present work, grain refinement is considered to be the main factor for higher local strength, as suggested by the Hall-Petch law. This issue will be addressed in details in the following section.

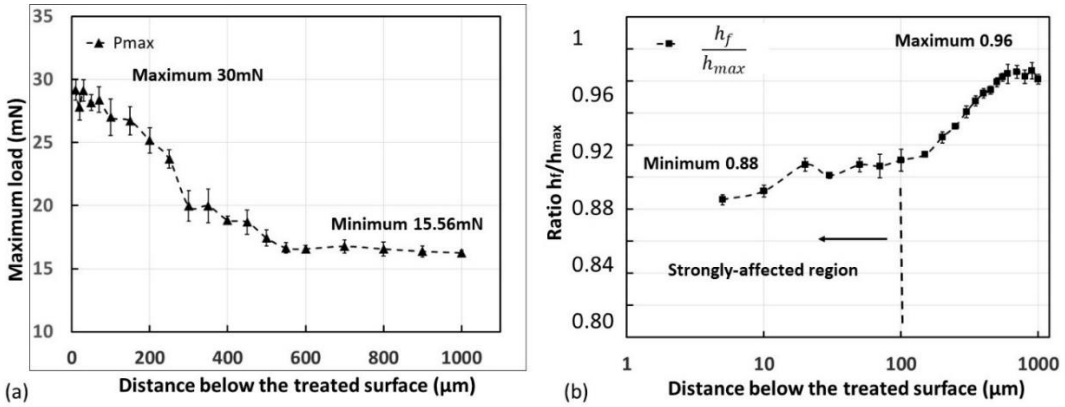

Fig. 4.11 (a) Maximum loads for indentations performed along the cross-section of SMATed sample, (b) Corresponding ratio of h_f/h_{max}.

Besides the loading part, the unloading curve of nanoindentation also gives important information about the indented material, such as contact stiffness and sign/magnitude of residual stress [14], [149]. For instance, the ratio between the final displacement and the maximum displacement, h_f/h_{max} could be correlated to residual stress and pile-up behaviour of the studied material [148], [149], [176], [248], [249]. Xu et al. [248] established an empirical model based on finite element simulations for residual stress determination from the elastic recovery (h_f/h_{max}) of nanoindentation. The empirical model has been used to derive the plastic properties and to estimate the residual stress of the mechanically polished fused quartz beam. Unfortunately, this method could not be applied to our case because most of the experiments conducted in the literature do not take into account a variation of the grain size. For a SMATed sample, grain size refinement induces an additional changing parameter, grain size d, which makes the interpretation of indentation measurements challenging. Hence, the ratio of h_f/h_{max} for the present experiments could not be directly correlated to superficial compressive residual stresses. The ratios of h_f/h_{max} for the

indentations performed along the cross-section of the SMAT-processed sample are illustrated in Fig. 3b. It can be noticed that the elastic recovery is larger in the near treated surface while almost no elastic recovery can be found in the bulk of the sample which is not affected by SMAT. It is concluded previously that residual stresses do not have a significant influence on the load-displacement curves of nanoindentation [149]. Therefore, the variation of elastic recovery for our experiments can be attributed to different local yield strengths along the cross-section of the sample. In fact, the local yield strength in the strongly-affected region is increased as a result of strain hardening and grain refinement phenomena, which in turn contribute to larger elastic recovery during unloading [234]. The ratio of h_f/h_{max} can also be correlated to pile-up amount. It was reported that pile-up amount is large when h_f/h_{max} is very close to 1 and the degree of work hardening is small [179]. This observation is consistent with our experimental results. Pile-up phenomenon was investigated in the SMAT-affected region, which will be discussed in details in Section 4.4.

4.3 Measurement of elastic modulus and hardness

4.3.1 Elastic modulus of nanocrystalline material

As discussed in Section 1.4.2, attention needs to be paid to the imperfections of nanocrystalline materials when their mechanical properties are evaluated. The porosity and incomplete bonding among the grains was a major concern for the early bottom-up synthesis methods as imperfections like porosity could distort properties of nanocrystalline materials. It was observed that Young's modulus and yield stress [2] decreased as a function of porosity for nanocrystalline Pd and Cu. The existing pores provide initiation sites for fractures. On the other hand, nanocrystalline materials produced by severe plastic deformation are reported to contain little porosity [7] and lower values of elastic moduli in copper and copper composites exposed to ECA pressing were also revealed in some works [250]–[252]. For instance, the detailed studies of the elastic properties of nanostructured copper samples processed by ECA pressing were conducted by Akhmadeev et al. [253], where values of these moduli in nanostructured copper were lower by 10-15%, as compared to coarse-grained copper. The comparison of the elastic moduli behaviour after annealing with TEM data allowed the conclusion that the transformation of non-equilibrium grain boundaries to an equilibrium state is responsible for the main recovery of elastic moduli in nanostructured copper [253]. It is known that elastic modulus is an intrinsic property of a

solid and is governed by the nature of interatomic bonding (or chemical bonding) of the constituent atoms. The analysis of various mechanisms showed that neither internal stresses nor lattice dislocations can cause such changes in elastic moduli. One possible explanation for the decrease of elastic moduli for nanostructured materials has been proposed, assuming that the elastic moduli of near boundary regions differs from the elastic moduli of an ideal crystal, then the overall moduli of nanostructured material could be combinations of the elastic modulus of the matrix and of the near grain boundary region. Since nanocrystalline materials contain a large fraction volume of grain boundaries, therefore, it is reasonable to observe a lower elastic modulus for these materials. The estimates showed that the change in elastic moduli observed in nanostructured copper can be explained if we accept that the value of the elastic moduli of the near boundary regions is 15-17% of the value of the elastic moduli in coarse-grained metal [7].

4.3.2 Measurements of elastic modulus and hardness

The results of Young's modulus measured along the cross-section of the treated sample are plotted in Fig. 4.12 (b). It can be observed that Young's modulus measured along the cross-section is almost constant with an average value of about 200GPa, except for the values near the sample edge. The Young's modulus measured for indentations performed at 5μm beneath the treated surface is about 180GPa, which is 10% lower than the average value. As the areas near the sample edge are also the nanocrystalline region in the case of SMATed sample, two possible reasons may be responsible for the decreased value of Young's modulus. The first one might be attributed to microstructure of nanocrystalline material discussed in the previous Section. Another reason may be due to the fact that the indentations were conducted in the regions near the edge of the sample. Therefore, edge effect may occur due to insufficient distance between indentation and the edge of the sample, leading to lower values of contact stiffness/Young's modulus [254], [255]. From the results obtained in Chapter 3, the thickness of nanocrystalline region generated by SMAT is about 5μm. Indentation carried out in this region may be too close to the edge of the sample and a small edge spacing will induce severe edge effects into the results of the tests. To better understand the influence of edge effects on nanoindentation measurements, a non-SMATed reference sample was prepared and the obtained results is presented in Section 4.3.3. It turned out that the decrease of Young's modulus was due to edge effects which can be corrected by the method proposed by Gerber and Jakes [254], [255]. Details of the correction of the Young's modulus/contact stiffness regarding edge effects can be found in Section 4.3.3.

In Section 4.1.2, the profile of the compressive residual stresses along the cross-section of SMATed sample has been obtained, which are present up to a depth of 500µm below the treated surface. In the literature, residual stresses have been reported to have influence on nanoindentation measurements. For example, the compressive residual stress in the material tend to push the indenter up more, leading to a higher measured value of Young's modulus [149], [174]. It is argued that compressive residual stress tends to increase the amount of pile-up and affect the true contact area, which leads to higher measured values (while tensile residual stress has the opposite effect). Nevertheless, our measurements on Young's modulus imply that compressive residual stresses generated by SMAT have little influence on the measured value of Young's modulus (seen in Fig. 4.12(b)). Similar results have been found by Mady et al. [150] that measured elastic modulus of TiN films with different levels of compressive residual stress. The corresponding results are shown in Fig. 4.12 (a) in which no direct correlation could be found between hardness/elastic modulus and residual stress. Contrary to the results of Tsui et al. [174] where the values of hardness/Young's modulus were severely influenced by residual stress when calculated by the standard Oliver-Pharr method, Mady argued that one important difference between the indentations conducted in both cases referred to the indented material, which was TiN film in his case and an aluminum alloy for Tsui. Thus, conditions such as the ratio between final displacement and maximum displacement, h_f/h_{max} and Y/E were different. Although the results of Tsui showed a dependence of hardness/elastic modulus on residual stress, he argued that standard Oliver-Pharr method failed to account for the change of contact area caused by residual stress (compressive residual stress increases the true contact area while tensile residual stress has opposite effect). Once the proper contact area is used, the hardness and elastic modulus are significantly independent of stress [149], [174]. Moreover, determination of the true contact area is a very difficult research topic which involves usually atomic force microscope measurements. Various methods have been proposed to correct the true contact area in the case of pile-up based on the data obtained from AFM but each has their own restrictions. For example, some methods are only suitable for a specific material and in a certain loading range [152], [230], [256].

It remains a question whether the true contact area should be corrected for our experimental results despite the pile-up phenomenon in the SMAT-affected region. Firstly, the measured average value of Young's modulus along the cross-section of SMATed sample is about 200 GPa which is quite close to the generally accepted value despite the presence of severe compressive residual stress. In addition, the contact area calculated by

standard Oliver-Pharr method for our indentations along the cross-section is almost constant, which is an important parameter to calculate Young's modulus according to Eq.(2-10) and Eq.(2-11). On the one hand, SEM results show that pile-up occurred for the SMAT-affected regions of our sample. On the other hand, it is argued that pile-up increased the contact area between the material and the indenter, systematically leading to erroneous contact area values and consequently to an overestimation of the hardness and the indentation modulus values [149], [174], [178]. A primary problem arises from this argument is that if the contact area is corrected with pile-up taken into account, the value of Young's modulus recalculated with new contact area will deviate from the generally accepted value. Anyhow, an modified correction model based on the semi-ellipse model of Kese [152] has been used to correct the true contact area due to pile-up. The hardness and Young's modulus in our experiments were corrected with the new contact area subsequently. The corresponding results are shown in Section 4.4.

The corresponding hardness measured along the cross-section of SMATed and non-SMATed samples is given in Fig. 4.13 (a). For the SMATed sample, the hardness is the highest in the nanocrystalline region with a value of about 5.06 GPa while this value is about 2.60 GPa for the non-affected bulk of the material. The hardness decreases with the distance along the cross-section and is stabilized at a depth of about 550 µm, which is consistent with the result of the maximum load presented above. For the non-SMATed sample, the hardness is also slightly higher near the sample surface. This could be mainly attributed to the work hardening unintentionally induced during machining. The value of hardness stabilizes at a depth of about 150 µm which could correspond to the depth affected by machining. This is consistent with the XRD measurements illustrated in Section 4.1.3.

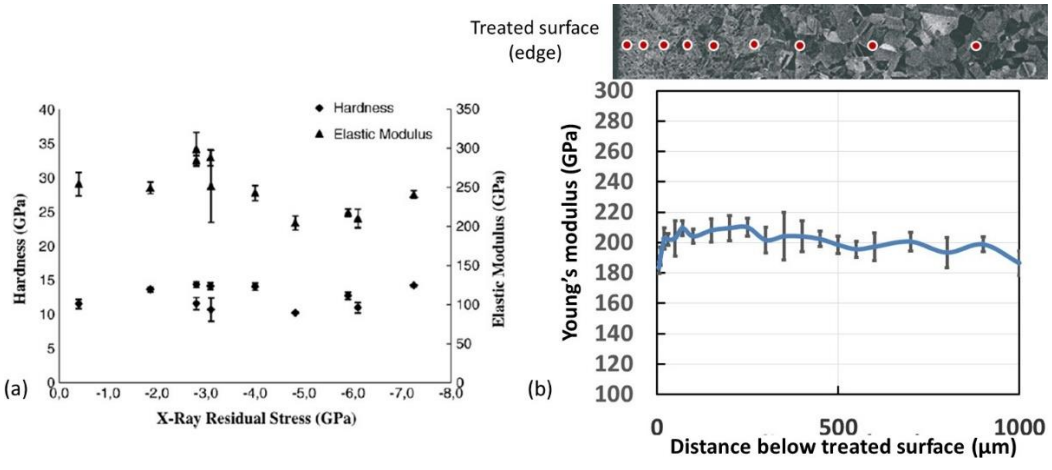

Fig. 4.12 (a) Measured hardness and elastic modulus of TiN films as a function of compressive residual stress [150] (b) Young's modulus measured along the cross-section of the SMATed sample.

Grain refinement effect, compressive residual stress and strain hardening all contribute to higher measured value of hardness. A major challenge would be to distinguish the influence of each factor individually. In the literature, the effect of residual stress on hardness is debatable. Dependence of hardness on residual stress was indicated by some researchers [174] while opposite results were reported by others [150]. Mady argued that the difference between these results might be due to the fact that the indented materials were different [150]. In our case, it would be difficult to investigate the influence of residual stress separately due to its coupling with the grain refinement induced by SMAT. An additional varying parameter (the grain size d) along the cross-section of SMATed sample must be taken into account to interpret the results of hardness. It should be mentioned that hardness is calculated by dividing the indentation load by the contact area. In the previous Section, it was indicated that the grain refinement effect has a primary influence on the indentation load while residual stress plays a relatively minor role [226], [227]. If we accept the assumption that the contact area calculated by the standard Oliver-Pharr method is reliable regardless of the pile-up observed in the SMAT-affected regions. Then, the increased hardness for regions strongly affected by SMAT (high treatment intensity) is mainly due to grain refinement effect, as suggested by the Hall-Petch law. The correction of the true contact area by taking into account pile-up phenomenon will be discussed later in Section 4.4.

In Section 3.5, the distribution of grain size along the cross-section of SMATed sample is highlighted according to EBSD observations. It could be concluded that grain refinement is severe down to a depth of about 100 µm. Hardness (before and after correction) at depths between 5 and 100 µm below the treated surface as function of the inverse of grain size square root, $\sqrt{d}^{-1}$, is plotted subsequently in Fig. 4.13 (b). The method used to correct the hardness with pile-up taken into account will be described in details in Section 4.4. The Hall-Petch coefficient K for the corrected hardness can then be determined and is about 251.5 $MPa * \mu m^{1/2}$. Experimentally, the value of K could vary depending on several factors such as strain levels, temperature and history/preparation of the sample [257]. To be able to compare the results of this study with those of the literature, it is important to note that the strain distribution under a pyramidal indenter is not uniformed. The concept of representative strain, ε_r, gives an overall estimation of the average strain level during a nanoindentation test. Tabor [258] estimated theoretically and experimentally that this value is about 8% for Vickers indenter. This value was extended to Berkovich tip. Kashyap et al.

[259] investigated the Hall-Petch coefficient K of tensile specimens of 316L stainless steel (grain size: 3.1 µm to 86.7 µm) at different strain levels and temperatures. Their results showed that the value of the K coefficient at room temperature (24°C) and at a 8% strain level was about 280 $MPa * \mu m^{1/2}$, which is very close to the value obtained in this work. This may indicate that the corrected hardness agrees well with the Hall-Petch law and that grain refinement effect could be the major factor that leads to higher local strength for SMAT-processed materials. On the basis of this conclusion, the contribution of strain hardening to the local yield strength can be assumed less significant in an indirect manner. This is mainly due to the fact that strain hardening is difficult to be individually and quantitatively characterized by experimental methods [260].

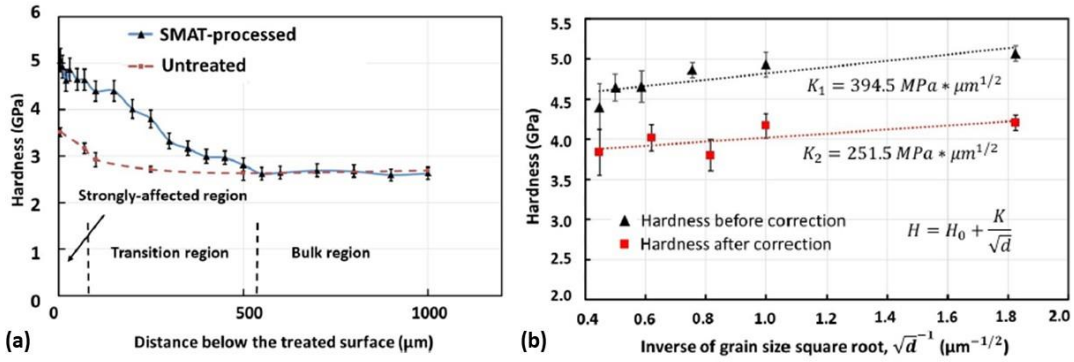

Fig. 4.13 (a) Hardness measured along the cross-section of SMATed and non-SMATed samples, (b) Hardness (before and after correction) plotted as function of the inverse of grain size square root for SMATed sample.

4.3.3 Influence of edge effect on nanoindentation measurements

Nanoindentation has a number of advantages in that it provides direct access to the local characterization of materials. Despite these advantages, systematic errors could occur during measurements and these errors strongly affect the validity of the measurements. Two major sources of errors can arise from pile-up formation in the SMAT-affected regions and sample edge effects. In this section, we will focus on sample edge effects during the nanoindentation measurements. Indeed, the standard Oliver–Pharr nanoindentation analysis tacitly assumes that the specimen is structurally rigid and that it is both semi-infinite and homogeneous [14]. However in practice, many specimens violate these assumptions [254, 255]. For instance, when the specimen flexes or possesses heterogeneities, such as free edges or interfaces between regions of different properties, artefacts arise in the standard analysis, which can affect the measurement of hardness and modulus [255]. In the case of

SMATed materials, the grain-refined area is located at the top surface of the sample (sample edge). Indentations performed in this grain-refined area are therefore inevitably perturbed. For example, the Young's modulus/contact stiffness measured in the near surface regions down to a depth of 30 µm (edge area) is about 10% to 15% lower than that measured in the bulk region. This drop of Young's modulus/contact stiffness due to an edge effect cannot be neglected.

With regard to the correction of Young's modulus, several points should be clarified. First, it is important to note that elastic modulus is an intrinsic property of a solid and is governed by the nature of interatomic bonding (or chemical bonding) of the constituent atoms [7]. As the gradient microstructure generated by SMAT involves a varied grain size (from tens of nanometers to tens of micrometers), any possible variation of Young's modulus/contact stiffness due to changing grain size is out of the scope of this work. Whether Young's modulus is influenced by the grain size is a subject that requires further study. Besides grain refinement effect, a compressive residual stress field was induced simultaneously along the cross-section of SMATed sample [228]. In this work, the original Young's modulus (without correction) measured in the strongly impacted region (100 µm to 150 µm below the treated surface) [228] and that in the bulk region show little difference. It can be confirmed that (at least in our case) Young's modulus is rather independent of compressive residual stresses. Although the dependence of Young's modulus on residual stress has been reported elsewhere [174], the indented materials used in these studies are different from the material used in this work. Mechanical properties such as the E/Y ratio are not the same. Based on the above discussion, the influence of residual stress on Young's modulus is considered to be small in this work and it is therefore not considered while correcting Young's modulus/contact stiffness.

According to Jakes et al. [255], the influence of specimen flexion or heterogeneities (sample edge in our case) on nanoindentation measurements could be quantified by a structural compliance (C_{str}). This structural compliance (C_{str}) should be added to the machine compliance (C_m). It should be noticed that C_{str} varies as a function of indentation location on the sample. The relationship between structural compliance, total compliance and machine compliance can be expressed by Eq. (4-1):

$$C_t = C_m + C_{meas} = C_m + C_s + C_{ind} + C_{str} \tag{4-1}$$

where C_t, C_m, C_{meas}, C_s, C_{ind} and C_{str} are the total compliance, machine compliance, measured compliance, sample compliance, indenter compliance and structural compliance, respectively. Note that the contact stiffness has a reciprocal relation with the sample compliance C_s as illustrated by Eq. (4-2):

$$S = \frac{1}{C_s} \tag{4-2}$$

by subtracting C_{str} from the sample compliance, the contact stiffness/Young's modulus could be therefore corrected. Based on papers written by Doerner and Nix [261] and Stone Yoder and Sproul [262], Jakes et al. [255] used two methods, namely "DN Plot" and "SYS Plot", for the determination of structural compliance. As severe pile-up formation was observed in the SMAT-affected regions, the "DN Plot" was chosen in this work because it requires direct imaging of the indentation imprints (Details of the measurements of indentation imprints/true contact area are given in Section 4.4). The principle of "DN Plot" is demonstrated in Eq. (4-3):

$$C_t = \frac{1}{E_r\sqrt{A}} + (C_m + C_{str}) \tag{4-3}$$

where E_r is the reduced modulus and A is the true contact area that relies on direct imaging by AFM. C_m and C_{str} are the machine compliance and structural compliance respectively. By plotting C_t as a function of $\sqrt{A}^{-1}$, the slope of the function is E_r^{-1} with the intercept being (C_m+C_{str}). Thus, for a series of indentations (with different indentation depths) performed at different distances below the treated surface, the corresponding intercepts of their "DN Plots" can be obtained. It is important to note that C_{str} is larger in the near edge area and it is almost negligible in the regions far away from the sample edge. Thus, the value of the structural compliance could be determined by comparing the intercepts of the DN Plots.

The DN Plots of a series of indentations performed at different distances below the treated surface are illustrated in Fig. 4.14(a). It should be underlined that the DN Plots for indentations located between 100 µm and 800 µm were nearly overlapped as a consequence of absence of edge effects. It is the reason for which the DN Plots of indentations between

these areas are not represented. The DN Plots in Fig. 4.14 (a) reveal a clear influence of sample edge on nanoindentation measurements, which can be inferred from the variation of the intercepts. Another feature to which attention should be paid is that the slopes of DN Plots are slightly different. In general, the slope of DN Plots of the same material (which is the inverse of the reduced modulus) is supposed to be constant [255, 261]. However, varied grain size and compressive residual stresses are both present along the heterogeneous gradient microstructure, and they both should contribute to a pile-up amount. Thus, the deviation of the slope might be due to the fact that pile-up formation in the SMAT-affected region is irregular (explications given in Section 4.4), which would affect the subsequent measurement of the true contact area by AFM.

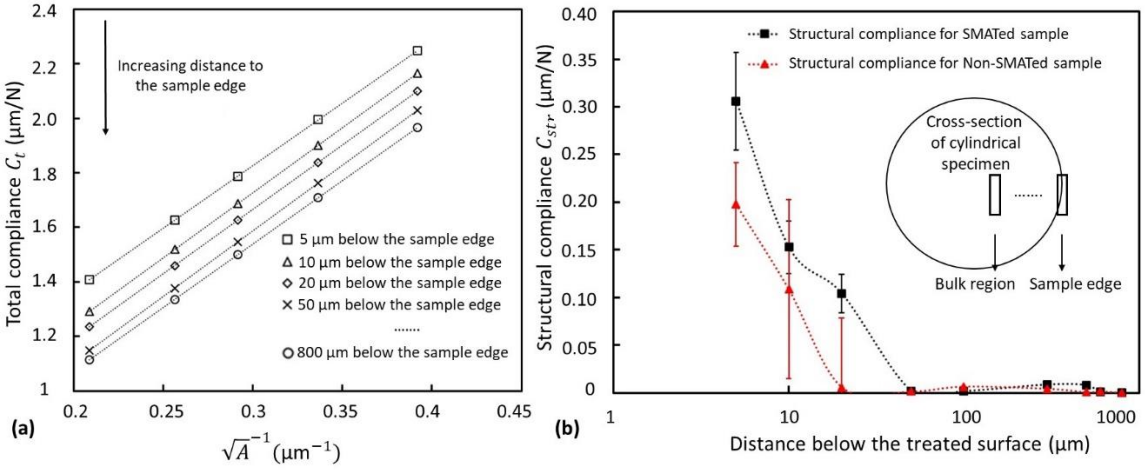

Fig. 4.14 (a) DN Plots for a series of indentations performed with different indentation depths and at different distances below the treated surface (cross-section), (b) Variation of the structural compliance C_{str} for SMATed and non-SMATed samples along the cross-section of the samples.

The intercept of the DN Plot for indentations located at 800 µm below the treated surface (sample edge) is about 0.1400 µm/N. As aforementioned, the structural compliance in this area is supposed to be zero. Therefore, the machine compliance is estimated to be 0.1400 µm/N. This value is slightly higher than the as-claimed value which is about 0.1235 µm/N (the as-claimed machine stiffness is 8100000 N/m). To determine the structural compliance, the machine compliance is set at 0.1400 µm/N. The variations of the structural compliance along the cross-section of both SMATed and non-SMATed samples are plotted in Fig. 4.14 (b). It can be deduced that the edge effects disappear at 20 µm below the sample edge for non-SMATed sample while this distance is slightly larger for SMATed sample. This might be attributed to different conditions of sample edges. As a matter of fact, the samples are subjected to mechanical polishing prior to the nanoindentation test in

order to achieve a mirro-like finish. The polishing durations of SMATed and non-SMATed samples could vary, as properties such as local strength [234], residual stress state [228] and wear properties [38] are different which in turn leads to different sample edge conditions. For the non-SMATed sample, it is important to note that a periphery volume of 300 µm was removed by electrolytic polishing from the outer layer of the specimen to eliminate the influence of work hardened layer unintentionally induced during machine (Seen in Section 4.1.3). Based on these results and discussions, the corrected contact stiffness, Young's modulus of SMATed sample (indentation depth 500 nm) were plotted in comparison with the original ones in Fig. 4.15. It can be seen that the influence of the edge effects is present down to a depth of about 50 µm. As for the correction of hardness, the edge effects were also reported to cause errors in the measurements of hardness. This issue will be addressed in Section 4.4 because the correction of hardness would require the simultaneous investigations in pile-up phenomenon and that of edge effects.

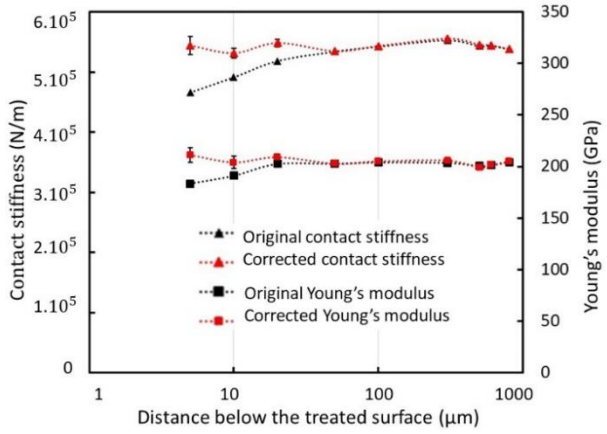

Fig. 4.15 Corrected contact stiffness and Young's modulus plotted in comparison with the original ones, with the edge effects taken into account

It is essential in this project to understand the influence of edge effects on nanoindentation measurements as the nanocrystalline region generated by SMAT is located at the edge areas of the sample. Theoretically, the influence of edge effects must be eliminated in order to ensure the validity of the subsequent interpretations of the corresponding measurements performed in the nanocrystalline region. In summary, the edge effects affect mainly the contact stiffness/Young's modulus, which can be corrected by the method provided by Gerber and Jakes [254], [255].

4.4 Pile-up behaviour of SMATed material

For an indentation into an elastic material, the surface of the material is typically drawn inwards and downwards underneath the indenter and sinking-in occurs. When the contact involves plastic deformation, the material may either sink in, or pile up around the indenter. This depends on the ratio E/Y (elastic modulus/yield stress) and the strain-hardening properties of the material [149], [162]. For 316L stainless steel usually with a high strain hardening exponent and a high ratio of E/Y, sink-in phenomenon is expected, as illustrated in Fig. 4.16 (b) in which AFM measurements were performed on an indentation imprint located at 800 µm below the treated surface. For this region far from the treated surface, the local microstructure and mechanical properties were not affected by SMAT. However, for the regions affected by SMAT, the local microstructure and mechanical properties, such as grain size, local yield stress and work hardening exponent [234], change accordingly. As a consequence, pile-up occurred in the SMAT-affected regions, as shown in Fig. 4.16 (a) for an indentation imprint obtained at 50 µm below the treated surface.

Pile-up behaviour during nanoindentation has been a popular research topic and it can be correlated to material's strain hardening exponent, residual stress states, ratio of E/Y [148], [150], [151], [175]–[177], [179], [230], [248]. The main parameter that affects the pile-up behaviour is the strain hardening properties of materials [149], [162], [256]. For materials with low strain-hardening, pile-up tends to occur while for materials that exhibit high strain-hardening (316L stainless steel, for instance), sink-in is expected. Moreover, residual stresses are also reported to have an influence on the pile-up behaviour. In the literature, many studies concluded that compressive residual stress increases the amount of pile-up while tensile residual stress has the opposite effect.

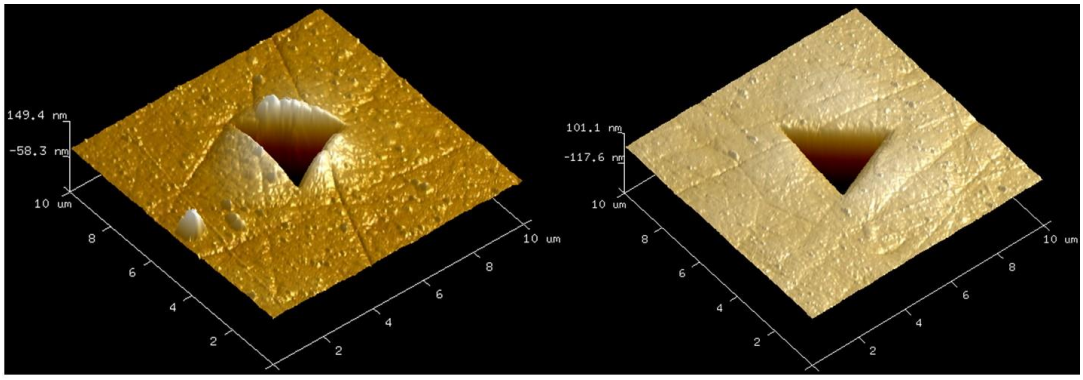

(a) (b)

Fig. 4.16 AFM measurements of indentation impressions (a) located at 50µm below the treated surface, (b) located at 800µm below the treated surface.

Standard Oliver-Pharr method [14] failed to account for pile-up phenomenon, which lead to an underestimation of the contact area [230, 256]. Correction of true contact area is therefore necessary for the sake of accuracy while treating indentation results. In the following section, a systematic study of the pile-up behaviour will be presented. For this purpose, a series of indentations was performed on the cross-section of a SMATed 316L stainless steel with different indentation depths. Pile-up behaviour (pile-up length, width, height and shape) [152] as well as its relationship with indentation depth were investigated.

Pile-up behaviour can be quantified by pile-up height [150], [230], [256] or pile-up width [152] depending on the developed method. It is generally accepted that pile-up increases the contact area between the material and the indenter, systematically leading to an erroneous contact area and consequently to an overestimation of the values of hardness and indentation modulus [174], [178]. In this work, a modified model based on the semi-ellipse model of Kese [152] was used in order to evaluate the true contact area affected by pile-up. Fig. 4.17 gives four examples of AFM 2D data of indentation imprints in the SMAT-affected regions (20 µm below the treated surface). For these tests, the indentation depth ranges from 500 nm to 1000 nm. Two features are worth noticing. First, it can be seen that pile-up height/pile-up amount increases with an increase of indentation depth, which will be discussed later in this section. The other characteristic is that the pile-up shapes and distribution around the three indentation edges are irregular for all the indentation imprints. This phenomenon is different from that observed in the studies presented in the literature [152], [256] where the pile-up behaviour was more regular and was rather evenly distributed along the entire indentation edges. This difference may be attributed to the gradient microstructure generated by SMAT. In the literature, the studied materials often have a fixed average grain size and a given residual stress state throughout the sample. Nevertheless, for the SMATed 316L stainless steel used in this work, a gradient microstructure is generated with a microstructure and mechanical properties varying according to the distance beneath the treated surface. This inhomogeneous microstructure probably leads to irregular pile-up shapes and distribution. In addition, grain orientations were reported to have an influence on the pile-up behaviour [178]. Therefore, the semi-ellipse model of Kese cannot be directly applied for the evaluation of the true contact area in our case of SMATed material.

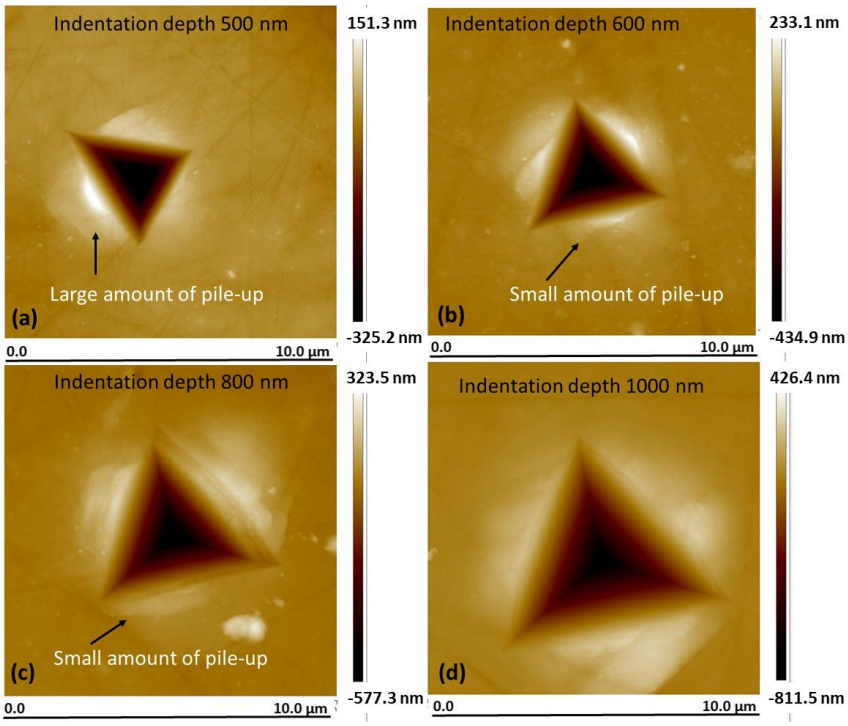

Fig. 4.17 AFM 2D data of indentation imprints in the SMAT-affected region (20 µm below the treated surface) with different indentation depths: (a) 500 nm, (b) 600 nm, (c) 800 nm, and (d) 1000 nm.

Fig. 4.18 (a) illustrates the semi-ellipse model of Kese [152] in which the pile-up is assumed to occur along the entire indentation edges. Therefore, the additional increased contact area due to pile-up would be the sum of the three projected areas of pile-up, namely the sum of three semi-ellipses, shown in Fig. 4.18 (a). The pile-up length b is considered to be constant and only the pile-up width, a, varies. Nevertheless, in the case of the 316L stainless steel studied in this work, the pile-up shapes and distributions are irregular, leading to varied pile-up length and width. Therefore, the additional increased contact area A_{pu} should be calculated with individual pile-up length and pile-up width measured with AFM, as demonstrated in Fig. 4.18 (b). In this work, the pile-up length, width and height (b_i, a_i, h_i where i=1,2,3) for each indentation imprint were measured. It should be mentioned that the indentation pattern is a triangle with three edges. Pile-up parameters (length, width and height) of the three indentation edges were measured simultaneously.

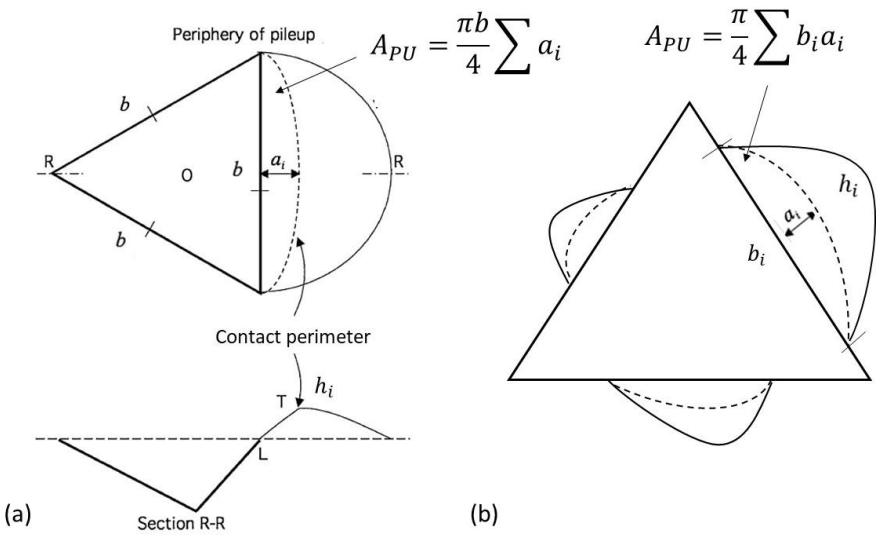

Fig. 4.18 (a) Ideal semi-elliptical pile-up projected contact area [152], (b) Real pile-up projected contact area of SMATed 316L stainless steel.

While the additional increased contact area due to pile-up can be calculated by pile-up length and width, the pile-up height is another crucial parameter to quantify pile-up behaviour [149], [256]. For our experiments, the pile-up height was measured for the three sides of each triangle indentation imprint and the average value was calculated subsequently. The average pile-up heights of indentation tests carried out with different indentation depths are plotted in Fig. 4.19 (a). For a given indentation depth especially when it is small (500 nm and 600 nm), the pile-up height is almost constant for indentations located at the near surface region until a depth of 100 µm. Beyond 100 µm, it decreases dramatically with a depth increase. The pile-up phenomenon seems to disappear at a depth of about 500 µm below the SMATed surface. This indicates that the depth affected by SMAT is at least 500 µm, which is consistent with the results of hardness presented previously in Section 4.3. It is worth mentioning that when the indentation depth is large (800 nm and 1000 nm), the behavior seems to be different. In fact, there is the presence of a slight decrease in pile-up height when the indentation site approaches the extra surface of the specimen. This decrease in pile-up height is probably due to the fact that the indentation imprints with large indentation depth start to interfere with the sample edge, i.e. the edge effect is involved in the indentation process. As a consequence, insufficient distance to the sample edge could affect the indentation measurements.

Higher values of pile-up height for indentations near the treated surface (up to a depth of 100 µm) could be related to the effect of severe grain refinement induced by SMAT according to the previous results of EBSD observations. Moreover, the multilayer

macroscopic model of SMATed 316L stainless steel of Petit et al. [234] showed that grain refinement was associated with a decrease in strain hardening exponent and an increase of yield stress. It was previously concluded that strain hardening exponent, n, is a major factor that results in pile-up phenomenon [162], [256]. Severe grain refinement near the treated surface provides the explanation for high values of pile-up height in this region as a consequence of low strain hardening exponent. When the SMAT intensity is low and no significant grain refinement occurs, the strain hardening exponent does not significantly change, which leads to lower value of pile-up height. This is the case of indentations performed at a depth of 300 µm below the treated surface, where a significant decrease of pile-up height value is observed. Another secondary factor that can increase the pile-up height is compressive residual stress according to the literature [148], [150], [151], [162], [174], [175], [177], [179], [230]. Numerous studies have been dedicated to quantify the influence of residual stress on pile-up height. For instance, Bolshakov et al. [175] used finite element method to study the relation between pile-up height and the residual stress for an 8009 aluminium alloy. It turned out that pile-up value for simulation with a residual stress magnitude of -300 MPa increased by about 20 nm, as compared to stress-free state. The studies of Zhu et al. [230] have led to similar conclusion for a 1045 steel. Pile-up height has also a straightforward link with the indentation load. It was demonstrated that pile-up height increases with increasing indentation load [256]. Gale et al. [256] studied the pile-up behaviour of SMATed copper. The results revealed that pile-up height has a linear relation with indentation load.

The residual stress profile measured along the cross-section (Fig. 4.4) in Section 4.1.2 shows that the magnitude of compressive residual stress in the strongly affected region (down to a depth of 150 µm) was in the range of -350 MPa to -450 MPa. Based on the above discussion, the influence of these compressive residual stresses on pile-up height can be qualitatively estimated to be tens of nanometers. Despite the efforts, it is almost impossible to quantify the influence of residual stress in SMATed 316L stainless steel as grain refinement effect and compressive residual stress in the affected region are strongly coupled and both vary according to the distance from the treated surface.

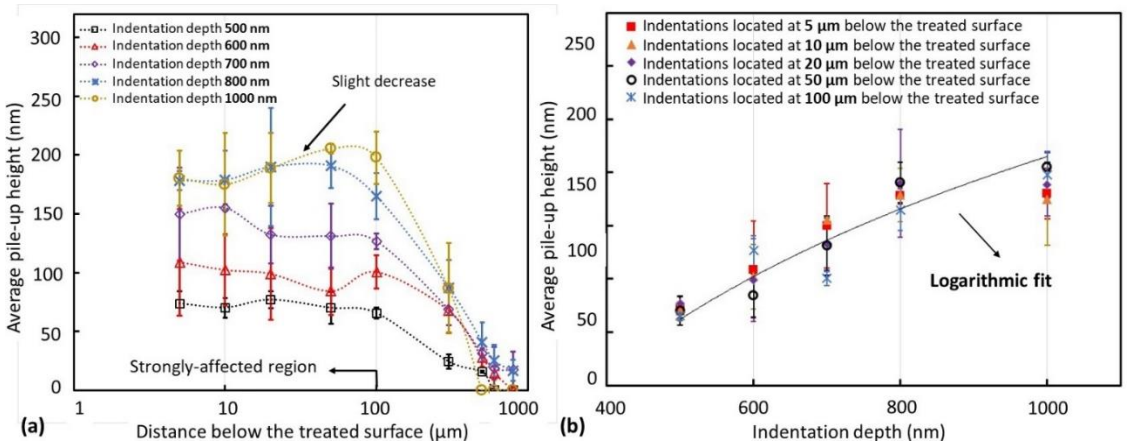

Fig. 4.19 (a) Averaged pile-up height for indentations with different indentation depths along the cross-section of a SMATed sample, (b) Averaged pile-up height in the strongly-affected region plotted as a function of the indentation depth.

The average pile-up height was plotted as a function of the indentation depth for indentations performed in the strongly-affected region (Fig. 4.19 (b)). A proportional increase in pile-up height with respect to indentation depth can be observed. This result is consistent with that presented by Gale et al. where a linear variation of pile-up height in regard to indentation load/depth was found for SMATed copper [256]. It can also be inferred that the errors caused by pile-up become more severe as indentation depth increases and the correction of the true contact area is necessary if accurate measurements are required. In the literature, pile-up height has been used to correct the area function of nanoindentation. For standard Oliver-Pharr method, the area function is F=A (h_c) where h_c is the contact depth. It is suggested [230], [256] that pile-up height could be added directly to the contact depth, leading to F=A (h_c+h_p), in an attempt to correct the true contact area. But this method was applied to our results in order to recalculate new hardness and Young's modulus, the recalculated hardness in the nanocrystalline region is almost the same as that in the bulk interior region non-affected by SMAT. This is clearly false as it disobeys the Hall-Petch law (deceasing grain size leads to increasing hardness). Therefore, a modified method based on the semi-ellipse model of Kese [152] was used to evaluate the true contact area using the AFM data (pile-up length and pile-up width), as discussed previously.

The corrected true contact area are plotted in comparison with the original one, as shown in Fig. 4.20 (a). With pile-up taken into account, the real contact area should be $A=A_{O-P}+A_{pu}$ where A_{O-P} is the original contact area calculated by standard Oliver-Pharr method and A_{pu} is the sum of the projected areas of three pile-ups around the indentation

imprint edges. The variation of A_{pu} with respect to indentation depth in Fig. 4.20 (b) is similar to that of pile-up height presented previously. The new contact area is subsequently used to recalculate the hardness (indentation depth 500 nm). A decrease in hardness can be observed (Fig. 4.21 (a)). Here, the hardness is merely corrected with pile-up taken into account. However, edge effects were reported to affect the hardness by causing errors in both h_{max} and C_{meas} [255], as expressed by Eq. (4-4):

$$h_c = h_{max} - \varepsilon P_{max} C_{meas} \tag{4-4}$$

where ε is a geometric constant approximately equal to 0.75 for a Berkovich indenter [14], and h_c, h_{max}, P_{max} and C_{meas} are the contact depth, maximum depth, maximum load and measured compliance, respectively.

Jakes et al. [255] explained that the edge effects could also affect the contact area by causing errors in both h_{max} and C_{meas}. Even though the errors in C_{meas} and h_{max} tend to partly cancel each other, the latter term dominates. In order to understand whether the hardness is influenced by the edge effects, a series of indentation tests (with an indentation depth of 500 nm) was performed on a non-SMATed reference sample (all other experiment conditions were kept the same as those used for the SMATed one). It is important to note that the surface of a mechanical component could be unintentionally work-hardened during machining [260]. Zhou et al. used the Full width at half maximum (FWHM) evaluated by XRD to estimate the plastic deformation of a non-SMATed 316L stainless steel [260]. Their results show that the thickness of the work-hardened layer due to machining could be up to 170 μm in their case. To eliminate the influence of the work hardened layer, a periphery volume of 300 μm was removed by electrolytic polishing from the outer layer of the specimen. In this way, both the influence of pile-up and unintentionally work-hardened layer are eliminated. Hence, any possible variation of hardness measured in the near surface region is related to the edge effects. Our results revealed little difference in hardness between the region near the sample edge and the other locations in the sample (Fig. 4.21 (b)).This seems to indicate that the errors in C_{meas} and h_{max} cancel each other in our case of a SMATed 316L stainless steel with an indentation depth of 500 nm. As a result, only the pile-up formation was considered during the correction of hardness.

It should be stressed out that several methods exist to account for the true contact area in the case of pile-up [149], [152], [230], [256], but each method is restricted to a specific studied material or to a certain loading range. It is possible that our modified method might

not precisely correct the pile-up. It will therefore be interesting to find a method to more accurately correct pile-ups for SMATed materials in future work.

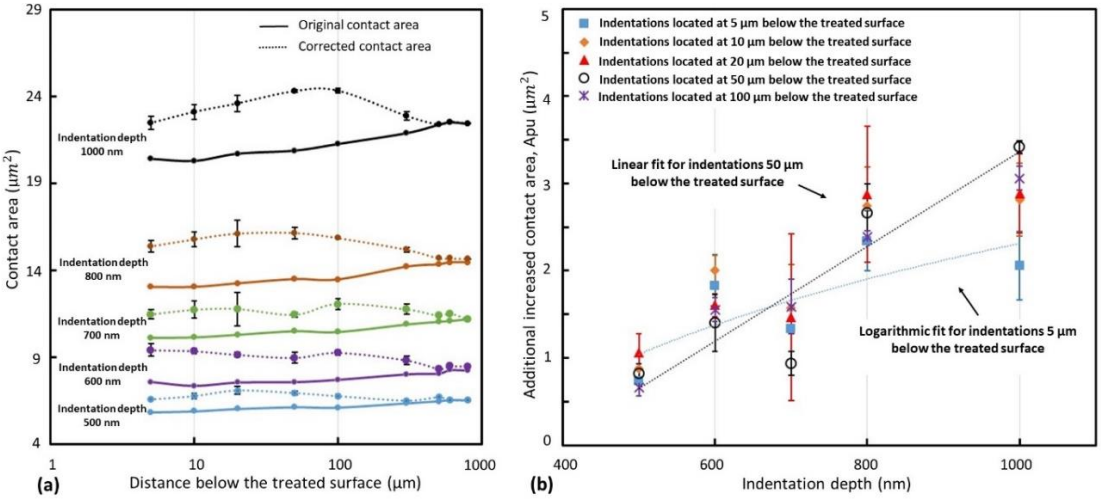

Fig. 4.20 (a) Comparison between original contact areas and corrected contact areas for indentations with different indentation depths, (b) Additional increased contact areas in the strongly-affected region plotted as a function of the indentation depth.

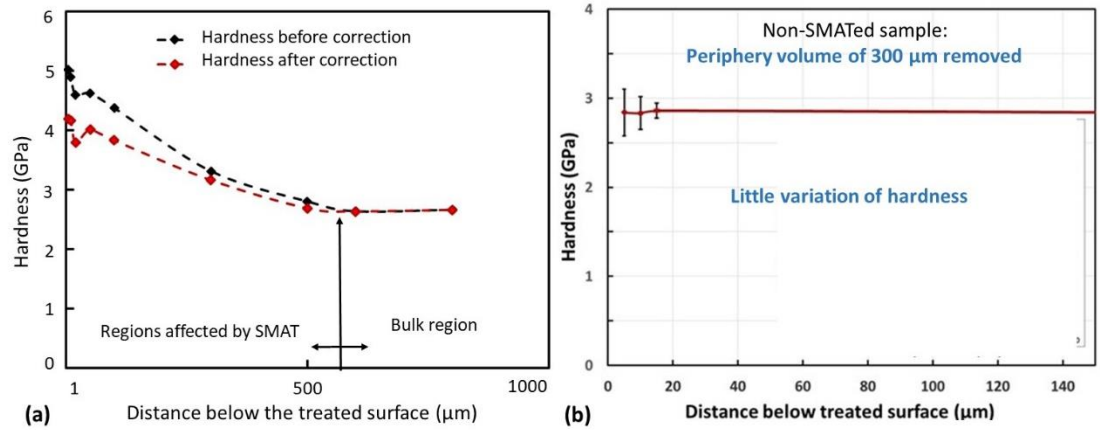

Fig. 4.21 (a) Corrected hardness compared to original hardness with a pile-up phenomenon taken into account. Note that for these indentation tests, the indentation depth is 500 nm, (b) Hardness measured along the cross-section of a non-SMATed sample with indentation depth of 500 nm.

4.5 Indentation size effect

It is well-known by now that the micro and nanoindentation hardness of metallic materials displays a strong size effect, which is commonly referred to as the indentation size effect (ISE). There are numerous indentation tests at scales on the order of a micron or a submicron have shown that the measured hardness increases significantly with decreasing the indentation size [144], [264]–[266]. This has been attributed to the evolution of the geometrically necessary dislocations (GNDs) at the vicinity of the indenter, which gives rise to strain gradients [144], [267], [268]. One expects a constant hardness value for a homogeneous material when applying the classical continuum plasticity theory, which failed to account for ISE for the reason that it does not take material length scale into consideration.

For materials with indentation size effect, the indentation hardness is observed to increase with decreasing indentation depth as a result of the nucleation of dislocations within the plastic zone [144]. Two types of dislocations are created, the statistically stored dislocation (SSD) and geometrically necessary dislocation (GND). The presence of dislocations will increase the effective yield strength and in turn results in an increase in hardness. Nix and Gao [144] proposed the calculation of the density of GND showing that ρ_g has a reciprocal relation with indentation depth, as illustrated in Eq. (2-17). The presence of GND can be linked to the existence of strain gradients generated in the vicinity of the indentation. In addition, in the case of small indentation depth, the strain gradient is relatively larger, leading to higher measured hardness.

The presence of GND and strain gradient are length scale effects that classical continuum plasticity theory failed to account for. In the literature, efforts have been dedicated to strain gradient plasticity theories in an attempt to explain ISE [144], [265], [269], [270]. The common practice of these theories is to incorporate an intrinsic material length scale in the constitutive equations. Nix et al. [144] proposed a model to accurately describe the indentation size effect for crystalline materials using the concept of GND. The depth dependence of hardness can be explained by the following equation

$$\frac{H}{H_0} = \sqrt{1 + \frac{h^*}{h}} \tag{4-1}$$

Where H is the measured hardness for a given depth of indentation h. H_0 is the hardness in the limit of infinite depth and h^* is a characteristic length that describes the ISE.

A higher value of h^* signifies a more pronounced ISE. H_0 and h^* can be calculated by the following equations:

$$H_0 = 3\sqrt{3}\alpha\mu b\sqrt{\rho_s} \tag{4-2}$$

$$h^* = \frac{81}{2} b\alpha^2 tan^2\theta \left(\frac{\mu}{H_0}\right)^2 \tag{4-3}$$

Where ρ_s is the density of statistically stored dislocations, μ is the shear modulus, b is the Burgers vector and α is a constant, θ is the angle between the surface of the indenter and the plane of the indented surface, H_0 is the hardness that would arise from the statistically stored dislocations alone, in the absence of any geometrically necessary dislocations. According to Eq. (4-1), if the square of the measured hardness, H^2, is plotted versus the inverse of indentation depth, h^{-1}, then, the values of H_0 and h^* can be obtained from the slope of the curve and the intercept with the axis. Nix [144] presented data for experiments on cold-worked polycrystalline copper and single crystal copper and this model was subsequently applied. The calculated values of H_0 and h^* and those obtained from experimental data were in reasonable agreement. The cold-worked copper has a higher value of H_0 and lower value for h^*, as compared to the non-cold-worked sample. A decrease of h^* signifies a less pronounced ISE. It is concluded that materials with smaller length scale value (h^*) are harder but exhibit lower ISE [144], [265], as is the effect introduced to copper by cold hardening. The model developed suggested that the hardness of a material should not depend strongly on the depth of indentation if the material is intrinsically hard (high value of H_0). Specifically, large values of H_0 would cause h^* to be very small according to Eq. (4-3) and this would cause the hardness to depend less strongly on depth at a given depth of indentation. Take fused quartz for example, whose hardness (about 9GPa) is essentially independent of depth of indentation. We are well aware that an improved method based on that of Nix has been proposed by Rashid [265]. But since the model of Nix seems to be well fitted with our experimental data, the method proposed by Rashid is out of our consideration.

In this project, indentations with varying indentation depths were performed for the regions located at 1000μm, 350μm and 5μm below the treated surface. The SMAT treatment intensity are zero, low and high respectively for the selected regions. The corresponding results of measured hardness are plotted in Fig. 4.22 (a), (b) and (c). It seems that the ISE is severe for the region located at 1000 μm below the treated surface where a

variation of about 25% can be detected between the hardness measured at small depth and larger depth (Fig. 4.22 (a)). While almost no ISE can be observed for the nanocrystalline region, as the hardness is almost constant as a function of indentation depth (Fig. 4.22(c)). ISE is intermediate for indentations performed in the regions located at 350μm below the treated surface (Fig. 2.22 (b)). To have a straightforward view of the ISE, the square of the measured hardness, H^2, should be plotted against the inverse of indentation depth, h^{-1}, as illustrated in Fig. 4.23 (a), (b) and (c). The intercepts and the slopes of the curves were exploited to calculate H_0 and h^*, which are indicated simultaneously in the figures. For the regions where the SMAT intensity is high and grain size refinement occurred (Fig. 4.23(c)), a high value of 4.86 GPa is found for H_0 and a small value of 24.91 nm is obtained for h^*. As mentioned earlier, h^* is a length scale parameter which describes the size effect behaviour. It can be inferred that the nanocrystalline region generated by SMAT is strongly independent of the imposed indentation depth owing to the extremely small h^*. On the other hand, for the regions non-affected by SMAT (Fig. 4.23 (a)), H_0 is small and h^* is calculated to be 129.54 nm, which is about five times larger than that observed in the nanocrystalline region. It seems that SMAT treatment strongly decreases ISE judging from this difference. It should be pointed out that even for the regions where SMAT intensity is low (Fig. 4.23 (b)), the value of h^* is merely 36.98nm, which is only slightly higher than that of the nanocrystalline region where the SMAT intensity is high. It can be concluded that even the material is only slightly cold hardened, the intrinsic hardness of the material, H_0, is increased subsequently, leading to a dramatic decrease of the length scale parameter, h^*.

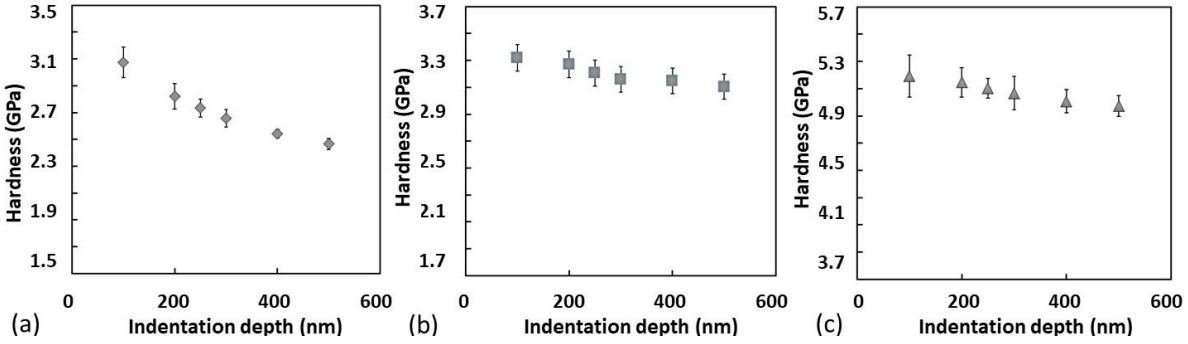

Fig. 4.22 Hardness measured with various indentation depths for regions located at (a) 1000μm below the treated surface, (b) 350μm below the treated surface and (c) 5μm below the treated surface.

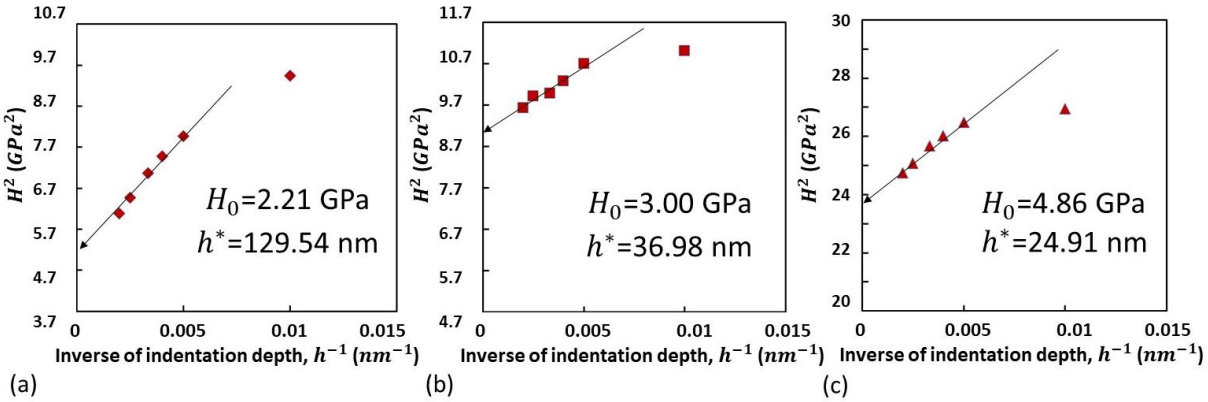

Fig. 4.23 Hardness measured with various indentation depths (H^2 vs h^{-1}) for regions located at (a) 1000µm below the treated surface, (b) 350µm below the treated surface and (c) 5µm below the treated surface.

4.6 Cyclic loading behaviour and edge effects

The fatigue/cyclic loading behaviour of nanocrystalline materials is of great interest in recent years. Numerous reports seem to reach an agreement that the fatigue life is enhanced for nanocrystalline metals by virtue of their higher yield stress [271]–[274]. It is concluded that the fatigue strength of materials increases with decreasing grain size and follows the Hall-Petch relationship in a similar way as the yield stress in conventional polycrystals. This enhancing effect is especially significant in the high cycle regime where the yield stress/ultimate strength has a major influence on the fatigue behaviour while both yield stress and ductility affect the fatigue performance in the low cycle fatigue regime [274]. It is also argued that small grain size can result in more homogeneous deformation, which can retard crack nucleation by reducing stress concentrations (which is the case for coarse-grained material) and ultimately raise the fatigue limit of the material [3].

However, there are exceptions, for instance, wavy slip materials like copper (pure FCC metal) do not exhibit a strong dependence of fatigue strength on grain size, despite a remarkable enhancement of their monotonic strength [275]–[277]. This might be explained in view of their lower ductility and poor resistance to macroscopic and microscopic plastic instabilities such as necking, shear banding, cracking, etc. Such behaviour is typical of metals with low levels of strain hardening [275]–[277]. In fact, the ductility of the metal is also a significant factor in the case of low cycle fatigue [278]. In this work, the studied material is a 316L stainless steel (FCC metal) treated by SMAT. A gradient microstrucutre is generated subsequently with a nanostructured layer on the treated surface of about 5 µm. Nanoindentation technique provides a great opportunity to perform cyclic loadings individually on each layer of the gradient microstructure in an attempt to investigate the

corresponding cyclic loading behaviour. A series of indentations were conducted at 5, 30, 70 and 300 μm below the treated surface with the cyclic loading methods described in Section 2.6.5 (constant P_{max} and linearly-increasing P_{max}). The results of indentations carried out using the cyclic loading method with a constant P_{max} show no difference compared to monotonic loading results in Section 4.2. Hence, the corresponding results (load-displacements curves etc.) are not presented here.

On the other hand, the cyclic loading tests with linearly-increasing P_{max} show a softening behaviour in the nanocrystalline layer while for other regions (30, 70 and 300 μm below the treated surface), the results show no difference, as compared to that in monotonic test in Section 4.2. The cyclic loading curves performed in the nanocrystalline region (indentation depth 1000 nm) is illustrated in Fig. 4.24 (a). An outlined zone in Fig. 4.24 (b) shows the nanocrystalline region where these indentations were performed. It can be seen that the maximum indentation load decreases with increasing number of cycles. The maximum load for indentation with 20 cycles decreases by about 30%, as compared to single step test. As discussed previously in Section 2.6.5, thermal drift could be large when the indentation test lasts for hours, which consequently affects the validity of the measured displacement. In our case, an indentation test of 20 cycles lasts about 30 min, the corresponding thermal drift rate measured is merely about 0.02 nm/s, which is below the allowable drift rate (0.05 nm/s). Therefore, the influence of thermal drift can be first eliminated.

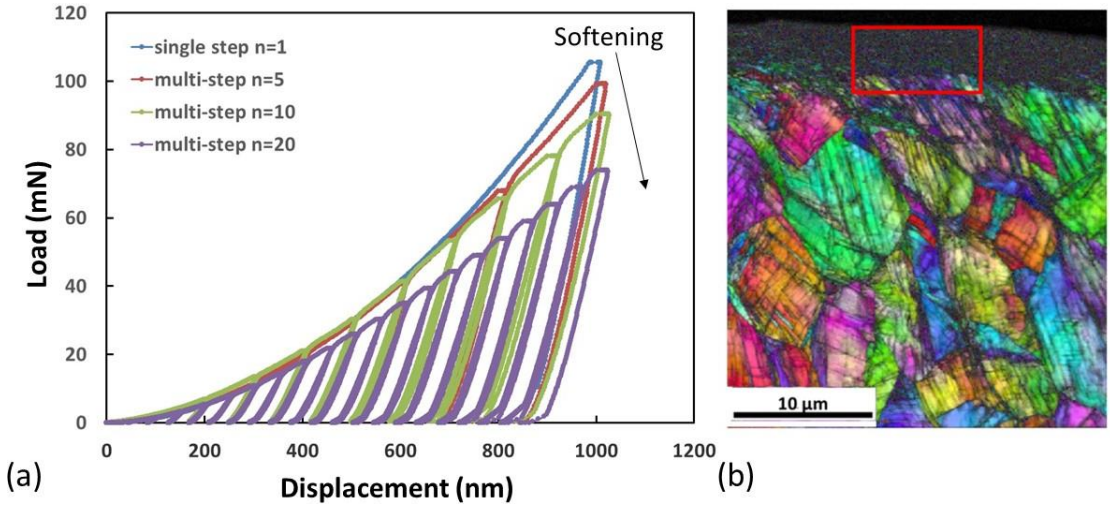

Fig. 4.24 (a) Cyclic load-displacement curves of indentations performed in the nanocrystalline region with a cyclic loading-unloading method described in Section 2.6.5 and (b) Inverse pole figure of EBSD observation with an outlined zone where the corresponding indentations were performed.

Efforts were made in an attempt to explain the cyclic softening behavior observed in our case. Unfortunately, there are little results reporting softening behavior of nanocrystalline materials in (nanoindentation) compression test. Although, typical wavy-slip materials such as copper and Al-alloys were reported to show significant degradation in strain-controlled cyclic properties as suggested by Pelloux et al. [275]–[277]. Their explanations to this degradation would not perfectly apply for our case because most of the fatigue/cyclic loading tests in the literature were either tension-tension or tension-compression while nanoindentation tests were purely compression. Hence, different loading conditions make the interpretations of our results difficult.

Another important factor that may be responsible for the softening observed in the nanocrystalline region is edge effect. As investigated in Section 4.3.3, edge effects resulted from insufficient distance to the sample edge could severely affect the indentation behavior [254], [255]. In the case of SMATed 316L stainless steel, the nanocrystalline region is also the sample edge areas. To figure out the influence of edge effects on cyclic loading behavior, a non-SMATed reference sample (the same one as discussed in Section 4.3.3) was prepared. All other conditions were kept the same as the SMATed one. The corresponding results were illustrated in Fig. 4.25. When the indentation depth is 500 nm, the monotonic curves and cyclic curve are overlapped and no difference could be noticed. Nevertheless, when the indentation depth is larger than 500 nm, the indentation load of the cyclic curve begins to fall behind compared to the monotonic curve, as demonstrated in Fig. 4.25 (b). This is due to the fact that larger indentation depth will shorten the distance of indentation impression to the sample edge, causing severe edge effects (decreased contact stiffness/decreased indentation load). As a conclusion, the softening observed previously in the nanocrystalline region is mainly due to edge effects rather than the mechanical properties of this region. Indeed, attention shall always be paid to edge effects as the nanostructured layer in SMATed materials is also the edge area of the sample.

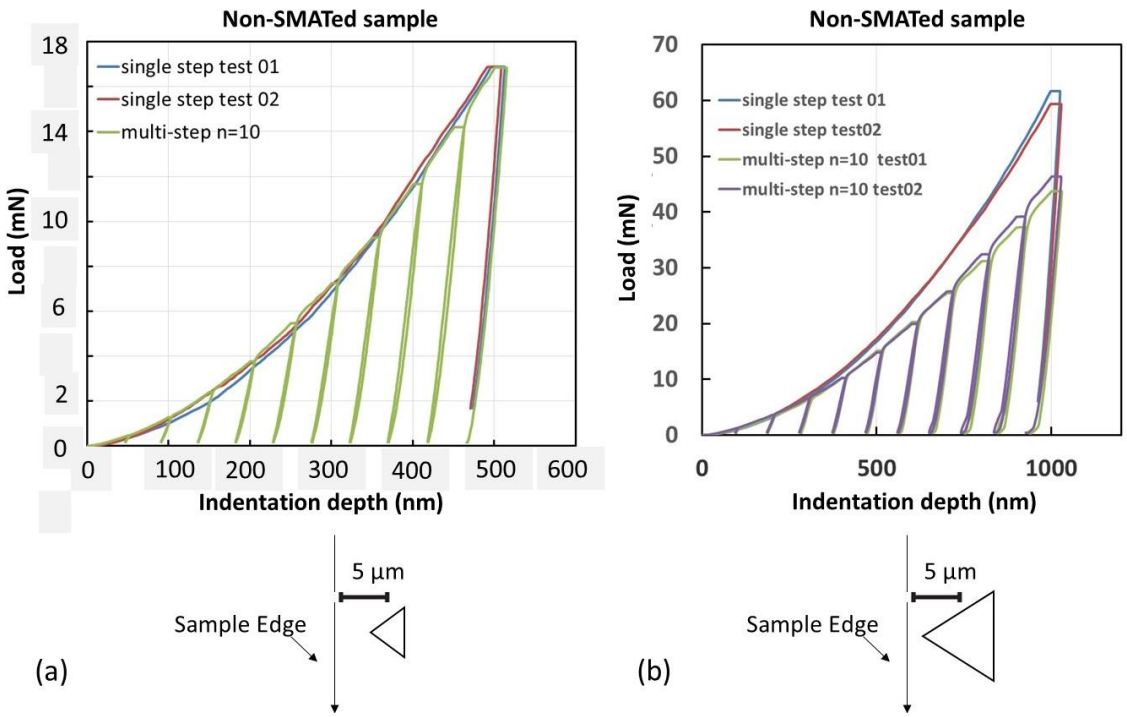

Fig. 4.25 Influence of edge effects on cyclic loading behavior. (a) Cyclic loading curve in comparison with monotonic loading ones (indentation depth 500 nm), (b) Cyclic loading curves in comparison with monotonic loading ones (indentation depth 1000 nm).

4.7 Conclusion

Three major changes induced by SMAT that will affect the nanoindentation measurements. The obtained results (load-displacement curves, Young's modulus, hardness indentation size effect and pile-up behavior) are interpreted subsequently in terms of these SMAT induced changes along the cross-section of the SMATed sample. Several conclusions could be made as follows:

1) Grain refinement is the major factor that contributes to higher indentation load/hardness and compressive residual stress plays a relatively minor role.
2) As the nanocrystalline region is also the sample edge areas in the case of SMATed 316L stainless steel, the influence of edge effects should be considered during the interpretation of nanoindentation measurements. Edge effects were found to affect the contact stiffness, Young's modulus and cyclic loading behavior in the nanocrystalline region.
3) The measured hardness and Young's modulus seem to be independent of compressive residual stress.

4) Pile-up occurred in the SMAT-affected region as a result of decreasing strain hardening exponent. Pile-up should be taken into account in order to correct the true contact area. The recalculated hardness with corrected new contact area was found to slightly decrease.

Chapter 5: Characterization of SMATed material by micro-pillar compression

Micro-pillar compression test is emerging as a novel way to measure mechanical properties of materials at small scale. In the present work, the studied material is a SMATed 316L stainless steel with a gradient microstructure generated by SMAT. This gradient structure can be roughly divided into core material region, transition region and nanocrystalline layer. The beneficial effects owing to this gradient microstructure have been investigated in previous studies performed within our laboratory [13], [37], [211], [212], [228], [279]. Nevertheless, emphasis was placed on the global properties of the whole gradient microstructure and few efforts were dedicated to investigate the individual properties of each layer. For instance, Zhou et al. [228] investigated the influence of SMAT on fatigue behaviour of this 316L stainless steel. It is concluded that the gradient microstructure enhanced the fatigue resistance of the treated material. The beneficial effects of the gradient microstructure were also found in improving the tensile strength of SMATed 316L stainless steel [37]. On the other hand, Petit et al. [234] proposed a macroscopic multilayer model to describe the mechanical properties of each layer of the gradient microstructure generated by SMAT. Compared to the model of Petit et al., micro-pillar compression provides a more straightforward method for the characterization of each layer at micro scale. In Chapter 3, it is indicated according to the EBSD observations that the thickness of the nanocrystalline layer induced by SMAT is only about 5μm.

Compressing micro-pillars fabricated in this layer gives direct access to the local mechanical properties of the nanostructured material generated by SMAT.

In this chapter, micro-pillar compression technique is applied for the characterization of each characteristic layer of the gradient microstructure generated by SMAT. Several geometrical factors (Fig. 5.1) affecting the compression test are first investigated using Finite Element Model with the code Abaqus (version 6.12). For this purpose, a macroscopic constitutive law ($\sigma = 290 + 1255\varepsilon_p^{0.733}$) derived from the multilayer model for a SMATed material proposed by Petit et al. [234] is used to perform the analysis. The results of the simulations are interpreted along with the experimental observations to better understand the eventual problems encountered during the compression tests. Finally, the results of the micro-pillar compression tests were presented, followed by a detailed discussion.

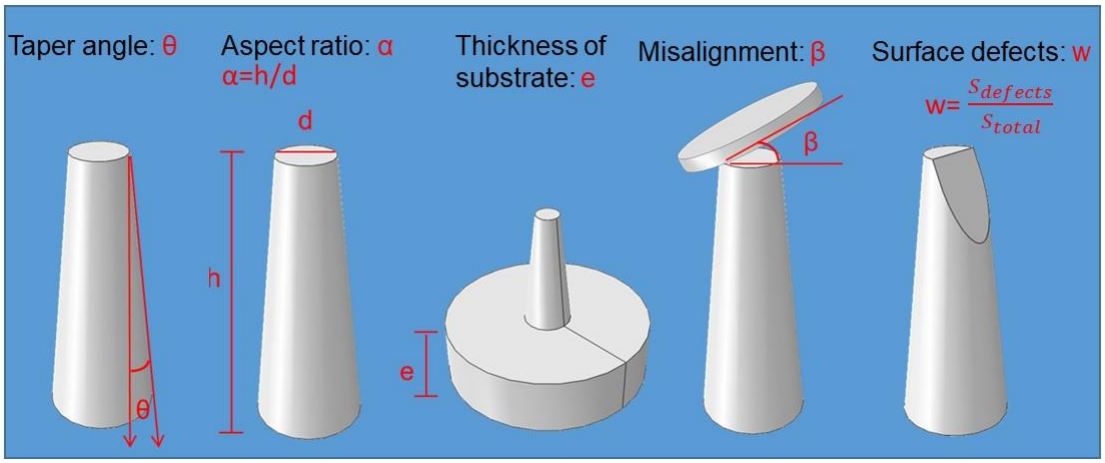

Fig. 5.1 Illustration of the geometrical factors which can affect micro-pillar compression tests.

5.1 Misalignment

Misalignment between flat indenter and micro-pillar could cause deviation from reliable results during compression tests. It could either arise from the bad positioning of the indenter or an inclined sample surface. Several simulations with the misalignment parameter, β, varying from 0° to 20° were conducted to investigate its influence. The corresponding results were shown in Fig. 5.2. It is demonstrated that the misalignment affects the recorded force in both the elastic and the plastic regime, leading to a global decrease of the recorded force during compression test, as compared to the case of perfect alignment β=0°. Moreover, even for a small misalignment of 5°, the recorded force in the elastic regime is noticeably influenced (with the presence of a smaller slope) while the plastic regime is only slightly affected (with the same slope but slightly lower force). Fig.

5.2 (b) illustrates the equivalent plastic strain fields for pillars with misalignments of 0° and 20° respectively. It can be seen that a severe misalignment results in localized deformation on the top side and buckling of the pillar. During the compression tests, it seems that pre-mature failures of pillars due to misalignment occurred. An example is given in Fig. 5.3 (a) showing the buckling of a pillar probably due to a bad misalignment. To resolve this problem, a correction device, shown in Fig. 5.3 (b), was used, which allows to delicately adjust the sample surface with respect to the flat indenter via the two screws illustrated in Fig. 5.3 (b). The correction of misalignment is usually performed locally (right next to the to-be-indented area) whereby an optimized correction can be attained.

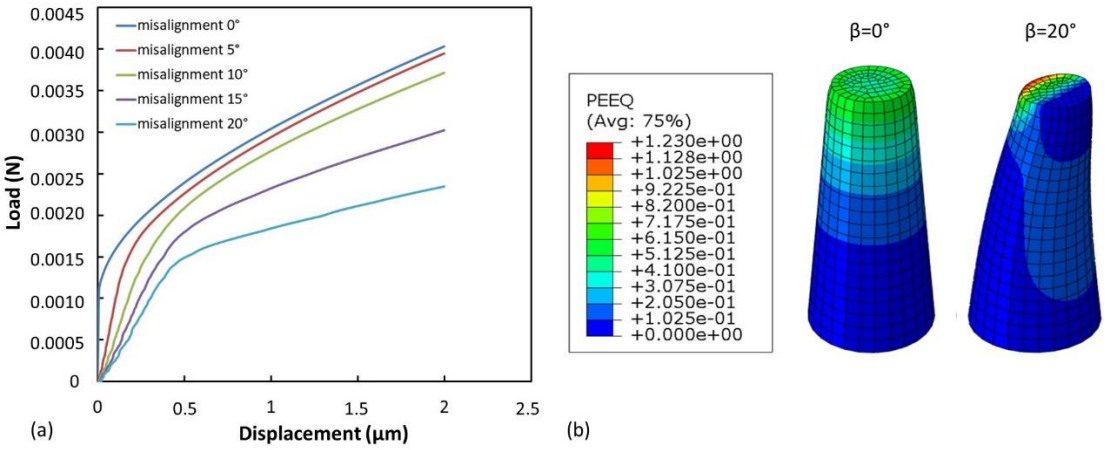

Fig. 5.2 Simulations with different misalignment values: (a) Corresponding force-displacement curves and (b) Equivalent plastic strain fields for pillars with misalignments of 0° and 20° respectively.

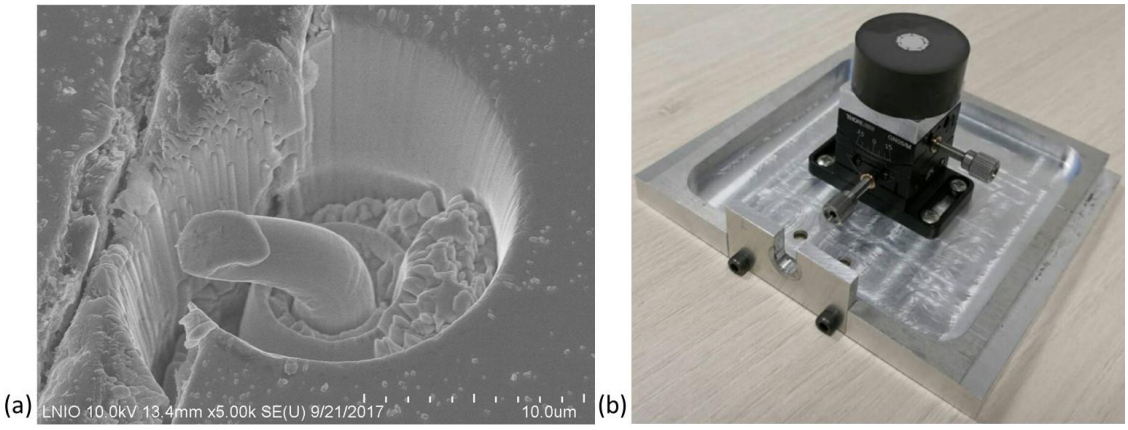

Fig. 5.3 (a) Pre-mature failure of micro-pillar due to misalignment, (b) Device for correcting the misalignment between the sample surface and the surface of the flat indenter.

Misalignment could arise due to bad positioning of indenter or inclined sample surface. For a diamond flat indenter fixed in the indentation system, it is reasonable to assume that the flat indenter is well placed and it is less likely that misalignment is caused by the indenter. One possible explanation would be that the misalignment is induced as a

consequence of an inclined sample surface. This can be confirmed by AFM measurements performed on the surface of our sample, as shown in Fig. 5.4. It turns out that when the sample was exposed to mechanical polishing (described in Section 3.2.2), the sample edge area is more vulnerable and more material was removed during the polishing procedure. As a consequence, the sample surface is inclined with a height variation of 1.5 μm ranging from the edge area to the interior of the sample, according to the AFM measurements. It should be stressed out that the polishing procedure usually lasts several hours or even days in order to have a mirror-like finish. Exposure to mechanical polishing during a long period of time may result in a significantly inclined sample surface, as is observed in our case.

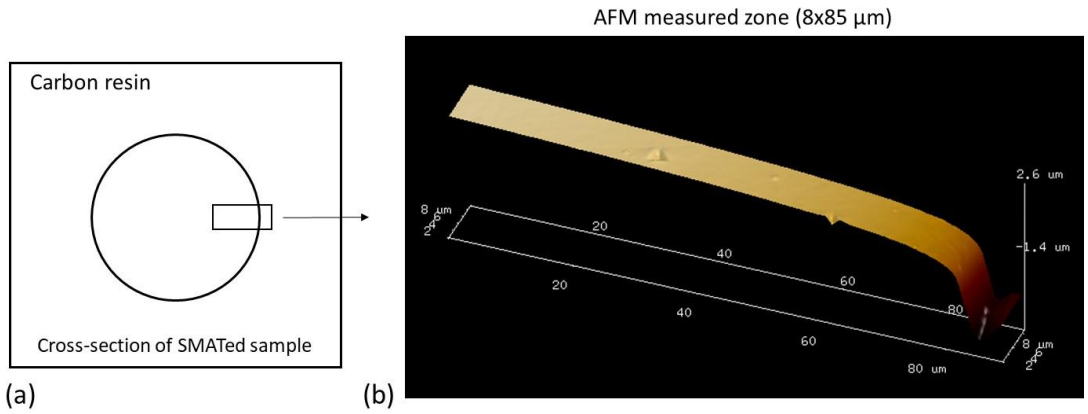

Fig. 5.4 (a) Illustration of the cross-section of the SMATed sample. Outlined area indicates the AFM measured area ranging from the sample edge to the interior of the sample, (b) Corresponding AFM 3D profile of the measured area.

5.2 Geometry of micro-pillar

Several geometrical factors (taper angle, aspect ratio, thickness of substrate and surface defects) affecting micro-pillar compression were individually varied for a series of simulation for the purpose of understanding their influences. According to the obtained results, the influences of aspect ratio and thickness of substrate were negligible. Hence, the corresponding force-displacement curves, stress fields and strain fields were not presented in this work. As for surface defect, its influence is similar to that of misalignment leading to a global decrease of recorded force, but with a less significant consequence. Since the influence of surface defects is relatively small, the corresponding simulation results were not presented in this work either. In fact, our initially-fabricated micro-pillars were poorly milled with severe surface defects shown in Fig. 5.5 (a). A new fabrication procedure with

three milling steps were adopted in order to obtain smooth surface for the micro-pillars. Firstly, a rough cut around the micro-pillar was made with a high current intensity of 21nA. Then, the micro-pillar was shaped using an intermediate probe current of 0.8nA. Finally, the surface of the micro-pillar was “polished” with the same current intensity in order to obtain a smooth lateral surface. An example of a micro-pillar with smooth surface is illustrated in Fig. 5.5 (b).

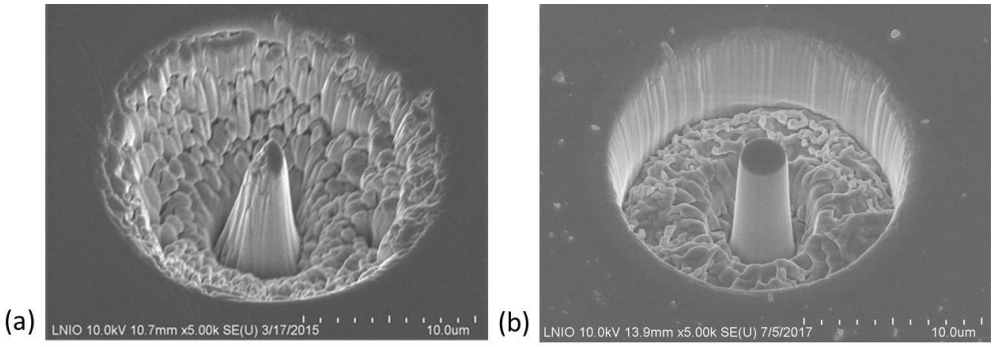

Fig. 5.5 (a) Former micro-pillar with poor surface quality, (b) Better surface quality obtained owing to new fabrication procedure.

Among the investigated geometrical factors, taper angle is the most important one that severely affects the micro-pillar compression results. A series of simulations with different taper angles ranging from 0° to 11.3° was conducted. It should be mentioned here that the average diameter of each pillar was set to be the same (Fig. 5.6). The results of the simulation are illustrated in Fig. 5.7 and Fig. 5.8. According to the load-displacement curves, taper angle has a significant influence on the plastic regime of the recorded force. With increasing the taper angle, a dramatic drop in the recorded force can be observed, along with a decrease of the slope of the curves. The decrease of the slope signifies a poor resistance to plastic deformation as a result of large taper angle. This can be confirmed by the corresponding strain fields illustrated in Fig. 5.8. When the taper angle is 0°, the strain field is homogeneously distributed along the pillar. As the taper angle increases, the strain fields become more and more inhomogeneous as a consequence of localisation of deformation in the upper area of the pillar. For instance, the localisation of deformation in the upper area is severe for the pillar with a taper angle of 11.3° while for the rest part of the pillar, almost no plastic deformation can be observed. It can be concluded that taper angle has a major influence on micro-pillar compression. According to the load-displacement curves, the influence of taper angle is relatively small when its value is less than 2.8°, as compared to a perfect cylinder (taper angle 0°). As a matter of fact, it is

suggested that the taper angle needs to be inferior to 3°, which is crucial to obtain a reliable stress-strain curve according to previous work presented in the literature [187]. Ideally speaking, the taper angle should be 0° (a perfect cylinder) but in practice this is difficult to achieve due to the restrictions of FIB. Therefore, a sufficiently small taper angle is recommended in order to minimize its influence. In this work, the initially-fabricated pillars have a taper angle of 5.7° which is evidently too large according to the results of the simulations. For this reason, the taper angle of our lately-fabricated micro-pillars is about 2°. The upper and the lower diameters are respectively 2.5 and 3.5 μm, and the height is 10 μm. A comparison was demonstrated in Fig. 5.9 between initially-fabricated pillar (taper angle 5.7°) and newly-fabricated pillar (taper angle 2°).

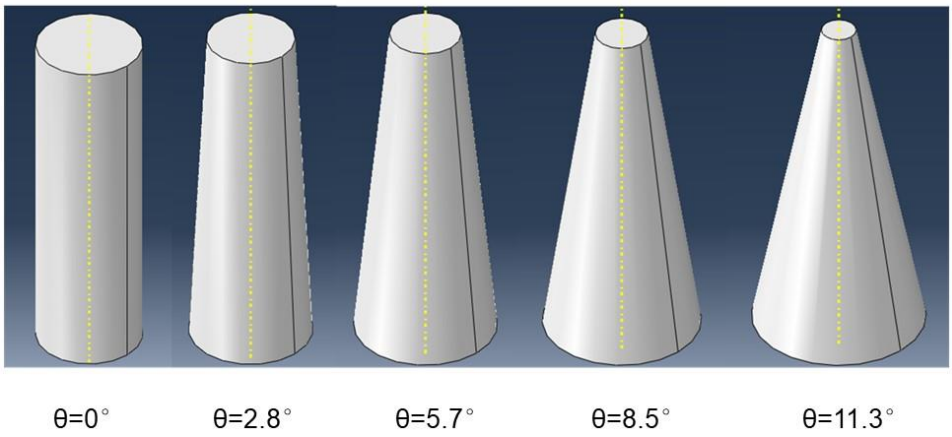

Fig. 5.6 A series of simulations with different taper angles ranging from 0° to 11.3°. The average diameter of each pillar was set to be the same.

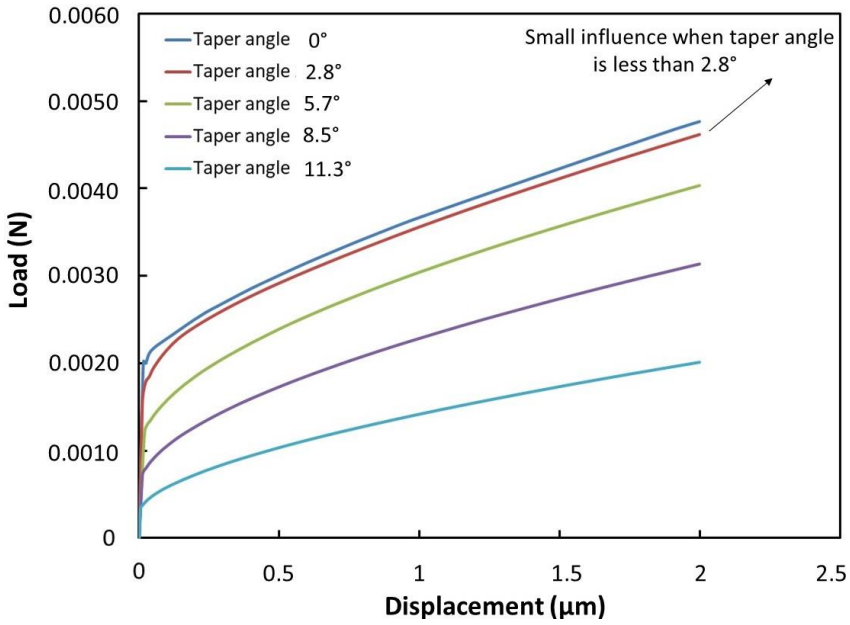

Fig. 5.7 Force-displacement curves for micro-pillars with taper angles ranging from 0° to 11.3°.

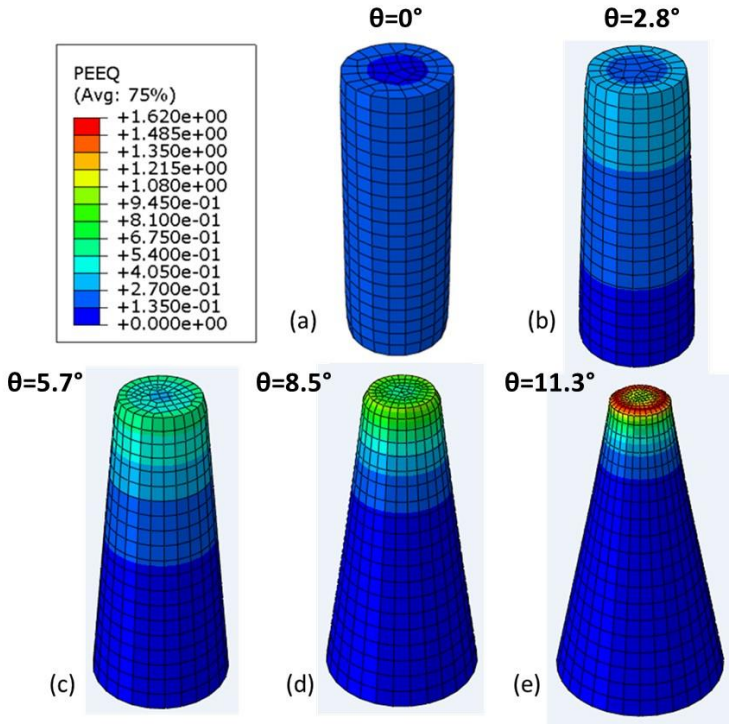

Fig. 5.8 Strain fields of micro-pillars with different taper angles: (a) θ=0°, (b) θ=2.8°, (c) θ=5.7°, (d) θ=8.5° and (e) θ=11.3°

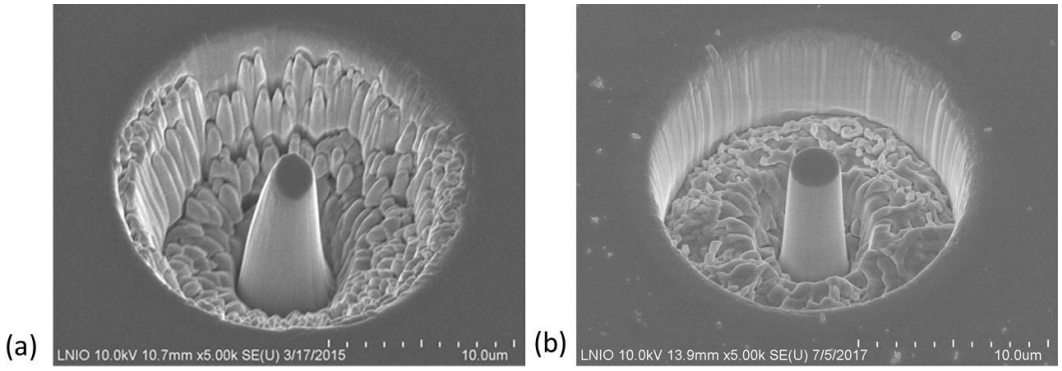

Fig. 5.9 (a) Initial micro-pillar with taper angle θ=5.71°, (b) Improved micro-pillar with taper angle=2°.

5.3 Other influencing factors

Besides the aforementioned geometrical factors of the micro-pillar such as misalignment and taper angle, there exists several other factors that might affect the micro-pillar compression tests. In this section, the influences of FIB milling, residual stress and indenter state are briefly discussed.

5.3.1 Influence of FIB milling

As discussed in Section 2.5, FIB which enables the milling of micro-pillars is destructive to the sample. On the other hand, the gallium atoms will also be implanted into a depth of few nanometers beneath the outer surface, which can be considered as contamination or damage [188]. This contamination by the implantation of gallium ions at the top surface of the sample can lead to the modification of local structure, for instance, by rendering the local structure amorphous [135], [136]. The affected zone is estimated to be in the range of about tens of nanometers [188], [280], [281]. When the size of micro-pillar/nano-pillar is comparable to that of the zone affected by gallium ions, FIB-induced artifacts and contaminations cannot be neglected. An example is given in Fig. 5.10 showing a molybdenum nano-pillar studied by Lowry et al. [188]. In addition, Xiao et al. [282] studied the mechanical properties of single crystalline and ultrafine-grained aluminum micro-pillars (aspect ratio 3 and diameter 7 μm) made using Xe and Ga ion beam machining. Exposure to FIB in their case is at least 2 hours. It turned out that the mechanical properties of coarse-grained micro-pillars were less sensitive to FIB and only slight change can be detected while FIB milling with Ga ions appears to reduce the mechanical strength (tens of MPa) of ultrafine-grained micro-pillar. According to these work, this phenomenon is attributed to the segregation of Ga at grain boundaries, which is similar to the liquid metal embrittlement effect. As a consequence, the Ga ions appear to weaken the grain boundaries and promote their motion or sliding [282].

Based on the elements mentioned above, it is acceptable to assume that the FIB milling with Ga^+ has relatively small effects on our micro-pillar compression tests for the following reasons. First, the size of our micro-pillars is about 2.5 μm in diameter and 10 μm in height. The thickness of Ga^+ implanted layer is estimated to be tens of nanometers [188] which is relatively small compared to the size of our micro-pillars. Second, the material studied by Xiao et al. is aluminum [282]. Although the segregation of Ga^+ at the grain boundaries weakened the Al-Al atomic bonds (Ga-Ga atomic bonds are also weaken), Fe-Fe atomic bonds are much stronger than aluminum, hence, less sensitive to Ga^+ influence. Even in the case of ultrafine-grained aluminum micro-pillar, the yield strength was found to decease by only tens of MPa due to segregation of Ga^+ while the yield strength of our micro-pillar in the nanostructured region is about 1500 MPa, which is evidently not in the same magnitude. It should also be noted that the time of exposure to FIB in the case of Xiao et al. is at least 2 hours, while the time duration is about 20 minutes in our case.

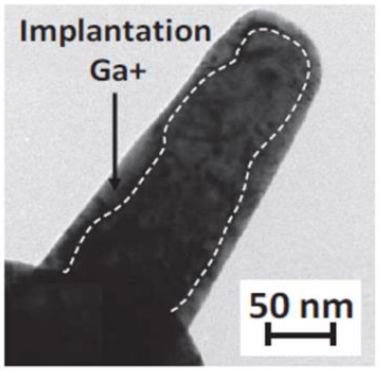

Fig. 5.10 Implantation of Ga^+ in molybdenum nano-pillars [188].

5.3.2 Influence of residual stress generated by SMAT

Residual stress fields can be classified according to characteristic length scales $l_{0,I}$, $l_{0,II}$, and $l_{0,III}$ over which they self-equilibrate (macroscopic scale, inter-granular scale or atomic scale) [226], [227]. The residual stresses generated by SMAT are of Type I (macroscopic scale) because the misfit regions span microscopic or submicroscopic dimensions. The influence of the compressive residual stresses generated by SMAT on micro-pillar compression tests is considered negligible in our case for the following reasons. Firstly, residual stresses originate from misfits between different regions. During milling of micro-pillars in the SMAT-affected regions of our sample, the removal of the surrounding material next to the pillar leads to rapid relaxation of the elastic mismatch whereby a great amount of residual stress is released. Secondly, even if there remains a small amount of residual stresses in the micro-pillar, its influence is still quite small. Indeed, it is concluded that the beneficial effects of the residual stresses are pronounced when the applied external load does not exceed the yield stress of the material (for example, high cycle fatigue). When the imposed load exceeds the yield strength, residual stress has small effects because the elastic/plastic misfit strains are small and therefore are soon washed out by plasticity [226], [227].

In addition, it will be rather difficult to measure the possible remained residual stress within the micro-pillar given its small dimensions (a few micrometers). Most of the available techniques (either destructive or non-destructive) for measuring residual stresses are restricted to their capacity of sampling volume [226], [227]. It is useful to consider the characteristic volume, $V_0 = l_0^3$, where V_0 is the sampling volume and l_0 is the length scale of the residual stress over which a given type of stress averages to zero. If the measured

sampling volume is greater than V_0, then the stress will not be recorded, since it averages to zero over that length scale [226], [227]. Table 7 shows a summary of several commonly available techniques for the measurement of residual stress.

Table 7 Summary of various measurement techniques for residual stress [226]

Method	Penetration	Spatial resolution
Hole drilling	~1.2 x hole diameter	50 μm depth
Curvature	0.1 to 0.5 of thickness	0.05 of thickness; no lateral resolution
X-ray diffraction	<50 μm (Al), <5 μm (Ti) < 1 mm (with layer removal)	1 mm laterally, 20 μm depth
Hard X-rays	150 to 50 mm (Al)	20 μm lateral to incident beam 1 mm parallel to beam
Neutrons	200 mm (Al)	500 μm
Ultrosonics	>10 cm	5 mm

5.3.3 State of flat indenter

The diamond indenters in a nanoindentation system may be damaged or contaminated after a long period in service. To examine the state of our flat indenter, SEM observations were performed accordingly. The results are illustrated in Fig. 5.11. It can be observed that the surface of the indenter is severely contaminated, especially the lower surface that is brought in contact with the micro-pillar during compression test. This results in poor surface roughness, which will lead to higher friction coefficient than smooth surfaces. A series of simulations with the previously described finite element model was conducted with friction coefficient varying from 0 to 0.5. No difference could be noticed according to the corresponding results obtained with different values of friction coefficient. Hence, the load-displacement curves, and the stress and strain fields are not presented here. In addition, an attempt was made to remove the contaminated layer by ultrasonic cleaner for tens of minutes. However, it did not work out. Despite of the observed contaminations, the flat indenter is in good shape in general and no severe damages can be detected. Therefore, it is convincing to assume that micro-pillar tests conducted with this indenter are reliable.

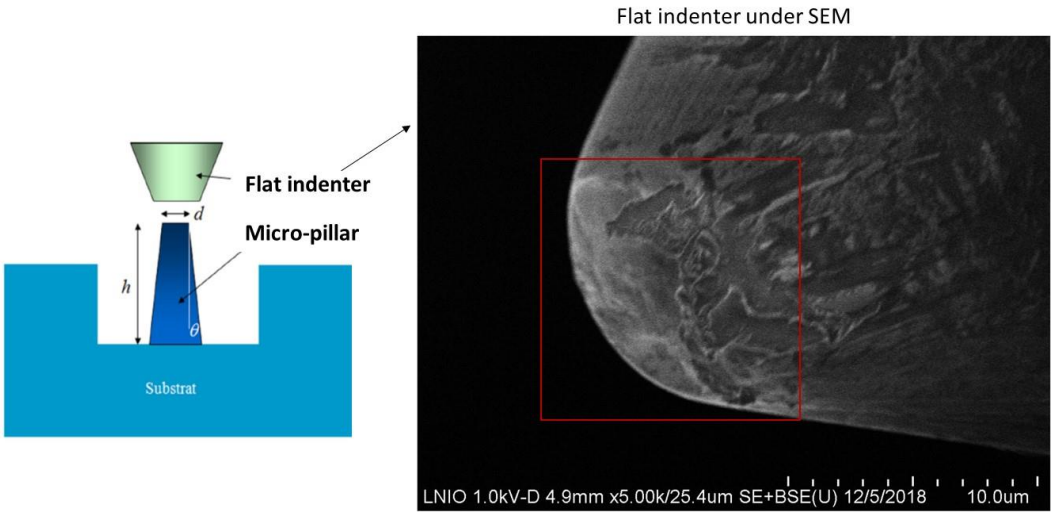

Fig. 5.11 Flat indenter under SEM. The outlined area indicates the lower surface of the indenter which is brought in contact with the micro-pillar during compression tests.

5.4 Micro-pillar compression tests

5.4.1 Fabrication of micro-pillars

In Chapter 3, the gradient microstructure generated by SMAT was highlighted by EBSD. The nanocrystalline layer, the transition region and the core material region could be distinguished. Therefore, four depths were selected as sites for the fabrication of micro-pillars, namely 5, 30, 70, 300 μm below the treated surfaces, as illustrated in Fig. 5.12 (a). The micro-pillars were milled using a FIB operating with a gallium Liquid Metal Ion Source. The milling process includes three steps. First, a rough cut around the micro-pillar was made with a high current of 21nA. Then, the micro-pillar was shaped using an intermediate probe current of 0.8nA. Finally, the surface of the micro-pillar was polished with the same current in order to obtain a smooth lateral surface. The obtained micro-pillars have a truncated cone shape. The upper and the lower diameters are respectively 2.5 and 3.5μm, and the height is 10μm. Their taper angle (the angle between the axis and the conical circumferential surface) is about 2°. It should be specified here that the taper angle needs to be inferior to 3°, which is crucial to obtain a reliable stress-strain curve according to previous work presented in the literature [187]. An example of micro-pillar is presented in Fig. 5.12 (b) which shows a sufficiently small taper angle as well as rather satisfying surface state.

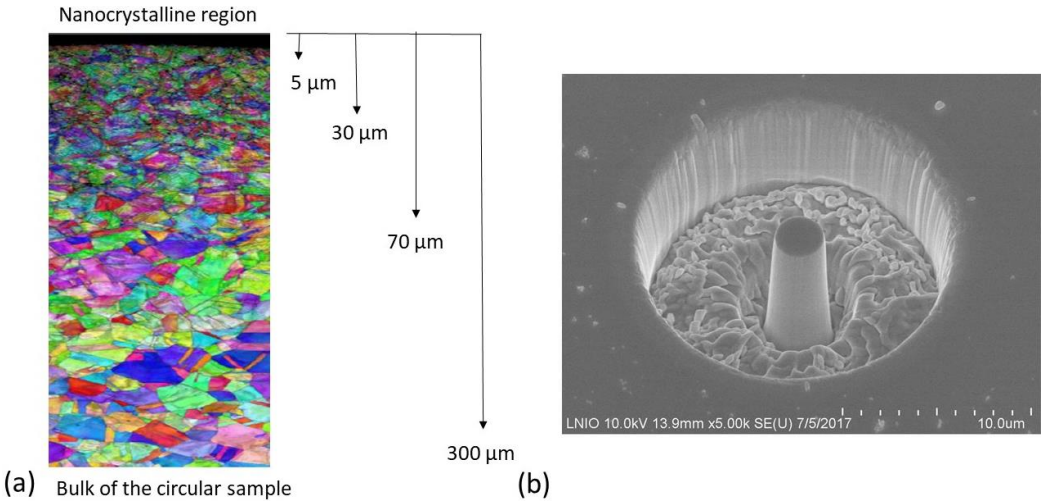

Fig. 5.12 (a) Selected regions for the fabrication of micro-pillars, (b) An example of lately-fabricated micro-pillar.

5.4.2 Monotonic compression of micro-pillar

As the micro-pillars described in Section 5.4.1 were fabricated in different selected regions of the gradient microstructure, the corresponding mechanical properties of these micro-pillars get to represent the mechanical properties of a specific region, for example, the nanocrystalline layer. Compared to nanoindentation tests in Chapter 4, micro-pillar compression tests have an obvious advantage of a relatively uniform stress/strain field. This allows to derive the stress-strain curves in a straightforward manner. The force-displacement curves could be subsequently exploited to calculate the stress-strain curves. It should be specified here that the measured force divided by the average surface of the micro-pillar was used for the stress calculation. In regard to the calculation of strain, Sneddon criterion [155] was used to calculate the displacement of the upper surface purely due to micro-pillar deformation. In this criterion, the elastic deformation of the substrate below the micro-pillar and that of the diamond indenter were subtracted from the displacement measured by the instrument. With this criterion, the real displacement of the upper surface of micro-pillar, d_p, is given by the equation as follows:

$$d_{pillar} = d_{meas} - \frac{(1-\nu_i^2)}{E_i}\frac{F_{meas}}{D_{top}} - \frac{(1-\nu_b^2)}{E_b}\frac{F_{meas}}{D_{bottom}} \tag{5-1}$$

where d_{meas} and F_{meas} represent the displacement of the micro-pillar surface and the force measured by the nanoindenter respectively. E_i, E_b, ν_i and ν_b are respectively the Young's

moduli and Poisson's ratios of the diamond indenter (1141 GPa and 0.07) and the substrate of the micro-pillars. Finally, D_{top} and D_{bottom} represent the upper and the lower diameter of each micro-pillar respectively. Knowing the real displacement of the upper surface of micro-pillar, the strain can be calculated by dividing it by the initial length of each micro-pillar.

The stress-strain curves of the monotonic compression tests are subsequently obtained by the aforementioned calculation method. The results are plotted in Fig. 5.13. It can be seen that for most of the stress-strain curves, an initial non-linearity occurred when the head of the diamond indenter was brought in contact with the upper surface of each micro-pillar. According to the results shown in Section 5.1, this is probably due to the misalignment between the indenter and the upper surface of the micro-pillar. Simulation results with different misalignment values suggested that even with a small misalignment of 5°, the elastic regime (the slope of the curve) is clearly affected, leading to non-linearity in the elastic regime and a certain amount of decrease on the recorded force/calculated stress. As the displacement of the indenter proceeds, the indenter was fully in contact with the upper surface of the pillar. Hence, the stress begins to increase linearly with the deformation, which corresponds to the elastic deformation range of the material.

When the displacement of indenter continues, the micro-pillars begin to deform plastically. The yield stress of each pillar could be derived directly from the stress-strain curves. As is observed, the yield strength of micro-pillar in the nanocrystalline layer is about 1450 MPa, which is about 2.5 times higher than that (580 MPa) of micro-pillar in the bulk interior of the sample (300 μm below the treated surface). It has been already concluded in Chapter 4 that for the nanocrystalline layer where the SMAT intensity is high, grain refinement effect is the major contribution to higher hardness/yield strength, as suggested by Hall-Petch law. In regard to the compressive residual stresses generated by SMAT, its influence on the yield strength of micro-pillar is negligible as concluded in Section 5.3.2. Micro-pillar milled in the nanocrystalline layer is composed of nano-grains and submicron grains with grain sizes ranging from 50 to 300 nm. With grain size at this range, dislocation activities are prevented as a result of large volume fraction of grain boundaries which in turn enhance the strength of the material [2], [52], [57], [69], [71], [130]. Similar results have been found by Tumbajoy-Spinel et al. who studied that the gradient structure generated by impact-based surface treatments [283]. A schematic representation summarizing the different involved mechanical effect contributions is given in Fig. 5.14 [283]. Hence, the following conclusions could be drawn:

1) The yield stress for micro-pillar in the nanocrystalline region (high SMAT intensity) is about 2.5 times higher than that of micro-pillar in the non-affected region.
2) Grain refinement effect is the predominant factor that contributes to higher yield strength for micro-pillars located at regions strongly-affected by SMAT.
3) In the regions where SMAT intensity is low and no grain refinement occurred, dislocation hardening is the main strengthening mechanism.

Besides the difference in yield strength, the work hardening behavior of the micro-pillars are of our interest. In the literature, it is believed that nanocrystalline materials possess an improved yield stress but relatively low level (or absence) of strain hardening, compared to their coarse-grained counterparts [3], [7]. This is consistent with our results. The strain hardening for micro-pillars in the strongly-affected region (5 and 30 μm below the treated surface) is low as a consequence of small grain size. For micro-pillars located at 70 μm below the treated surface, a relatively high strain hardening is noticed, which is attributed to larger grain size in this area. As for the coarse-grained region (300 μm below the treated surface), a high strain hardening exponent is expected [234] as the microstructure and mechanical properties here are only slightly affected by SMAT. On the contrary, a small strain hardening behavior is observed. It should be specified that the grain size in this region ranges from 10 to 50 μm while the size of micro-pillar is merely a few μm. It is, therefore, possible that the micro-pillar was fabricated on a single grain and that the micro-pillar is monocrystalline accordingly. Once loaded, the monocrystalline micro-pillar would plastically deform more easily in a preferential direction, depending on the grain orientation. Thus, the low (or absence) strain hardening of the stress-strain curve in the coarse-grained region does not represent the hardening behavior of this region. The different mechanical behaviors observed for micro-pillars located at different regions result from their corresponding deformation mechanisms. In the following Section, SEM observations were performed to investigate the deformed states of micro-pillars after compression. The corresponding results were interpreted in terms of their deformation mechanisms.

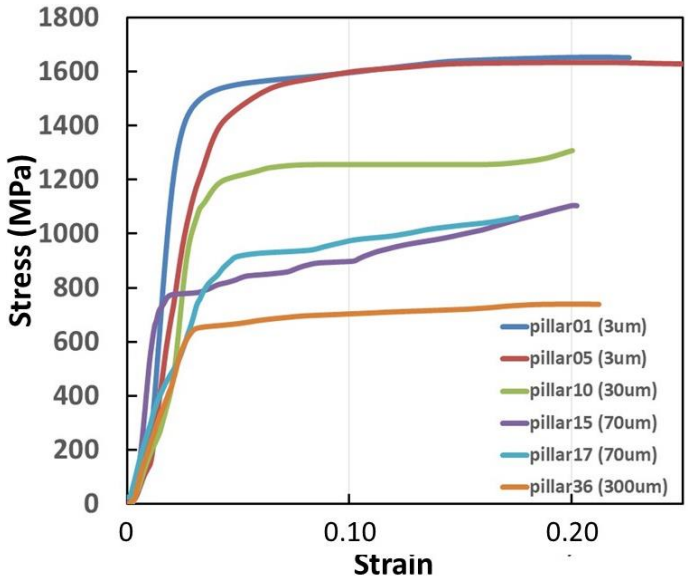

Fig. 5.13 Stress-strain curves of micro-pillars fabricated at different selected regions on the cross-section of the SMATed sample.

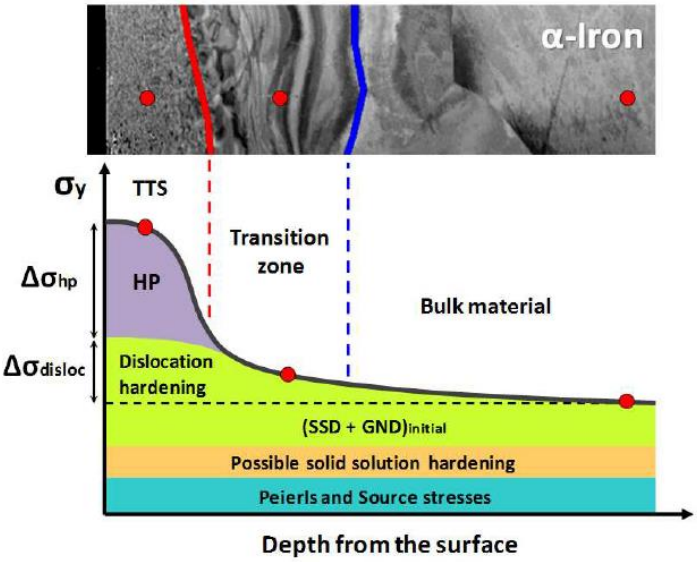

Fig. 5.14 Schematic representation summarizing the different mechanical effect contributions involved in the strengthening of ferritic steels by means of impact-based surface treatments [283].

5.4.3 Deformed states of micro-pillar

It is believed that the strengthening of the nanocrystalline materials is at the expense of their ductility. This is manifested by low value of elongation to failure in tensile test. The amount of strain that nanocrystalline materials can undergo before failure when subjected to tension loading is significantly smaller than their coarse-grained counterparts [3], [7], [48], [49], [271]. In the case of compression test, nanocrystalline materials exhibit low strain hardening behavior, as is observed in Section 5.4.2. Low strain hardening behavior is attributed to the increase in volume fraction of grain boundaries with the decrease of grain

size [3], [7], [71]. The increased amount of grain boundaries act as obstacles for dislocation motions. Thus, higher resistance to dislocation motion leads to localization of deformation, which is the case for micro-pillar located in the nanocrystalline region, as illustrated in Fig. 5. 15 (a). It can be noticed that the deformation is confined in the upper area of the micro-pillar and that no plastic slips can be detected. The deformation seems to occur in a homogenous way. As a matter of fact, when grain size is decreased to nanometer scale, grain boundary sliding and /or rotation of the grains tend to be dominant. The deformation mechanism is henceforth grain-boundary-mediated rather than dislocation-mediated. On the other hand, Fig. 5.15 (b) demonstrates the deformed state of a micro-pillar located at 300 μm below the treated surface. It can be observed that the deformation is essentially accommodated by plastic slips, which is typically characteristics of coarse-grained deformation behavior. The slip bands, which are clearly visible on the pillar, tend to occur in two preferential directions. This is perhaps because the micro-pillar is composed of one or two coarse grains. It seems that the deformed states of micro-pillars could provide direct insight into their deformation mechanism.

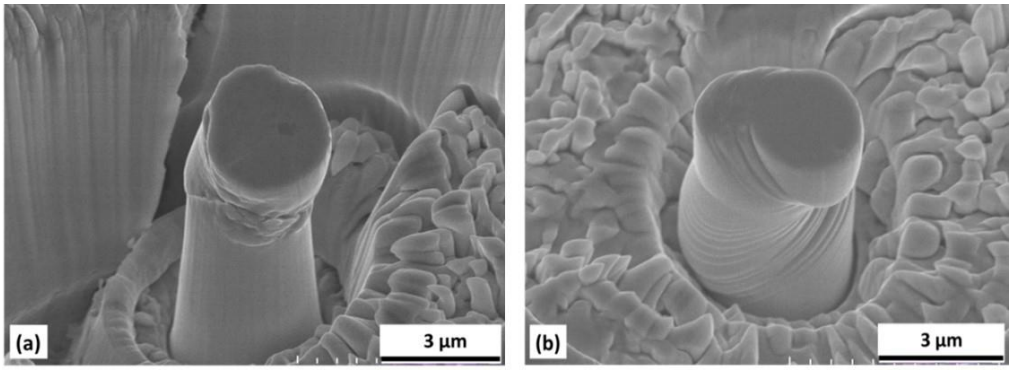

Fig. 5.15 SEM observation of deformed micro-pillars (a) in the nanostructured layer and (b) at a distance of 300 μm from the SMATed surface.

5.5 Conclusion

In this chapter, several factors affecting the micro-pillar compression tests were first discussed. It is concluded that the taper angle has a significant influence on the validity of the compression results and that its value should be less than 2.8°. Misalignment is another factor that could result in premature failure of the micro-pillar. This problem can be resolved by first reducing the mechanical polishing time and introducing a correction device which is attached to the sample. Furthermore, the influences of FIB, compressive residual stress generated by SMAT and conditions of the flat indenter were found to be negligible in this work.

Both monotonic and cyclic loading tests were conducted on the FIB-fabricated micro-pillar at different regions along the cross-section of the treated sample. The results of monotonic loading tests showed that micro-pillars in the nanostructured region have a higher yield stress associated with a low (absence) strain hardening as a result of severe grain refinement effects. Small nano-grains which constitute the micro-pillar in this region lead to a more homogeneous deformation. On the other hand, the deformation mechanism for the coarse-grained micro-pillar located at 300 μm was different. Plastic deformation proceeds as a result of the activation of preferential slip systems in a classical manner.

Chapter 6: Simulation of mechanical properties of SMATed material

In this Chapter, two major modelling methods for nanocrystalline materials are first introduced. A crystal plasticity model is presented and is subsequently applied for the later simulations. Several considerations, such as volume fraction of grain boundaries, length scale effects, are discussed as well. Voronoi diagram, Level-Set function are used for the construction of a Representative Elementary Volume (REV) model to performs finite element analysis with different microstructural configurations. The corresponding results

are presented and discussed to try to analyse the deformation mechanisms of nanocrystalline material.

6.1 Numerical modelling of nanocrystalline materials

At present, finite element method (FEM) and molecular dynamics are the two major numerical methods used to model nanocrystalline materials and each has its own advantages and weakness. FEM is a continuum modelling method, and therefore has no intrinsic length scale. Length scale effects must be introduced through the material models in the finite element calculation [3]. The absence of an intrinsic length scale in FEM could be either an advantage or a disadvantage depending on how it is reviewed. On the one hand, the absence of an intrinsic length scale allows the simulations of crystalline systems having dimensions several orders of magnitude apart [284] with approximately the same amount of computational work. On the other hand, one major concern about simulating deformation behavior at nanoscale is that whether a continuum model is valid. It is previously adressed in Section 1.4.6 that the deformation mechanism for nanocrystalline materials is grain-boundary-mediated rather than dislocation-mediated. Conventional model like crystal plasticity is based on dislocation motion whereas little dislocations exist inside a nano-grain. Hence, traditional dislocation structures do not exist or do not behave in the classical manner [2], [5], [7], [56], [57], [71], [284].

One obvious strength of molecular dynamics simulations is that it allows directly modelling the atoms and therefore directly incorporating the atomic length scales of the crystal into the computation. The behaviour of atoms is defined by potential functions which are derived from insights obtained from quantum mechanical simulations. Nevertheless, molecular dynamics has its own restrictions. The first one is attributed to its small time scale. The time step size of molecular dynamics is a few percent of the period of atomic vibration. All current molecular dynamics calculations therefore occur at extremely high strain rates that are generally inaccessible experimentally [3]. The second limitation would be its intrinsic length scale. The largest simulated sample dimensions are in the nanocrystalline regime, which makes direct comparisons to macroscopic experiments impossible.

As mentioned above, the current modelling methods available for nanocrystalline materials are not perfect. However, they still provide interesting insights into the behaviour of nanocrystalline materials. In the following Section, a crystal plasticity-based finite

element method is used to simulate the mechanical behaviour of material at nano-scale. The obtained results are interpreted subsequently.

6.2 Crystal plasticity

6.2.1 Core and mantle model

A core and mantle model [285]–[287] has been proposed in regard with the structure of nanocrystalline materials, as illustrated in Fig. 6.1 [3]. One major characteristic of nanocrystalline materials is their large volume fraction of grain boundaries, as compared to conventional polycrystals. The core and mantle model suggests that the deformation within a grain is composed of two parts: (1) the core, or grain interior, which is subjected to a more homogeneous state of stress (low strain hardening); and (2) the mantle, or grain-boundary region, in which an increased resistance to plastic flow and work hardening can be observed.

Fig. 6.2 [3] describes a grain in the conventional polycrystalline regime, slip system S_1 is activated in the grain interior (core), which corresponds to easy slide and consequently a low work hardening rate. As for the grain boundary region (mantle), dislocation activities are impeded, leading to increased work hardening. The global deformation behaviour of the material is determined by the relative fractions of grain interior (core) and the grain boundaries (mantle). As the grain size is reduced down to nanocrystalline regime, the increased volume fraction of the mantle begins to significantly interfere with the deformation mechanism or even dominates the plastic flow process. A model proposed by Benson et al. [288] suggested that plastic deformation was most likely to initiate in the grain boundaries region as a result of its increasing volume fraction. As discussed in Section 1.4.6, large volume fraction of grain boundaries become sources of dislocations that initiate plastic deformation [60], [64], [109]–[112], [122]. Consequently, grain boundaries often exhibit faster rise in the dislocation density and the hardening rate. It is also argued that grain boundaries regions are more prone to concentrated/localisation of plastic deformation [89].

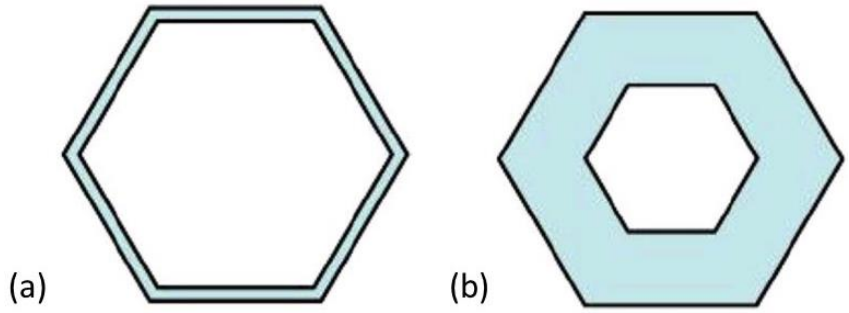

Fig. 6.1 Core and mantle model, showing relative fractions of grain boundary and grain interior regions in the (a) microcrystalline and (b) nanocrystalline regimes [3].

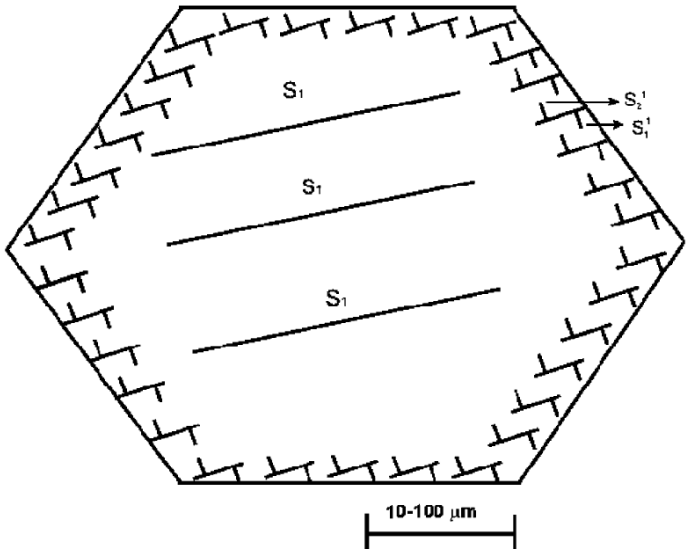

Fig. 6.2 Schematic depiction of a deformed grain showing the more intense cross slip and work hardening along the grain-boundary regions [3].

6.2.2 The applied crystal plasticity model

In conventional microcrystalline regime, the deformation behavior of metallic materials can be attributed to dislocation motions, for instance, sliding along a preferential crystallographic plane inside a grain. If the size and orientation of each grain inside a polycrystal is known, it is therefore possible to describe its mechanical behavior with a crystal plasticity model [289]. The critical resolved shear stress (CRSS) of a slip system, s, can be obtained by:

$$\tau^s = \underline{\underline{\boldsymbol{\sigma}}} : \underline{\underline{\boldsymbol{m}}}^s \tag{6-1}$$

$$\underline{\underline{\boldsymbol{m}}}^{s} = \frac{1}{2}\left(\underline{\boldsymbol{n}}^{s} \otimes \underline{\boldsymbol{l}}^{s} + \underline{\boldsymbol{l}}^{s} \otimes \underline{\boldsymbol{n}}^{s}\right) \tag{6-2}$$

where $\underline{\underline{\mathbf{m}}}^{s}$ is the orientation tensor of the slip system, s; $\underline{\boldsymbol{n}}^{s}$ and $\underline{\boldsymbol{l}}^{s}$ are respectively the slip plane normal direction and the unit vectors in the slip direction. According to Schmid's law, if a crystal is stressed, slip begins when shear stress on a slip system reaches a critical value, τ_c, often called the critical resolved shear stress. For instance, in the case of uniaxial tension, Schmid factor, m, could be written as $m = \cos\lambda\cos\phi$, as illustrated in Fig. 6.3 (a). To describe multiaxial stress state (Fig. 6.3(b)), the orientation of the slip system with respect to the applied multiaxial stresses should be expressed by a tensor, $\underline{\underline{\mathbf{m}}}^{s}$. Thus, the critical resolved shear stress, τ^s, in the case of multiaxial stress state can be calculated subsequently.

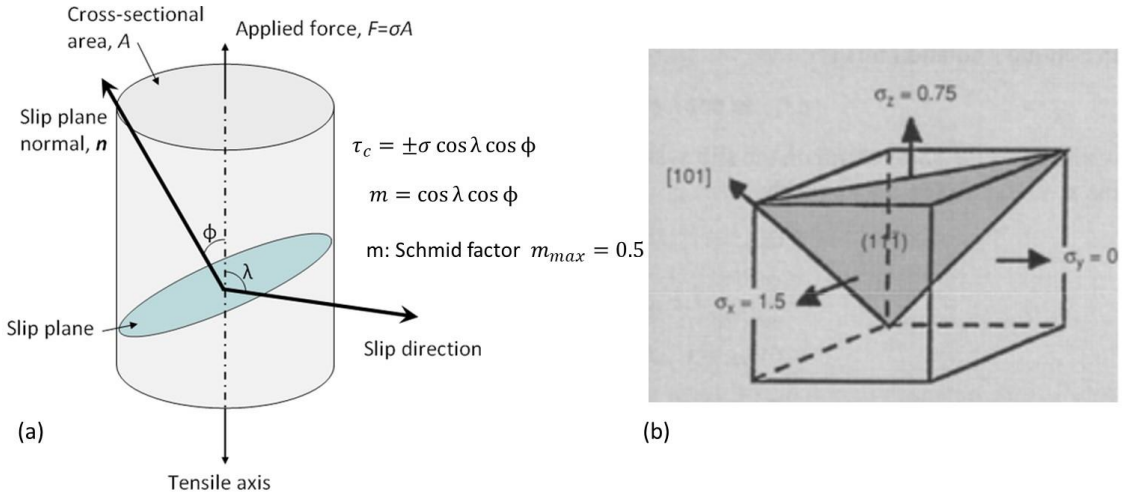

Fig. 6.3 Illustrations of Schmid factor (a) in uniaxial tension test, (b) in multiaxial stress state.

It should be specified that the current model does not consider the case of large deformation where the undeformed and deformed configurations of the continuum are significantly different. In this model, $\dot{\gamma}^s$, the shearing rate on slip system, s, can be expressed by a power law with regard to τ^s :

$$\dot{\gamma}^{s} = \left\langle \frac{\left|\tau^{s} - \chi^{s}\right| - \kappa^{s}}{g} \right\rangle^{n} \operatorname{sgn}\left(\tau^{s} - \chi^{s}\right) \tag{6-3}$$

where g and n are viscosity parameters. n is dependent on strain rate ; and χ^s is the corresponding slip system back stress. The kinematic hardening, i.e., evolution of the back

stress, χ^s, depends on the shearing rate on the current slip system and the current back stress, as described by Eq.(6-4). The isotropic hardening is described by κ^s, as illustrated in Eq.(6-5). The kinematic hardening and isotropic hardening are determined by some state variables, such as α^s and υ^r. Thus, the macroscopic plastic deformation rate can be calculated with the shearing rate of each slip system, as described in Eq.(6-6). Finally, the elasticity tensor allows to relate the elastic deformation to Cauchy stress tensor according to Hooke's law: $\sigma_{ij} = C_{ijkl}\varepsilon_{kl}$. The simulated material in this work is copper with FCC (face centered cubic) crystallographic structure. The material parameters (g, n, C, D, κ_0, Q, B) and interaction matrix, h^{sr}, used in the present crystal plasticity model are listed in Table 8 [290].

$$\chi^s = C\alpha^s \quad \text{with} \quad \dot{\alpha}^s = \dot{\gamma}^s - D\left|\dot{\gamma}^s\right|\alpha^s \tag{6-4}$$

$$\kappa^s = \kappa_0 + Q\sum_{r=1}^{N} h^{sr}\left(1-\exp\left(-B\upsilon^r\right)\right) \quad \text{with} \quad \dot{\upsilon}^r = \left|\dot{\gamma}^r\right| \tag{6-5}$$

$$\dot{\underline{\underline{\varepsilon}}}^p = \sum_{s=1}^{N} \dot{\gamma}^s \underline{\underline{\underline{\underline{\mathbf{m}}}}}^s \tag{6-6}$$

Table 8. Material parameters and interaction matrix for copper [290].

Elasticity tensor (GPa)			**Viscosity**		**Isotropic hardening**		**Kinematic Hardening**		**Interact. Matrix**
C11	C12	C14	K (MPa.s$^{1/n}$)	n	B	Q (MPa)	C (MPa)	D	h^{sr}
168.4	121.4	75.4	5	10	15	6	4500	600	1

6.3 Voronoi diagram

In mathematics, a Voronoi diagram [291] is a partitioning of a plane into regions based on distance to points in a specific subset of the plane. That set of points (called seeds, sites, or generators) is pre-defined and for each seed there is a corresponding region consisting of all points closer to that seed than to any other. An example is illustrated in Fig. 6.4 (a) [291]. These regions are called Voronoi cells. The Voronoi diagram of a set of points is dual to its Delaunay triangulation [292], as is shown in Fig. 6.4 (b) [291]. In the following Section,

Voronoi diagram will be used to generate a 2D model with several random grains. Details of the construction of the 2D model used for the finite element simulation will be discussed in detail later in this chapter.

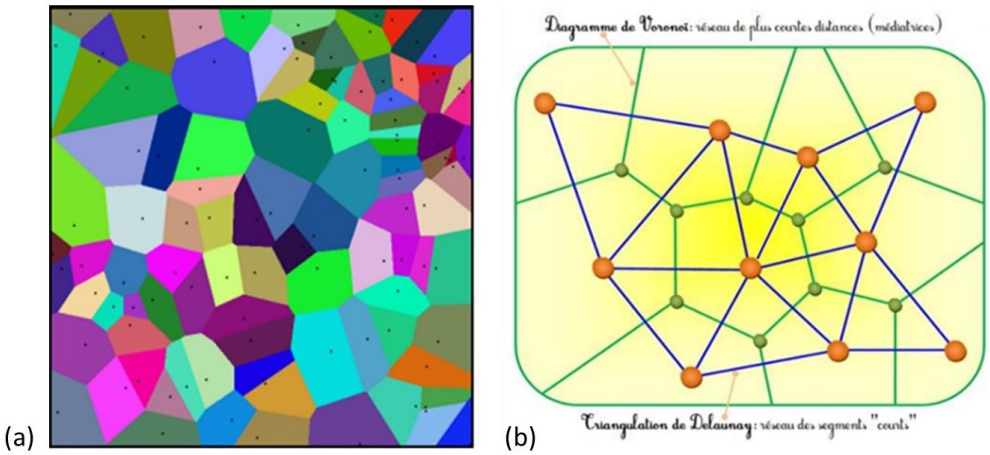

Fig. 6.4 (a) Illustration of Voronoi diagram, (b) Delaunay triangulation [291].

6.4 Level-Set method

Level-set method (LSM) is a conceptual framework for using level sets as a tool for numerical analysis of surfaces and shapes [293], [294]. The advantage of the level-set model is that one can perform numerical computations involving curves and surfaces on a fixed Cartesian grid without having to parameterize these objects. Also, the level-set method makes it very easy to follow shapes that change topology, for example, when a shape splits in two, develops holes, or the reverse of these operations. An example is given in Fig. 6.5 [294]. The general idea of Level-Set method to define a varying surface or object is to represent the desired boundaries as the zero contour (in 2D) or isolated-surface (in 3D) of a Level-Set function with one higher dimension [294]. For instance, if the symbol Γ denotes zero Level-Set function, namely the boundaries. Then, D and Ω represents the domains outside and inside the boundaries, respectively. The Level-Set function could be, therefore, described by Eq. (6-7). In the following Section, Level-Set functions will be subsequently applied to generate the grain boundaries regions.

$$\begin{cases} \Phi(\mathbf{x}, t) > 0, & (\mathbf{x} \in \Omega) \\ \Phi(\mathbf{x}, t) = 0, & (\mathbf{x} \in \Gamma) \\ \Phi(\mathbf{x}, t) < 0, & (\mathbf{x} \in D \setminus \Omega) \end{cases} \tag{6-7}$$

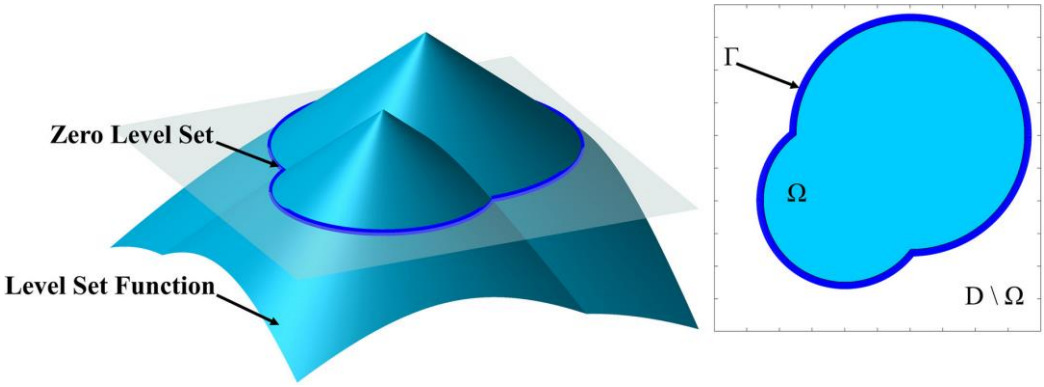

Fig. 6.5 The Level-Set function and its corresponding zero Level-Set [294].

6.5 Construction of a 2D model for nanocrystalline materials

As aforementioned, the simulations of nanocrystalline materials are often quite time-consuming as a result of their abundant quantities of nano-grains that constitute a mechanical component [3]. For this reason, only a model of representative elementary volume (REV) is constructed in this work. In the theory of composite materials, the REV is the smallest volume over which a measurement can be made that will yield a value representative of the whole [295]. An example is given in Fig. 6.6 [296]. Hill et al. [295] defined the REV as a sample of a heterogeneous material that:

1) is entirely typical of the whole mixture on average
2) contains a sufficient number of inclusions for the apparent properties to be independent of the surface values of traction and displacement, so long as these values are macroscopically uniform.

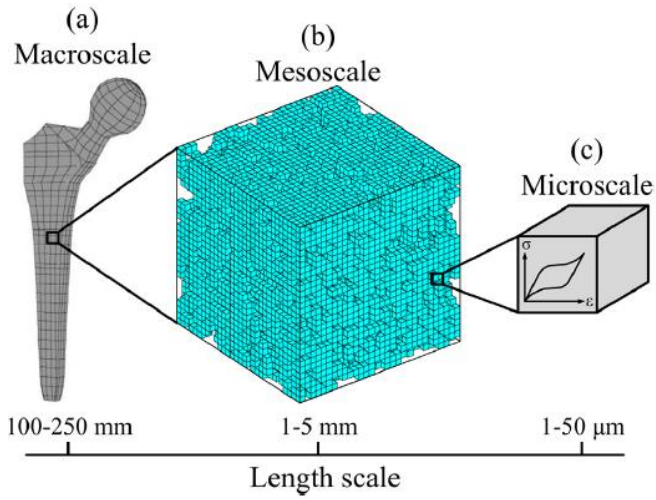

Fig. 6.6 Illustration of the multiscale modelling approach using Representative Elementary Volume [296].

By applying the concept of REV, a two-dimensional model is established, based on the core-mantle model, Voronoi diagram and Level-Set function discussed previously. In the first place, Voronoi diagram was applied for the generation of random grains, for example, grain 1 and grain 2 in Fig. 6.7 (a). To generate the grain boundary areas, Level-Set function was adopted, as illustrated in Fig. 6.7 (b). It should be specified that Level-Set function is capable of determining the volume fraction of grain boundaries by adjusting the desired domain. Moreover, the grain boundary region between grain 1 and grain 2 is evenly divided into two portions, namely grain boundary zone of grain 1 and grain boundary zone of grain 2, as illustrated in Fig. 6.7 (b). The grain boundary here is assumed to have a crystalline structure as discussed in Section 1.4.5.2 [102]–[104]. Now the grain interior (core) and grain boundary (mantle) are established, one subsequent concern would be how to define their mechanical properties respectively. As is discussed in Section 6.1, crystal plasticity is based on dislocation motion, however the dimensions of the individual grains in a nanocrystalline material may be small enough that traditional dislocation structures do not exist or do not behave in the classical manner. Secondly, it is argued that plastic deformation was most likely to initiate in the grain boundaries region as a result of their large volume fraction [60], [64], [109]–[111], [114], [122], [288]. Thus, it is necessary to consider length scale effects in finite element model.

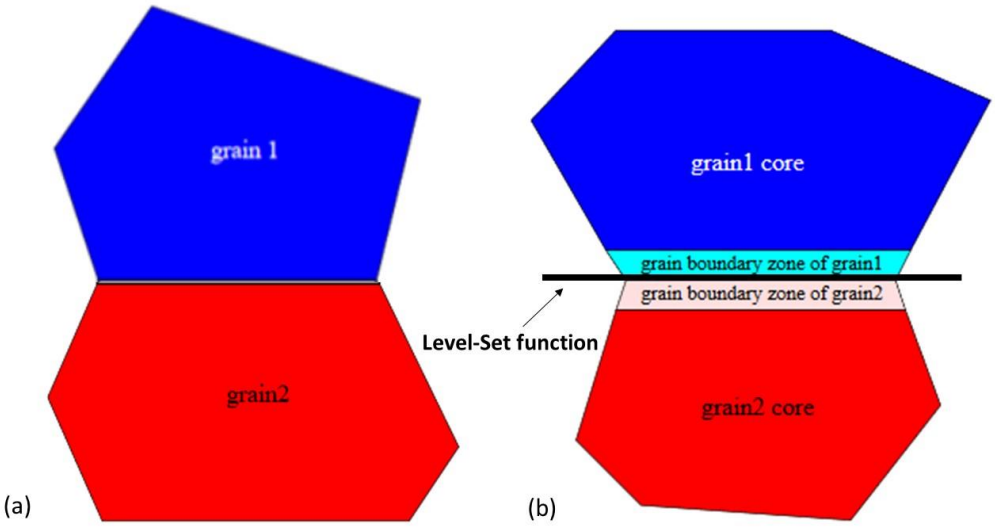

Fig. 6.7 Construction of a two-dimensional model for nanocrystalline material (a) Generation of random grains with Voronoi diagram, (b) Generation of grain boundary areas with Level-Set function.

In the literature, a length scale is introduced into a finite element model [3], [76], [297]–[299] of a polycrystal material by

1) Using a material model having a length scale.

2) Modifying the behavior of the grain boundary, thereby introducing a length scale as the ratio of the grain-boundary volume to its surface area.

3) Modelling the grain boundary with a finite thickness, which directly imposes a length scale.

With all the above discussions taken into account, several modifications of the simulation parameters are adjusted accordingly. First, given that dislocation activities are less likely to occur inside a nano-grain, a high value of critical resolved shear stress (CRSS) is attributed to the grain (core) for this concern. Moreover, with increasing volume fraction of grain boundaries, the deformation mechanism is grain-boundary-mediated rather than dislocation-mediated, for example, grain-boundary shear [81]. The plastic deformation is most likely to initiate in the grain boundary areas [60], [109]. Therefore, a smaller critical resolved shear stress (CRSS) is distributed to the grain boundary area (mantle). In our case, the CRSS of the grain interior (core) is set to be two times higher than that of grain boundary (mantle). Finally, two models (with ten grains) are generated with varying volume fraction of grain boundaries, as illustrated in Fig. 6.8. The orientations of the ten grains are randomly distributed. The corresponding simulation parameters are listed in Table 9. It should be clarified that volume fraction of grain boundaries has an inversely-proportional relation with grain size, d. Model 1 has a larger volume fraction of grain boundaries and consequently has a smaller grain size [100]. For this reason, the values of CRSS for Model 1 are higher than that of Model 2. According to literature [3], [100], the grain size for Model 1 and Model 2 might be roughly estimated to be 20 nm and 50 nm respectively. The models were subjected to tension test with a strain rate of 0.01 s^{-1}.

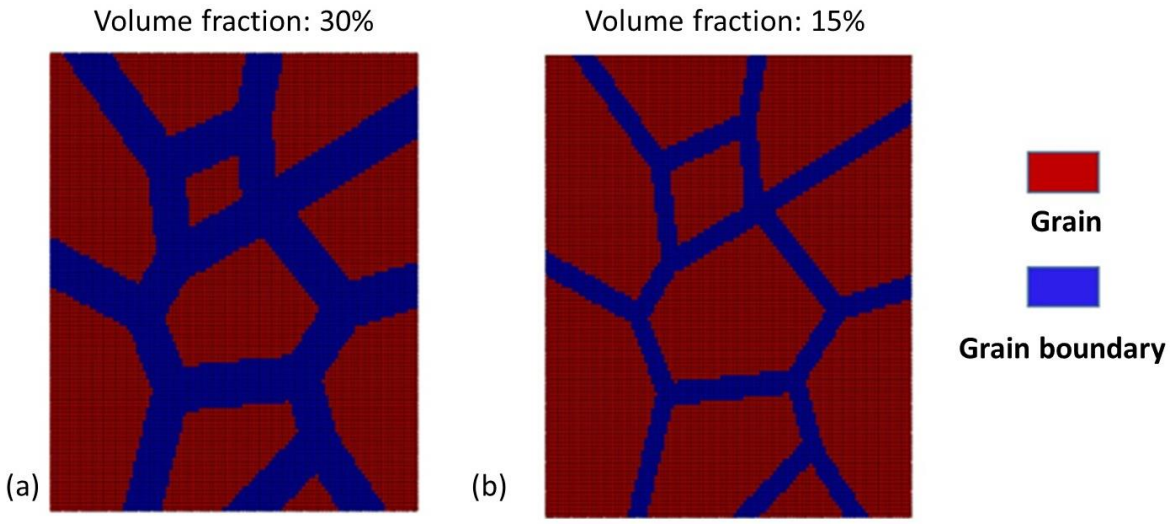

Fig. 6.8 Two-dimensional REV models (a) Model 1: Volume fraction of grain boundaries of about 30%, (b) Model 2: Volume fraction of grain boundaries of about 15%.

Table 9 Parameters used for the two FEM models with different volume fraction of grain boundaries.

Simulation Model	Volume fraction	CRSS (core)	CRSS (mantle)	Grain size
Model 1	~30%	603MPa	301 MPa	20 nm
Model 2	~15%	242 MPa	121 MPa	50 nm

6.6 Results of simulation

The results of simulations (evolution of plastic deformation, stress and stress-strain curves) are illustrated in Fig. 6.9, Fig. 6.10 and Fig. 6.11. For both FEM models, the initiation of plastic deformation occurred in the grain boundary regions due to lower values of critical resolved shear stress. This is consistent with the results presented in the literature [71], [109], [112], [122], [288]. Indeed, lower values of critical resolved shear stress along with large volume fraction of grain boundaries also lead to localisation of deformation at grain boundary areas [89]. For Model 1, the initiation and localisation of plastic deformation are more obvious as a result of larger volume fraction of grain boundaries, as compared to Model 2. Similar results have been found by Anand et al. [300] who introduced cohesive elements along the grain boundaries to model grain-boundary slip. The interior of the grains was modelled with single crystal plasticity. They applied their model to the study of nanocrystalline nickel. Plastic deformation was found to initiate in the grain boundary areas which eventually led to facture. The stress-strain curves for Model 1 and Model 2 are plotted in Fig. 6.11 (a). Model 1 exhibits higher value of yield strength as compared to Model 2 as a consequence of smaller grain size. The simulation curves are in

relatively reasonable agreement with the results presented in the literature, as shown in Fig. 6.11 (b). It can be noticed that for both Model 1 and Model 2, softening seems to occur according to the stress-strain curves. It is argued that when grain size decreases to nanocrystalline regime, softening might occur, namely the inverse Hall-Petch phenomenon [52], [55]. In our case, the softening may be related to large volume fraction of grain boundaries with low value of critical resolved shear stress.

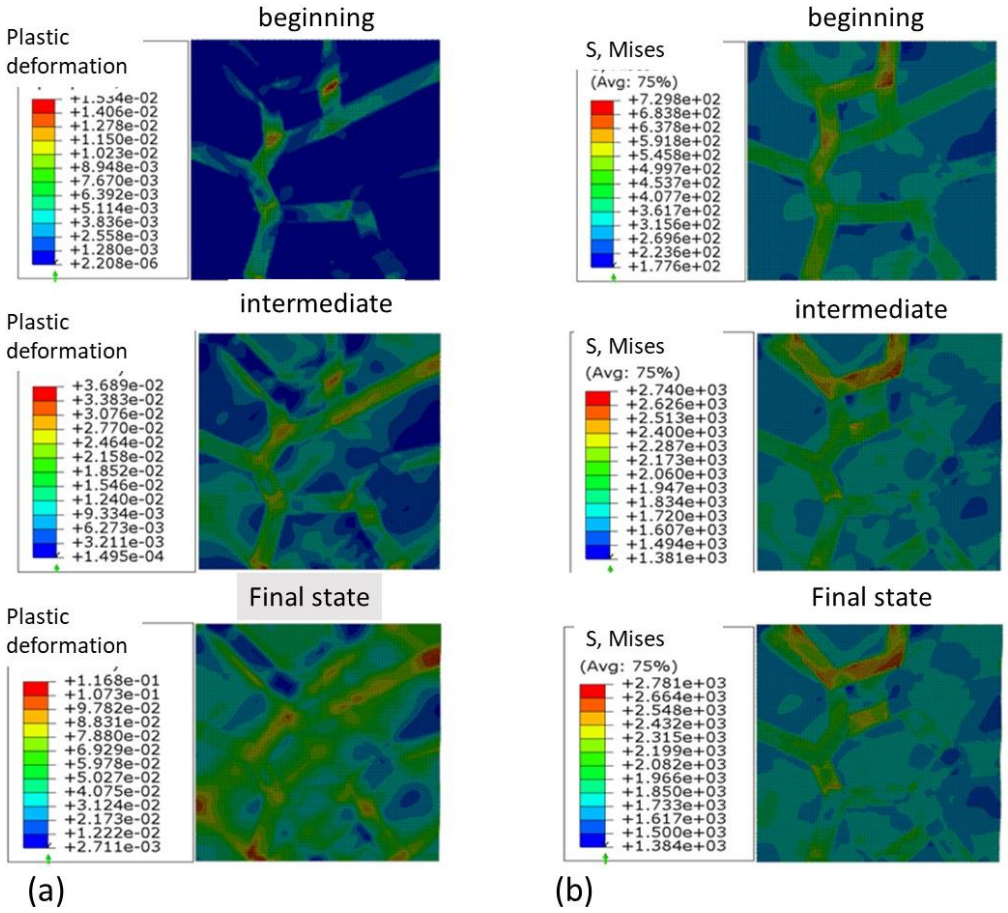

Fig. 6.9 Simulation results of Model 1 (Volume fraction of grain boundary 30%): (a) Evolution of plastic deformation, (b) Evolution of stress.

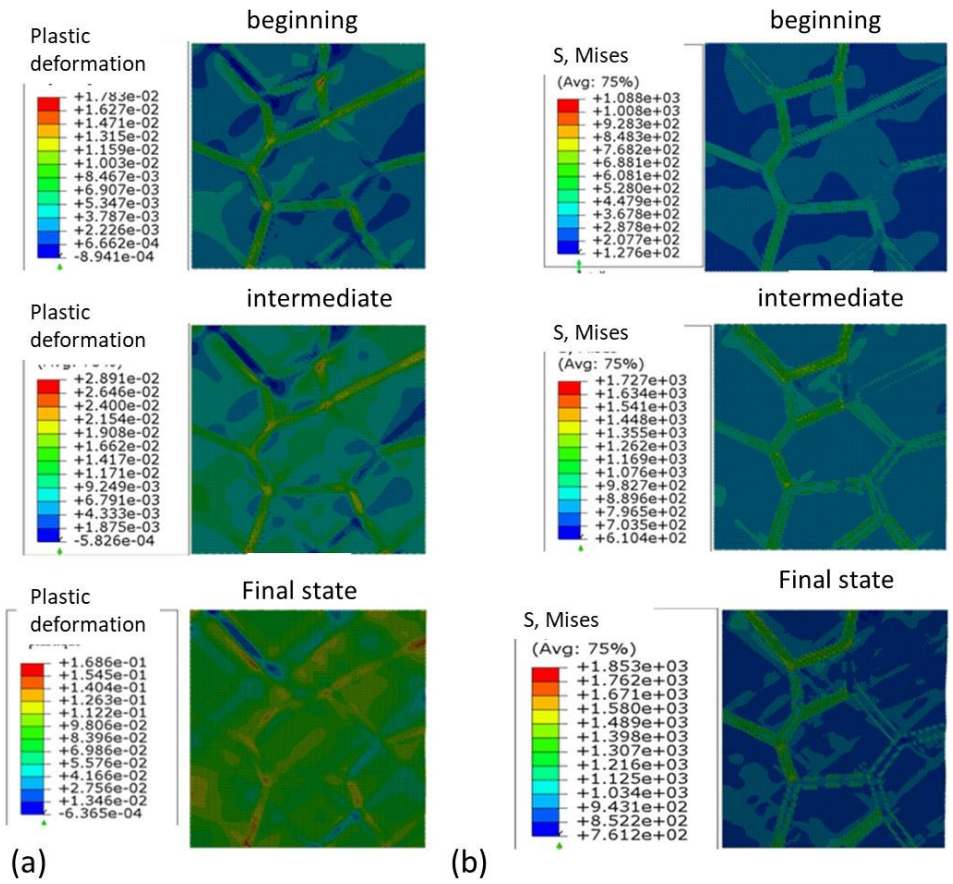

Fig. 6.10 Simulation results of Model 2 (Volume fraction of grain boundary 15%): (a) Evolution of plastic deformation, (b) Evolution of stress.

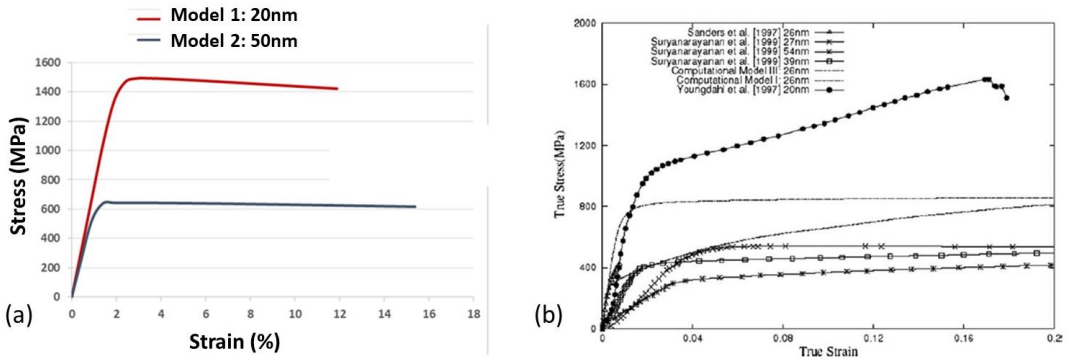

Fig. 6.11 (a) Simulation stress-strain curves for Model 1 and Model 2, (b) Divers sources of experimental results in the literature [3].

6.7 Conclusion

In this Chapter, Finite element method was used for the simulation of nanocrystalline material despite of its limitations. A crystal plasticity model was used and efforts were made to take into account the length scale effects by modifying several parameters, such as volume fraction of grain boundaries, critical resolved shear stress. The core-mantle model, Voronoi diagram and Level-Set function were applied for the generation of the FEM models. Two models with varied volume fraction were generated. The simulation results suggested that plastic deformation initiated in the grain boundary area, which is consistent with the results presented in the literature.

Chapter 7: Conclusion and prospects

7.1 Conclusion

It has been demonstrated that SMAT is able to generate a gradient microstructure in the near surface region of metallic materials. SMAT-induced changes, namely grain refinement, residual stresses and work hardening co-exist along the cross-section of the treated material. This gradient microstructure has been found to be able to improve the mechanical properties of materials, such as fatigue properties and tensile strength. Nevertheless, emphasis was mainly placed on the global properties of the gradient microstructure and little effort was devoted to the individual characterization of the different layers of the gradient microstructure. The aim of this thesis was to characterize separately the local properties of different layers in order to better understand the beneficial effects of the gradient microstructure. Thus, a variety of characterization techniques were used in this work to study the gradient microstructure generated by SMAT, such as EBSD, X-ray diffraction, AFM, nanoindentation, FIB and micro-pillar compression testing.

In Chapter 1, several methods available for the generation of nanocrystallized materials are first introduced. The advantages and drawbacks of these techniques are also

addressed. Synthesis methods by severe plastic deformation are able to generate samples free of porosity and contamination, which makes them stand out among other synthesis methods. Surface Mechanical Attrition Treatment (SMAT) can be classified as one of these SPD synthesis method. A detailed description of the SMAT technique is presented in this chapter. Several mechanical and chemical properties can be improved after SMAT, such as hardness, friction and wear properties, yield strength, fatigue and diffusion properties. In the last section of this chapter, the novel properties of NC materials (yield strength, ductility, strain-rate sensitivity and structure of NC materials) are discussed in detail. A brief introduction about the current understandings of the deformation mechanisms of nanocrystalline metals is presented. The deformation mechanisms proposed so far include grain boundary sliding, grain boundary rotation, grain boundary diffusion, partial dislocations etc. At the end of this chapter, we focus on a few models of three main deformation mechanisms (grain boundary sliding, grain boundary rotation and dislocation activities). This chapter is dedicated to the literature review and will be applied subsequently for the interpretation of the experimental results in the following chapters.

In regard to Chapter 2, the gradient microstructure generated by SMAT has beneficial effects in terms of improving the mechanical properties of the treated component. The thickness of the gradient microstructure is in the micro-scale, especially the nanostructured layer in the near surface region which has a thickness betweena few micrometers to tens of micrometers depending on the treatment intensity. For this reason, characterization techniques at micro- or nano-scale are essential for direct investigations of the local microstructure characteristics and mechanical properties. This chapter lists a variety of characterization techniques that have been used for the individual characterization of different layers in the gradient microstructure and each is capable of revealing important information about the properties of the tested regions. For instance, the microstructure (grain size distribution and phase transformation etc.) of the sample was investigated by means of SEM, XRD and EBSD. The mechanical properties of the SMATed samples were mainly examined by nanoindentation and micro-pillar compression tests. AFM measurements were performed to investigate the pile-up behaviour of the SMATed steel. The working principles of these characterization techniques as well as their capabilities have been described.

In Chapter 3, EBSD observations were performed to investigate the gradient microstructure generated by SMAT as well as its thermal stability. Special attention needs to be paid to the sample preparation for EBSD observation as delicate smooth state of the

sample surface is required. Otherwise, bad condition of the sample surface will lead to degradation of the imaging quality and non-indexing areas. The results revealed that the thickness of the nanostructured layer is about 5 μm and grain size refinement is down to a depth of about 100 μm. As for the thermal stability of the gradient microstructure, it is found by in-situ EBSD that the microstructure generated by SMAT was stable up to 600°C, which is consistent with the literature. In addition, the nanocrystalline region is more prone to oxidation due to large volume fraction of grain boundaries which provide short circuit diffusion path for oxygen to more easily penetrate in the material.

In Chapter 4, it is demonstrated that three major changes induced by SMAT will affect the nanoindentation measurements. The obtained results (load-displacement curves, Young's modulus, hardness indentation size effect and pile-up behavior) are interpreted subsequently in terms of these SMAT induced changes along the cross-section of the SMATed sample. Several conclusions could be made as follows:

(1) Grain refinement is the major factor that contributes to higher indentation load/hardness and residual stresses play a relatively minor role.

(2) As the nanocrystalline region is also the sample edge areas in the case of SMATed 316L stainless steel, the influence of edge effects should be considered during the interpretation of nanoindentation measurements. Edge effects were found to affect the contact stiffness, Young's modulus and cyclic loading behavior in the nanocrystalline region.

(3) The measured hardness and Young's modulus seem to be independent of residual stress.

(4) Pile-up occurred in the SMAT-affected region as a result of decreasing strain hardening exponent of the material. Pile-up should be taken into account in order to correct the true contact area. The recalculated hardness with corrected new contact area was found to slightly decrease.

In Chapter 5, several factors affecting the micro-pillar compression tests were first discussed. It is concluded that the taper angle and misalignment have a significant influence on the validity of the compression results while the influences of FIB, residual stresses generated by SMAT and conditions of the flat indenter were found to be negligible in this work. Both monotonic and cyclic loading tests were conducted on the FIB-fabricated micro-pillars in different regions along the cross-section of the treated sample. The results of monotonic loading tests showed that micro-pillars in the nanostructured region have a

higher yield stress associated with a low level (absence) of strain hardening as a result of severe grain refinement effects. Small nano-grains which constitute the micro-pillars in this region lead to a more homogeneous deformation. On the other hand, the deformation mechanism for the coarse-grained micro-pillars located at 300 μm beneath the treated surface was different. Plastic deformation proceeds as a result of the activation of preferential slip systems in a classical manner.

In Chapter 6, Finite element method was used for the simulation of nanocrystalline material despite of its limitations. A crystal plasticity model was used and efforts were made to take into account the length scale effects by modifying several parameters, such as volume fraction of grain boundaries and critical resolved shear stress. The core-mantle model, Voronoi diagram and Level-Set function were applied for the generation of the finite element model. Two models with different volume fractions were generated. The simulation results suggested that plastic deformation initiated in the grain boundary area, which is consistent with the results presented in the literature.

Hence, systematic studies performed both experimentally and numerically, were devoted to the individual characterization of different regions of the gradient microstructure. The innovative aspect of the present work, compared to the previous work, is that individual characterization of different layers of the gradient microstructure was realised owing to various characterization techniques at micro- and nano-scale. The understanding of the beneficial effects of the gradient microstructure is henceforth enhanced and the current investigation methods, such as nanoindentation, EBSD technique and X-ray diffraction, could be possibly applied for the optimisation of the SMAT treatment intensity in order to design a gradient microstructure with optimal properties.

7.2 Prospects

As aforementioned, systematic studies conducted, both experimentally and numerically, were devoted to the individual characterization of different regions of the gradient microstructure. In this work, individual characterization of different layers of the gradient microstructure were realised owing to various characterization techniques at micro- and nano-scale, such as nanoindentation, EBSD technique and X-ray diffraction. However, some observed phenomena have not been clearly understood and some modelling methods deserve further improvement.

EBSD observations revealed the microstructure of the nanostructured layer. However, the precision is not enough for the characterization of the structure of the grain boundary

areas. As discussed previously, a large fraction of grain boundaries interfere in the deformation mechanism of nanocrystalline materials. Hence, more precise investigations about the structure of grain boundaries in the nanostructured region is recommended as valuable insights could be obtained accordingly. TEM seems to be a qualified tool for further investigations of the grain boundary structure of nanostructured region (dislocation structure, arrangements of atoms and grain boundary thickness etc.). Ideally speaking, the precise volume fraction of grain boundaries could be estimated according to TEM observations.

The micro-pillar compression tests conducted in this work are not in-situ tests. As a consequence, the deformed states of the micro-pillars were observed after the compression tests and the evolution of the deformation process of the micro-pillar cannot be monitored. In the future, in-situ micro-pillar compression tests are preferred as they allow the recording of the deformation process and provides valuable insights regarding the deformation mechanisms of micro-pillars. Moreover, possible microstructural changes of the micro-pillar at different strain levels shall be observed using more precise characterization method (TEM for example) even though this is rather difficult to realise. For instance, microstructural changes such as grain boundary sliding, grain boundary shear and emission of dislocations at the grain boundaries might take place in the nanocrystalline region while dislocation activities and subsequent activation of preferential slip systems are expected in the coarse-grained region.

Concerning the simulation of nanocrystalline material, only a two-dimensional representative elementary volume model (ten grains) was established. Crystal plasticity was applied for the simulations in this work despite of its limitations. It is clear that this model is not perfect. Hence, it will be valuable to come up with a better model that accounts for length scale effects when the grain size is reduced down to nano-scale and hopefully extend this improved model to three-dimensional simulations.

Résumé étendu en français

1 Introduction

Depuis l'article écrit par H. Gleiter en 1989, des efforts ont été consacrés à une nouvelle orientation en science des matériaux. Dans cet article, Gleiter souligne les possibilités remarquables des matériaux nanocristallins. Ces matériaux nanocristallins sont des polycristaux, typiquement caractérisés par des petits grains inférieurs à 100 nm. En raison de ces dimensions extrêmement réduites, les matériaux nanocristallins présentent une fraction volumique importante de joints de grains ce qui peut modifier de manière significative leurs propriétés physiques, mécaniques ou chimiques par rapport à leurs homologues conventionnels présentant une taille de grains à l'échelle micrométrique. En fait, la plupart des propriétés des matériaux nanocristallins sont souvent reconnues comme étant supérieures à celles de leurs homologues avec une taille de grains conventionnelle. Par exemple, les matériaux nanocristallins présentent une dureté et une résistance mécanique plus élevées.

Les matériaux nanocristallins peuvent être synthétisés soit en consolidant de petites particules nanométriques, soit en décomposant les matériaux polycristallins en unités cristallines de dimensions nanométriques. Ces approches ont été classées en approches bottom-up ou top-down. Dans l'approche bottom-up, il est nécessaire d'organiser les nanograins atome par atome, couche par couche. Dans l'approche top-down, nous commençons par le matériau conventionnel à taille de grains micrométrique et décomposons la microstructure en une nanostructure. Jusqu'alors, plusieurs techniques ont été développées pour la synthèse des matériaux nanocristallins. Parmi elles, nous pouvons citer la technique de condensation sous gaz inertes, la mécanosynthèse, l'électrodéposition, la cristallisation complète des solides amorphes ou encore les procédés par déformation plastique sévère. Toutefois, la production de ces nanomatériaux avec ces techniques reste cantonnée à la formation de structures de faibles tailles et des difficultés persistent pour l'obtention de matériaux nanocristallins massifs libres de porosité, sans contamination ou autres défauts (excepté pour la technique par déformation plastique sévère). L'obtention d'échantillons de taille importante ne semble toujours pas facilement envisageable au regard des solutions technologiques actuelles.

Le procédé Surface Mechanical Attrition Treatment (SMAT) est l'une des techniques de traitement mécanique de surface les plus prometteuses pour générer des matériaux nanocristallins via une déformation plastique sévère. Il est basé sur des impacts multidirectionnels répétés entre la surface d'une pièce et des billes projetées par un générateur à ultrasons. La zone proche de la surface est affectée mécaniquement par le SMAT. Cette technique peut conduire à un raffinement progressif de la taille de grains par déformation plastique sévère, alors que le matériau à cœur de la pièce n'est pas affecté par le traitement. Par conséquent, les caractéristiques microstructurales de ce dernier restent inchangées ainsi que ses propriétés mécaniques. Une microstructure à gradient est ainsi formée de la surface traitée vers le coeur du matériau. La particularité du SMAT par rapport au grenaillage conventionnel réside dans le fait qu'il peut transformer la couche superficielle des matériaux à grains micrométriques en grains nanométriques. Cette couche nanostructurée, même si elle est fine en général, pourrait avoir un effet significatif sur les performances des matériaux, puisque en général les pièces mécaniques sont plus chargées en surfaces, comme c'est par exemple le cas en frottement, torsion ou lors de charges de contact. Un autre avantage de SMAT par rapport aux autres méthodes de synthèse est qu'elle permet de générer une nanostructure sans porosité et contamination.

La microstructure à gradient induite par SMAT peut être divisée en trois zones : la zone du matériau à cœur qui n'est pas affectée par le traitement, la zone de transition et la couche nanocristalline qui se trouve à la surface supérieure. Les effets bénéfiques dus à la microstructure à gradient générée par SMAT ont été étudiés dans des études antérieures. Néanmoins, l'accent a surtout été mis sur les propriétés globales de la microstructure à gradient et peu d'efforts ont été consacrés à l'étude des propriétés individuelles de chaque couche. Par exemple, Zhou et al. ont étudié l'influence du SMAT sur le comportement en fatigue de l'acier inoxydable 316L. Il a été conclu que la microstructure à gradient peut augmenter la résistance à la fatigue du matériau traité. Les effets bénéfiques de la microstructure à gradient ont également été observés en termes d'amélioration de la résistance à la traction de l'acier inoxydable 316L SMATé. En effet, lorsqu'une pièce mécanique est soumise au SMAT, le raffinement de la microstructure, les contraintes résiduelles de compression superficielles et l'écrouissage sont simultanément introduits en raison d'une déformation plastique sévère. Ces trois facteurs existent simultanément le long de la section transversale de la pièce traitée et tous varient en fonction de la distance à la surface traitée. Par conséquent, les propriétés améliorées par la microstructure à gradient sont dues aux effets combinés de ces paramètres induits par SMAT.

Pour mieux comprendre les effets bénéfiques de la microstructure à gradient, il serait utile de caractériser le comportement mécanique à différentes profondeurs par rapport à la surface SMATée, comme par exemple, dans la couche nanostructurée ou dans la zone de transition qui est mécaniquement déformée. La caractérisation du comportement mécanique local de la couche nanostructurée est difficile, étant donné sa très faible épaisseur (de quelques microns à plusieurs dizaines de microns, selon l'intensité du traitement). Dans la littérature, la technique de nanoindentation a été largement utilisée pour étudier le comportement mécanique local de matériaux à l'échelle micro ou nanométrique, comme les couches minces ou les matériaux multiphasés. Ainsi, la nanoindentation donne accès à la caractérisation individuelle des différentes couches de la microstructure à gradient. Les propriétés mécaniques locales de chaque couche peuvent être obtenues en fonction de leur comportement à l'indentation, comme la charge maximale, le déplacement final pendant le déchargement ou encore l'empreinte d'indentation résiduelle.

Par ailleurs, la compression de micro-piliers est une autre technique potentiellement performante pour la caractérisation des propriétés mécaniques de la microstructure à gradient générée par SMAT. À l'origine, la compression de micro-piliers était utilisée pour étudier les propriétés mécaniques et comprendre les mécanismes de déformation des monocristaux. Grâce à sa simplicité et à sa capacité d'accès direct au comportement mécanique uniaxial des matériaux à l'échelle micrométrique, elle devient une méthode populaire pour caractériser quantitativement les propriétés mécaniques locales des matériaux. Grâce à cette technique, la courbe contrainte-déformation peut être facilement calculée à partir des courbes charge-déplacement obtenues après les essais de compression des micro-piliers et l'obtention d'autres informations telles que la limite d'élasticité est plus simple que par exemple en utilisant la technique de nanoindentation. Cependant, la technique de compression de micro-piliers n'a pas encore été largement utilisée pour étudier les matériaux traités par des traitements de surface mécaniques tels que le SMAT.

Dans ce travail, le comportement mécanique local de la microstructure à gradient de l'acier inoxydable 316L générée par SMAT a été étudié en utilisant la technique de compression de micro-piliers et la nanoindentation.

Pour la première partie de ce travail, les résultats de la caractérisation de la microstructure par SEM et EBSD sont présentés. Tout d'abord, la microstructure initiale de l'acier inoxydable 316L est examinée par SEM, suivie d'une étude détaillée de la microstructure par EBSD après le traitement SMAT. Une comparaison détaillée entre la microstructure initiale et la microstructure finale est faite à la fin.

Dans la deuxième partie de ce travail, une discussion est menée sur trois paramètres majeurs induits par SMAT qui affecteront les mesures de nanoindentation. Ensuite, les résultats obtenus sont listés (courbes de déplacement-charge, module de Young, dureté, effet de taille et comportement de pile-up) suivis d'interprétations détaillées. Outre les essais de chargement monotone, les résultats des essais de chargement cyclique sont également présentés et discutés.

La troisième partie est consacrée aux essais de compression de micro-piliers. Tout d'abord, plusieurs facteurs affectant les essais de compression sont discutés, suivis par les résultats expérimentaux et les interprétations. Outre les essais monotones, des essais de chargement cyclique ont été également effectués sur des micro-piliers.

La quatrième partie de ce travail est consacrée aux simulations par éléments finis. Un modèle de plasticité cristalline a été utilisé pour simuler les propriétés mécaniques du matériau SMATé. Les résultats correspondants sont interprétés en tenant compte des informations présentées dans la littérature.

2 Microstructure à gradient générée par SMAT

Dans cette partie, plusieurs méthodes de caractérisation (MEB, MET, DRX, EBSD) ont été utilisées pour étudier la microstructure des matériaux traités par SMAT. Pour compléter la caractérisation microstructurale, des résultats obtenus par MET pour des travaux antérieurs de notre laboratoire sont également présentés. Ces méthodes de caractérisation ont leurs propres avantages et inconvénients et sont capables de révéler différentes informations sur la microstructure de l'échantillon traité. Cette partie présente une introduction générale du matériel étudié dans le cadre de ce projet, y compris ses propriétés chimiques et physiques ainsi que sa structure cristallographique. Dans la section suivante, nous nous concentrerons principalement sur les caractéristiques des microstructures révélées avant et après SMAT et une comparaison entre les deux états de matériau sera également faite.

Dans ce projet, un acier inoxydable austénitique AISI 316 est choisi comme matériau cible pour le traitement par SMAT et les études ultérieures. Sa composition chimique est indiquée dans le tableau 1. Le tableau 2 donne les propriétés mécaniques typiques de l'acier inoxydable 316L.

Tableau 1 - Composition chimique (wt.%) de l'acier inoxydable 316L étudié.

Fe	C	Mn	Si	P	S	Cr	Ni	Mo	Cu	N	Ti	V
Balance	0.013	1.7	0.26	0.017	0.003	17.37	14.52	2.80	0.08	0.088	<0.005	0.07

Tableau 2 - Propriétés mécaniques typiques de l'acier inoxydable 316L étudié.

Nuance	Résistance à traction (MPa)	Limite d'élasticité de 0,2 % de déformation (MPa)	Allongement	Dureté Hv	Allongement à la rupture
316L	490	170	40%	195	<60%

La métallographie a été d'abord faite pour observer la microstructure. Pour ce faire, la section transversale des échantillons a été polie mécaniquement puis attaquée chimiquement, suivie par une observation avec un microscope numérique. La microstructure est présentée dans la Fig.1. Elle montre que le matériau à l'état de réception a une taille de grains initiale d'environ 10-20 μm.

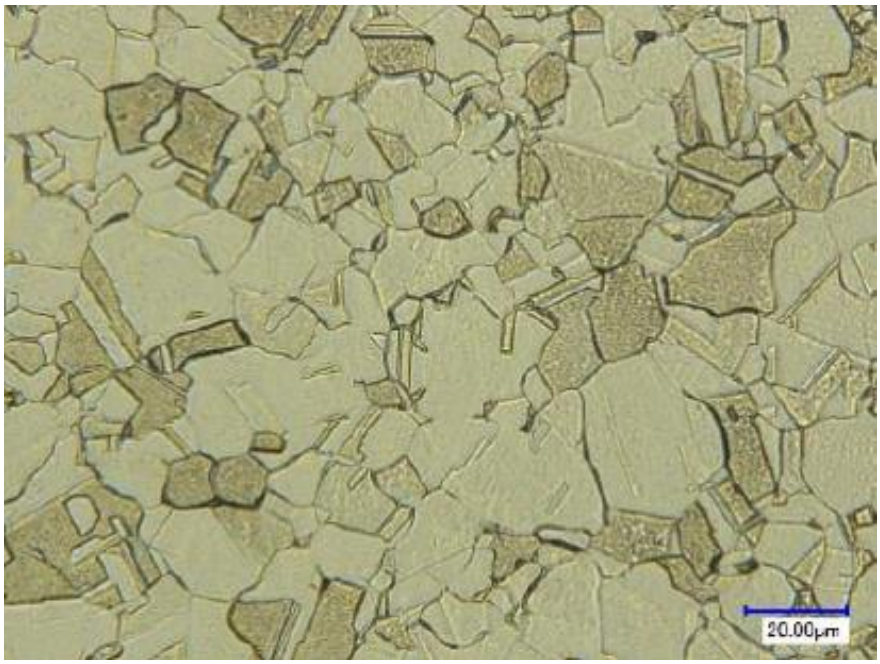

Fig. 1 Microstructure de l'acier inoxydable 316L à l'état de réception.

2.1 Procédure expérimentale

Le matériau étudié dans ce travail est un acier inoxydable austénitique AISI 316L comme mentionné précédemment. Des échantillons typiques prélevés dans une tôle et sous forme d'haltères pour les essais de fatigue ont été choisis pour le traitement par SMAT, comme illustré dans la Fig. 2. La tôle d'acier a une forme rectangulaire avec une longueur

de 240 mm et une largeur de 120 mm. L'épaisseur de la tôle est de 1 mm. Pour l'échantillon sous forme d'haltère, la longueur de la partie centrale est de 12 mm avec un diamètre de 6 mm. Les dimensions de l'échantillon sont illustrées dans la Fig.2 (b). Le SMAT a été réalisé séparément sur les deux échantillons pour générer une microstructure à gradient. Le SMAT est basé sur la vibration de billes sphériques (3 mm de diamètre) projetées par un générateur à ultrasons de haute fréquence (20 kHz). Dans ce travail, les échantillons ont été soumis à un traitement de 15 minutes avec une puissance de générateur de 27%, suivi d'un traitement de 5 minutes avec une puissance de 50%. Les conditions SMAT sont récapitulées dans le tableau 3.

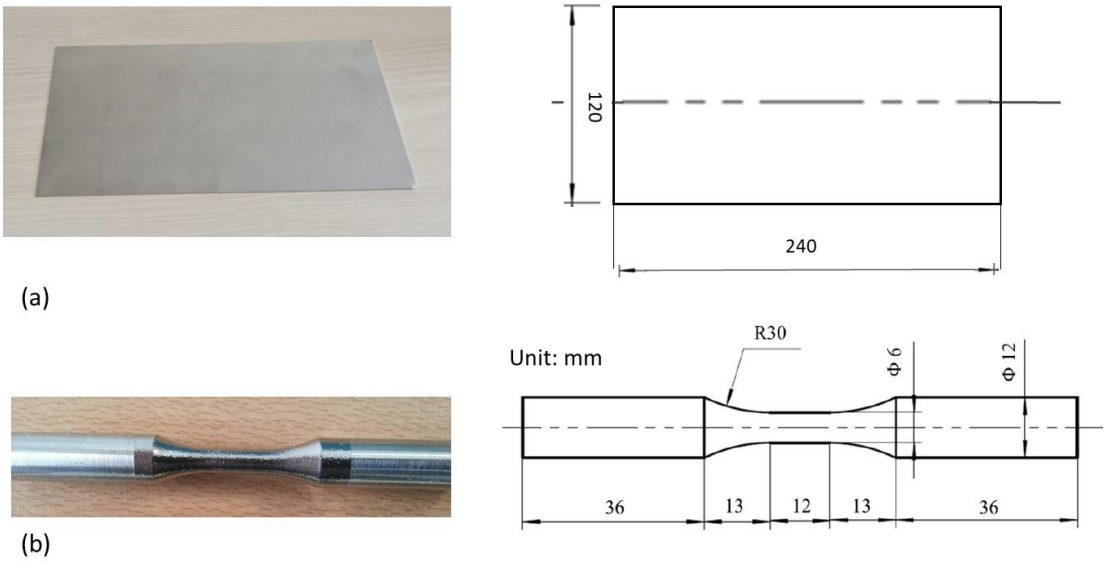

Fig. 2 (a) Tôle d'acier inoxydable 316L et ses dimensions (b) Échantillon sous forme d'haltère en acier 316L pour essais de fatigue et ses dimensions.

Tableau-3 Conditions SMAT pour l'acier inoxydable 316L.

Echantillon	acier inoxydable 316L	
Puissance de générateur	27%	50%
Durée	15 minutes	5 minutes
Bille	Matériau: 100 Cr 6, diamètre: 3mm	
Distance	12 mm	

2.2 Préparation des échantillons

Les échantillons ont été prélevés à la fois dans la partie centrale de l'échantillon sous forme d'haltère et dans la zone traitée de l'échantillon en tôle. Les échantillons ont ensuite été enrobés avec de la résine carbonée conductrice, comme le montre la Fig. 3 (a). Deux petites barres rectangulaires en acier (non-SMATé) ont été placées en contact avec la pièce découpée cyclindrique pour protéger la couche nanocristalline produite proche de la surface. Dans le même but, deux barres rectangulaires coupées dans les zones SMATées de l'échantillon en tôle ont été mises en contact, comme illustré dans la Fig. 3 (d). L'utilisation de résine carbonée conductrice est essentielle pour les observations MEB/EBSD. Les échantillons enrobés ont ensuite été polis mécaniquement jusqu'à l'obtention d'un état poli miroir, puis polis avec une solution OPS.

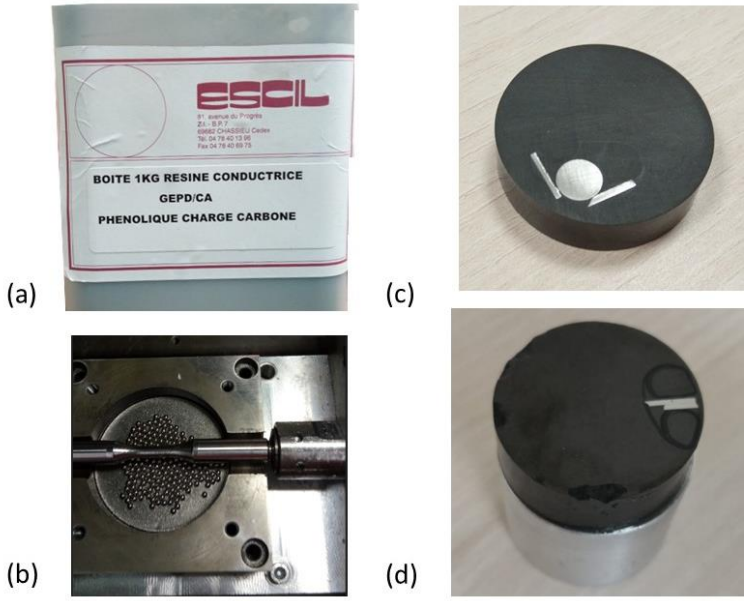

Fig. 3 (a) Résine carbonée conductrice utilisée pour l'enrobage de l'échantillon, (b) Exemple d'échantillon traité après SMAT et (c) Pièce découpée dans l'échantillon d'haltère et enrobée en résine et (d) Pièce découpée dans l'échantillon en tôle.

2.3 Mécanisme de raffinement de grains engendré par SMAT

Les mécanismes de raffinement de grains dû au SMAT pour l'acier inoxydable 316L ont été étudiés par Roland et al. en microscopie électronique en transmission (MET). La Fig. 4 (a) montre une micrographie de la couche superficielle d'un acier inoxydable soumis au SMAT. On peut constater que les nano-grains présentent des orientations cristallographiques très aléatoires. En étudiant plusieurs micrographies électroniques, on peut estimer la taille moyenne des grains, qui est d'environ 20 nm. La Fig. 4 (b) est une micrographie d'un nanograin spécifique à fort grossissement. La limite du grain est bien définie. Une densité élevée de défauts d'empilement induits par la déformation est observée à l'intérieur du grain.

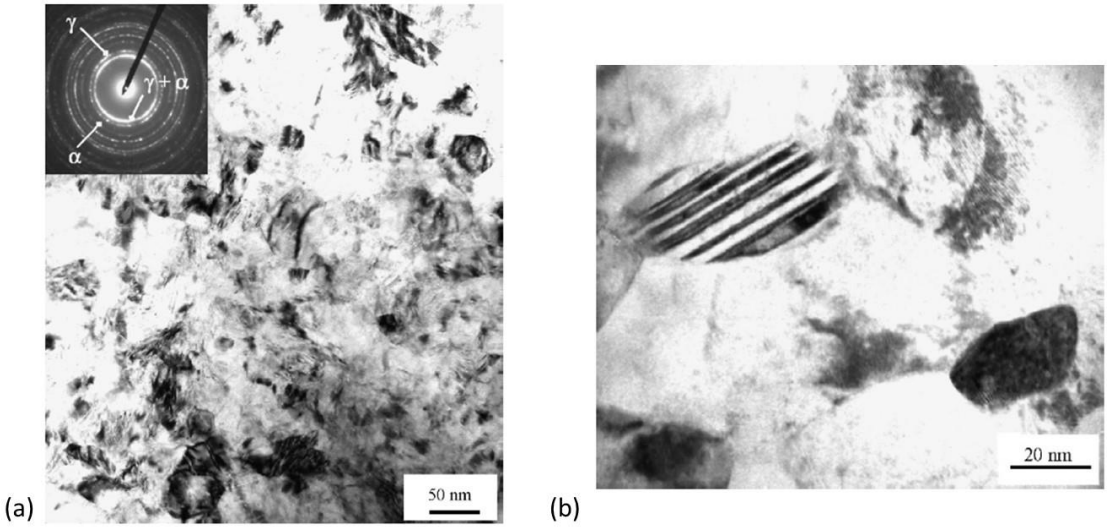

Fig. 4 Observations par MET de l'acier inoxydable 316L traité par SMAT (a) Vue plane typique de la surface supérieure traitée, (b) image en champ clair d'un grain ultrafin avec deux grains.

Afin de clarifier le mécanisme de formation des nano-graine dans la couche de surface supérieure, il est nécessaire d'étudier les microstructures de la couche superficielle à différents stades de la déformation. En effet, la déformation induite par SMAT varie en fonction de la profondeur sous la surface traitée. Ainsi, une microstructure à gradient est formée de la surface jusqu'au cœur du matériau qui est non-affecté. L'observation de la microstructure à différentes profondeurs sous la surface traitée peut donc fournir des informations sur les mécanismes de raffinement des grains. La Fig. 5 (a) est une micrographie prise à une profondeur d'environ 200 µm sous la surface traitée et le niveau de déformation à cette profondeur est relativement faible. La micrographie révèle la présence de macles parallèles unidirectionnelles mécaniquement formées. Ces macles conduisent à la formation d'une structure lamellaire. Certaines dislocations sont arrangées en réseaux planaires qui sont caractéristiques des matériaux à faible énergie de défaut

d'empilement. La Fig. 5 (b) est une micrographie prise à une profondeur de 50 µm sous la surface traitée où l'intensité de traitement est relativement élevée. Comme le montre la micrographie, des interactions entre les macles se produisent avec l'augmentation de la déformation, ce qui permet de subdiviser les grains austénitiques d'origine en blocs plus petits, et finalement de former des nano-grains (de 50 à 400 nm) impliquant des mécanismes tels que le glissement de joints de grains et la rotation de grains. Par conséquent, le SMAT génère un gradient de taille de grains et des défauts structuraux dans la région affectée mécaniquement sous la surface du matériau.

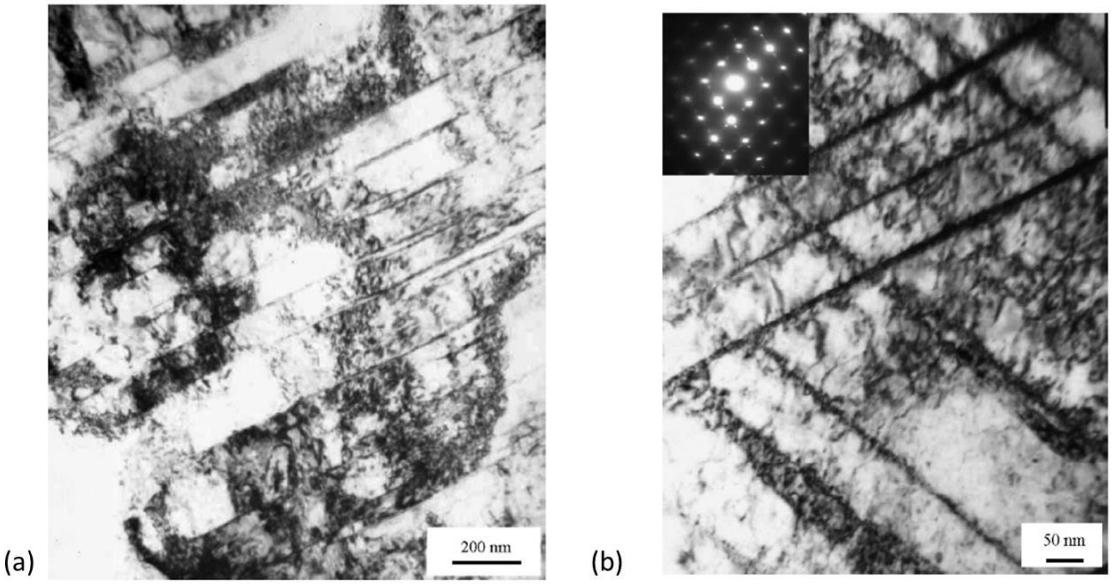

Fig. 5 Observations par MET de l'acier inoxydable 316L traité par SMAT (a) Microstructure de la couche à environ 200 µm de profondeur sous de la surface traitée, (b) Interactions entre macles à 50 µm sous la surface traitée.

2.4 Observation par EBSD de l'acier traité par SMAT

La technique de diffraction des électrons rétrodiffusés (EBSD) a été utilisée pour caractériser la microstructure à gradient générée par SMAT en collaboration avec l'équipe de Thierry Baudin de l'Université Paris Sud (ICMMO). Les données expérimentales ont été obtenues à l'aide d'un microscope électronique à balayage FEG-SEM SUPRA 55 VP fonctionnant à 20 kV équipé du système logiciel OIM™.

Un échantillon pour les observations par EBSD a été prélevé à partir de l'éprouvette sous forme d'haltère SMATée décrite précédemment. La Fig. 6 (a) montre la microstructure à gradient globale générée par SMAT sur la section transversale de l'échantillon, tandis que les Fig. 6 (b), (c), (d) et (e) illustrent les microstructures de différentes zones sous la surface traitée, ce qui révèle les caractéristiques des différentes zones observées. Afin d'obtenir une meilleure résolution pour des zones intéressantes (par exemple la couche nanocristalline), un pas d'acquisition plus fin (25 nm) a été utilisé, sachant que le pas classique est de 0.1 µm pour la zone à grains grossiers. De plus, les données initialement obtenues ont été post-traitées à l'aide du logiciel OIM™ pour améliorer encore la qualité de l'image. D'après la Fig. 6 (a), on peut observer que les impacts aléatoires des billes à grande vitesse sur l'échantillon génèrent une microstructure à gradient. Cette microstructure peut être grossièrement divisée en trois zones : la zone non-affectée, la zone de transition et la zone nanocristalline en extrême surface.

La Fig. 6 (b) illustre la zone non-affectée où la microstructure initiale est intacte avec une taille de grains moyenne comprise entre 10 et 20 µm. Dans cette zone, il n'est pas possible de détecter des grains déformés ni de traces de glissement plastique. De plus, une fraction importante de macles peut être observée dans cette zone. La zone de transition est située entre la zone non-affectée et la zone nanocristalline. Par conséquent, la microstructure de cette zone est plutôt un mélange de grains grossiers et de de grains raffinés. La Fig. 6 (c) illustre le début de la zone de transition située à environ 200 µm sous la surface traitée. Bien qu'aucun changement dans la taille des grains dans cette zone ne puisse être détecté, plusieurs couleurs peuvent être distinguées dans un seul grain. Ceci indique que les grains sont légèrement affectés par le SMAT mais l'influence du SMAT n'est pas assez forte pour diviser les grains. D'autre part, il est possible d'observer clairement des glissements plastiques au sein d'un grain, comme indiqué dans le coin en haut à droit de la Fig. 6 (c). Ces glissements plastiques qui se produisent dans les différents systèmes de glissements sont engendrés par les impacts multidirectionnels des billes pendant le traitement SMAT. On peut donc conclure que les grains d'origine dans cette zone sont subdivisés par des glissements plastiques localisés et qu'aucun nouveau grain n'est clairement formé. Cette observation est conforme à la littérature (Roland 2007, Sun 2017). Avec la diminution de la profondeur, on observe un raffinement progressif des grains qui est due à une déformation plastique plus sévère induite par le SMAT. En raison de l'augmentation du taux de raffinement des grains et aux défauts structuraux générés par le SMAT, une dégradation de la qualité de la cartographie obtenue par EBSD peut être

observée dans la zone de transition proche de la surface traitée. La Fig. 6 (d) montre la fin de la zone de transition située à une profondeur d'environ 15 µm où des nouveaux grains plus petits se sont formés sous l'effet des impacts avec une intensité plus élevée. La taille des grains dans cette zone peut atteindre quelques micromètres. Enfin, la zone nanocristalline est située dans la couche superficielle avec une épaisseur inférieure à 10 µm. Comme l'indique la cartographie, le taux d'indexation dans cette région est faible et un pas de balayage plus petit est nécessaire pour obtenir une diffraction de meilleure qualité. La Fig. 6 (e) est une cartographie de la zone nanocristalline avec un pas de balayage de 25 nm. La taille de grains varie de 50 nm à 300 nm. L'épaisseur de la couche nanocristalline est d'environ 5 µm.

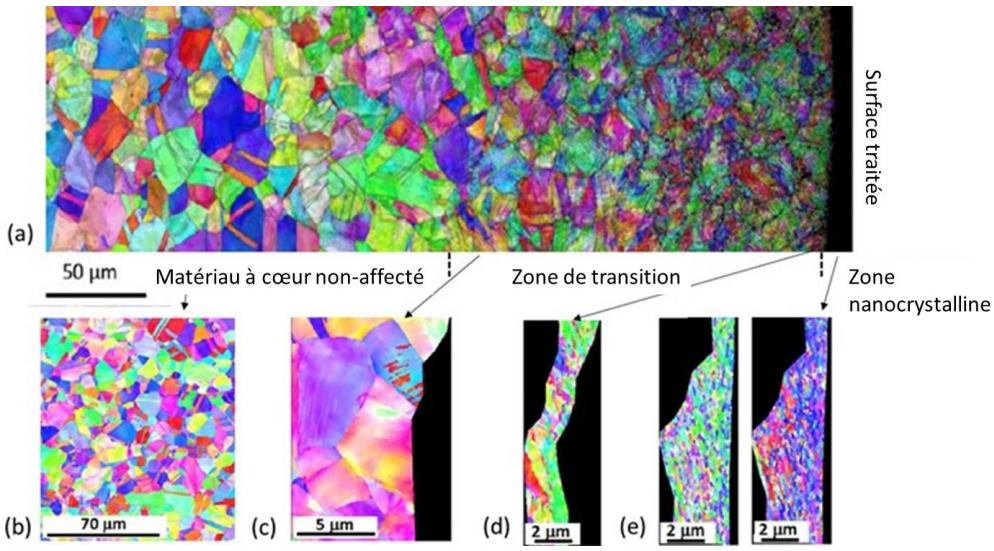

Fig. 6 Observations par EBSD d'un échantillon en acier inoxydable 316L traité par SMAT. (a) Microstructure à gradient générée par SMAT, (b) Matériau à cœur non-affecté, (c) Début de la zone de transition, (d) Fin de la zone de transition (d) zone nanocrystalline.

3 Nanoindentation

Dans cette partie, la nanoindentation est utilisée pour caractériser les propriétés locales de la microstructure à gradient générée par SMAT. Les trois paramètres majeurs induits par SMAT sont respectivement le raffinement des grains, les contraintes résiduelles et l'écrouissage, qui affecteront les mesures de nanoindentation. Les résultats obtenus (courbes de déplacement-charge, module d'Young, dureté et taille et comportement de pile-up) sont ensuite interprétés en fonction de ces paramètres induits par SMAT sur la section transversale de l'échantillon SMATé.

Un certain nombre de distances (de 5 à 1000 µm) sous la surface traitée ont été choisies pour des indentations. La Fig. 7 montre les observations des empreintes par MEB. Pour chaque distance, cinq tests d'indentation ont été réalisées, comme indiqué dans la Fig. 7 (a). Il faut rappeler ici que l'épaisseur de la zone nanocristalline générée par SMAT est d'environ 5 µm. Ainsi, les indentations dans cette zone étaient situées à une profondeur de 5 µm sous la surface traitée, comme l'illustre la Fig. 7 (b) où la taille des empreintes varie de 3,5 µm à 3,7 µm.

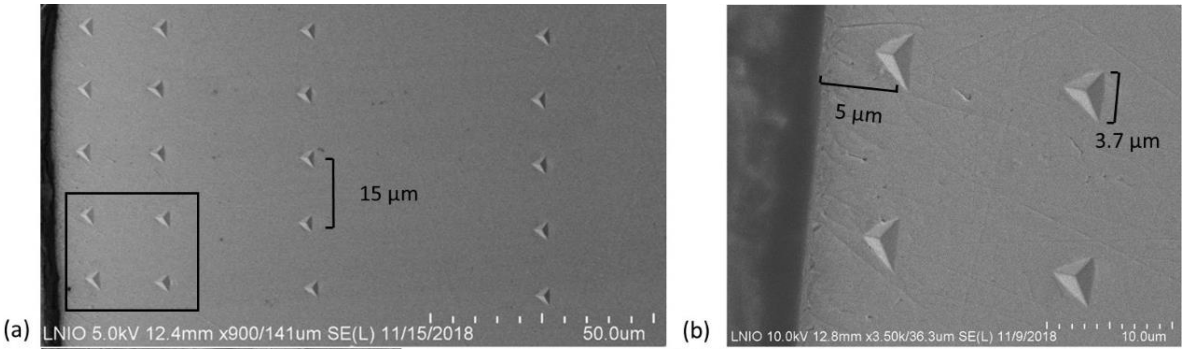

Fig. 7 (a) Illustration des empreintes de la nanoindentation réalisées sur l'échantillon SMATé, (b) Agrandissement de la zone délimitée.

Après les essais d'indentation réalisés le long de la section transversale de l'échantillon SMATé, les courbes charge-déplacement ont été obtenues pour un déplacement imposé de 500 nm. Les résultats correspondants sont représentés sur la Fig. 8.

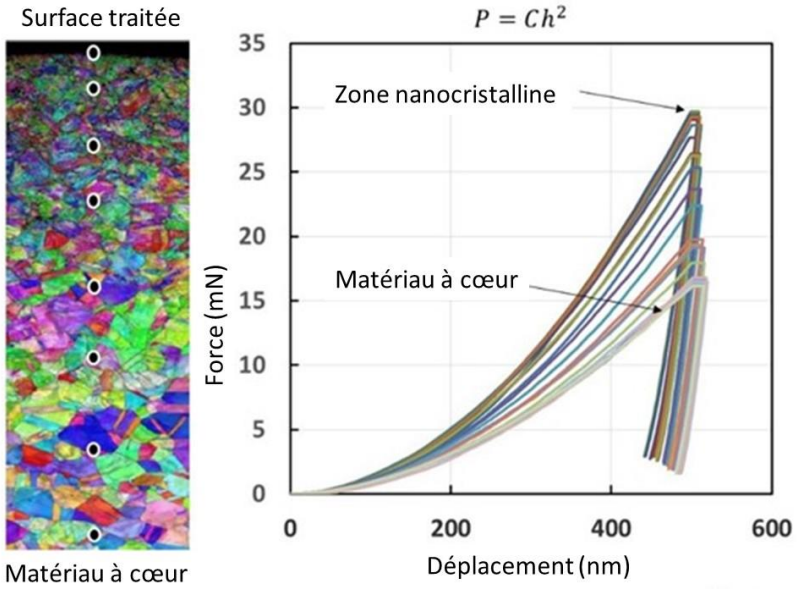

Fig. 8 Courbes force-déplacement des indentations à différentes distances sous la surface traitée.

Les charges maximales et les rapports h_f/h_{max} pour les indentations le long de la section de l'échantillon SMATé sont également illustrés dans la Fig. 9. La charge maximale dans la zone nanocristalline est d'environ 30 mN, ce qui est environ deux fois plus élevé que la charge maximale de la zone qui n'est pas affectée par le SMAT. La charge maximale est stabilisée à une profondeur d'environ 550 µm sous la surface traitée. Ceci indique que la profondeur affectée par SMAT est d'au moins 550 µm. Les trois facteurs induits par SMAT (raffinement des grains, contrainte résiduelle de compression et écrouissage, respectivement) contribuent à une charge de pénétration plus élevée. Dans ce travail, des efforts ont été faits pour tenter de distinguer individuellement l'influence de chacun de ces trois paramètres.

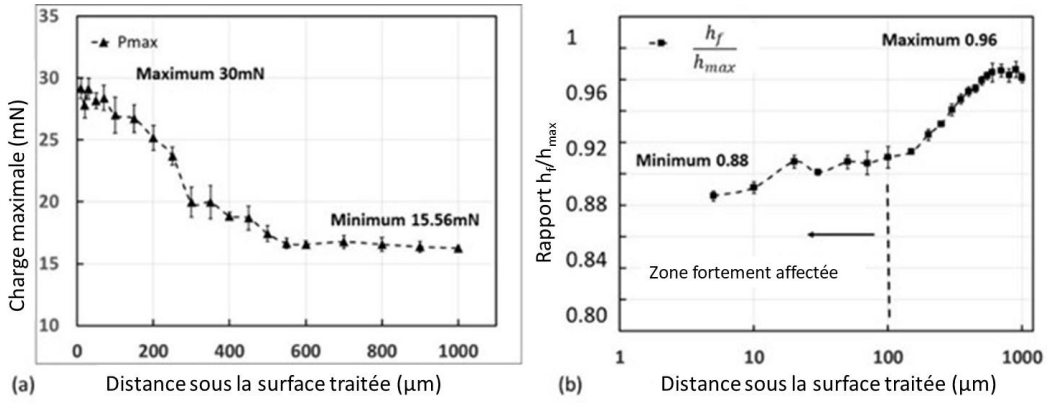

Fig. 9 (a) Charges maximales pour les indentations réalisées le long de la section transversale de l'échantillon SMATé, (b) Rapport h_f/h_{max}.

Tout d'abord, il convient de préciser que lorsque l'intensité du SMAT est élevée, les principaux paramètres induits par ce traitement sont le raffinement des grains, écrouissage et les contraintes résiduelles de compression par rapport à la zone non-affectée. Lorsque l'intensité du SMAT est faible et qu'il n'y a pas de raffinement des grains, le matériau n'est écroui qu'avec une quantité limitée de contraintes résiduelles de compression. Par conséquent, une charge plus élevée dans les zones fortement raffinées pourrait être corrélée aux ces trois facteurs induits par SMAT. Dans la littérature, des études systématiques ont été menées pour étudier l'influence des contraintes résiduelles sur la charge atteinte pendant la nanoindentation. Par exemple, Zhu et al. ont effectué des tests de nanoindentation (profondeur de pénétration de 700 nm) sur un cuivre monocristallin avec différents états de contrainte résiduelle. La contrainte résiduelle variait de -137,4 MPa à 68,4 MPa. Leurs résultats ont montré que l'influence des contraintes résiduelles sur la charge d'enfoncement est de l'ordre de quelques µN, ce qui est négligeable par rapport à la charge maximale (plusieurs mN). Bolshakov et al. ont utilisé la méthode des éléments finis pour étudier le comportement de l'alliage d'aluminium 8009 pendant l'indentation afin de déterminer

comment le processus d'indentation était influencé par les contraintes résiduelles. Les contraintes résiduelles varient de -300 MPa à +350 MPa pour une série de simulations. Les résultats ont montré que la charge maximale augmentait d'environ 1 mN pour une simulation avec un niveau de contrainte résiduelle de -300 MPa. Des résultats similaires ont été trouvés par Mady pour des films céramiques simulés par la méthode des éléments finis. Pour une contrainte résiduelle de compression de -5 GPa, la charge maximale n'augmente que de 2 mN par rapport à un état sans contrainte. Dans notre cas, le matériau étudié est un acier inoxydable 316L, et il a un module d'Young et une dureté plus élevés que ceux du cuivre et de l'aluminium. Selon nos travaux précédents, la contrainte résiduelle de compression générée par SMAT est d'environ -450 MPa dans la zone fortement affectée. Il est raisonnable de conclure que la valeur élevée de la charge maximale dans la zone nanocristalline est principalement due au raffinement des grains induit par SMAT, et que la contrainte résiduelle de compression générée simultanément a une influence relativement faible sur la valeur de charge. Cette hypothèse est cohérente avec la description de la loi Hall-Patch. Cet argument sera expliqué plus tard dans ce travail. En effet, lorsque la charge imposée dépasse la limite d'élasticité du matériau (comme c'est le cas lors de la nano-indentation), l'effet descontraintes résiduelles est faible car l'incompatibilité de déformations élastiques (lié aux contraintes résiduelles) est faible et rapidement effacé par la plasticité.

En plus de la partie de chargement, la courbe de déchargement en nano-indentation donne également des informations importantes sur le matériau étudié, comme la rigidité de contact et l'état de contrainte résiduelle. Par exemple, le rapport entre le déplacement final et le déplacement maximal, h_f/h_{max}, pourrait être corrélé au niveau de contrainte résiduelle et au comportement de pile-up du matériau étudié. Xu et al. ont établi un modèle empirique basé sur des simulations par éléments finis pour la détermination des contraintes résiduelles à partir de la récupération élastique (h_f/h_{max}) en nanoindentation. Un modèle empirique a été utilisé pour déterminer les propriétés plastiques et pour estimer le niveau de contrainte résiduelle au sein du faisceau de quartz fondu mécaniquement poli. Malheureusement, cette méthode n'a pu être appliquée à notre cas parce que la plupart des expériences menées dans la littérature ne tiennent pas compte d'une variation de la taille des grains. Pour un échantillon SMATé, l'affinement de la taille de grains induit un paramètre supplémentaire qui change, la taille de grains d, qui rend l'interprétation des mesures d'indentation difficile. Par conséquent, le rapport h_f/h_{max} de nos essais ne peut pas être corrélé à la contrainte résiduelle de compression. Les rapports h_f/h_{max} pour nos indentations réalisées le long de la

section transversale de l'échantillon SMATé sont illustrés dans la Fig. 9 (b). On peut remarquer que la récupération élastique est plus importante dans la zone fortement raffinée alors qu'il n'y a pratiquement pas de récupération élastique dans la zone du matériau à cœur qui n'est pas affectée par le SMAT. Ceci est principalement dû aux limites d'élasticités élevées dans la zone raffinée.

Pour une indentation où la déformation est élastique, la surface du matériau est généralement tirée vers l'intérieur et vers le bas sous l'effet de l'indentation et un phénomène de sink-in se produit. Lorsque la déformation entre dans le régime plastique, le matériau peut présenter soit du sink-in, soit du pile-up autour de l'indenteur. Cela dépend du rapport E/Y (module d'élasticité / limite d'élasticité) et des propriétés d'écrouissage du matériau. Pour l'acier inoxydable 316L, généralement avec un écrouissage élevé et un rapport E/Y élevé, on s'attend à un phénomène de sink-in, comme illustré dans la Fig. 10 (b) où les mesures AFM ont été effectuées sur une empreinte d'indentation située à 800 µm sous la surface traitée. Pour cette zone éloignée de la surface traitée, la microstructure locale et les propriétés mécaniques n'ont pas été affectées par le SMAT. Cependant, pour les zones affectées par SMAT, la microstructure locale et les propriétés mécaniques, telles que la taille des grains, la limite d'élasticité locale et l'écrouissage, changent en conséquence. Ainsi, un phénomène de pile-up s'est produit dans les zones affectées par SMAT, comme le montre la Fig. 10 (a) pour une empreinte d'indentation obtenue à 50 µm sous la surface traitée.

Le comportement de pile-up pendant la nanoindentation a été un sujet de recherche populaire et il peut être corrélé aux propriétés d'écrouissage du matériau, à l'état de contrainte résiduelle, au rapport E/Y. Le principal paramètre qui affecte le comportement de pile-up est le comportement à l'écrouissage. Pour les matériaux ayant un faible écrouissage, le pile-up a tendance à se produire alors que pour des matériaux présentant un phénomène d'écrouissage marqué (acier inoxydable 316L, par exemple), on s'attend au phénomène de sink-in. De plus, les contraintes résiduelles auraient également une influence sur le comportement de pile-up. Dans la littérature, de nombreuses études ont conclu qu'un état de contrainte résiduelle de compression augmente la quantité de pile-up alors que des contraintes résiduelles de traction ont un effet contraire.

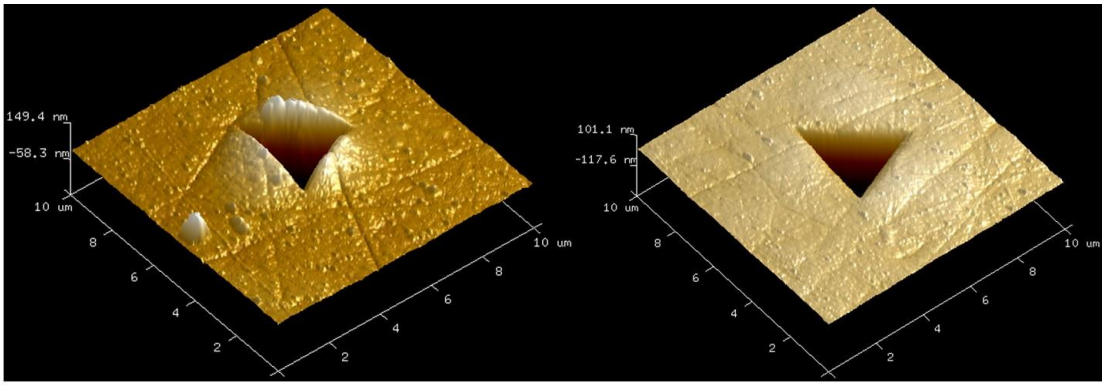

(a) (b)

Fig. 10 Mesures par AFM des empreintes d'indentation (a) situées à 50 µm sous la surface traitée, (b) situées à 800 µm sous la surface traitée.

Il est généralement admis que le phénomène de pile-up augmente la surface de contact entre le matériau et l'indenteur, ce qui conduit systématiquement à une surface de contact erronée et donc à une surestimation des valeurs de dureté et de module d'Young. Dans ce travail, un modèle modifié basé sur le modèle semi-elliptique de Kese a été utilisé afin d'évaluer la vraie surface de contact affectée par le pile-up en utilisant les données AFM (longueur et largeur du pile-up). La surface de contact réelle corrigée est tracée par rapport à la surface d'origine, comme le montre la Fig. 11 (a). Les résultats correspondants de la dureté avant et après correction sont également illustrés dans la Fig. 11 (b). En tenant compte du pile-up, la surface de contact réelle devrait être $A=A_{O-P}+A_{pu}$ où A_{O-P} est la surface de contact originale calculée par la méthode standard d'Oliver-Pharr et A_{pu} est la somme des surfaces projetées de trois pile-up autour des bords de l'empreinte. La nouvelle surface de contact est ensuite utilisée pour recalculer la dureté. Une légère diminution de la dureté peut être observée (Fig. 11 (b)). Par exemple, la dureté d'origine pour la zone nanocristalline est d'environ 5,03 GPa alors que cette valeur est réduite à 4,20 GPa lorsqu'une correction est appliquée pour obtenir la nouvelle surface de contact. Il convient de souligner qu'il existe plusieurs méthodes pour tenir compte de la vraie surface de contact dans le cas d'un pile-up, mais chaque méthode est limitée à un matériau étudié spécifique ou à une certaine gamme de charges. Il est possible que notre méthode modifiée utilisée pour évaluer la surface de contact réelle ne soit pas parfaite. Il serait donc intéressant de trouver une méthode pour corriger avec plus de précision le pile-up des matériaux SMATés dans de futurs travaux.

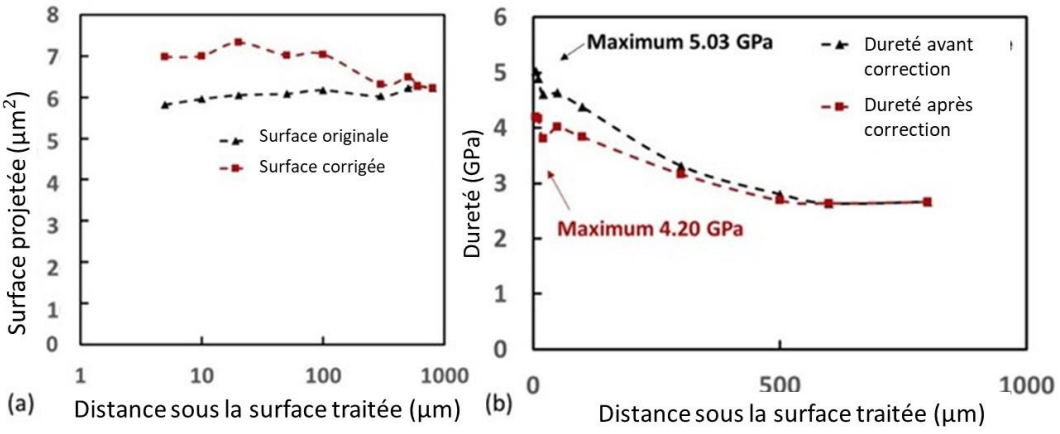

Fig. 11 (a) Surface de contact d'origine selon la méthode d'Oliver-Pharr standard vs surface de contact corrigée selon une méthode modifiée, (b) Résultats de dureté correspondants avant et après correction.

4 Compression de micro-piliers

4.1 Fabrication de micro-piliers

Dans la partie précédente, la microstructure à gradient générée par SMAT a été caractérisée par EBSD. La zone nanocristalline, la zone de transition et la zone du matériau à cœur ont pu être distinguées. Par conséquent, quatre endroits ont été choisis comme sites de fabrication de micro-piliers, à savoir 5, 30, 70, 300 µm sous la surface traitée, comme illustré dans la Fig.12 (a). Les micro-piliers ont été fabriqués à l'aide d'un FIB fonctionnant avec une source d'ions métalliques liquides au gallium. Le processus de fabrication comprend trois étapes. Tout d'abord, une coupe grossière autour du micro-pilier a été réalisée avec un courant élevé de 21 nA. Ensuite, le micro-pilier a été mis en forme à l'aide d'un courant de sonde intermédiaire de 0,8 nA. Enfin, la surface du micro-pilier a été polie avec le même courant afin d'obtenir une surface latérale lisse. Les micro-piliers ont une forme légèrement tronconique. Les diamètres supérieur et inférieur sont respectivement 2,5 et 3,5 µm, et la hauteur est 10 µm. Leur angle de conicité (angle entre l'axe et la surface périphérique conique) est d'environ 2°. Il faut préciser ici que l'angle de conicité doit être inférieur à 3°, ce qui est crucial pour obtenir une courbe contrainte-déformation fiable selon les travaux antérieurs présentés dans la littérature (Fei 2012). Un exemple de micro-pilier est illustré dans la Fig. 12 (b).

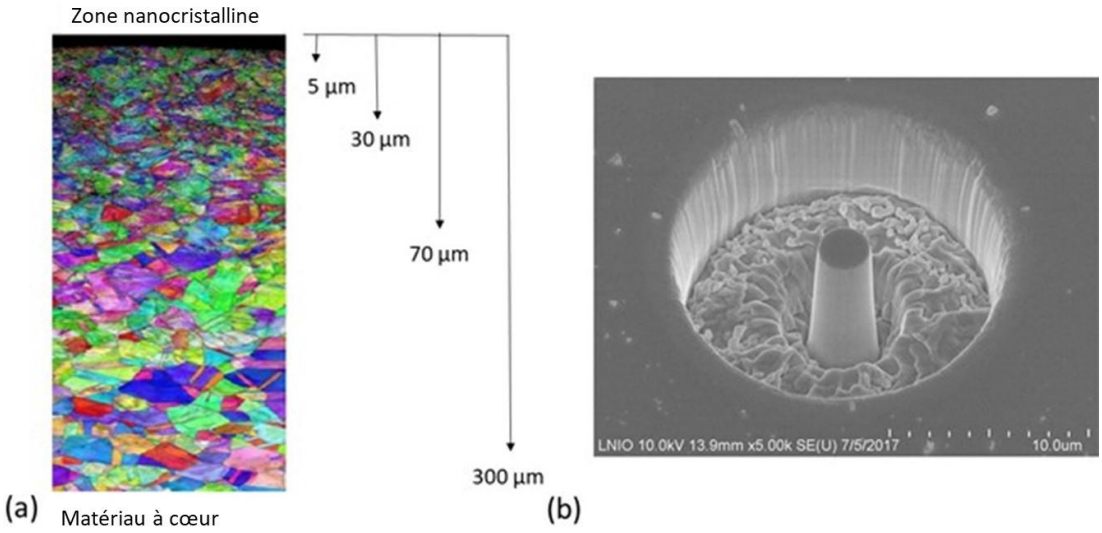

Fig. 12 (a) Zones sélectionnées pour la fabrication de micro-piliers, (b) Un exemple de micro-pilier.

4.2 Compression monotone de micro-piliers

Les courbes contrainte-déformation de micro-piliers ont été obtenues après des essais de compression monotone. Les résultats sont présentés sur la Fig.13. On constate que pour la plupart des courbes contrainte-déformation, une non-linéarité initiale s'est produite lorsque l'indenteur est mis en contact avec la surface supérieure de chaque micro-pilier. D'après nos travaux antérieurs, cela est probablement dû au désalignement entre l'indenteur et la surface supérieure du micro-pilier. Ces travaux antérieurs montrent que même avec un léger désalignement de 5°, le régime élastique (la pente de la courbe) est clairement affecté, entraînant une non-linéarité du régime élastique et une certaine diminution de la force enregistrée et par conséquent de la contrainte calculée. Au fur et à mesure du déplacement de l'indenteur, l'indenteur est entièrement en contact avec la surface supérieure du pilier. Ainsi, la contrainte commence à augmenter linéairement avec la déformation, ce qui correspond au régime de déformation élastique du matériau.

Lorsque le déplacement de l'indenteur se poursuit, les piliers commencent à se déformer plastiquement. La limite d'élasticité de chaque pilier peut être obtenue directement des courbes contrainte-déformation. Comme on peut le constater, la limite d'élasticité du micro-pilier dans la couche nanocristalline est d'environ 1450 MPa, soit environ 2,5 fois plus élevée que celle (580 MPa) du micro-pilier dans la zone du matériau à cœur (300 µm sous la surface traitée). Il est déjà conclu dans la troisième partie que pour la zone nanocristalline où l'intensité du SMAT est élevée, l'effet de raffinement des grains est

la principale contribution à l'augmentation de la dureté et de la limite d'élasticité, comme le suggère la loi de Hall-Petch. En ce qui concerne la contrainte résiduelle de compression générée par SMAT, son influence sur la limite d'élasticité du micro-pilier semble négligeable. Le micro-pilier usiné dans la couche nanocristalline est composé de nano-grains et de grains submicroniques dont la taille varie de 50 à 300 nm. Avec de tels petits grains, les activités de dislocations sont limitées en raison de la grande fraction volumique des joints des grains, ce qui, à son tour, augmente la résistance du matériau. Des résultats similaires ont été trouvés par Tumbajoy-Spinel et al. qui ont étudié la structure à gradient générée par des traitements de surface par impact. Une représentation schématique résumant les différentes contributions des effets mécaniques impliqués est donnée dans la Fig. 14. On peut donc en tirer les conclusions suivantes :

1) La limite d'élasticité du micro-pilier dans la zone nanocristalline (où l'intensité d'impact est élevée) est environ 2,5 fois plus élevée que celle du micro-pilier dans la zone non affectée.

2) L'effet de raffinement de grains est le facteur prédominant qui contribue à l'augmentation de la limite d'élasticité des micro-piliers situés dans les zones fortement affectées par le SMAT.

3) Dans les zones où l'intensité du SMAT est faible et où il n'y a pas de raffinement de grains, l'écrouissage (augmentation de la densité de dislocations) est le principal mécanisme de renforcement.

Outre la différence de la limite d'élasticité, le comportement à l'écrouissage des micro-piliers est d'un grand intérêt. Dans la littérature, il est indiqué que les matériaux nanocristallins possèdent une limite d'élasticité augmentée, mais qu'ils s'écrouissent relativement peu (ou pas du tout) par rapport à leurs homologues à grains grossiers. Ceci est cohérent avec nos résultats. L'écrouissage des micro-piliers dans la zone fortement affectée (5 et 30 μm sous la surface traitée) est faible en raison de la faible taille de grains. Pour le micro-pilier situé à 70 μm sous la surface traitée, on remarque un écrouissage relativement élevé qui peut être attribué à une taille de grains plus importante dans cette zone. En ce qui concerne la zone à grains grossiers (300 μm sous la surface traitée), un écrouissage important est attendu car la microstructure et les propriétés mécaniques ne sont ici que peu affectées par le SMAT. En revanche, on observe un faible écrouissage également pour cette région loin de la surface. Il est important de préciser que la taille des grains dans cette zone varie de 10 à 50 μm alors que la taille du micro-pilier n'est que de quelques μm. Il est donc possible que le micro-pilier ait été fabriqué sur un seul grain et que par conséquent le

micro-pilier soit monocristallin. Une fois les glissements plastiques activés, le micro-pilier monocristallin se déforme plastiquement de façon parfaite et dans une direction préférentielle, selon l'orientation du grain. Ainsi, le faible écrouissage (ou l'absence d'écrouissage) de la courbe contrainte-déformation dans la zone à grains grossiers ne représente pas vraiment le comportement d'écrouissage global de cette zone. Les différents comportements mécaniques observés pour les micro-piliers situés dans différentes zones résultent de leurs mécanismes de déformation correspondants. Dans la section suivante, des observations par MEB de l'état déformé des micro-piliers après compression seront présentées. Les résultats correspondants ont été interprétés en fonction de leurs mécanismes de déformation.

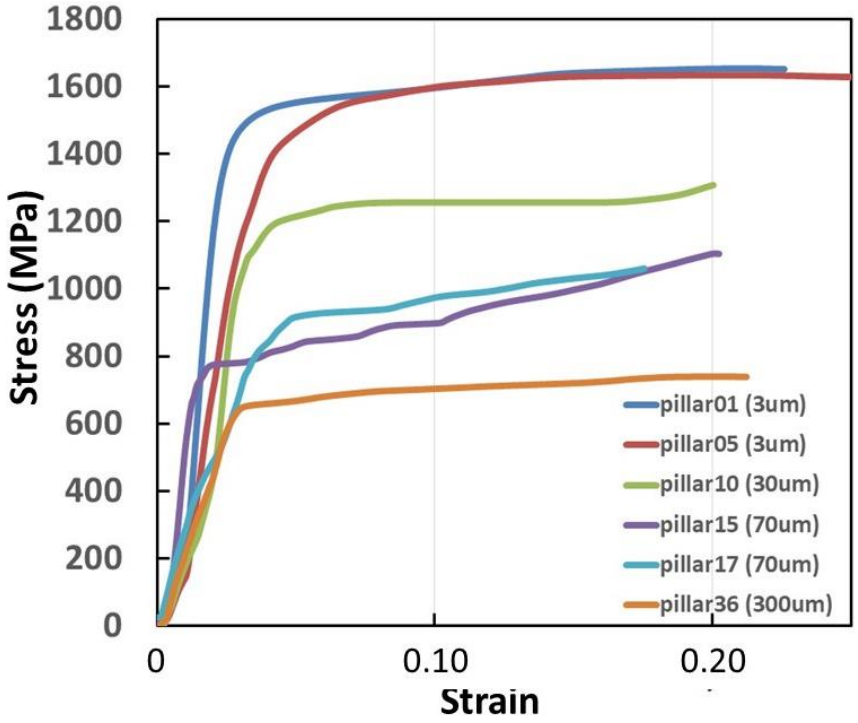

Fig. 13 Courbes contrainte-déformation des micro-piliers fabriqués dans différentes zones sélectionnées sur la section transversale de l'échantillon SMATé.

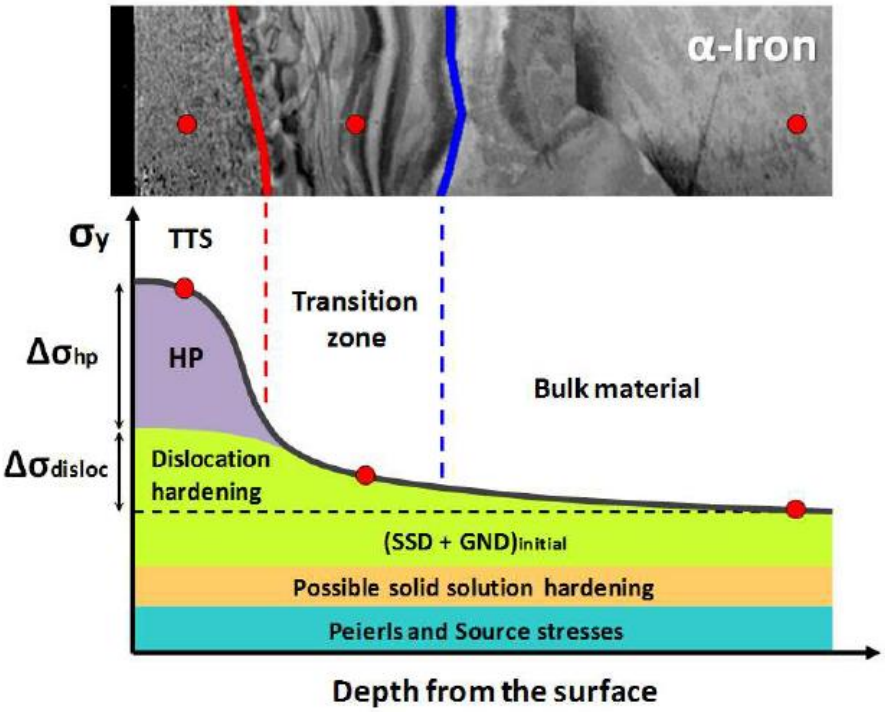

Fig. 14 Représentation schématique résumant les différentes contributions des effets mécaniques impliqués dans le renforcement des aciers ferrites traités par traitements de surface par impact (Tumbajoy-Spinel 2018).

4.3 État déformé des micro-piliers

Le renforcement des matériaux nanocristallins se fait en général au détriment de leur ductilité. Ceci se traduit par une faible valeur d'allongement à rupture lors de l'essai de traction. La déformation que les matériaux nanocristallins peuvent subir avant rupture lorsqu'ils sont soumis à un chargement de traction est beaucoup plus faible que celle de leurs homologues à grains grossiers. Dans le cas d'essais de compression, les matériaux nanocristallins présentent un faible écrouissage, ce qui peut être attribué à l'augmentation de la fraction volumique de joints des grains avec la diminution de la taille des grains. Ainsi, une plus grande résistance au mouvement des dislocations conduit à la localisation de la déformation, ce qui est le cas des micro-piliers situés dans la zone nanocristalline, comme illustré dans la Fig. 15 (a). On remarque que la déformation est confinée dans la zone supérieure du micro-pilier et qu'aucune trace de glissement plastique ne peut être détectée. En fait, lorsque la taille des grains est réduite à l'échelle du nanomètre, le glissement aux joints des grains et/ou la rotation des grains ont tendance à être dominants. Le mécanisme de déformation est désormais contrôlé par les joints du grain plutôt que par les dislocations.

Par ailleurs, la Fig. 15 (b) montre l'état déformé d'un micro-pilier situé à 300 μm sous la surface traitée. On peut observer que la déformation est essentiellement absorbée par le glissement plastique, caractéristique typique du comportement à la déformation de gros grains. Les bandes de glissement, qui sont clairement visibles sur le pilier, ont tendance à se produire dans deux directions préférentielles. C'est peut-être parce que le micro-pilier est composé d'un ou deux gros grains, comme suggéré précédemment. Ainsi, les états déformés des micro-piliers permettent de comprendre indirectement leur mécanisme de déformation.

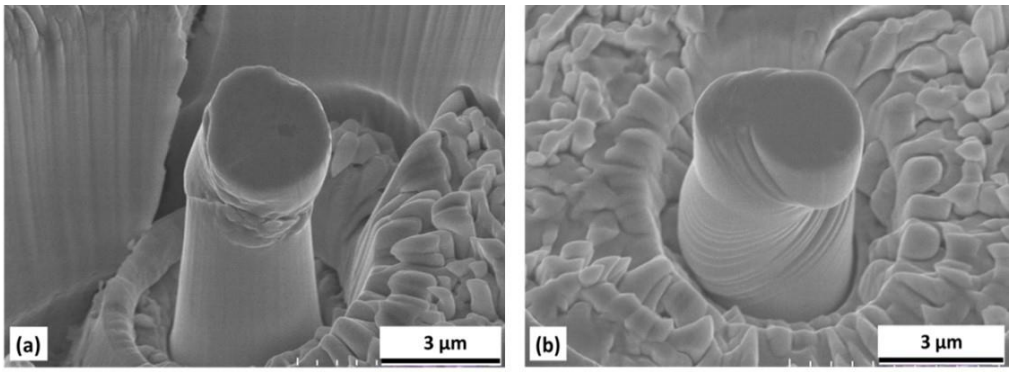

Fig. 15 Observation par MEB des micro-piliers déformés (a) dans la couche nanostructurée et (b) à une distance de 300 μm sous la surface traitée.

5 Simulation de déformation du matériau SMATé

5.1 Construction d'un modèle 2D pour les matériaux nanocristallins

Les simulations des matériaux nanocristallins prennent souvent beaucoup de temps en raison de l'abondance de nano-grains qui constituent une pièce mécanique. Pour cette raison, un modèle de volume élémentaire représentatif (VER) a été construit dans ce travail. Selon la théorie, le VER est le plus petit volume sur lequel on peut effectuer une mesure qui donnera une valeur représentative de l'ensemble. Un exemple est donné à la Fig. 16. Hill et al. ont défini le VER comme un échantillon d'un matériau hétérogène qui :

1) est tout à fait typique de l'ensemble du mélange en moyenne,
2) contient un nombre suffisant d'inclusions pour que les propriétés apparentes soient indépendantes des valeurs de traction et de déplacement de la surface, à condition que ces valeurs soient macroscopiquement uniformes.

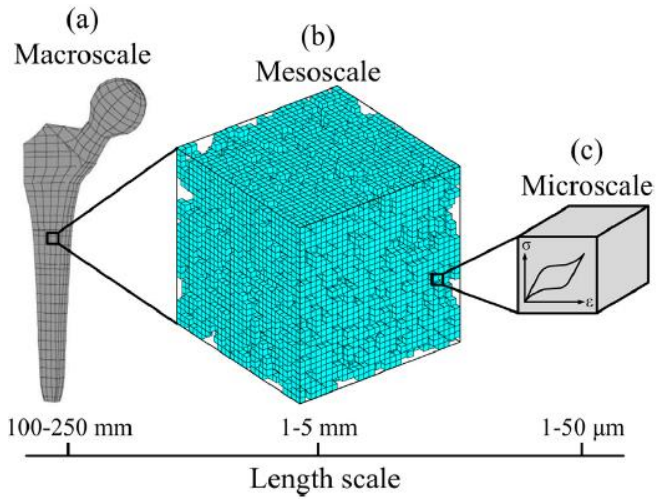

Fig. 16 Illustration de l'approche de modélisation multi-échelle à l'aide du volume élémentaire représentatif.

En appliquant le concept de VER, un modèle 2D est construit, basé sur le diagramme de Voronoi et la fonction Level-Set couplés avec la plasticité cristalline, comme illustré dans la Fig. 17. Le matériau simulé est un cuivre qui possède une structure CFC. Premièrement, étant donné que les activités des dislocations sont moins susceptibles de se produire à l'intérieur d'un nano-grain, une valeur élevée de cission critique résolue (CRSS) est attribuée au grain. De plus, avec l'augmentation de la fraction volumique de joints de grains, la déformation est gouvernée par les joints de grains plutôt que par les dislocations, comme par exemple le cisaillement aux joints de grains. La déformation plastique est plus susceptible de s'activer dans les zones aux joints de grains. Par conséquent, une cission critique résolue plus petite est répartie dans la zone des joints de grains. Dans notre cas, la cission critique résolue de l'intérieur du grain est réglée pour être deux fois plus élevée que celle des joints de grain. Enfin, deux modèles (avec dix grains) sont générés avec différentes valeurs de fraction volumique de joints de grains. Les orientations des dix grains sont réparties aléatoirement. Les paramètres utilisés dans les simulations sont récapitulés dans le tableau 9. Il faut préciser que la fraction volumique de joints de grains a une relation inversement proportionnelle à la taille des grains, d. Le modèle 1 a une fraction volumique plus grande de joints des grains et, par conséquent, a une taille de grains plus petite. Pour cette raison, les valeurs de la cission critique résolue pour le modèle 1 sont supérieures à celles du modèle 2. Selon la littérature, les tailles de grains du modèle 1 et du modèle 2 pourraient être estimées à environ 20 nm et 50 nm respectivement, pour les fractions volumiques des joints de grains données (30% et 15%). Les modèles ont été soumis à une simulation de traction monotone avec une vitesse de déformation de 0,01 s^{-1}.

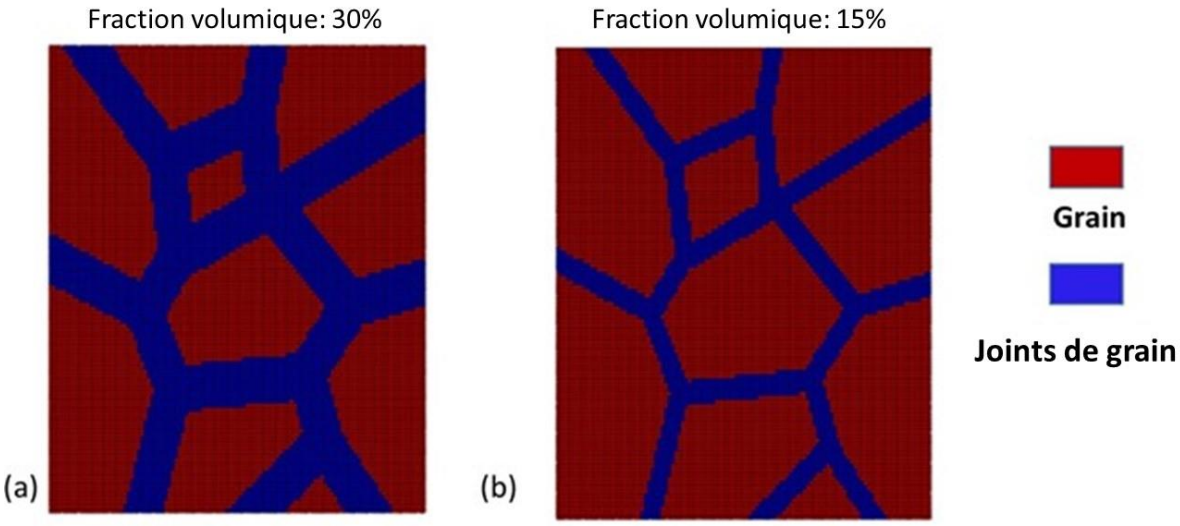

Fig. 17 VER en 2D (a) Modèle 1 : fraction volumique de joints de grains d'environ 30%, (b) Modèle 2 : fraction volumique de joints de grains d'environ 15%.

Tableau 4- Paramètres utilisés pour les deux modèles FEM avec différentes fractions volumiques de joints de grains.

Modèle	Fraction volumique	CRSS (grain)	CRSS (joints)	Taille de grains
Modèle 1	~30%	603MPa	301 MPa	20 nm
Modèle 2	~15%	242 MPa	121 MPa	50 nm

5.2 Résultats de la simulation

Les résultats des simulations (évolution de champs de déformation plastique et de contrainte, et courbes de contrainte-déformation) sont illustrés dans les Fig. 18, Fig. 19 et Fig. 20. Pour les deux modèles FEM, la déformation plastique s'est amorcée dans les joints des grains en raison de valeurs plus faibles de la cission critique résolue. Ceci est cohérent avec les résultats présentés dans la littérature. En effet, des valeurs plus faibles de la cission critique résolue ainsi qu'une fraction volumique importante de joints de grains mènent également à la localisation de la déformation au niveau des joints de grains. Pour le modèle 1, l'initiation et la localisation de la déformation plastique sont plus marquées en raison d'une fraction volumique plus importante de joints de grains par rapport au modèle 2. Des résultats similaires ont été obtenus par Anand et al. qui ont introduit des éléments cohésifs le long de joints de grains pour modéliser le glissement au niveau des joints de grains. L'intérieur des grains a été modélisé avec un modèle de plasticité cristalline. Ils ont appliqué leur modèle pour étudier le comportement d’un nickel nanocristallin. Ils ont

découvert que la déformation plastique s'amorçait dans les zones de joints de grains, ce qui a fini par entraîner une déformation significative. Les courbes contrainte-déformation pour les modèles 1 et 2 sont présentées sur la Fig. 20 (a). Le modèle 1 présente une limite d'élasticité plus élevée que le modèle 2 due à la taille réduite des grains. Les courbes de simulation correspondent qualitativement aux résultats présentés dans la littérature, comme le montre la Fig. 20 (b). On peut remarquer que pour les modèles 1 et 2, un phénomène d'adoucissement semble se produire en fonction des courbes contrainte-déformation. Il a été démontré que lorsque la taille des grains diminue jusqu'au régime nanocristallin, un adoucissement peut se produire, à savoir le phénomène inverse de Hall-Petch. Dans notre cas, l'adoucissement peut être lié à une fraction volumique importante de joints de grains associée avec une faible valeur de la cission critique résolue.

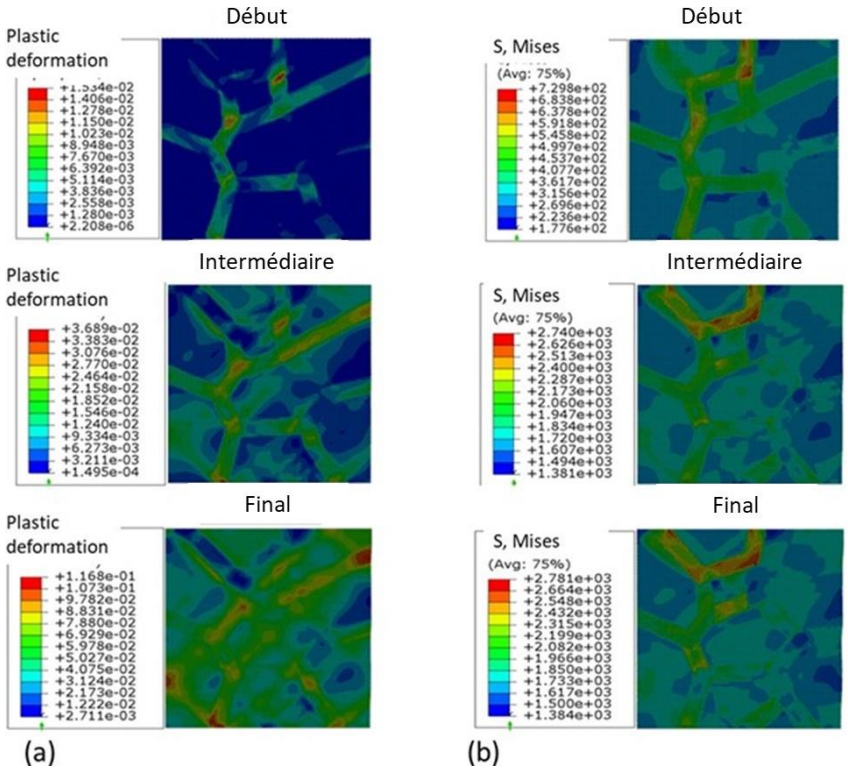

Fig. 18 Résultats de simulation obtenus avec le modèle 1 (fraction volumique de joints de grain 30%) : (a) Évolution de la déformation plastique, (b) Évolution de la contrainte équivalente.

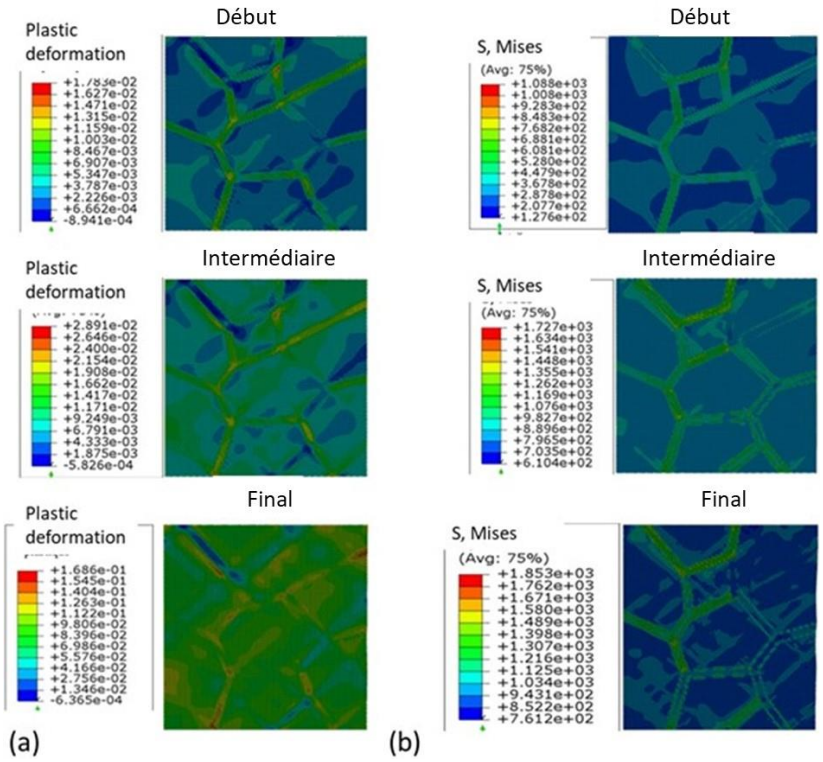

Fig. 19 Résultats de simulation obtenus avec le modèle 2 (fraction volumique de joints de grain 15%) : (a) Évolution de la déformation plastique, (b) Évolution de la contrainte équivalente.

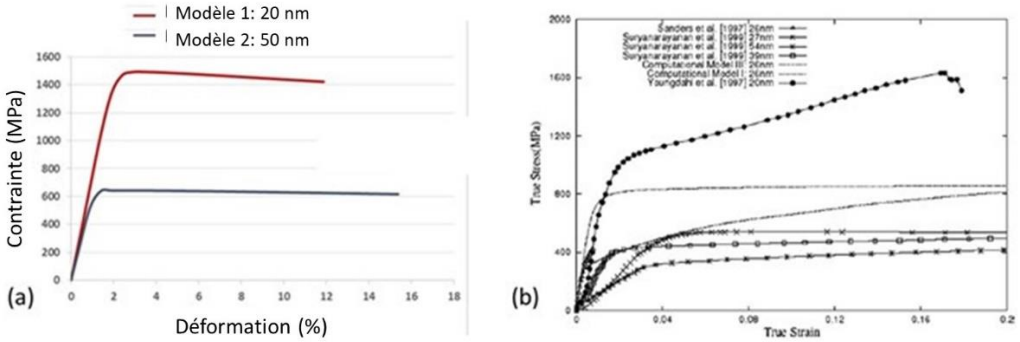

Fig. 20 (a) Courbes de contrainte-déformation de simulation pour les modèles 1 et 2, (b) Diverses sources de résultats expérimentaux de la littérature (Meyers 2006).

6 Conclusions et perspectives

6.1 Conclusions

Il a été démontré que le traitement SMAT peut générer une microstructure à gradient dans la zone proche de la surface des matériaux métalliques. Les paramètres induits par SMAT, à savoir le raffinement des grains, les contraintes résiduelles et l'écrouissage existent le long de la section transversale du matériau traité. On a constaté que cette microstructure à gradient peut améliorer les propriétés mécaniques des matériaux telles que les propriétés de fatigue et la résistance à la traction. Néanmoins, l'accent a surtout été mis

sur les propriétés globales de la microstructure à gradient et peu d'efforts ont été consacrés à la caractérisation individuelle des différentes profondeurs de la surface traitée. Le but de cette thèse est de caractériser respectivement les propriétés locales des différentes couches afin de mieux comprendre les effets bénéfiques de la microstructure à gradient. Ainsi, diverses techniques de caractérisation ont été utilisées pour étudier la microstructure à gradient générée par SMAT. Parmi ces techniques, on peut citer l'EBSD, la DRX, l'AFM, la MET, la nanoindentation, le FIB et la compression de micro-piliers.

Les observations par EBSD ont été effectuées pour étudier la microstructure à gradient générée par SMAT ainsi que sa stabilité thermique. Une attention particulière a été accordée à la préparation de l'échantillon pour l'observation par EBSD, car un bon état de surface de l'échantillon est nécessaire. Un mauvais état de surface de l'échantillon entraînera une dégradation de la qualité de l'image avec la présence de zones non indexées. Les résultats ont révélé que l'épaisseur de la couche nanostructurée est d'environ 5 μm et que le raffinement des grains est sévère jusqu'à 100 μm sous la surface traitée. La taille de grains pour la zone nanocristalline est entre 50 et 300 nm.

Dans la partie sur la nanoindentation, il a été démontré que trois paramètres majeurs induits par le SMAT affectent les mesures de nanoindentation. Les résultats obtenus (courbes de charge-déplacement, module d'Young, dureté et comportement de pile-up) ont été interprétés par la suite en fonction de ces paramètres induits par le traitement. Plusieurs conclusions peuvent être tirées comme suit :

(1) Le raffinement des grains est le principal facteur qui contribue à l'augmentation de la dureté et de la charge d'indentation, alors que l'état de contrainte résiduelle de compression joue un rôle relativement mineur.

(2) La dureté et le module de Young mesurés semblent être indépendants de l'état de contrainte résiduelle de compression.

(3) Un phénomène de pile-up s'est produit dans la zone affectée par SMAT en raison de la diminution de l'écrouissage. Le phénomène de pile-up doit être pris en compte afin de corriger la surface de contact réelle. La dureté recalculée avec la nouvelle surface de contact est légèrement diminuée.

Dans la partie de compression de micro-piliers, les résultats des essais de chargement monotone ont montré que les micro-piliers dans la zone nanostructurée ont une limite d'élasticité plus élevée associée à un faible écrouissage (ou absence d'écrouissage) en raison des effets sévères du raffinement des grains. De petits nano-grains qui constituent le micro-pilier dans cette zone conduisent à une déformation plus homogène. Par contre, le

mécanisme de déformation des micro-piliers à gros grains situé à 300 μm sous la surface traitée est différent. Dans cette zone à gros grains, la déformation plastique est le résultat de l'activation classique de systèmes de glissement préférentiel.

Dans la partie de simulation numérique, la méthode des éléments finis a été utilisée pour simuler la déformation de matériaux nanocristallins. Un modèle de plasticité cristalline a été utilisé et des efforts ont été faits pour prendre en compte les effets de plusieurs paramètres, tels que la fraction volumique des joints de grains, la cission critique résolue. Le diagramme de Voronoi et la méthode Level-Set ont été utilisés pour la génération de modèles par éléments finis. Deux modèles avec différentes fractions volumiques ont été générés. Les résultats de simulations suggèrent que la déformation plastique s'est amorcée au niveau des joints de grains, ce qui est cohérent avec les résultats de la littérature.

Des études systématiques, tant expérimentales que numériques, ont donc été consacrées à la caractérisation individuelle des différentes zones de la microstructure à gradient. La particularité de ce travail, par rapport aux travaux précédemment effectués dans la littérature, est que la caractérisation individuelle des différentes couches de la microstructure à gradient a été réalisée grâce à différentes techniques de caractérisation à l'échelle micro et nanométrique. La compréhension des effets bénéfiques de la microstructure à gradient est ainsi améliorée et les méthodes d’étude actuelles, telles que la nanoindentation, la technique EBSD et la DRX, pourraient être appliquées pour optimiser l'intensité du traitement par SMAT afin de générer une microstructure à gradient avec des propriétés optimales.

6.2 Perspectives

Comme nous l'avons déjà mentionné, des études systématiques, tant expérimentales que numériques, ont été consacrées à la caractérisation individuelle de différentes régions de la microstructure à gradient. La compréhension des effets bénéfiques de la microstructure à gradient est améliorée et les méthodes utilisées dans ce travail pourraient être appliquées pour optimiser les conditions de SMAT afin de concevoir une microstructure à gradient optimales en termes de résistance mécanique. Cependant, certains phénomènes observés n'ont pas été clairement compris et certaines méthodes de modélisation méritent d'être améliorées.

Le raffinement des grains, les contraintes résiduelles et l'écrouissage des matériaux SMATés ont été caractérisés sur la base des analyses par EBSD et DRX. En effet, les caractéristiques de la microstructure des matériaux SMATés sont très complexes car ces paramètres induits par SMAT sont fortement couplés. Par exemple, la mesure des contraintes résiduelles au sein de matériaux SMATés à l'aide de la diffraction des RX prend beaucoup de temps et seules des mesures qualitatives de l'écrouissage peuvent être effectuées. Il serait intéressant de trouver une méthode pratique pour calculer directement la contrainte résiduelle à partir des courbes de nanoindentation, par exemple la récupération élastique au déchargement.

L'observation par EBSD a révélé la microstructure de la couche nanostructurée. Cependant, la précision n'est pas suffisante pour la caractérisation de la structure des zones au niveau des joints de grains. Comme nous l'avons vu précédemment, une grande partie de joints de grains sont impliqués dans le mécanisme de déformation du matériau nanocristallin. Par conséquent, il est recommandé d'effectuer des observations plus précises sur la structure des joints des grains dans la zone nanostructurée. La MET semble être un outil qualifié pour des études plus approfondies de la structure des joints de grains de la zone nanostructurée (structure de dislocations, disposition des atomes et épaisseur de joints de grains, etc.).

Les essais de compression de micro-piliers réalisés dans le cadre de ce travail ne sont pas des essais in situ. Par conséquent, les états déformés des micro-piliers ont été observés après les essais de compression et aucune information concernant l'évolution du processus de déformation de micro-piliers n'a pu être obtenue. Dans le future, des essais de compression de micro-piliers in situ seront effectués car ils permettent d'enregistrer l'évolution du processus de déformation et fournissent des informations précieuses sur les mécanismes de déformation des micro-piliers. En outre, d'éventuels changements structurels de micro-piliers à différents niveaux de déformation doivent être observés à l'aide d'une méthode de caractérisation plus précise (MET par exemple) même si cela est assez difficile à réaliser. Par exemple, des changements structurels tels que le glissement aux joints de grains, le cisaillement de joints de grains et l'émission de dislocations aux joints de grains pourraient avoir lieu dans la zone nanocristalline tandis que des activités de dislocations et l'activation ultérieure des systèmes de glissement préférentiel sont prévues dans la zone de grains de taille ordinaire.

En ce qui concerne la simulation de la déformaiton des matériaux nanocristallins, seuls des VER en 2D avec dix grains ont été construits. La plasticité cristalline a été appliquée

pour les simulations dans ce travail malgré ses limites. Il est clair que ce modèle n'est pas parfait. Par conséquent, il sera nécessaire de trouver un modèle meilleur qui tienne compte des effets d’échelle de longueur lorsque la taille des grains est réduite à l'échelle nanométrique et, espérons-le, d'étendre ce modèle amélioré à des simulations tridimensionnelles.

Reference

[1] H. Gleiter, “Nanocyrstalline Materials,” *Prog. Mater. Sci.*, vol. 33, no. 4, pp. 223–315, 1989.

[2] J. A. Eastman, J. R. Weertman, and P. G. Sanders, “Elastic and tensile behavior of nanocrystalline copper and palladium,” *Acta Mater.*, vol. 45, no. 10, pp. 4019–4025, 1997.

[3] M. A. Meyers, A. Mishra, and D. J. Benson, “Mechanical properties of nanocrystalline materials,” *Prog. Mater. Sci.*, vol. 51, pp. 427–556, 2006.

[4] C. Suryanarayana, “Mechanical Alloying and Milling Marcel Dekker,” *Ee. Uu*, vol. 46, pp. 59–78, 2004.

[5] C. Cheung, F. Djuanda, U. Erb, and G. Palumbo, “Electrodeposition of nanocrystalline Ni-Fe alloys,” *Nanostructured Mater.*, vol. 5, no. 5, pp. 513–523, 1995.

[6] K. Lu, “Phase transformation from an amorphous alloy into nanocrystalline materials,” *Acta Metallurgica Sinica*, vol. 30, no. 1. pp. B1–B21, 1994.

[7] R. Z. Valiev and I. V. Alexandrov, *Nanostructured materials from severe plastic deformation*, vol. 12, no. 1–4. 1999.

[8] N. R. Tao, Z. B. Wang, W. P. Tong, M. L. Sui, J. Lu, and K. Lu, “An investigation of surface nanocrystallization mechanism in Fe induced by surface mechanical attrition treatment,” *Acta Mater.*, vol. 50, no. 18, pp. 4603–4616, 2002.

[9] K. Lu and J. Lu, “Nanostructured surface layer on metallic materials induced by surface mechanical attrition treatment,” *Mater. Sci. Eng. A*, vol. 375–377, no. 1–2 SPEC. ISS., pp. 38–45, 2004.

[10] G. Proust, D. Retraint, M. Chemkhi, A. Roos, and C. Demangel, “Electron Backscatter Diffraction and Transmission Kikuchi Diffraction Analysis of an Austenitic Stainless Steel Subjected to Surface Mechanical Attrition Treatment and Plasma Nitriding,” *Microsc. Microanal.*, vol. 21, no. 4, pp. 919–926, 2015.

[11] Y. Samih, B. Beausir, B. Bolle, and T. Grosdidier, “In-depth quantitative analysis of

the microstructures produced by Surface Mechanical Attrition Treatment (SMAT)," *Mater. Charact.*, vol. 83, pp. 129–138, 2013.

[12] Z. Sun *et al.*, "Experimental study of microstructure changes due to low cycle fatigue of a steel nanocrystallised by Surface Mechanical Attrition Treatment (SMAT)," *Mater. Charact.*, vol. 124, pp. 117–121, 2017.

[13] J. Zhou, D. Retraint, Z. Sun, and P. Kanouté, "Comparative study of the effects of surface mechanical attrition treatment and conventional shot peening on low cycle fatigue of a 316L stainless steel," *Surf. Coatings Technol.*, vol. 349, no. June, pp. 556–566, 2018.

[14] W.C. Oliver; G.M. Phar, "An improved technique for determining hardness and elastic modulus using load and displacement sensing indentation experiments," *J. Mater. Res.*, vol. 7, no. 6, p. p 1564-1583, 1992.

[15] L. Rabemananjara, X. Hernot, G. Mauvoisin, A. Gavrus, and J. M. Collin, "Formulation of a representative plastic strain and representative plastic strain rate by using a conical indentation on a rigid visco-plastic material," *Mater. Des.*, vol. 68, pp. 207–214, 2015.

[16] P. Taylor, M. F. Doerner, and W. D. Nix, "Critical Reviews in Solid State and Materials Sciences Stresses and deformation processes in thin films on substrates," no. June, pp. 37–41, 2012.

[17] R. Saha and W. D. Nix, "Effects of the substrate on the determination of thin film mechanical properties by nanoindentation," *Acta Mater.*, vol. 50, no. 1, pp. 23–38, 2002.

[18] W. D. Nix, "Elastic and plastic properties of thin films on substrates: nanoindentation techniques," *Mater. Sci. Eng. A*, vol. 234–236, pp. 37–44, 1997.

[19] A. F. Gerday, M. Ben Bettaieb, L. Duchêne, N. Clément, H. Diarra, and A. M. Habraken, "Interests and limitations of nanoindentation for bulk multiphase material identification: Application to the β phase of Ti-5553," *Acta Mater.*, vol. 57, no. 17, pp. 5186–5195, 2009.

[20] Q. Li, Y. Li, and L. Zhou, "Nanoscale evaluation of multi-layer interfacial mechanical properties of sisal fiber reinforced composites by nanoindentation technique," *Compos. Sci. Technol.*, vol. 152, pp. 211–221, 2017.

[21] F. Han, B. Tang, H. Kou, J. Li, Y. Deng, and Y. Feng, "Cyclic softening behavior of Ti–6Al–4V alloy at macro and micro-scale," *Mater. Lett.*, vol. 185, pp. 115–118, 2016.

[22] M. D. Uchic, D. M. Dimiduk, J. N. Florando, and W. D. Nix, "Sample dimensions

influence strength and crystal plasticity," *Science (80-.).*, vol. 305, no. 5686, pp. 986–989, 2004.

[23] J. R. Greer, J. Y. Kim, and M. J. Burek, "The in-situ mechanical testing of nanoscale single-crystalline nanopillars," *Jom*, vol. 61, no. 12, pp. 19–25, 2009.

[24] D.G. Morris, *Mechanical behavior of nanostructured materials*. Trans Tech Publication Ltd, 1998.

[25] K. M. Lee, D. J. Lee, and H. Ahn, "XRD and TEM studies on tin oxide (II) nanoparticles prepared by inert gas condensation," *Mater. Lett.*, vol. 58, no. 25, pp. 3122–3125, 2004.

[26] F. Zhou, X. Z. Liao, Y. T. Zhu, S. Dallek, and E. J. Lavernia, "Microstructural evolution during recovery and recrystallization of a nanocrystalline Al-Mg alloy prepared by cryogenic ball milling," *Acta Mater.*, vol. 51, no. 10, pp. 2777–2791, 2003.

[27] K. Lu, "Nanocrystalline metals crystallized from amorphous solids: Nanocrystallization, structure, and properties," *Mater. Sci. Eng. R Reports*, vol. 16, no. 4, pp. 161–221, 1996.

[28] N. X. Sun, K. Zhang, X. H. Zhang, X. D. Liu, and K. Lu, "Nanocrystallization of amorphous Fe33Zr67alloy," *Nanostructured Mater.*, vol. 7, no. 6, pp. 637–649, 1996.

[29] M. M. Nicolaus, H. R. Sinning, and F. Haessner, "Crystallization behaviour and generation of a nanocrystalline state from amorphous Co33Zr67," *Mater. Sci. Eng. A*, vol. 150, no. 1, pp. 101–112, 1992.

[30] M.G. Scott, *Amorphous metallic alloys*. In: Luborsky FE, 1988.

[31] N. Azam, "Cristallisation et effets d'irradiation dans un alliage amorphe du type Fe40Ni38Mo4B18," *J. Nucl. Mater.*, vol. 83, no. 2, pp. 298–304, 1979.

[32] T. Aihara, *Amorphous and nanocrystalline materials*. 2000.

[33] K. Edalati and Z. Horita, *A review on high-pressure torsion (HPT) from 1935 to 1988*, vol. 652. Elsevier, 2016.

[34] J. Zrnik, S. V Dobatkin, and I. MamuziÄ□, "Processing of metals by severe plastic deformation (SPD) - Structure and mechanical properties respond," *Metalurgija*, vol. 47, no. 3, pp. 211–216, 2008.

[35] N.R. Tao, "Surface Nanocrystallization by Surface Mechanical A ttrition Treatment," *Mater. Sci. Forum*, vol. 579, pp. 91–108, 2008.

[36] J. Chen, L. Lu, and K. Lu, "Hardness and strain rate sensitivity of nanocrystalline Cu," *Scr. Mater.*, vol. 54, no. 11, pp. 1913–1918, 2006.

[37] T. Roland, D. Retraint, K. Lu, and J. Lu, "Enhanced mechanical behavior of a

nanocrystallised stainless steel and its thermal stability," *Mater. Sci. Eng. A*, vol. 445–446, pp. 281–288, 2007.

[38] N.R. Tao, "Mechanical and wear properties of nanostructured surface layer in iron induced by surface mechanical attrition treatment," *J. Mater. Sci. Technol.*, vol. 19, no. 6, pp. 563–566, 2003.

[39] Z. B. Wang *et al.*, "Effect of surface nanocrystallization on friction and wear properties in low carbon steel," *Mater. Sci. Eng. A*, vol. 352, no. 1–2, pp. 144–149, 2003.

[40] Y. S. Zhang, Z. Han, and K. Lu, "Fretting wear behavior of nanocrystalline surface layer of copper under dry condition," *Wear*, vol. 265, no. 3–4, pp. 396–401, 2008.

[41] W. P. Tong, N. R. Tao, Z. B. Wang, J. Lu, and K. Lu, "Nitriding Iron at Lower," *Sci.* , vol. 299, no. January, pp. 2002–2004, 2003.

[42] W. P. Tong, Z. Han, L. M. Wang, J. Lu, and K. Lu, "Low-temperature nitriding of 38CrMoAl steel with a nanostructured surface layer induced by surface mechanical attrition treatment," *Surf. Coatings Technol.*, vol. 202, no. 20, pp. 4957–4963, 2008.

[43] K. Y. Zhu, A. Vassel, F. Brisset, K. Lu, and J. Lu, "Nanostructure formation mechanism of α-titanium using SMAT," *Acta Mater.*, vol. 52, no. 14, pp. 4101–4110, 2004.

[44] H. W. Zhang, Z. K. Hei, G. Liu, J. Lu, and K. Lu, "Formation of nanostructured surface layer on AISI 304 stainless steel by means of surface mechanical attrition treatment," *Acta Mater.*, vol. 51, no. 7, pp. 1871–1881, 2003.

[45] X. Wu *et al.*, "Strain-induced grain refinement of cobalt during surface mechanical attrition treatment," *Acta Mater.*, vol. 53, no. 3, pp. 681–691, 2005.

[46] X. Wu, N. Tao, Y. Hong, B. Xu, J. Lu, and K. Lu, "Microstructure and evolution of mechanically-induced ultrafine grain in surface layer of AL-alloy subjected to USSP," *Acta Mater.*, vol. 50, no. 8, pp. 2075–2084, 2002.

[47] K. Wang, N. R. Tao, G. Liu, J. Lu, and K. Lu, "Plastic strain-induced grain refinement at the nanometer scale in copper," *Acta Mater.*, vol. 54, no. 19, pp. 5281–5291, 2006.

[48] N. R. Tao, M. L. Sui, J. Lu, and K. Lua, "Surface nanocrystallization of iron induced by ultrasonic shot peening," *Nanostructured Mater.*, vol. 11, no. 4, pp. 433–440, 1999.

[49] G. Liu, J. Lu, and K. Lu, "Surface nanocrystallization of 316L stainless steel induced by ultrasonic shot peening," *Mater. Sci. Eng. A*, vol. 286, no. 1, pp. 91–95, 2000.

[50] E. O. Hall, "the Deformation and Ageing of Mild Steel .2. Characteristics of the

Luders Deformation," *Proc. Phys. Soc. London Sect. B*, vol. 64, no. 381, p. 742-, 1951.

[51] N.J. Petch, "The cleavage strength of polycrystals," *J. Iron Steel Inst.*, vol. 174, pp. 25–28, 1953.

[52] G. E. Fougere, "Grain size dependent hardening," *Scr. Metall. Mater.*, vol. 26, no. c, pp. 1879–1883, 1992.

[53] A. Giga, Y. Kimoto, Y. Takigawa, and K. Higashi, "Demonstration of an inverse Hall-Petch relationship in electrodeposited nanocrystalline Ni-W alloys through tensile testing," *Scr. Mater.*, vol. 55, no. 2, pp. 143–146, 2006.

[54] Y. Tang, E. M. Bringa, and M. A. Meyers, "Inverse Hall-Petch relationship in nanocrystalline tantalum," *Mater. Sci. Eng. A*, vol. 580, pp. 414–426, 2013.

[55] A.H. Chokshi, "On the validity of the Hall-Petch relationship in nanocrystalline materials," *Scr. Metall.*, vol. 23, pp. 1679–1684, 1989.

[56] K. Lu, "AN EXPLANATION TO THE ABNORMAL HALL-PETCH RELATION IN NANOCRYSTALLINE MATERIALS," *Scr. Metall. Mater.*, vol. 28, pp. 1465–1470, 1993.

[57] J. R. Weertman, "Hall-Petch strengthening in nanocrystalline metals," *Mater. Sci. Eng. A*, vol. 166, no. 1–2, pp. 161–167, 1993.

[58] H. Li *et al.*, "Strain-dependent deformation behavior in nanocrystalline metals," *Phys. Rev. Lett.*, vol. 101, no. 1, pp. 1–4, 2008.

[59] J. Schiøtz, F. D. Di Tolla, and K. W. Jacobsen, "Softening of nanocrystalline metals at very small grain sizes," *Nature*, vol. 391, no. 6667, pp. 561–563, 1998.

[60] H. Van Swygenhoven, "Grain boundaries and dislocations," *Science (80-.).*, vol. 296, no. 5565, pp. 66–67, 2002.

[61] L. Wang *et al.*, "Grain rotation mediated by grain boundary dislocations in nanocrystalline platinum," *Nat. Commun.*, vol. 5, pp. 1–7, 2014.

[62] M. Murayama, J. M. Howe, H. Hidaka, and S. Takaki, "Atomic-level observation of disclination dipoles in mechanically milled, nanocrystalline Fe," *Science (80-.).*, vol. 295, no. 5564, pp. 2433–2435, 2002.

[63] V. Yamakov, D. Wolf, S. R. Phillpot, and H. Gleiter, "Deformation twinning in nanocrystalline Al by molecular-dynamics simulation," *Acta Mater.*, vol. 50, no. 20, pp. 5005–5020, 2002.

[64] M. Chen, "Deformation Twinning in Nanocrystalline Aluminum," *Science (80-.).*, vol. 300, no. 5623, pp. 1275–1277, 2003.

[65] Z.W. Shan, "Grain Boundary-Mediated Plasticity in Nanocrystalline Nickel,"

Science (80-.)., vol. 305, no. 5684, pp. 654–657, 2004.

[66] V. Yamakov, D. Wolf, S. R. Phillpot, and H. Gleiter, “Grain-boundary diffusion creep in nanocrystalline palladium by molecular-dynamics simulation †,” vol. 50, pp. 61–73, 2002.

[67] C. C. Koch and J. Narayan, “The Inverse Hall-Petch Effect Fact or Artifact ?,” vol. 634, pp. 1–11, 2001.

[68] J. Schiøtz, “A Maximum in the Strength of Nanocrystalline Copper,” *Science (80-.).*, vol. 301, no. 5638, pp. 1357–1359, 2003.

[69] G. W. Nieman and J. R. Weertman, “Mechanical behavior of nanocrystalline Cu and Pd,” *J. Mater. Res.*, vol. 6, no. 5, pp. 1012–1027, 1991.

[70] F. A. Mohamed and Y. Xun, “Correlations between the minimum grain size produced by milling and material parameters,” vol. 354, pp. 133–139, 2003.

[71] A. Phillips, “THE PHYSICS OF PLASTIC DEFORMATION ErIas C. AIFANTIS,” *Int. J. Plast.*, vol. 3, pp. 211–247, 1987.

[72] A.W. THOMPSON, “YIELDING IN NICKEL AS A FUNCTION OF GRAIN OR CELL SIZE,” *ACTA Metall.*, vol. 23, pp. 1337–1342, 1975.

[73] M.Y. Gutkin, *Plastic deformation in nanocrystalline materials*. Springer-Verlag Berlin, 2004.

[74] R.W. Armstrong, *The limiting strength properties of nanocrystalline materials*, Y.W. Chubn. The Julia Weertman symposium, 1999.

[75] E. Ma, “Instabilities and ductility of nanocrystalline and ultrafine-grained metals,” vol. 49, pp. 663–668, 2003.

[76] X. Zhang, H. Wang, R. O. Scattergood, J. Narayan, and C. C. Koch, “Modulated oscillatory hardening and dynamic recrystallization in cryomilled nanocrystalline Zn,” *Acta Mater.*, vol. 50, pp. 3995–4004, 2002.

[77] Y.T. Zhu, “Retaining ductility,” *Nat. Mater.*, vol. 3, no. 6, pp. 351–352, 2004.

[78] C. C. Koch, D. G. Morris, K. Lu, and A. Inoue, “Ductility of Nanostructured Materials,” no. February, pp. 54–58, 1999.

[79] H. Conrad and K. Jung, “Effect of grain size from mm to nm on the flow stress and plastic deformation kinetics of Au at low homologous temperatures,” *Mater. Sci. Eng. A*, vol. 406, pp. 78–85, 2005.

[80] H. Conrad, J. Narayan, and K. Jung, “Grain size softening in nanocrystalline TiN,” *Int. J. Refract. Metals Hard Mater.*, vol. 23, pp. 301–305, 2005.

[81] H. Conrad and J. Narayan, “Mechanisms for grain size hardening and softening in Zn,” *Acta Mater.*, vol. 50, pp. 5067–5078, 2002.

[82] Y. M. Wang and E. Ma, “Temperature and strain rate effects on the strength and ductility of nanostructured copper Temperature and strain rate effects on the strength and ductility,” vol. 3165, no. 2003, 2013.

[83] Y. Wang, M. Chen, F. Zhou, and E. Ma, “High tensile ductility in a nanostructured metal,” vol. 419, no. October, 2002.

[84] L. Lu, X. Chen, X. Huang, and K. Lu, “Revealing the Maximum Strength,” vol. 323, no. January, pp. 2007–2010, 2009.

[85] C. C. Koch, “Ductility in Nanostructured and Ultra Fine-Grained Materials : Recent Evidence for Optimism,” vol. 18, pp. 9–20, 2003.

[86] D. Jia, “Deformation behavior and plastic instabilities of ultrafine-grained titanium,” *Appl. Phys. Lett.*, vol. 79, pp. 611–613, 2001.

[87] Y.M. Wang, “Enhanced tensile ductility and toughness in nanostructured Cu,” *Appl. Phys. Lett.*, vol. 80, pp. 2395–2397, 2002.

[88] T. R. Malow, C. C. Koch, P. Q. Miraglia, and K. L. Murty, “Compressive mechanical behavior of nanocrystalline Fe investigated with an automated ball indentation technique,” vol. 252, pp. 36–43, 1998.

[89] G.T. Gray, “Influence of strain & temperature on the mechanical response of ultrafine-grained Cu, Ni and Al-4Cu0.5Zr,” *Nanostructured Mater.*, vol. 9, pp. 477–480, 1997.

[90] Q. Wei, S. Cheng, K. T. Ramesh, and E. Ma, “Effect of nanocrystalline and ultrafine grain sizes on the strain rate sensitivity and activation volume : fcc versus bcc metals,” vol. 381, pp. 71–79, 2004.

[91] R. Z. Valiev and I. V Alexandrov, “Paradox of strength and ductility in metals processed by severe plastic deformation,” pp. 5–8, 2002.

[92] L. Lu, S. X. Li, and K. Lu, “An abnormal strain rate e € ect on tensile behavior in nanocrystalline copper,” vol. 45, pp. 1163–1169, 2001.

[93] I. Corporation, N. Langley, and M. Science, “Activation volume analysis of plastic deformation in fcc materials using nanoindentation,” vol. 750, pp. 1–6, 2003.

[94] J. Chen, L. Lu, and K. Lu, “Hardness and strain rate sensitivity of nanocrystalline Cu,” vol. 54, pp. 1913–1918, 2006.

[95] L. Lu, “Nano-sized twins induce high rate sensitivity of flow stress in pure copper,” vol. 53, pp. 2169–2179, 2005.

[96] N. Wang, Z. Wang, K. T. Aust, and U. Erb, “Room temperature creep behavior of nanocrystalline produced by an electrodeposition technique,” vol. 5093, no. 97, 1997.

[97] H. Tanimoto, S. Sakai, and H. Mizubayashi, “MECHANICAL PROPERTY OF

HIGH DENSITY NANOCRYSTALLINE GOLD PREPARED BY GAS DEPOSITION METHOD," vol. 12, pp. 751–756, 1999.

[98] B. Cai, Q. P. Kong, P. Cui, L. Lu, and K. Lu, "Creep behavior of cold-rolled nanocrystalline pure copper," vol. 45, pp. 1407–1413, 2001.

[99] H. Gleiter, "NANOSTRUCTURED MATERIALS : BASIC CONCEPTS AND MICROSTRUCTURE," vol. 48, 2000.

[100] G. Palumbo, "A COINCIDENT AXIAL DIRECTION (CAD) APPROACH TO THE STRUCTURE OF TRIPLE JUNCTIONS IN POLYCRYSTALLINE MATERIALS," *Scr. Metall. Mater.*, vol. 24, pp. 1771–1776, 1990.

[101] X. Zhu, "X-ray diffraction studies of the structure of nanometer-sized crystalline materials," *Phys. Rev. B*, vol. 35, no. 17, pp. 9085–9090, 1987.

[102] G.J. Thomas, "GRAIN BOUNDARIES IN NANOPHASE PALLADIUM: HIGH RESOLUTION ELECTRON MICROSCOPY AND IMAGE SIMULATION," *Scr. Metall. Mater.*, vol. 24, pp. 201–206, 1990.

[103] J.A. Eastman, "CHARACTERIZATION OF NANOCRYSTALLINE Pd BY X-RAY DIFFRACTION AND EXAFS," *Nanostructured Mater.*, vol. 1, pp. 47–52, 1992.

[104] W. Wunderlich, "HREM-STUDIES OF THE MICROSTRUCTURE OF NANOCRYSTALLINE PALLADIUM," *Scr. Metall. Mater.*, vol. 24, pp. 403–408, 1990.

[105] J.A. Lupo, "STRUCTURE AND ELASTIC PROPERTIES OF NANOPHASE SILICON," *Nanostructured Mater.*, vol. 1, pp. 131–136, 1992.

[106] Y. C. Wang, D. H. Ping, and D. X. Li, "The potential for ordered grain boundary sliding in nanocrystalline palladium," vol. 88, no. 5, pp. 343–351, 2008.

[107] L. Zhang, "Structure and Bond Properties of Compacted and Heat-Treated Silicon Nitride Particles," *phys. stat. sol.*, vol. 136, pp. 291–300, 1993.

[108] K.S. Kumar, "Deformation of electrodeposited nanocrystalline nickel," *Acta Mater.*, vol. 51, no. 2, pp. 387–405, 2003.

[109] H. V. A. N. Swygenhoven, M. Spaczer, and A. Caro, "MICROSCOPIC DESCRIPTION OF PLASTICITY IN COMPUTER GENERATED METALLIC NANOPHASE SAMPLES : A COMPARISON BETWEEN Cu AND Ni," *Acta Mater.*, vol. 47, no. 10, pp. 3117–3126, 1999.

[110] Z. W. Shan, J. M. K. Wiezorek, E. A. Stach, D. M. Follstaedt, J. A. Knapp, and S. X. Mao, "Dislocation Dynamics in Nanocrystalline Nickel," *Phys. Rev. Lett.*, vol. 98, pp. 1–4, 2007.

[111] X. Li, Y. Wei, L. Lu, K. Lu, and H. Gao, “Dislocation nucleation governed softening and maximum strength in nano-twinned metals,” *Nature*, vol. 464, no. April, pp. 25–27, 2010.

[112] H. Van Swygenhoven, A. Caro, and D. Farkas, “A molecular dynamics study of polycrystalline fcc metals at the nanoscale : grain boundary structure and its influence on plastic deformation,” *Mater. Sci. Eng. A*, vol. A309-310, pp. 440–444, 2001.

[113] B. J. Weissmüller and J. Markmann, “Deforming Nanocrystalline Metals : New Insights , New Puzzles,” *Adv. Eng. Mater.*, vol. 7, no. 4, pp. 202–207, 2005.

[114] B. Chen, “Texture of Nanocrystalline Nickel: Probing the Lower Size Limit of Dislocation Activity,” *Science (80-.).*, vol. 338, pp. 1448–1451, 2012.

[115] A. Ball, “A theory of geological faults and shear zones,” *Tectonophysics*, vol. 61, pp. 1–5, 1980.

[116] H. Hahn, P. Mondal, and K. A. Padmanabhan, “PLASTIC DEFORMATION OF NANOCRYSTALLINE MATERIALS,” *Nanostructured Mater.*, vol. 9, pp. 603–606, 1997.

[117] H. Conrad and J. Narayan, “ON THE GRAIN SIZE SOFTENING IN NANOCRYSTALLINE MATERIALS,” *Scr. mater.*, vol. 42, pp. 1025–1030, 2000.

[118] H. Hu, “Direct Observations on the Annealing of a Si-Fe Crystal in the Electron Microscope,” *Trans. Metall. Soc. AIME*, vol. 224, no. 1, pp. 75–80, 1962.

[119] J. C. M. Li, “Possibility of Subgrain Rotation during Recrystallization,” *J. Appl. Phys.*, vol. 33, pp. 2958–2965, 1962.

[120] A. H. King and K. E. Harris, “GRAIN ROTATION IN THIN FILMS OF GOLD,” *Mat. Res. Soc. Symp. Proc.*, vol. 403, pp. 15–20, 1996.

[121] I.A. Ovid’ko, “Deformation of nanostructures,” *Science (80-.).*, vol. 295, p. 2386, 2002.

[122] W.T. Read, “Dislocation models of crystal grain boundaries,” *Phys. Rev.*, vol. 78, no. 3, pp. 275–289, 1950.

[123] J. W. Cahn and J. E. Taylor, “A unified approach to motion of grain boundaries , relative tangential translation along grain boundaries , and grain rotation,” *Acta Mater.*, vol. 52, pp. 4887–4898, 2004.

[124] M. Upmanyu, “Simultaneous grain boundary migration and grain rotation,” *Acta Mater.*, vol. 54, pp. 1707–1719, 2006.

[125] T. Gorkaya, K. D. Molodov, and D. A. Molodov, “Concurrent grain boundary motion and grain rotation under an applied stress,” *Acta Mater.*, vol. 59, pp. 5674–

5680, 2011.

[126] V. Yamakov, D. Wolf, M. Salazar, and S. R. Phillpot, “LENGTH-SCALE EFFECTS IN THE NUCLEATION OF EXTENDED DISLOCATIONS IN NANOCRYSTALLINE Al BY MOLECULAR-DYNAMICS SIMULATION,” *Acta Mater.*, vol. 49, pp. 2713–2722, 2001.

[127] “Scanning Electron Microscopy (SEM).” [Online]. Available: https://serc.carleton.edu/research_education/geochemsheets/techniques/SEM.html.

[128] “Different Types of SEM Imaging – BSE and Secondary Electron Imaging.” [Online]. Available: https://www.azom.com/article.aspx?ArticleID=14309.

[129] “Transmission Electron Microscopy (TEM).” [Online]. Available: https://warwick.ac.uk/fac/sci/physics/current/postgraduate/regs/mpagswarwick/ex5/techniques/structural/tem/.

[130] “X-Ray Diffraction – XRD.” [Online]. Available: http://particle.dk/methods-analytical-laboratory/xrd-analysis/.

[131] “X-ray reflection in accordance with Bragg’s Law.” [Online]. Available: https://serc.carleton.edu/research_education/geochemsheets/BraggsLaw.html.

[132] H.P. Klug, *X-ray Diffraction Procedures for Polycrystalline and Amorphous Materials*. New York: Wiley, 1974.

[133] “Electron Backscatter Diffraction (EBSD).” [Online]. Available: https://serc.carleton.edu/research_education/geochemsheets/ebsd.html.

[134] “Focused Ion Beam.” [Online]. Available: https://www.fei.com/introduction-to-electron-microscopy/fib/.

[135] J. P. Mccaffrey, M. W. Phaneuf, and L. D. Madsen, “Surface damage formation during ion-beam thinning of samples for transmission electron microscopy,” *Ultramicroscopy*, vol. 87, pp. 97–104, 2001.

[136] Y. Greenzweig, Y. Drezner, S. Tan, R. H. Livengood, and A. Raveh, “Current density profile characterization and analysis method for focused ion beam,” *Microelectron. Eng.*, vol. 155, pp. 19–24, 2016.

[137] G. Mauvoisin, O. Bartier, A. Nayebi, and R. El Abdi, “Mesure du profil de dureté par perçag des aciers traité en surface: Principe, applications et limitations,” *Mec. Ind.*, vol. 4, no. 5, pp. 525–530, 2003.

[138] B. B. He, Z. Y. Liang, and M. X. Huang, “Nanoindentation investigation on the initiation of yield point phenomenon in a medium Mn steel,” *Scr. Mater.*, vol. 150, pp. 134–138, 2018.

[139] J. M. Collin, T. Parenteau, G. Mauvoisin, and P. Pilvin, “Material parameters

identification using experimental continuous spherical indentation for cyclic hardening," *Comput. Mater. Sci.*, vol. 46, no. 2, pp. 333–338, 2009.

[140] C. Moussa, X. Hernot, O. Bartier, G. Delattre, and G. Mauvoisin, "Identification of the hardening law of materials with spherical indentation using the average representative strain for several penetration depths," *Mater. Sci. Eng. A*, vol. 606, pp. 409–416, 2014.

[141] C. Moussa, O. Bartier, X. Hernot, G. Mauvoisin, J. M. Collin, and G. Delattre, "Mechanical characterization of carbonitrided steel with spherical indentation using the average representative strain," *Mater. Des.*, vol. 89, pp. 1191–1198, 2016.

[142] J. M. Collin, G. Mauvoisin, and P. Pilvin, "Materials characterization by instrumented indentation using two different approaches," *Mater. Des.*, vol. 31, no. 1, pp. 636–640, 2010.

[143] M. Sebastiani, K. E. Johanns, E. G. Herbert, and G. M. Pharr, "Measurement of fracture toughness by nanoindentation methods : Recent advances and future challenges," *Curr. Opin. Solid State Mater. Sci.*, vol. 19, pp. 324–333, 2015.

[144] W.D. Nix, "INDENTATION SIZE EFFECTS IN CRYSTALLINE MATERIALS : A LAW FOR STRAIN GRADIENT PLASTICITY," *J. Mech. Phys. Solids*, vol. 465, no. 3, pp. 411–425, 1998.

[145] R. Ã. Rao, J. E. Bradby, S. Ruffell, and J. S. Williams, "Nanoindentation-induced phase transformation in crystalline silicon and relaxed amorphous silicon," *Microelectronics J.*, vol. 38, pp. 722–726, 2007.

[146] D. Tumbajoy Spinel, "Caractérisation du comportement mécanique de surfaces hyper-déformées par des phénomènes de contact," Université de Lyon, 2016.

[147] E.S. Berkovich, "Three-Faceted Diamond Pyramid for Studying Microhardness by Indentation," *Zavod. Lab.*, vol. 13, pp. 345–347, 1950.

[148] A. E. Giannakopoulos and S. Suresh, "Determination of elastoplastic properties by instrumented sharp indentation," *Scr. Mater.*, vol. 40, no. 10, pp. 1191–1198, 1999.

[149] L. N. Zhu, B. S. Xu, H. D. Wang, and C. B. Wang, "Measurement of residual stresses using nanoindentation method," *Crit. Rev. Solid State Mater. Sci.*, vol. 40, no. 2, pp. 77–89, 2015.

[150] C. E. K. Mady, S. A. Rodriguez, A. G. Gómez, and R. M. Souza, "Effects of mechanical properties, residual stress and indenter tip geometry on instrumented indentation data in thin films," *Surf. Coatings Technol.*, vol. 205, no. 5, pp. 1393–1397, 2010.

[151] M. K. Khan, M. E. Fitzpatrick, S. V. Hainsworth, and L. Edwards, "Effect of

residual stress on the nanoindentation response of aerospace aluminium alloys," *Comput. Mater. Sci.*, vol. 50, no. 10, pp. 2967–2976, 2011.

[152] K. Kese and Z. C. Li, "Semi-ellipse method for accounting for the pile-up contact area during nanoindentation with the Berkovich indenter," *Scr. Mater.*, vol. 55, no. 8, pp. 699–702, 2006.

[153] K. O. Kese, Z. C. Li, and B. Bergman, "Influence of residual stress on elastic modulus and hardness of soda-lime glass measured by nanoindentation," *J. Mater. Res.*, vol. 19, no. 10, pp. 3109–3119, 2004.

[154] J. Woirgard *et al.*, "A new technology for nanohardness measurements : principle and applications," *Surf. Coatings Technol.*, vol. 101, 1998.

[155] I.N. Sneddon, "THE RELATION BETWEEN LOAD AND PENETRATION IN THE AXISYMMETRIC BOUSSINESQ PROBLEM FOR A PUNCH OF ARBITRARY PROFILE," *Znt. J. Engng Sci.*, vol. 3, pp. 47–57, 1965.

[156] R.B. King, "ELASTIC ANALYSIS OF SOME PUNCH PROBLEMS FOR A LAYERED MEDIUM," *Int. J. Solids Struct.*, vol. 23, no. 12, pp. 1657–1664, 1987.

[157] X. Li and B. Bhushan, "DEVELOPMENT OF CONTINUOUS STIFFNESS MEASUREMENT TECHNIQUE FOR COMPOSITE MAGNETIC TAPES," *Scr. mater.*, vol. 42, pp. 929–935, 2000.

[158] S. A. S. A., "Nanoindentation creep of single- crystal tungsten and gallium arsenide," *Philos. Mag. A*, vol. 76, no. 6, pp. 1105–1118, 1997.

[159] B. Merle, V. Maier-Kiener, and G. M. Pharr, "Influence of modulus-to-hardness ratio and harmonic parameters on continuous stiffness measurement during nanoindentation," *Acta Mater.*, vol. 134, pp. 167–176, 2017.

[160] G. Guillonneau, "Nouvelles techniques de nano-indentation pour des conditions expérimentales difficiles : très faibles enfoncements, surfaces rugueuses, température," Université de Lyon, 2012.

[161] M. F. Hardiman, T. J. Vaughan, and C. T. Mccarthy, "The effects of pile-up, viscoelasticity and hydrostatic stress on polymer matrix nanoindentation," *Polym. Test.*, 2016.

[162] F. Anthony, *Nanoindentation*. New York, 2002.

[163] H. Hertz, "Über die Berührung fester elastischer Körper (Sur le contact entre corps élastiques)," *J. für reine und Angew. Math.*, vol. 92, pp. 156–171, 1881.

[164] G.Z. Voyiadjis, "Review of Nanoindentation Size Effect : Experiments and Atomistic Simulation," *Crystals*, vol. 7, no. 10, p. 321, 2017.

[165] Y. H. Lee and D. Kwon, "Measurement of residual-stress effect by nanoindentation

on elastically strained (1 0 0) W," *Scr. Mater.*, vol. 49, no. 5, pp. 459–465, 2003.

[166] R. K. Khatirkar and S. G. Sapate, "Effect of heat input on the microstructure , residual stresses and corrosion resistance of 304L austenitic stainless steel weldments," *Mater. Charact.*, vol. 93, pp. 10–23, 2014.

[167] L. Zhang, H. Yang, X. Pang, K. Gao, and A. A. Volinsky, "Microstructure , residual stress , and fracture of sputtered TiN films," *Surf. Coat. Technol.*, vol. 224, pp. 120–125, 2013.

[168] S. K. Sharma and D. Y. Kim, "Abnormal residual stress in nanostructured Al thin fi lms grown on Ti / glass substrates," *Curr. Appl. Phys.*, vol. 13, no. 9, pp. 1874–1879, 2013.

[169] Y. Y. Santana, P. O. Renault, M. Sebastiani, J. G. La Barbera, J. Lesage, and E. Bemporad, "Characterization and residual stresses of WC – Co thermally sprayed coatings," *Surf. Coat. Technol.*, vol. 202, pp. 4560–4565, 2008.

[170] A. Dey and A. K. Mukhopadhyay, "Evaluation of residual stress in microplasma sprayed hydroxyapatite coating by nanoindentation," *Ceram. Int.*, vol. 40, no. 1, pp. 1263–1272, 2014.

[171] Y. Huang, S. Chang, and C. Chang, "Effect of residual stresses on mechanical properties and interface adhesion strength of SiN thin fi lms," *Thin Solid Films*, vol. 517, no. 17, pp. 4857–4861, 2009.

[172] H. Tae, Y. Lee, X. Jackson, C. Llc, C. Drive, and A. Hills, "Effects of residual stress and heat treatment on fatigue strength of weldments," *Mater. Sci. Eng. A*, vol. 497, pp. 37–43, 2008.

[173] S. Novak, M. Kalin, P. Lukas, G. Anne, J. Vleugels, and O. Van Der Biest, "The effect of residual stresses in functionally graded alumina – ZTA composites on their wear and friction behaviour," *J. Eur. Ceram. Soc.*, vol. 27, pp. 151–156, 2007.

[174] T. Y. Tsui, "Influences of stress on the measurement of mechanical properties using nanoindentation : Part I . Experimental studies in an aluminum alloy," *J. Mater. Res.*, vol. 11, no. 3, pp. 752–759, 1996.

[175] A. Bolshakov, W. C. Oliver, and G. M. Pharr, "Influences of stress on the measurement of mechanical properties using nanoindentation: Part II. Finite element simulations," *J. Mater. Res.*, vol. 11, no. 03, pp. 760–768, 1996.

[176] L. N. Zhu, B. S. Xu, H. D. Wang, and C. B. Wang, "Effect of residual stress on the nanoindentation response of (100) copper single crystal," *Mater. Chem. Phys.*, vol. 136, no. 2–3, pp. 561–565, 2012.

[177] K. O. Kese, Z. C. Li, and B. Bergman, "Method to account for true contact area in

soda-lime glass during nanoindentation with the Berkovich tip," *Mater. Sci. Eng. A*, vol. 404, no. 1–2, pp. 1–8, 2005.

[178] E. Renner, Y. Gaillard, F. Richard, F. Amiot, and P. Delobelle, "Sensitivity of the residual topography to single crystal plasticity parameters in Berkovich nanoindentation on FCC nickel," *Int. J. Plast.*, vol. 77, pp. 118–140, 2016.

[179] A. Bolshakov and G. M. Pharr, "Influences of pileup on the measurement of mechanical properties by load and depth sensing indentation techniques," *J. Mater. Res.*, vol. 13, no. 4, pp. 1049–1058, 1998.

[180] J. M. Collin, G. Mauvoisin, P. Pilvin, and R. El Abdi, "Use of spherical indentation data changes to materials characterization based on a new multiple cyclic loading protocol," *Mater. Sci. Eng. A*, vol. 488, no. 1–2, pp. 608–622, 2008.

[181] Z. H. Cao, M. Z. Wei, C. Sun, H. M. Lu, Z. Fan, and X. K. Meng, "Cyclic deformation induced strengthening and unusual rate sensitivity in Cu/Ru nanolayered films," *Int. J. Plast.*, 2017.

[182] Y. Shen, C. B. Blada, J. J. Williams, and N. Chawla, "Cyclic indentation behavior of metal – ceramic nanolayered composites," *Mater. Sci. Eng. A*, vol. 557, pp. 119–125, 2012.

[183] R. Trivedi and V. Cech, "Mechanical properties of plasma polymer fi lm evaluated by conventional and alternative nanoindentation techniques," *Surf. Coat. Technol.*, vol. 205, pp. S286–S289, 2010.

[184] S. Jain, A. Gokhale, and J. Jain, "Fatigue Behavior of Aged and Solution Treated AZ61 Mg Alloy at Small Length Scale Using Nanoindentation," *Mater. Sci. Eng. A*, vol. 684, pp. 652–659, 2017.

[185] M.Y. N'Jock, "Work-of-indentation coupled to contact stiffness for calculating elastic modulus by instrumented indentation," *Mech. Mater.*, vol. 94, pp. 170–179, 2016.

[186] F. N. Tavadze, J. V Lominadze, A. G. Khvedelidze, G. V Tsagareishvili, and S. I. Bulichev, "THE EFFECT OF IMPURITIES ON THE MECHANICAL PROPERTIES OF ZONE-MELTED BORON," *J. Less-Common Met.*, vol. 82, pp. 95–99, 1981.

[187] H. Fei, "Evaluation of Micro-Pillar Compression Tests for Accurate Determination of Elastic-Plastic Constitutive Relations," *J. Appl. Mech.*, vol. 79, pp. 1–9, 2012.

[188] M. B. Lowry *et al.*, "Achieving the ideal strength in annealed molybdenum nanopillars," *Acta Mater.*, vol. 58, no. 15, pp. 5160–5167, 2010.

[189] J. Y. Zhang, G. Liu, and J. Sun, "Strain rate effects on the mechanical response in

multi- and single-crystalline Cu micropillars : Grain boundary effects," *Int. J. Plast.*, vol. 50, pp. 1–17, 2013.

[190] M. D. Uchic and D. M. Dimiduk, "A methodology to investigate size scale effects in crystalline plasticity using uniaxial compression testing," *Mater. Sci. Eng. A*, vol. 401–401, pp. 268–278, 2005.

[191] "Atomic force microscopy." [Online]. Available: https://en.wikipedia.org/wiki/Atomic_force_microscopy.

[192] M.F. Ashby and D.R.H. Jones, *Engineering materials 2*, Third edit. Oxford.

[193] T. Roland, "Génération de nanostructures par traitement de nanocristallisation superficielle SMAT sur matériaux métalliques et étude des propriétés mécaniques associées," University of Technology of Troyes, 2007.

[194] P. Muraleedharan, J. B. Gnanamoorthy, and P. Rodriguez, "Comparative Study: Degree of Sensitization and Intergranular Stress Corrosion Cracking Susceptibility of Type 304 Stainless Steel," *Corrosion*, vol. 52, no. 10, pp. 790–800, 1996.

[195] I. Chattoraj, A. K. Bhattamishra, S. Jana, S. K. Das, S. P. Chakraborty, and P. K. De, "The association of potentiokinetic reactivation and electrochemical pitting tests on a nitrogen bearing 19 Cr-17 Mn steel with its thermal history," *Corros. Sci.*, vol. 38, no. 6, pp. 957–969, 1996.

[196] P. Shankar, H. Shaikh, S. Sivakumar, S. Venugopal, D. Sundararaman, and H. S. Khatak, "Effect of thermal aging on the room temperature tensile properties of AISI type 316LN stainless steel," *J. Nucl. Mater.*, vol. 264, no. 1–2, pp. 29–34, 1999.

[197] H. Sahlaoui, K. Makhlouf, H. Sidhom, and J. Philibert, "Effects of ageing conditions on the precipitates evolution, chromium depletion and intergranular corrosion susceptibility of AISI 316L: Experimental and modeling results," *Mater. Sci. Eng. A*, vol. 372, no. 1–2, pp. 98–108, 2004.

[198] M. Terada, D. M. Escriba, I. Costa, E. Materna-Morris, and A. F. Padilha, "Investigation on the intergranular corrosion resistance of the AISI 316L(N) stainless steel after long time creep testing at 600 °C," *Mater. Charact.*, vol. 59, no. 6, pp. 663–668, 2008.

[199] B. Weiss and R. Stickler, "Phase instabilities during high temperature exposure of 316 austenitic stainless steel," *Metall. Mater. Trans. B*, vol. 3, no. 4, pp. 851–866, 1972.

[200] J. Barcik, "Mechanism of σ-phase precipitation in Cr–Ni austenitic steels," *Mater. Sci. Technol.*, vol. 4, no. 1, pp. 5–15, 1988.

[201] M. Matula *et al.*, "Intergranular corrosion of AISI 316L steel," *Mater. Charact.*, vol.

46, no. 2–3, pp. 203–210, 2001.

[202] S. Ningshen, U. Kamachi Mudali, G. Amarendra, P. Gopalan, R. K. Dayal, and H. S. Khatak, “Hydrogen effects on the passive film formation and pitting susceptibility of nitrogen containing type 316L stainless steels,” *Corros. Sci.*, vol. 48, no. 5, pp. 1106–1121, 2006.

[203] A. F. Padilha, D. M. Escriba, E. Materna-Morris, M. Rieth, and M. Klimenkov, “Precipitation in AISI 316L(N) during creep tests at 550 and 600 °C up to 10 years,” *J. Nucl. Mater.*, vol. 362, no. 1, pp. 132–138, 2007.

[204] M. M. Nowell, R. A. Witt, and B. True, “EBSD Sample Preparation: Techniques, Tips, and Tricks,” *Microsc. Microanal.*, vol. 11, no. S02, pp. 1–4, 2005.

[205] J.A. venables, *Deformation twinning*. New York: Gordon and Breach, 1963.

[206] R. Hull *et al.*, “Grain Boundary – Mediated Plasticity in Nanocrystalline Nickel,” *Science (80-.).*, vol. 305, no. July, pp. 654–658, 2004.

[207] V. Tsakiris and D. V Edmonds, “Martensite and deformation twinning in austenitic steels,” *Mater. Sci. Eng. A*, vol. A273-275, pp. 430–436, 1999.

[208] P. Peyre *et al.*, “Surface modifications induced in 316L steel by laser peening and shot-peening. Influence on pitting corrosion resistance,” *Mater. Sci. Eng. A*, vol. 280, no. 2, pp. 294–302, 2000.

[209] C. L. Wu, C. P. Chang, D. Chen, J. F. Tu, and C. Y. Huang, “Microstructural characterization of deformation-induced martensite in an ultrafine-grained medium Mn advanced high strength steel,” *Mater. Sci. Eng. A*, vol. 721, no. December 2017, pp. 145–153, 2018.

[210] V. Kain, K. Chandra, K. N. Adhe, and P. K. De, “Effect of cold work on low-temperature sensitization behaviour of austenitic stainless steels,” *J. Nucl. Mater.*, vol. 334, no. 2–3, pp. 115–132, 2004.

[211] L. Waltz, “Comportement mécanique de structures multicouches obtenues par co-laminage de tôles nanostructurées : Essais et simulation,” University of Technology of Troyes, 2009.

[212] J. Zhou, “Experimental study and Multi-scale modelling of LCF behaviour of austenitic steels treated by SMAT,” University of Technology of Troyes, 2018.

[213] S. N. Sharma, R. K. Sharma, K. N. Sood, and S. Singh, “Structural and morphological studies of chemical bath-deposited nanocrystalline CdS films and its alloys,” *Mater. Chem. Phys.*, vol. 93, no. 2–3, pp. 368–375, 2005.

[214] É. Cossette, D. Schneider, P. Audet, B. Grasemann, and G. Habler, “Seismic properties and mineral crystallographic preferred orientations from EBSD data:

Results from a crustal-scale detachment system, Aegean region," *Tectonophysics*, vol. 651, pp. 66–78, 2015.

[215] S. I. Wright, M. M. Nowell, R. De Kloe, P. Camus, and T. Rampton, "Electron imaging with an EBSD detector," *Ultramicroscopy*, vol. 148, pp. 132–145, 2015.

[216] A. Zingales, G. Quartarone, and G. Moretti, "Sigma Phase Intergranular Corrosion Effects in Austenitic Weids Containing Ferrite *," no. 2137, pp. 136–141, 1985.

[217] P. Muraleedharan, J. B. Gnanamoorthy, and P. Rodriguez, "The effect of ageing at 973 K on stress corrosion cracking of type 304 stainless steel," *Corros. Sci.*, vol. 38, no. 7, pp. 1187–1201, 1996.

[218] Z. B. Wang, J. Lu, and K. Lu, "Chromizing behaviors of a low carbon steel processed by means of surface mechanical attrition treatment," *Acta Mater.*, vol. 53, no. 7, pp. 2081–2089, 2005.

[219] S. Bagherifard, R. Ghelichi, and M. Guagliano, "Numerical and experimental analysis of surface roughness generated by shot peening," *Appl. Surf. Sci.*, vol. 258, no. 18, pp. 6831–6840, 2012.

[220] P. Delgado, I. I. Cuesta, J. M. Alegre, and A. Díaz, "State of the art of Deep Rolling," *Precis. Eng.*, vol. 46, pp. 1–10, 2016.

[221] M. Dogra, V. S. Sharma, J. S. Dureja, and S. S. Gill, "Environment-friendly technological advancements to enhance the sustainability in surface grinding- A review," *J. Clean. Prod.*, vol. 197, pp. 218–231, 2018.

[222] X. H. Chen, J. Lu, L. Lu, and K. Lu, "Tensile properties of a nanocrystalline 316L austenitic stainless steel," *Scr. Mater.*, vol. 52, no. 10, pp. 1039–1044, 2005.

[223] D. Tumbajoy-Spinel *et al.*, "Microstructural and micromechanical investigations of surface strengthening mechanisms induced by repeated impacts on pure iron," *Mater. Des.*, vol. 147, pp. 56–64, 2018.

[224] P. Cavaliere, "Cyclic deformation of ultra-fine and nanocrystalline metals through nanoindentation: Similarities with crack propagation," *Procedia Eng.*, vol. 2, no. 1, pp. 213–222, 2010.

[225] T. Saraswati, T. Sritharan, S. Mhaisalkar, C. D. Breach, and F. Wulff, "Cyclic loading as an extended nanoindentation technique," *Mater. Sci. Eng. A*, vol. 423, no. 1–2, pp. 14–18, 2006.

[226] P. J. J. Withers and H. K. D. H. Bhadeshia, "Residual stress Part 1 – Measurement techniques," *Mater. Sci. Technol.*, vol. 17, no. 4, pp. 355–365, 2001.

[227] P. J. Withers and H. K. D. H. Bhadeshia, "Residual stress. Part 2 – Nature and origins," *Mater. Sci. Technol.*, vol. 17, no. 4, pp. 366–375, 2001.

[228] J. Zhou, Z. Sun, P. Kanouté, and D. Retraint, “Effect of surface mechanical attrition treatment on low cycle fatigue properties of an austenitic stainless steel,” *Int. J. Fatigue*, vol. 103, pp. 309–317, 2017.

[229] E. Salvati and A. M. Korsunsky, “An analysis of macro- and micro-scale residual stresses of Type I, II and III using FIB-DIC micro-ring-core milling and crystal plasticity FE modelling,” *Int. J. Plast.*, vol. 98, pp. 123–138, 2017.

[230] L. N. Zhu, B. S. Xu, H. D. Wang, and C. B. Wang, “Measurement of residual stress in quenched 1045 steel by the nanoindentation method,” *Mater. Charact.*, vol. 61, no. 12, pp. 1359–1362, 2010.

[231] Q. N. Meng *et al.*, “Influence of the residual stress on the nanoindentation-evaluated hardness for zirconiumnitride films,” *Surf. Coatings Technol.*, vol. 206, no. 14, pp. 3250–3257, 2012.

[232] J. Lu, *Handbook of measurement of residual stresses*. Fairmont Press, 1996.

[233] S. I. Rao *et al.*, “Large-scale dislocation dynamics simulations of strain hardening of Ni microcrystals under tensile loading,” *Acta Mater.*, vol. 164, pp. 171–183, 2019.

[234] J. Petit, L. Waltz, G. Montay, D. Retraint, A. Roos, and M. François, “Multilayer modelling of stainless steel with a nanocrystallised superficial layer,” *Mater. Sci. Eng. A*, vol. 536, pp. 124–128, 2012.

[235] L. Llanes, A. D. Rollett, C. Laird, and J. L. Bassani, “Effect of grain size and annealing texture on the cyclic response and the substructure evolution of polycrystalline copper,” *Acta Metall. Mater.*, vol. 41, no. 9, pp. 2667–2679, 1993.

[236] G. Dieter, *Mechanical Metallurgy*. McGraw Hill Book Company, 1988.

[237] “Work hardening.” [Online]. Available: https://en.wikipedia.org/wiki/Work_hardening.

[238] “Bauschinger effect.” [Online]. Available: https://en.wikipedia.org/wiki/Bauschinger_effect.

[239] B. Dylewski, M. Risbet, and S. Bouvier, “Experimental Characterization of the Tridimensional Gradient of Microstructure Induced by RCF in the Rolling Band of Rails,” *Procedia Eng.*, vol. 133, pp. 202–210, 2015.

[240] B. Dylewski, M. Risbet, and S. Bouvier, “The tridimensional gradient of microstructure in worn rails – Experimental characterization of plastic deformation accumulated by RCF,” *Wear*, vol. 392–393, no. July 2016, pp. 50–59, 2017.

[241] L. Cauvin, B. Raghavan, S. Bouvier, X. Wang, and F. Meraghni, “Multi-scale investigation of highly anisotropic zinc alloys using crystal plasticity and inverse analysis,” *Mater. Sci. Eng. A*, vol. 729, no. February, pp. 106–118, 2018.

[242] D. Barbier, N. Gey, S. Allain, N. Bozzolo, and M. Humbert, “Analysis of the tensile behavior of a TWIP steel based on the texture and microstructure evolutions,” *Mater. Sci. Eng. A*, vol. 500, no. 1–2, pp. 196–206, 2009.

[243] D. J. Child, G. D. West, and R. C. Thomson, “Assessment of surface hardening effects from shot peening on a Ni-based alloy using electron backscatter diffraction techniques,” *Acta Mater.*, vol. 59, no. 12, pp. 4825–4834, 2011.

[244] P. S. Prevéy and J. T. Cammett, “The influence of surface enhancement by low plasticity burnishing on the corrosion fatigue performance of AA7075-T6,” *Int. J. Fatigue*, vol. 26, no. 9, pp. 975–982, 2004.

[245] R. Fathallah, A. Laamouri, H. Sidhom, and C. Braham, “High cycle fatigue behavior prediction of shot-peened parts,” *Int. J. Fatigue*, vol. 26, no. 10, pp. 1053–1067, 2004.

[246] Y. Li, P. Kanouté, and M. François, “Disturbance induced by surface preparation on instrumented indentation test,” *Mater. Sci. Eng. A*, vol. 642, pp. 381–390, 2015.

[247] P. Juran, P. J. Liotier, C. Maurice, F. Valiorgue, and G. Kermouche, “Investigation of indentation-, impact- and scratch-induced mechanically affected zones in a copper single crystal,” *Comptes Rendus - Mec.*, vol. 343, no. 5–6, pp. 344–353, 2015.

[248] Z. H. Xu and X. Li, “Estimation of residual stresses from elastic recovery of nanoindentation,” *Philos. Mag.*, vol. 86, no. 19, pp. 2835–2846, 2006.

[249] L. N. Zhu, B. S. Xu, H. D. Wang, and C. B. Wang, “Pileup behavior in sharp nanoindentation of AISI 1045 steel,” *Phys. Procedia*, vol. 50, no. October 2012, pp. 214–218, 2013.

[250] R. Mulyukov, M. Weller, R. Valiev, T. Gessmann, and H. E. Schaefer, “Internal friction and shear modulus in submicrograined Cu,” *Nanostructured Mater.*, vol. 6, no. 5–8, pp. 577–580, 1995.

[251] A.B. Lebedev, “THERMAL STABILITY OF SUBMICROCRYSTALLINE COPPER AND Cu: ZrO2 COMPOSITE,” *Scr. Mater.*, vol. 35, no. 9, pp. 1077–1081, 1996.

[252] A. B. Lebedev, Y. A. Burenkov, A. E. Romanov, V. I. Kopylov, V. P. Filonenko, and V. G. Gryaznov, “Softening of the elastic modulus in submicrocrystalline copper,” *Mater. Sci. Eng. A*, vol. 203, no. 1–2, pp. 165–170, 1995.

[253] N. A. Akhmadeev, N. P. Kobelev, R. R. Mulyukov, Y. M. Soifer, and R. Z. Valiev, “The effect of heat treatment on the elastic and dissipative properties of copper with the submicrocrystalline structure,” *Acta Metall. Mater.*, vol. 41, no. 4, pp. 1041–1046, 1993.

[254] C.E. Gerber, *Contact problems for the elastic quarter-plane and for the quarter space*. UMI Diss. services, 1993.

[255] J. E. Jakes, C. R. Frihart, J. F. Beecher, R. J. Moon, and D. S. Stone, "Experimental method to account for structural compliance in nanoindentation measurements," *J. Mater. Res.*, vol. 23, no. 4, pp. 1113–1127, 2008.

[256] J. D. Gale and A. Achuthan, "The effect of work-hardening and pile-up on nanoindentation measurements," *J. Mater. Sci.*, vol. 49, no. 14, pp. 5066–5075, 2014.

[257] Z. C. Cordero, B. E. Knight, and C. A. Schuh, "Six decades of the Hall–Petch effect – a survey of grain-size strengthening studies on pure metals," *Int. Mater. Rev.*, vol. 61, no. 8, pp. 495–512, 2016.

[258] M. Tiryakioğlu and J. S. Robinson, "On the representative strain in Vickers hardness testing of 7010 aluminum alloy," *Mater. Sci. Eng. A*, vol. 641, no. August, pp. 231–236, 2015.

[259] B. P. Kashyap and K. Tangri, "ON THE HALL-PETCH RELATIONSHIP A N D S U B S T R U C T U R A L EVOLUTION IN TYPE 316L STAINLESS STEEL," vol. 43, no. 11, 1995.

[260] J. Zhou, Z. Sun, P. Kanouté, and D. Retraint, "Reconstruction of residual stress and work hardening and their effects on the mechanical behaviour of a shot peened structure," *Mech. Mater.*, vol. 127, no. September, pp. 100–111, 2018.

[261] W. D. N. M.F. Doerner, "A method for interpreting the data from depth-sensing indentation instruments," *J. Mater. Res.*, vol. 1, pp. 601–609, 1986.

[262] W. D. S. D.S. Stone, K.B. Yoder, "Hardness and elastic modulus of TiN based on continuous indentation technique and new correlation," *J. Vac. Sci. Technol.*, vol. 9, pp. 2543–2547, 1991.

[263] J. C. Hay, A. Bolshakov, and G. M. Pharr, "A critical examination of the fundamental relations used in the analysis of nanoindentation data," *J. Mater. Res.*, vol. 14, no. 06, pp. 2296–2305, 1999.

[264] A. A. Elmustafa and D. S. Stone, "Indentation size effect in polycrystalline F.C.C. metals," *Acta Mater.*, vol. 50, no. 14, pp. 3641–3650, 2002.

[265] R. K. Abu Al-Rub, "Prediction of micro and nanoindentation size effect from conical or pyramidal indentation," *Mech. Mater.*, vol. 39, no. 8, pp. 787–802, 2007.

[266] Y. C. Kim *et al.*, "Indentation size effect for spherical nanoindentation on nanoporous gold," *Scr. Mater.*, vol. 143, pp. 10–14, 2018.

[267] J. A. Muñoz, "Geometrically Necessary Dislocations (GNDs) in iron processed by Equal Channel Angular Pressing (ECAP)," *Mater. Lett.*, vol. 238, pp. 42–45, 2019.

[268] M. F. Ashby, “The deformation of plastically non-homogeneous alloys,” *Philos. Mag.*, vol. 21, no. 170, pp. 399–424, 1970.

[269] H. Yuan and J. Chen, “Identification of the intrinsic material length in gradient plasticity theory from micro-indentation tests,” *Int. J. Solids Struct.*, vol. 38, no. 46–47, pp. 8171–8187, 2001.

[270] R. K. Abu Al-Rub and G. Z. Voyiadjis, “A physically based gradient plasticity theory,” *Int. J. Plast.*, vol. 22, no. 4, pp. 654–684, 2006.

[271] A. Vinogradov, S. Nagasaki, V. Patlan, K. Kitagawa, and M. Kawazoe, “Fatigue properties of 5056 Al-Mg alloy produced by equal-channel angular pressing,” *Nanostructured Mater.*, vol. 11, no. 7, pp. 925–934, 1999.

[272] Y. H. Chen, I. A. Polonsky, Y. W. Chung, and L. M. Keer, “Tribological properties and rolling-contact-fatigue lives of TiN/SiNx multilayer coatings,” *Surf. Coatings Technol.*, vol. 154, no. 2–3, pp. 152–161, 2002.

[273] A. Di Schino and J. M. Kenny, “Grain size dependence of the fatigue behaviour of a ultrafine-grained AISI 304 stainless steel,” *Mater. Lett.*, vol. 57, no. 21, pp. 3182–3185, 2003.

[274] Y. Estrin and A. Vinogradov, “Fatigue behaviour of light alloys with ultrafine grain structure produced by severe plastic deformation: An overview,” *Int. J. Fatigue*, vol. 32, no. 6, pp. 898–907, 2010.

[275] R.M. Pelloux, *Ultrafine-grain metals*. Syracuse University Press, 1970.

[276] A. W. Thompson and W. A. Backofen, “The effect of grain size on fatigue,” *Acta Metall.*, vol. 19, no. 7, pp. 597–606, 1971.

[277] P. Lukáš and L. Kunz, “Effect of grain size on the high cycle fatigue behaviour of polycrystalline copper,” *Mater. Sci. Eng.*, vol. 85, no. C, pp. 67–75, 1987.

[278] H. A. Padilla and B. L. Boyce, “A Review of fatigue behavior in nanocrystalline metals,” *Exp. Mech.*, vol. 50, no. 1, pp. 5–23, 2010.

[279] Z. Sun *et al.*, “Low cycle fatigue of 316L stainless steel processed by surface mechanical attrition treatment (SMAT),” *MATEC Web Conf.*, vol. 165, p. 15002, 2018.

[280] C. P. Frick, B. G. Clark, S. Orso, A. S. Schneider, and E. Arzt, “Size effect on strength and strain hardening of small-scale [1 1 1] nickel compression pillars,” *Mater. Sci. Eng. A*, vol. 489, no. 1–2, pp. 319–329, 2008.

[281] S. Lee, J. Jeong, Y. Kim, S. M. Han, D. Kiener, and S. H. Oh, “FIB-induced dislocations in Al submicron pillars: Annihilation by thermal annealing and effects on deformation behavior,” *Acta Mater.*, vol. 110, pp. 283–294, 2016.

[282] Y. Xiao *et al.*, “Investigation of the deformation behavior of aluminum micropillars produced by focused ion beam machining using Ga and Xe ions,” *Scr. Mater.*, vol. 127, pp. 191–194, 2017.

[283] D. Tumbajoy-spinel, X. Maeder, G. Guillonneau, S. Descartes, J. Bergheau, and G. Kermouche, “Microstructural and micromechanical investigations of surface strengthening mechanisms induced by repeated impacts on pure iron,” *Mater. Des.*, 2018.

[284] T. Volpp, E. Giiring, E. Arzt, and U. D. B. Mtinchen, “GRAIN SIZE DETERMINATION AND LIMITS TO HALL-PETCH BEHIAVIOR IN NANOCRYSTALLINE NiAl POWDERS,” *Nanostructured Mater.*, vol. 8, no. 7, pp. 855–865, 1997.

[285] A.W. Thompson, *Work hardening in tension and fatigue*. 1977.

[286] J.P. Hirth, *Theory of dislocations*. New York: McGraw-Hill, 1982.

[287] H. Margolin, “Polycrystalline yielding - Perspectives on its onset,” *Acta Mater.*, vol. 46, no. 17, pp. 6305–6309, 1998.

[288] D. J. Benson, H. H. Fu, and M. A. Meyers, “On the effect of grain size on yield stress: Extension into nanocrystalline domain,” *Mater. Sci. Eng. A*, vol. 319–321, pp. 854–861, 2001.

[289] L. Méric, G. Cailletaud, and M. Gaspérini, “F.E. calculations of copper bicrystal specimens submitted to tension-compression tests,” *Acta Metall. Mater.*, vol. 42, no. 3, pp. 921–935, 1994.

[290] A. Musienko, “Plasticité cristalline en présence de grandes déformations et d’endommagement,” ECOLE DES MINES DE PARIS, 2005.

[291] “Voronoi diagram.” [Online]. Available: https://en.wikipedia.org/wiki/Voronoi_diagram.

[292] A. D. Parakkat, U. Bondi Pundarikaksha, and R. Muthuganapathy, “A Delaunay triangulation based approach for cleaning rough sketches,” *Comput. Graph.*, vol. 74, pp. 171–181, 2018.

[293] L. Cheng, P. Burchard, B. Merriman, and S. Osher, “Motion of Curves Constrained on Surfaces Using a Level-Set Approach,” *J. Comput. Phys.*, vol. 175, pp. 604–644, 2002.

[294] L. Jiang, “Parametric structural shape & topology optimization with a variational distance-regularized level set method,” *Comput. Methods Appl. Mech. Engrg.*, vol. 321, pp. 316–336, 2017.

[295] R. Hill, “ELASTIC PROPERTIES OF REINFORCED SOLIDS : SOME

THEORETICAL PRINCIPLE,” *J. Mech. Phys. Solids*, vol. 11, pp. 357–372, 1963.

[296] C. Simoneau, P. Terriault, J. Rivard, and V. Brailovski, “Modeling of metallic foam morphology using the Representative Volume Element approach : Development and experimental validation,” *Int. J. Solids Struct.*, vol. 51, pp. 3633–3641, 2014.

[297] H. S. Kim, Y. Estrin, and M. B. Bush, “PLASTIC DEFORMATION BEHAVIOUR OF FINE- GRAINED MATERIALS,” *Acta Mater.*, vol. 48, pp. 493–504, 2000.

[298] Y. Estrin, “Diffusion controlled creep in nanocrystalline materials under grain growth,” *Scr. Mater.*, vol. 50, pp. 993–997, 2004.

[299] L. Capolungo, S. Benkassem, M. Cherkaoui, and J. Qu, “Self-consistent scale transition with imperfect interfaces : Application to nanocrystalline materials,” *Acta Mater.*, vol. 56, pp. 1546–1554, 2008.

[300] Y. J. Wei and L. Anand, “Grain-boundary sliding and separation in polycrystalline metals : application to nanocrystalline fcc metals,” *J. Mech. Phys. Solids*, vol. 52, pp. 2587–2616, 2004.

Yangcan WU

Doctorat : Matériaux, Mécanique, Optique, Nanotechnologie

Année 2019

Etude expérimentale et simulation numérique des propriétés mécaniques à gradient d'aciers 316L générées par SMAT

Ce travail concerne la caractérisation et la simulation numérique des propriétés mécaniques locales d'aciers 316L austénitiques traités par SMAT. Un raffinement des grains, des contraintes résiduelles de compression et un phénomène d'écrouissage sont trois paramètres majeurs induits par SMAT en raison d'une déformation plastique sévère. Ainsi, de meilleures propriétés mécaniques sont obtenues avec cette microstructure à gradient, grâce aux effets combinés des différents changements induits SMAT. Alors que l'accent a surtout été mis sur les propriétés globales de la microstructure à gradient dans de précédentes études, peu d'efforts ont été consacrés à la caractérisation individuelle de chaque couche. L'objectif de ce travail est donc d'étudier individuellement les propriétés mécaniques de chaque couche constituant la zone affectée par le traitement au moyen de différentes techniques de caractérisation. La microstructure à gradient générée par SMAT a d'abord été caractérisée par EBSD. Une couche nanocristalline est générée à la surface traitée dont la taille de grains varie entre 50 et 300nm. En ce qui concerne les propriétés mécaniques, la nanoindentation et des essais de compression de micro-piliers ont été mis en œuvre sur différentes zones de la microstructure à gradient. Les propriétés mécaniques de ces zones sont ainsi obtenues localement. Une autre partie de ce travail a consisté à utiliser la méthode des éléments finis pour la simulation du comportement mécanique de matériaux nanocristallins. Un modèle en 2D de plasticité cristalline a été utilisé pour cette simulation.

Mots clés : grenaillage de précontrainte – acier inoxydable austénitique – nanoindentation – analyse EBSD.

Experimental Study and Numerical Simulation of the Gradient Properties of 316L Steels Generated by SMAT

This work focuses on the local experimental characterization of the gradient microstructure of 316L steels treated by SMAT. The gradient microstructure could be roughly divided into a top surface nanostructured layer, a transition layer and the bulk region. Grain refinement, compressive residual stress and strain hardening are three major SMAT-induced parameters as a result of severe plastic deformation induced by SMAT. Consequently, the enhanced mechanical properties of the gradient microstructure are due to the combined effects of these SMAT-induced changes. However, emphasis was mainly placed on the global properties of the gradient microstructure in previous studies and little effort was devoted to the individual characterization of each layers. The aim of this work is thus to investigate individually the mechanical properties of each layer by means of various characterization techniques. Characteristics of the gradient microstructure are first highlighted by EBSD which reveals the formation of a top surface nanostructured layer. The grain size for this layer ranges from 50 to 300 nm. As for the mechanical properties, nanoindentation and micro-pillar compression tests were carried out for the individual characterization of each layer of the gradient microstructure. The local mechanical properties could be subsequently derived according to the corresponding mechanical reponse. Another part of this work consisted of using Finite element method for the simulation of the mechanical behaviour of nanocrystalline materials. A two-dimensional crystal plasticity model was thus used for the simulation.

Keywords: shot peening – austenitic stainless steel – nanoindentation – EBSD.

Thèse réalisée en partenariat entre :

CHINA SCHOLARSHIP COUNCIL

utt UNIVERSITÉ DE TECHNOLOGIE TROYES

Ecole Doctorale "Sciences pour l'Ingénieur"